Terminal Fluvial Systems in a Semi-arid Endorheic Basin, Salar de Uyuni (Bolivia)

Jiaguang Li

Terminal Fluvial Systems in a Semi-arid Endorheic Basin, Salar de Uyuni (Bolivia)

PROEFSCHRIFT

ter verkrijging van de graad van doctor
aan de Technische Universiteit Delft,
op gezag van de Rector Magnificus prof. ir. K. C. A. M. Luyben,
voorzitter van het College voor Promoties,
in het openbaar te verdedigen op dinsdag 30 september 2014 om 10:00 uur

door

Jiaguang LI

Master of Mineral Resources Prospecting and Exploration

China University of Geosciences (Beijing), China

geboren te Fujian, China

Dit proefschrift is goedgekeurd door de promotor:

Prof. dr. S.M. Luthi

Copromotor:

Dr. M.E. Donselaar

Samenstelling promotiecommissie:

Rector Magnificus	voorzitter
Prof. dr. S.M. Luthi	Technische Universiteit Delft, promotor
Dr. M.E. Donselaar	Technische Universiteit Delft, copromotor
Prof. dr. M. Menenti	Technische Universiteit Delft
Prof. dr. G. Bertotti	Technische Universiteit Delft
Prof. dr. G.J. Weltje	Katholieke Universiteit Leuven
Dr. B. Makaske	Wageningen Universiteit
Dr. J.E.A. Storms	Technische Universiteit Delft
Prof. dr. S.B. Kroonenberg	Technische Universiteit Delft, reservelid

To my family

Contents

Chapter 1   Introduction

1.1   General Introduction

Endorheic basins, internally drained basins with no direct hydrological connection to the marine environment, can form in various tectonic settings and different sizes (García-Castellanos et al., 2003; Nichols, 2007). For example, the Lake Eyre Basin spreading over 1.14 million km^2 of mostly arid central Australia (Kotwicki and Allan, 1998) is typical of the present-day endorheic basins. Endorheic basins at high altitudes play an important role in sediment accumulations, such as the Puna-Altiplano in the Central Andes, the Tibetan Plateau and Tarim Basin in China (Sobel et al., 2003). These basins are characterized by accounting for 20% of the Earth's land surface, mostly developing in arid regions and collecting only 2% of the global river runoff (García-Castellanos et al., 2003). Globally, there have been many ancient sedimentary basins interpreted as endorheic basins, such as the Mesozoic Sichuan Basin and Ordos Basin in the western China (Zhao et al., 2010), the Triassic Newark-Gettysburg Basin of eastern North America (Faill, 1973), Devonian basin in the North Atlantic area (Friend et al., 2000), the Oligocene to late Miocene Ebro foreland basin in Spain (Nichols, 2004; Nichols and Fisher, 2007), and the late Cenozoic of the South Caspian Sea (Hinds et al., 2004). The endorheic basin fills mainly consist of lacustrine and fluvial sediments, and aeolian accumulations or evaporite deposits, and their thickness can reach hundreds to thousands of metres (Nichols, 2007).

To date, many studies have been conducted on fluvial systems in endorheic basins. Friend (1978) suggested three distinctive characteristics about ancient fluvial stratigraphic units: (1) a downstream decrease in river depth; (2) an absence of alluvial incision; and (3) a convex-upwards, lobate topography of the river systems. This theory was expanded by other researchers (Hirst and Nichols, 1986; Kelly and Olsen, 1993; Nichols and Fisher, 2007; Sáez et al., 2007). They proposed terminal fans or distributary fluvial systems, characteristic of channels decreasing in size and vanishing due to strong evapotranspiration (Figure 1.1A). On the contrary, North and Warwick (2007) argued that the apparent distributary fluvial fan formed as a result of nodal avulsions and subsequent superimposition of active channels over abandoned channels (Figure 1.1B). In addition, Cain and Mountney (2009) claimed that in a fluvial fan system, flow terminated before a significant standing body of water (e.g., the sea or a lake) with the analysis of the Organ Rock Formation. Rock record interpretation is significantly based on what is known about modern settings (Davidson et al., 2011). Modern dryland analogue depositional system are not only essential for developing conceptual geological models of subsurface reservoirs (e.g. the

Rotliegend sediments of the southern North Sea), but also for understanding the distribution of reservoir heterogeneities and properties (Nagtegaal, 1979; Glennie and Provan, 1990; Glennie, 1997a, 2005; Amthor and Okkerman, 1998; Sweet et al., 1996; Fischer et al., 2007; McKie, 2011). In addition, modern depositional systems help to explain basic sedimentological concepts to a broader public (McKie, 2011). There are, however, few studies on modern terminal fluvial systems in semi-arid areas, perhaps because of difficulties such as poor accessibility (Millington et al., 1989; Bryant, 1996) and hazardous situations during peak discharge events (Li et al., 2014).
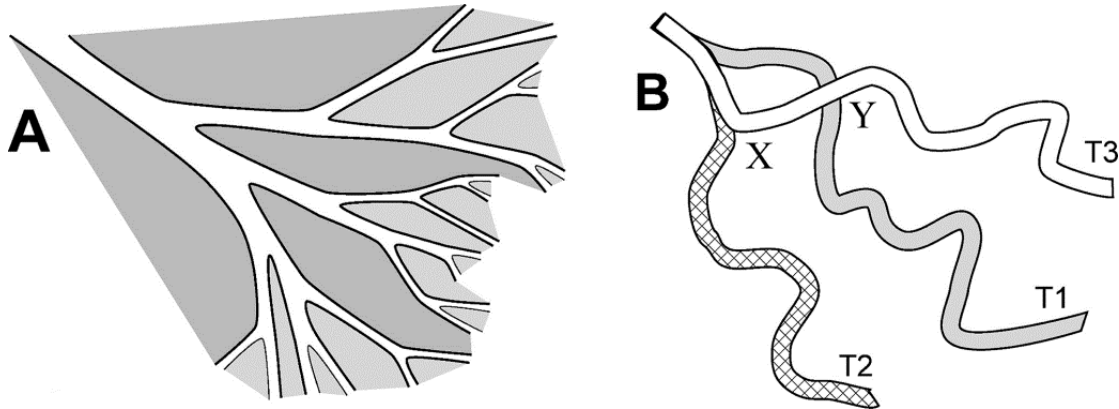
Figure 1.1: *The distinction between truly distributary channels (A) and a radiating set of channel (B) (North and Warwick, 2007).*

1.2 Economic Relevance

As the production of conventional fossil-fuel declines and its demand increases, it is a great challenge to economically produce gas from unconventional sources such as coalbed methane, shale gas, gas hydrate and tight (low-permeability) gas (Naik, 2010). Unconventional gas resources show the potential of significant gas production growth these years. For instance, conventional gas accounted for 43% of the US gas production, approximately 70% of which was from tight gas reservoirs (Khlaifat, et al., 2011). Likewise, once the largest and now the major gas producer in West Europe, the giant Dutch Groningen Gas field, experiences a significant decline in natural gas production (Eker and van Daalen, 2012). Alternatives such as unconventional gas resources have been paid more attention in the Netherlands as the US has successfully utilized them.

As part of the Silverpit Formation in the Southern Permian Basin of NW Europe, the Ten Boer Member (ROCLT; Upper Rotliegend), which consists of a 40-110 m thick mudstone with thin (5-50-cm-thick), very-fine and medium-grained sandstones beds intercalated and which overlies the Slochteren Sandstone reservoir, is interpreted as distal fluvial deposits on a mud flat bordering the Silverpit Desert Lake (Donselaar et al., 2009). It was originally classified as a non-productive "waste zone" due to its low net-to-gross (N/G) ratio (Donselaar et al., 2009, 2011), but a significant amount of gas (30 Mm3) was produced in a depleted well from a thin ROCLT interval through a recent re-perforation test (Donselaar et al., 2011). This successful test stimulated more research into these low N/G thin-bedded fluvial sequences.

The Southern Permian Basin formed as a result of thermal subsidence after the Saalian tectonic phase and the start of a rifting period and associated upper-mantle basalt extrusion at the end of the Hercynian Orogeny (Gebhardt et al., 1991; Glennie, 1998). The basin was structurally surrounded by the London-Brabant Massif and the Variscan Mountain Range in the south, and the Mid North Sear High and the Ringkøbing-Fyn High in the north (Donselaar et al., 2011). With a length of more than 2000 km and a width of 300-600 km from the east coast of the UK to Poland, the Southern Permian Basin lacked any rugged internal topographic relief caused by regionally active tectonism, despite locally active basement faults (Geluk, 2005; McCann et al., 2008). The basin was positioned in the general region of the northeast trade wind belt (Glennie, 1997b), and its climate was characterized by aridity throughout the Permian due to Pangaean continentality and its location in the rain shadow of the Variscan mountains (Roscher and Schneider, 2006; Roscher et al., 2008). In addition, the climatic changes influenced by waning Gondwanan glaciations including global aridity, a lowered sea level and intensified wind strengths, exerted an impact on the fluctuations in water table and fluvial runoff (Glennie, 1997b, 1998). The basin fill is composed of some 2500 m of Upper Rotliegend siliciclastic and evaporite sediments and 2000 m of Zechstein siliciclastic, carbonate, and evaporite deposits (Ziegler, 1990). As part of the Silverpit Formation, the ROCLT succession has five cycles, interpreted as the result of wet-dry-wet climate cyclicity and associated expansion and contraction of the saline lake in the centre of the Southern Permian Basin (Donselaar et al., 2011). According to these characteristics of the ROCLT succession, the Salar de Uyuni in the Southern Altiplano Plateau (Bolivia) is in this study selected as a modern analogue because of the following similarities: (1) Both the Uyuni Basin and the Southern Permian Basin are characterized by a large salt lake in the basin centre; (2) These basins have experienced successive periods of lake expansion-contraction; (3) The main catchments are in nearby mountain ranges in compressional tectonic settings (the London-Brabant Massif for the Southern Permian Basin and the Eastern Cordillera for the Salar de Uyuni Basin), with fluvial systems feeding the basins directly from mountains; (4) The mountain ranges generate rain shadows; (5) The lake edges are typified with low to very low gradients. More detailed information about the geological and climatic settings of the Salar de Uyuni is contained in Section 1.4.

1.3 Objectives and Approaches

The major objective of this work is to investigate the channel morphology and sediment distribution of distal fluvial systems in a semi-arid climatic setting from a modern outcrop analogue, and to build up knowledge for establishing a 3D sedimentary architecture model. The focus of this research is a river terminus system of the world largest salt lake, Salar de Uyuni in Bolivia (Figure 1.2). The unconfined and largely un-vegetated river terminus provides the opportunity to acquire a large data set including field and satellite data, which enables the analysis of channel morphology and sediment characteristics (e.g., avulsion history, splay morphology and surface dynamics). Primary data acquisition consists of daily precipitation data, Global Digital Elevation Model (GDEM), a time series of Landsat imagery and high resolution WorldView-02 and QuickBird-02 satellite images, surface and shallow surface sediment samples, and high precision GPS data.
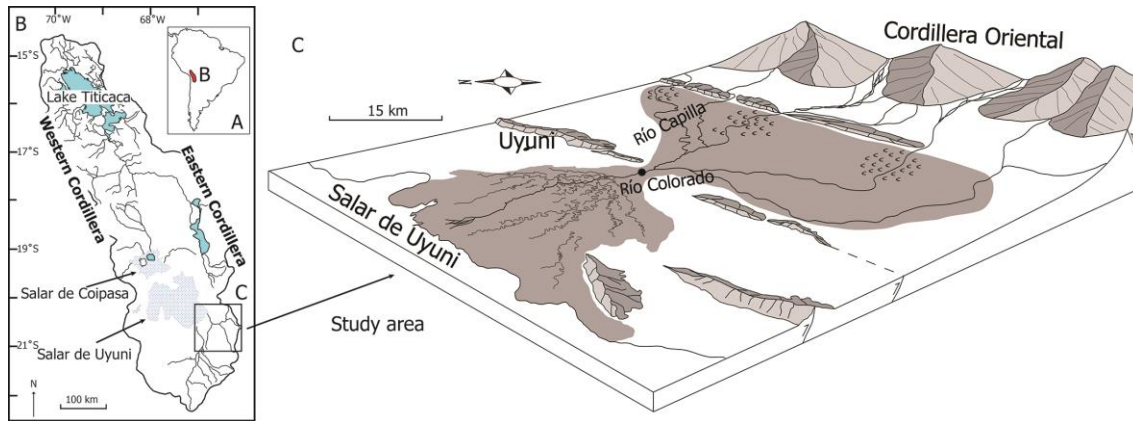
Figure 1.2: *Map of the study area (modified after Placzek et al. 2013 and Donselaar et al., 2013). A indicates the location of Altiplano plateau in the South America. B shows the Altiplano plateau and the site of the river terminus. C is a diagram of the Río Colorado and shows five segments in the study area: (1): Upstream segment, (2)-(3): Confined segment at fault escarpment and bajada, (4): Upper lacustrine coastal plain, (5): Lower lacustrine coastal plain. Grey area indicates upper coastal plain and lower coastal plain.*

Properties of the catchment area (e.g., catchment area and slope) are analysed using a geographic information system software (Arcmap 10). Discharge modelling is performed in combination with catchment parameters and daily precipitation data using an empirical model. Discharge modelling analysis makes it possible to pinpoint peak flood events in the study area and a time series of Landsat imagery is used to detect geomorphological changes before and after peak flood events.

Bi-temporal high-resolution satellite images are used to quantify channel morphology in the tributary catchment. Bank accretion and erosion areas are calculated based on the positions of left bank and right bank in different periods, and analysed in terms of kilometre-based distribution, statistics of areas and shift magnitude. The mechanisms of river bank erosion and the impacts of river bank activities on channel planforms are also investigated.

The bi-temporal high-resolution satellite images are also used to analyse splay morphodynamics in the river terminus in combination with precipitation data, cross-sectional area of channels and high resolution GPS data. WorldView-02 images were registered to QuickBird-02 images with the help of ENVI. Splay morphodynamics are analysed based on the statues of crevasse splays in two periods. A Trimble R7 dual frequency geodetic GPS receiver was used to measure the gradient along the river. The relationship between the downstream reduction in cross-sectional area and the number of crevasse splays is investigated.

The sediment dispersion pattern is investigated in combination with the analysis of field outcrops and grain size distributions. Grain size distribution is decomposed to investigate sediment distribution along the river system. The central logratio method is used to calculate the mean value of each end member at a single point with multiple samples (e.g., point bars), and these mean values are then used to investigate downstream changes of sediment loads. High precision GPS data are used to investigate the slope changes in the low-gradient river system and

grain size distribution along the longitudinal profile is established. Geomorphological changes are analysed along the profile with the help of high-resolution satellite images.

Landsat time series imagery is analysed in terms of playa morphodynamics in combination with precipitation data and field work measurements. Several types of sediments (e.g. silt-rich and clay-rich sediments) are used to establish a relationship with spectral reflectance and therefore to build spectral libraries for each type of surface materials. Such spectral libraries are then used to classify Landsat time series data from 1985 to 2011 over the study area. A maximum likelihood classification (MLC) method is used as a supervised classifier, where the training data are introduced using spectral libraries.

1.4   Geological Settings and Climate

1.4.1   Tectonic Evolution

The Andean history is divided into four major stages (Gansser, 1973). In the first stage, the proto-margin of Gondwana was reconstructed and this process included amalgamation and collision of different terranes against the late Proterozoic margin of Gondwana. In the second stage, the Gondwanides and the Alleghanides formed in the Late Paleozoic. The Gondwanides were the first mountain chain developed along the Pacific margin by an Andean-type subduction, while the Alleghanides were associated with the closure of the Iapetus Ocean and the formation of the Pangea Supercontinent. In the third stage, a generalized extension occurred during Pangea break-up that predated the opening of the South Atlantic and related oceans, and this stage was punctuated by the collision of island arcs in the Northern Andes. The present orogeny occurred in the last stage, which included many tectonic processes from collision of island arcs, seismic and aseismic ridges, and normal subduction of oceanic crust under the South American Plate.

As one of the largest continental plateaus on Earth, the Altiplano is located in the central Andean orogenic belt (Figure 1.2 and Figure 1.3, Horton, 1999; Murray et al., 2010). The uplift of the Altiplano plateau is attributed primarily to crustal thickening, which accounts for 70-80% of the contribution, while other processes such as lithospheric thinning, upper mantle hydration, or tectonic underplating may contribute to the rest of the thickening (Allmendinger et al, 1997), although some studies questioned the current estimates of total shortening (Kley and Monaldi, 1998; McQuarrie, 2002). Allmendinger et al. (1997) also demonstrated that the uplift began around 25 Ma in the region of the Altiplano, coincident with increased convergence rate and inferred shallowing of subduction. Furthermore, the Altiplano Basin has been tectonically quiescent in the Late Pleistocene and Holocene (Bills et al., 1994; Baucom and Rigsby, 1999; Rigsby et al., 2005).
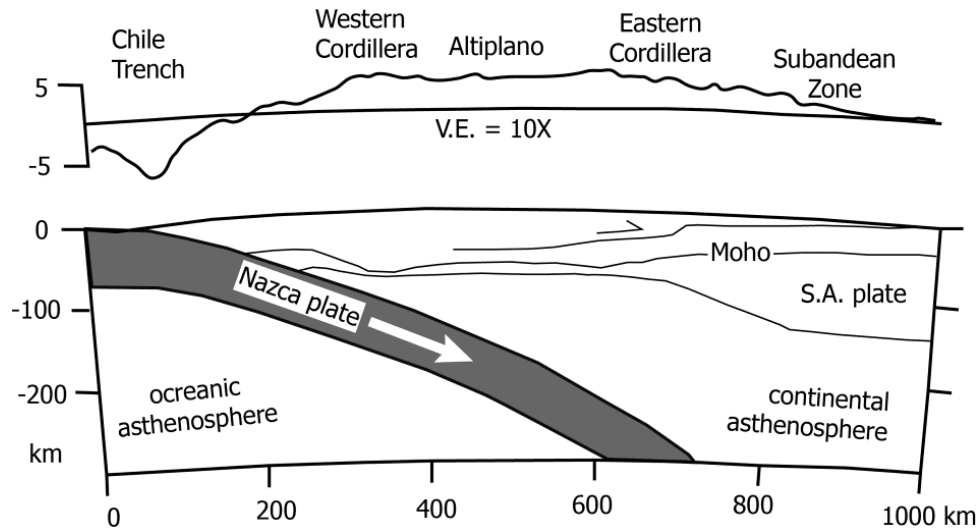
Figure 1.3: Lithospheric cross section showing the topography and structure of the central Andes (Horton, 1999).
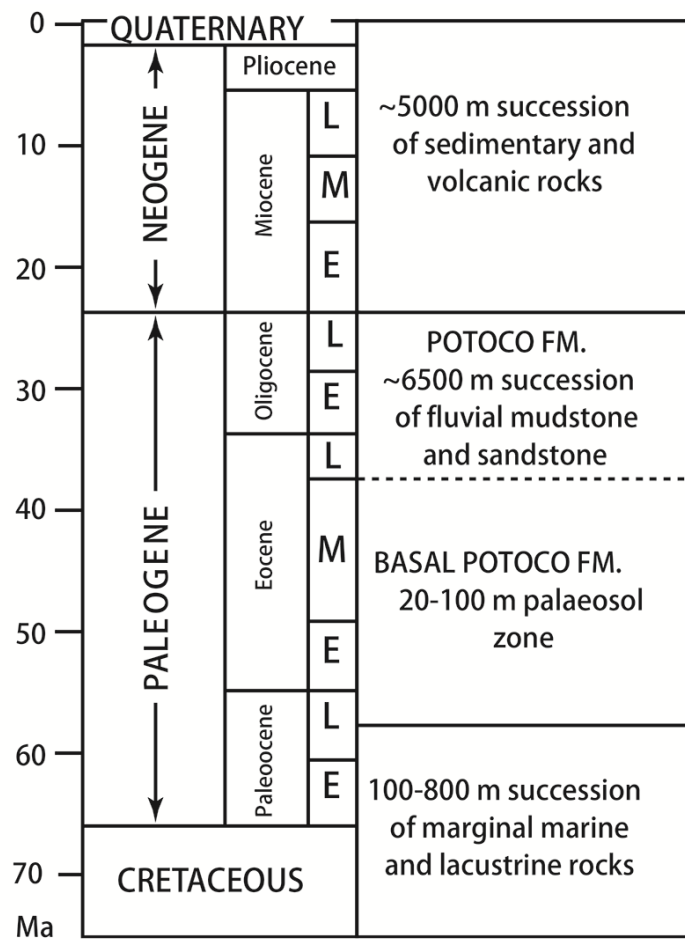

Figure 1.4: Chronostratigraphic diagram of the uppermost Cretaceous-Cenozoic rocks in the northern and central Altiplano (Horton et al., 2001).

1.4.2   Stratigraphy

The Altiplano includes three major successions: (1) a lower succession of regionally extensive, Maastrichtian to mid-Paleocene, marginal marine and nonmarine sedimentary rocks (El Molino and Santa Lucia Formation); (2) an intermediate, poorly dated succession of nonmarine sedimentary rocks (Potoco Formation); and (3) an upper interval of upper Oligocene to Quaternary nonmarine sedimentary and volcanic rocks (Figure 1.4, Horton et al., 2001; Hampton and Horton, 2007).

The El Molino Formation is the lowest succession and is widely distributed over the Altiplano and Eastern Cordillera. This formation is a 200-600-m-thick section of carbonate and subordinate mudstone, which indicates depositional environments of shallow marine, lacustrine and distal fluvial settings (Horton et al., 2001). The El Molino formation records the final marine conditions in the Altiplano-Eastern Cordillera region (Lundberg et al., 1998). Conformably overlying the El Molino Formation, the Santa Lucia Formation is a 50-300-m-thick section of inter-bedded mudstone and sandstone deposited in distal fluvial settings.

The Potoco Formation comprises the greatest volume of Tertiary deposits in the Altiplano and possibly the entire central Andes (Horton et al., 2001). Overlying the Santa Lucia strata and underlying Neogene rocks, this 3000-6500-m-thick succession consists of sandstone, mudstone, limited evaporite and fluvial-lacustrine facies associations. Upper Oligocene to Quaternary sedimentary and volcanic rocks comprise the upper 1000-4000-m-thick interval. This succession consists of basal conglomerate and sandstone, which was deposited in alluvial-fan and fluvial systems (Sempere et al., 1990; Rochat et al., 1998), and Lower Miocene to Quaternary volcaniclastic deposits.

1.4.3   The Altiplano Palaeolake Chronology

Three large hydrographic basins (Titicaca in the North, Poopó in the centre, and Coipasa and Uyuni in the South) occupy the internally-drained intermontane depression, the Altiplano Basin (Figure 1.2). Sedimentological studies, which include paleoshorelines, carbonate bioherms, cored lake deposits, palynological studies, diatom analyses and U-Th and 14C dating, showed that the Altiplano Basin has undergone several wet-to-dry cycles since the late Pleistocene (Bills et al., 1994; Servant et al., 1995; Sylvestre et al., 1999; Baker et al., 2001a, b; Fornari et al., 2001; Fritz et al., 2004; Rigsby et al., 2005; Placzek et al., 2006; Placzek et al., 2013). Three wet periods in the Altiplano include the Minchín (46,000-36,000 cal. yr B.P.), Tauca (26,100-14,900 cal. yr B.P.) and Coipasa (13,400-11,500 cal. yr B.P.) periods (Figure 1.5, Bills et al., 1994; Placzek et al., 2006; Donselaar et al., 2013).
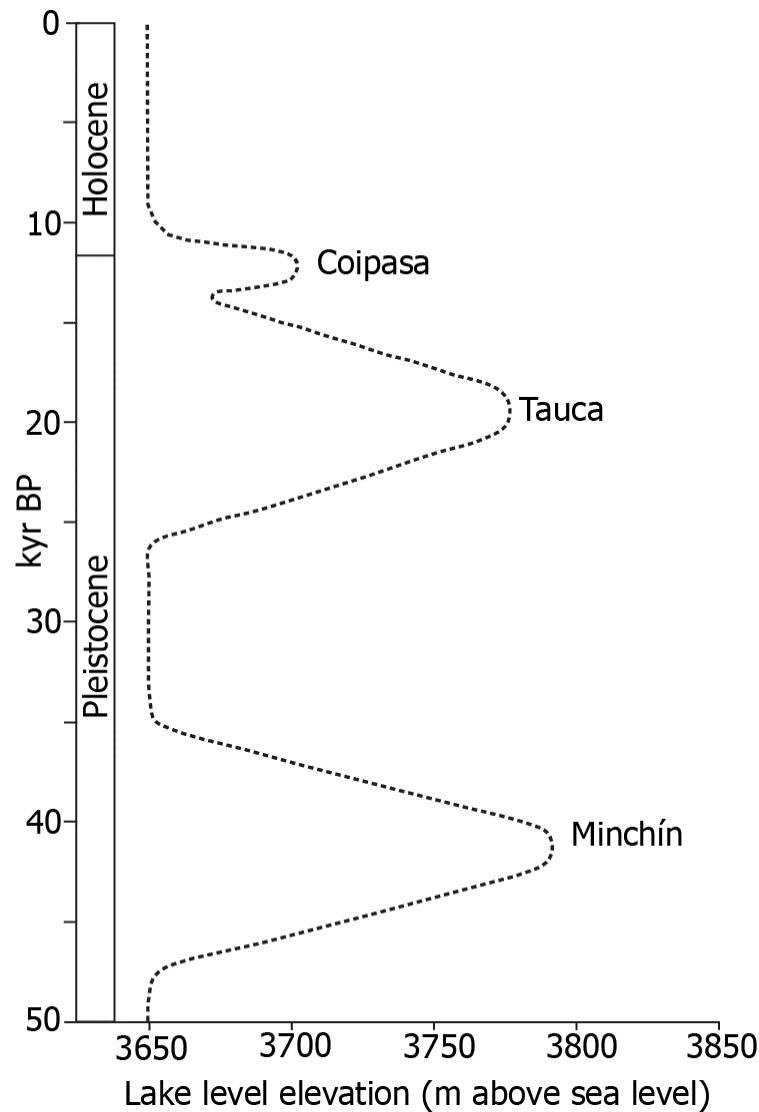
Figure 1.5: *Pleistocene-Holocene lake level fluctuations with lake highstands indicated (modified from Donselaar et al., 2013).*

1.4.4   Modern Climate and the Río Colorado

Placzek et al. (2013) found that modern interannual rainfall variability is strongly tied to the strength of the trade winds, the position of the Inter-tropical Convergence Zone (ITCZ), meridional temperature gradients and the temperature of the tropical Atlantic over the South America lowlands. The dominant moisture source over tropical and subtropical South America is the Atlantic Ocean to the east. The tropical moisture is carried onto the South American continent by the trade winds, which feed the ITCZ (Figure 1.6, Placzek et al, 2013). The ITCZ, displaced southward in the austral summer, brings heavy rainfall extending from the southern half of the Amazon Basin to northern Argentina (Garreaud et al., 2009). Meanwhile, the easterly winds

forced by a deep continental low over the Gran Chaco region of Argentina (~25 °S) flow over the Amazon to turn southward and transport moisture along the eastern slope of the Andes in a low-level jet (Seluchi et al., 2003). Significant moisture carried by this jet from the Amazon Basin into the subtropics feeds intense convective storms as far south as 35 °S (Garreaud et al., 2009). The latent heat driven from the Bolivian High over the Amazon Basin reinforces the transport of moisture onto the Altiplano (Lenters and Cook, 1997). This moisture source to the north and east of the Altiplano produces a north-south precipitation gradient, which leads to approximately 1000 mm/yr of annual precipitation in Lake Titicaca and less than 200 mm/yr in the southern basins (Argollo and Mourguiart, 2000). Zhou and Lau (1998) call this strong seasonal cycle the South American Summer Monsoon (SASM).
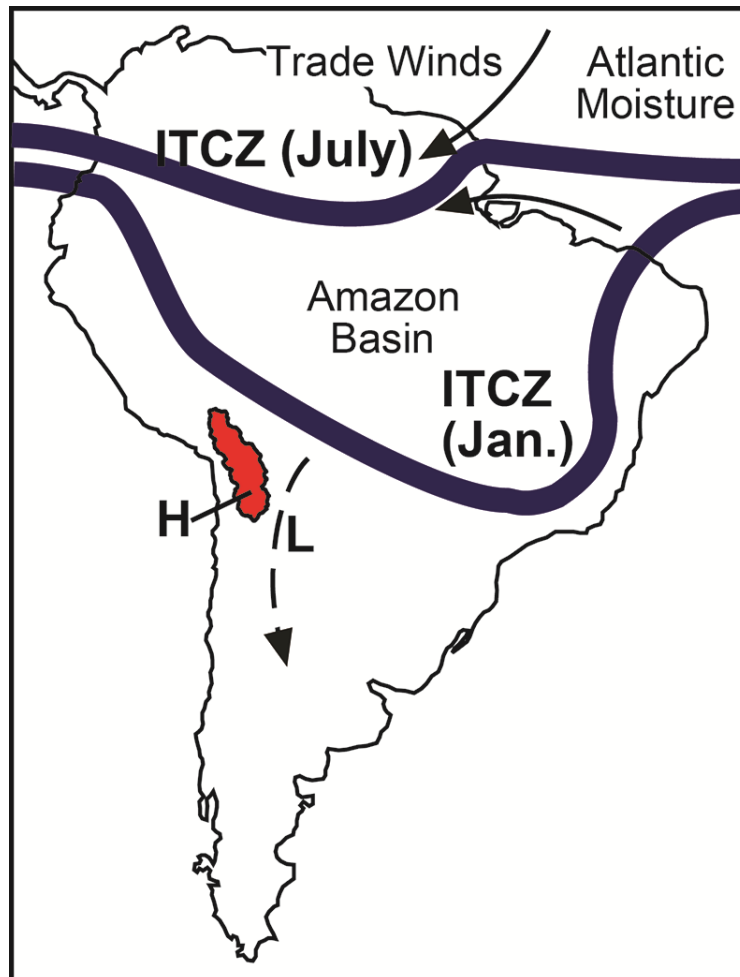
Figure 1.6: *The major climate features of South America (Placzek et al., 2013). The Altiplano lake basin is shown in red. The thick blue line is the ITCZ (Intertropical Convergence Zone). North easterly and southeasterly trade winds (black arrows) feed into the ITCZ and move tropical moisture from the Atlantic onto the South American continent. The approximate positions of the Chaco low (L) and Bolivian High (H) are shown. The Chaco low forces the easterly winds that flow over the Amazon to turn southward, channeling moisture southward along the eastern slope of the Andes in a low-level jet (dashed arrow).*

The availability of moisture at the eastern foot of the Andes and the transport of this moisture onto the Altiplano control modern interannual precipitation variability (Placzek, 2005). Precipitation over the northern Altiplano is controlled by easterly wind anomalies transporting Amazon moisture onto the Altiplano, and these easterly wind anomalies are related to the El Niño/Southern Oscillation (ENSO) (Garreaud and Aceituno, 2001; Vuille and Keimig, 2004). Analysis of daily precipitation data in the study area and ENSO records showed that La Niña years appear to correlate somewhat with more rainfall in the study area (Figure 1.7).

The Río Colorado dryland river system with a SE-to-NW flow direction terminates on a flat coastal plain at the south-eastern edge of the Salar de Uyuni, Bolivia (Figure 1.2). Characteristic of a dendritic pattern, the tributary streams in the catchment cover an area of 9.529×103 km^2. The rainy season in Uyuni concentrates over four months, from December to March, and the mean annual precipitation is 185 mm in the period of 1975-2012. The river terminus, with an area of about 475 km^2, shows successive channel paths that developed from multiple nodal avulsions (Figure 1.8, from Donselaar et al., 2013).
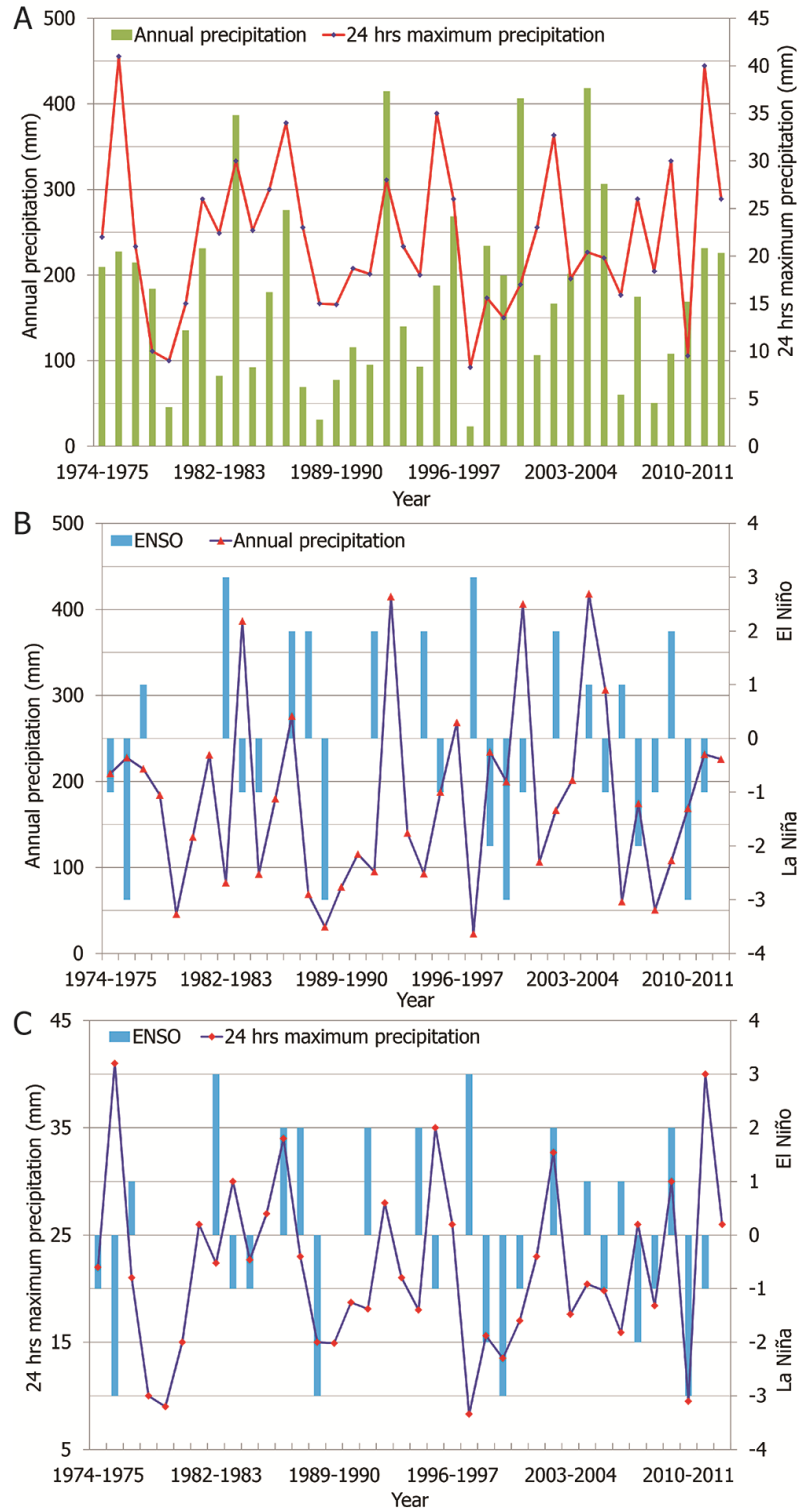
Figure 1.7: *Precipitation data in the Salar de Uyuni from 1974 to 2012 (A) and the relationship between Southern Oscillation (El Niño and La Niña) and precipitation in the study area (Annual precipitation (B) and 24 hrs maximum precipitation (C)), respectively. Note that El Niño and La Niña are divided into three levels: 1: weak; 2: intermediate; 3: strong.*
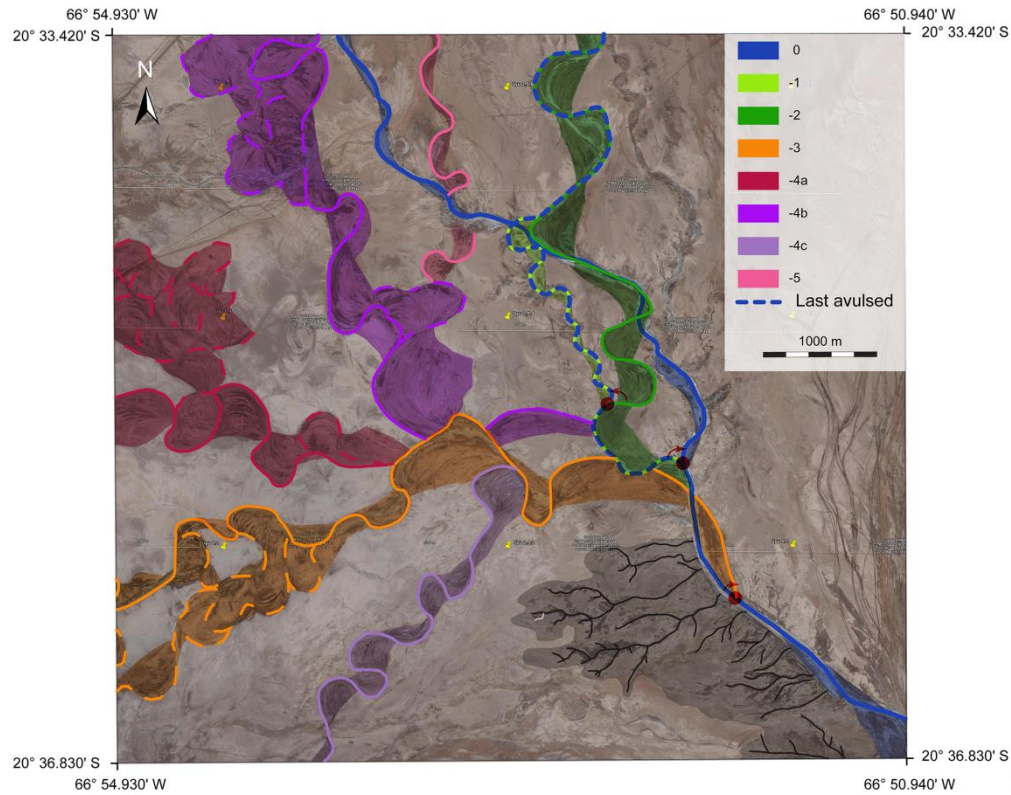
Figure 1.8: *Reconstruction of the abandoned channel pathways and indication of avulsion locations (Donselaar et al., 2013). Note that the apparent bifurcating pattern is created by avulsions and superposition of channels over older ones. Numbers − 5 to 0 indicate successive river paths, −5 is the oldest, 0 is the recent river channel. Dash line: last-avulsed channel which has remnant concave channel morphology. Channel group −4 is in age between −5 and −3, but relative age of −4a, −4b, and −4c could not be established.*

1.5   Thesis Outline

Chapter 1 provides a geological and climatic background in the study area for the following chapters.

In Chapter 2, the catchment area is analysed in terms of its area and slope. Peak discharge events are pinpointed by an empirical discharge model, which is performed in combination with catchment parameters such as its boundary, slope and soil etc. Landsat time series imagery is selected before and after peak floods for investigating geomorphological changes. The development of a crevasse splay and avulsion history in the distal part of the river terminus is described.

In Chapter 3, bank accretion and erosion in the tributary catchment is analysed with the help of high-resolution satellite images, with the accompanying channel morphology also being

analysed. The mechanisms of bank erosion and accretion, and their impacts on channel planforms, are discussed.

In Chapter 4, the splay morphodynamics in the distal part of the river terminus are analysed. Splays are categorised into three types based on their development over a given time period using high-resolution satellite images. The transport and depositional processes responsible for the development of crevasse splay are discussed.

In Chapter 5, the sediment dispersal pattern is investigated from alluvial fan to the river terminus in combination with high-precision GPS data. Grain size distribution is decomposed into suspended load and bed load. The downstream changes in different sediment loads are investigated, and diagrams of unconsolidated sediment dispersion are proposed.

In Chapter 6, the relationship between surface materials (clay-rich materials and silt-rich materials) and surface reflectance is established and its spectral library is applied to classify surface materials of Landsat time series imagery (1985-2011). This chapter also investigates the relationship between various surface materials and sedimentary facies, and the mechanisms of surface dynamics are discussed.

In Chapter 7, a summary of the major results is given and the preservation potential and sequence stratigraphy is analysed, followed by recommendations for future research.

Chapter 2   Climate analysis and channel morphology[1]

Abstract. *In this remote sensing-based study we present the analysis of the geomorphological development at the low-gradient terminus of the modern Río Colorado dryland river system in the endorheic Altiplano Basin (Bolivia). Changes in the river morphology occur after short periods of catastrophic peak discharge which result in the expansion of existing crevasse splays, formation of new crevasse splays and in river path avulsion. Episodic peak discharge events in the study area were pinpointed and quantified by combining daily precipitation records from gauging stations in the vicinity with catchment area analysis from ASTER global DEM (GDEM) remote sensing data. A time series of Landsat imagery for the period 1975 - 2001 was then used to analyze the river morphology changes after major peak discharge events. Compensational stacking of crevasse splays in combination with river avulsion produced a thin but aerially extensive connected sand sheet at the terminus of the fluvial system.*

2.1   Introduction

River systems in dryland areas are characterized by long intervals of river channel inactivity in the dry periods, alternating with short, episodic periods of peak discharge (Knighton and Nanson, 1997; Tooth, 2000b). Water discharge in the low-frequency, high-magnitude peak discharge periods greatly exceeds the river capacity, hence immediate and massive river flooding and over-spill of flood waters and sediment onto the adjacent floodplain occur. These processes are especially active in the dryland river terminus, where the dryland river channels show downstream decrease in cross-sectional area by the combination of low gradient, strong evapo-transpiration potential and water percolation through the channel floor. This results in significant downstream decrease in channel capacity of transporting water and sediment (Tooth, 2000a; Donselaar et al., 2013). It is in these peak discharge periods that the major geomorphological changes and landscape development take place, such as the formation and / or expansion of crevasse splays, changes in river course, and channel avulsion (Baker, 1977; Graf, 1983, 1988a and 1988b; Knighton and Nanson, 1997).

Due to the hazardous environment during peak discharge, it is difficult to access or directly observe the geomorphological changes. The present paper aims to reconstruct the relationship between peak discharge events in an ephemeral dryland river system and the development of river avulsions and crevasse splays, and to visualize with remote sensing imagery the resulting morphological changes at the terminus of the river system over a period of 30 years. We use daily precipitation data in the study area over the period 1975 – 2010, complemented with precipitation datasets around the catchment of the Río Colorado. In combination with ASTER and Landsat TM images the precipitation data analysis allows to quantify and pin-point the short, episodic flood periods. ASTER global digital elevation model (GDEM) data will be used to acquire the catchment information such as its boundary, area and slope. Double mass curves will be used to investigate the consistency of precipitation data from different meteorological stations. With the catchment information, the Thiessen polygon method will be used to calculate the areal precipitation in the catchment area. Landsat TM data will be used to extract spectral information about vegetation cover in the catchment area. Together with areal precipitation and catchment information, an empirical model will be used for peak discharge modeling and the magnitude of flood can be quantified. Through the results of discharge modeling and precipitation analysis in the study area, the flood periods will be pinpointed. In the process, Landsat Multispectral Scanner (MSS) and Thematic Mapper (TM) images are selected before and after flood events and the changes in the river morphology triggered by peak discharge will be analyzed. The visualization of the avulsion history and the development of crevasse splays are of significant importance in establishing three-dimensional sedimentary architecture models of sheet deposits in distal fluvial systems.

2.2   Data Acquisition and Methods

2.2.1   Data acquisition

Daily precipitation data and 24 h maximum precipitation data for the period 1975 – 2010 were obtained from the Bolivian Servicio Nacional de Meteorología e Hidrología (http://www.senamhi.gob.bo/). Data were from three gauging stations (Uyuni, Atocha and San Pablo de Lípez) in the study area and around the Río Colorado catchment area (Figure 2.1).
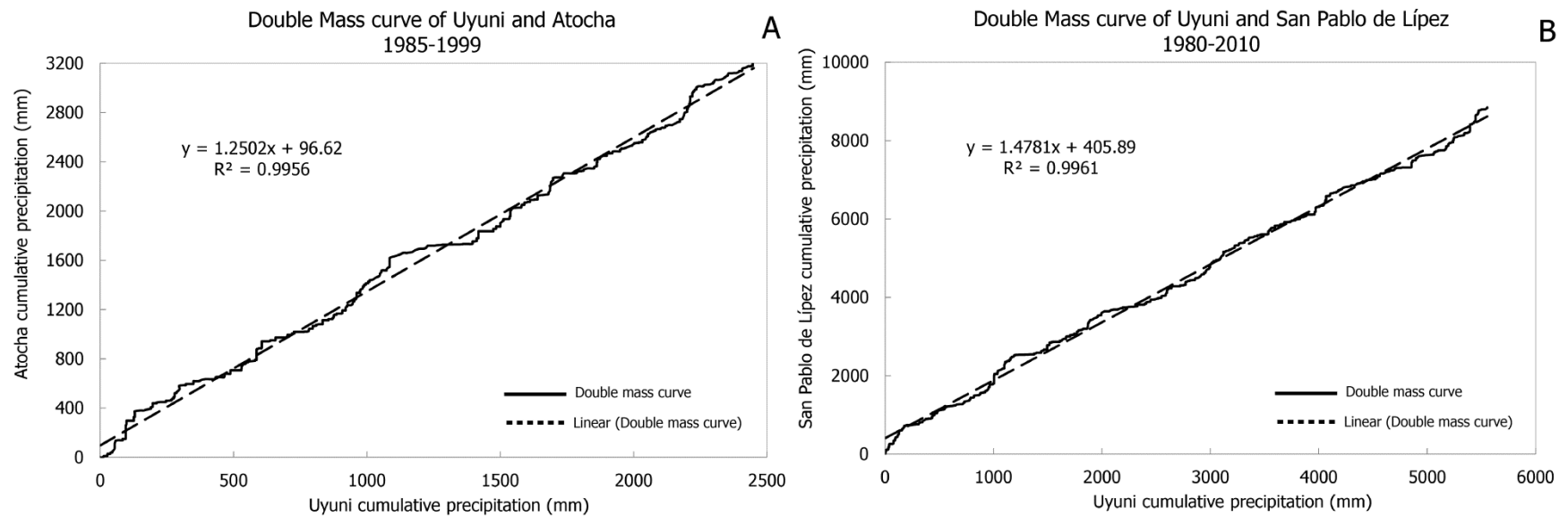
Figure 2.1: *Double mass curves of precipitation in Uyuni against precipitation from two other meteorological stations, Atocha (A) and San Pablo de Lípez (B).*

ASTER (Advanced Spaceborne Thermal Emission and Reflection Radiometer) aboard the Terra platform includes a nadir and 27.6° backward-looking telescope in the Near Infrared (NIR) spectral band and therefore this setup allows for the generation of photogrammetric digital elevation model (DEM) with vertical accuracies of 15-30 m or ±60 m in rough mountainous areas (Toutin, 2008; Kääb, 2002). The ASTER global DEM (GDEM) produced by automated processing of the entire 1.5 million scenes of the ASTER archive from 2000 to 2007 were released in 2009 by the Ministry of Economy, Trade and Industry (METI) of Japan and NASA (METI, 2009). ASTER GDEM data covered 99% of the Earth's land surface from 83°N to 83°S and have a horizontal resolution of 1 arc-second (~30 m). ASTER GDEM data were available for download from NASA Reverb (http://reverb.echo.nasa.gov/) and NASA Land Processes Distributed Active Archive Centre (http://gdex.cr.usgs.gov/gdex/). This paper analysed 16 ASTER GDEM scenes (Table 2.1).

S19W065	S19W066	S19W067	S19W068
S20W065	S20W066	S20W067	S20W068
S21W065	S21W066	S21W067	S21W068
S22W065	S22W066	S22W067	S22W068

Table 2.1: *ASTER GDEM scenes used in the paper.*

Landsat Multispectral Scanner (MSS) and TM (Thematic Mapper) imagery from Landsat 4/5 was used for monitoring flood-induced river morphology changes. MSS and TM data, located at U.S. Geological Survey (USGS) Centre for Earth Resources Observation and Science (EROS) (http://glovis.usgs.gov/) were collected for the period 1975 – 2011. Landsat MSS includes data in four bands, two visible bands and two near infrared bands. Landsat 4/5 TM data were acquired in two different resolutions (Table 2.2, Campbell, 2007): multispectral bands (bands 1-5, 7) with a resolution of 30 m and the thermal band (band 6) with 120 m resolution.

Spectral bands		Wavelength (µm)	Resolution (m)
1	Visible	0.45-0.52	30
2	Visible	0.52-0.61	30
3	Visible	0.63-0.69	30
4	Near-Infrared	0.76-0.90	30
5	Near-Infrared	1.55-1.75	30
6	Thermal	10.40-12.50	120
7	Mid-Infrared	2.08-2.35	30

Table 2.2: *Landsat Thematic Mapper bands.*

2.2.2   Methods

2.2.2.1   Precipitation analysis and discharge modeling
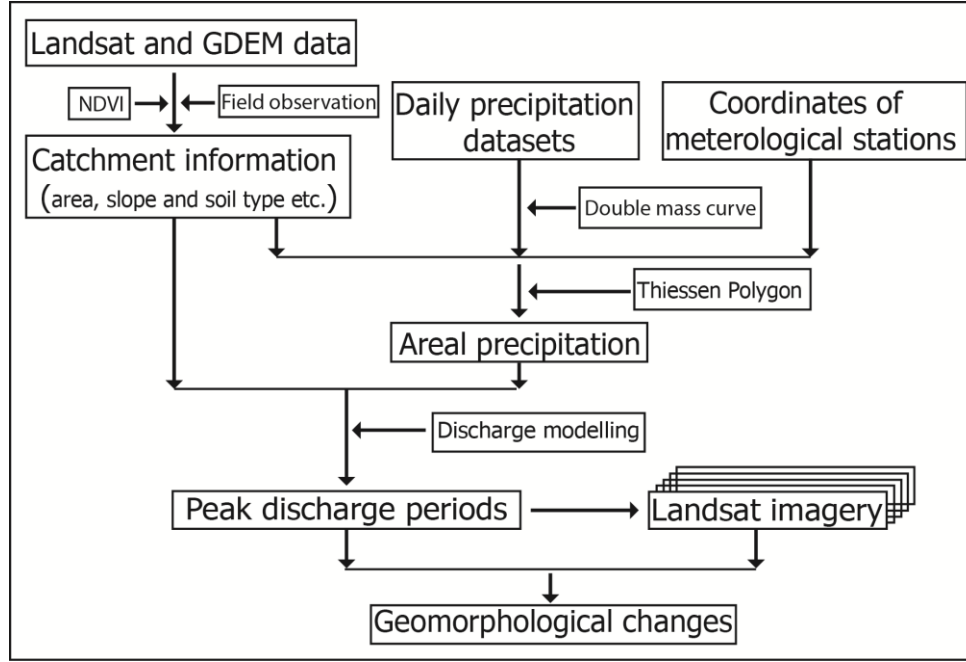
Figure 2.2: *Flow chart of methodology in the study.*

Analysis of the daily precipitation dataset was performed to pinpoint flood events and obtain flood magnitudes (Figure 2.2). Double mass curve analysis, as basic hydrologic analysis tools, was performed to assess the consistency of precipitation data between gauging stations over the same time period and to identify changes in trends by changes in the slope of the double mass curves (Searcy et al., 1960). In addition, Thiessen polygon, which is a method to analyze precipitation data from unevenly distributed measurement stations (Thiessen and Alter, 1911), was used to calculate areal precipitation in the catchment area. Areal precipitation data covered a time range of 1985-1999. Analysis of ASTER GDEM data with ArcMap 10 software yielded the drainage area values as well as slope and relief therein. An empirical method based on the Soil Conservation Service curve number and catchment characteristics developed by El-Hames (2012) was used to predict peak discharge in ungauged areas of the catchment. This method (Eq. 1) was derived from datasets of 76 rainfall-runoff events from 17 catchments located in arid and semi-arid regions such as Walnut Gulch, Arizona (USA) and Wadi Ahin, Oman (El-Hames, 2012).

$$Q_p = \frac{10 P_e A Y^{0.65}}{L^{0.2} d^{0.2}} \qquad (2-1)$$

Where P_e is effective rainfall (mm), A is catchment area (km^2), Y is catchment average slope (m/m), L is main channel length in the wadi (m), and d is catchment storage depth from the rainfall event due to abstraction, evaporation, infiltration, etc. (mm). To obtain effective rainfall and catchment storage depth, the catchment curve number (CN) is estimated from satellite

images, field observation, tabulated values or calibration with gauged catchments (Marek, 2011; El-Hames, 2012). In the present study CN was obtained by the combined analysis of satellite analysis (NDVI, see following text) and field observation (vegetation type and soil type). Moreover, CN values depend on wet (WCN) or dry (DCN) conditions. This could be calibrated by the following equations:

$$WCN = \frac{23CN}{10 + 0.13CN} \qquad (2-2)$$

$$DCN = \frac{4.2CN}{10 - 0.058CN} \qquad (2-3)$$

If the CN value is obtained, the maximum storage (S) of the catchment can be calculated by the following equation:

$$S = \frac{25400}{CN} - 254 \qquad (2-4)$$

The prerequisite to use the Eq. (2-1) is that a certain amount of the rainfall should satisfy the maximum storage in the catchment; otherwise it would not produce any runoff. The rainfall depth, the total amount of rain, should be at least greater than 20% of the maximum storage. Below this value all rainfall is assumed to fill the catchment storage and not produce any runoff. According to the defined CN and S values, effective rainfall (P_e) can be calculated from the following equation:

$$P_e = \frac{(P - 0.2S)^2}{P + 0.8S} \qquad (2-5)$$

where P is rainfall and S maximum storage of the catchment. The storage depth in Eq. (1) above is derived from rainfall depth (P) and effective rainfall depth (P_e):

$$d = P - P_e \qquad (2-6)$$

2.2.2.2 Landsat images processing

The visible and near-infrared bands 1-5 and 7) of Landsat images were calibrated to surface reflectance. Radiometric normalization called iteratively reweighted multivariate alteration detection (IR-MAD) has been used for a time series of Landsat TM images. IR-MAD is a method of change detection between two multi- or hyperspectral images of the same scene acquired at different times (Canty et al., 2004; Nielsen, 2007; Canty and Nielsen, 2008), due to variations in atmospheric conditions, solar illumination angles and sensor calibration trends (Du et al., 2002). To understand vegetation cover in the study area, Normalized Difference Vegetation Index (NDVI) was used to measure the vegetation cover in the catchment area. NDVI is a ratio that uses the NIR and red bands to distinguish the differences between vegetated and non-vegetated areas.

$$NDVI = \frac{NIR - RED}{NIR + RED} \qquad (2-7)$$

where NIR is the near-infrared band (TM band 4) and RED is the red response (TM band 3) (Tucker, 1979). The threshold value of NDVI for vegetation cover was determined in combination with field observation. In addition, we chose different bands to visualize channel paths and crevasse splays in different periods. Histogram stretching was applied to Landsat grayscale images; with this method the range of pixel intensity value is changed, thereby enhancing the image contrast. Changes in channel morphology and crevasse splays were detected by manual vectorization in the ENVI remote sensing image analysis environment of river channel path in geo-referenced satellite images.

2.3   Results and Analysis

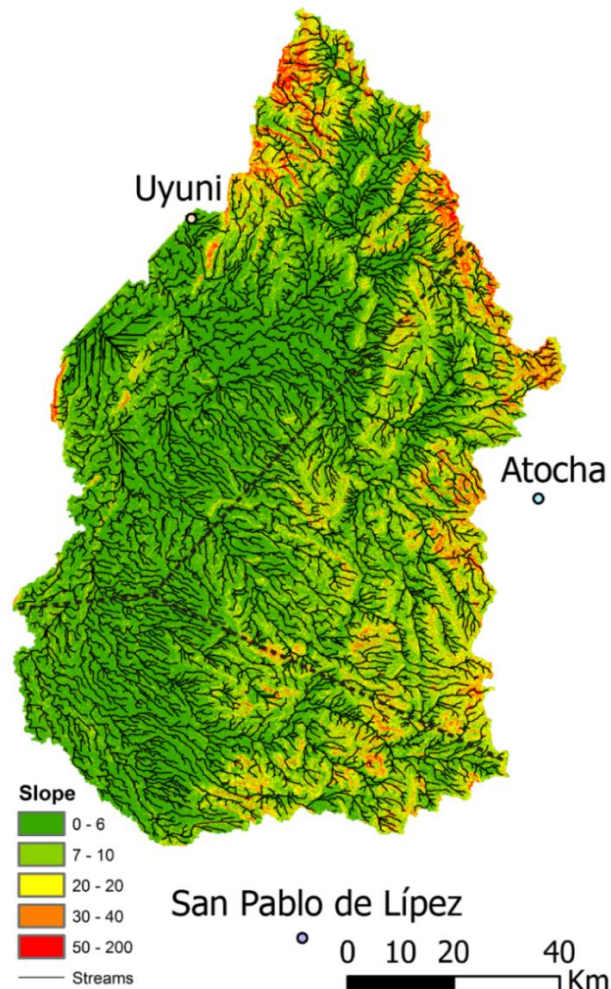### 2.3.1   Catchment area analysis

Figure 2.3: *Dendritic pattern of river system in the catchment area of the study area and its map of slope. Dashed lines show the Thiessen Polygons and the slope is derived by rise over run times 100 (m/m*100).*

Catchment area (km^2)	Mean slope (m/m)	Main Channel length (km)	CN	DCN	WCN
9549	0.0008	90	77	58	88

Table 2.3: *Catchment Parameters.*

Changes in channel morphology of the terminal fluvial system are a function of the precipitation intensity in the catchment area. The tributary streams in the catchment have a dendritic pattern (Figure 2.3), and cover an area of 9.549×10^3 km^2 (Table 2.3). The catchment profile shows a mean slope of 0.0008 m/m; the highest slope is near the margin and gradually decreases downstream (Figure 2.3). The surface sediment consists of Quaternary alluvium, which comprises Upper Oligocene to Quaternary sedimentary and volcanic rocks (Marshall et al., 1992; Horton et al., 2001). Analysis of double mass curves shows linear trend lines (Figure 2.1) with high coefficients (0.9956 and 0.9961 respectively), which indicates high consistency of the precipitation pattern in Uyuni with that of the catchment area. Thiessen polygon analysis indicates the weighted contribution of precipitation data from meteorological stations to the areal precipitation in the catchment area (Figure 2.3 and Table 2.4).

The threshold value of NDVI in the catchment was 0.097 according to NDVI analysis and field observation. NDVI analysis (Figure 2.4A) shows that vegetation cover in the mountainous regions is higher than that in the tributary delta and terminal fluvial fan. This is because the precipitation is higher in the mountainous areas due to moisture carried by the northwesterly wind and precipitated with increasing elevation. Vegetation is mainly in the form of shrubs (Figure 2.4B) due to high elevation (more than 3700 m above sea level) and low annual mean temperature (9 ℃). In such a region, the surface becomes more compacted because of raindrop impacts, by which space between coarse grains is filled by finer grains (Wainwright and Bracken, 2011). Therefore rainfall would quickly become overland flow, generally within minutes (Yair and Lavee, 1976; Reid and Frostick, 1986) and only little infiltration of the soil. Based on hydraulic soil groups (Marek, 2011), the soil in the catchment area was categorized as moderately high runoff potential due to slow infiltration rate (Group B). Combined with soil group and vegetation type and climatic condition, the curve number (77) in the catchment was obtained (Marek, 2011) and CN values were obtained for dry and wet conditions according to Eqs. (2) and (3) (Table 2.3).

Meterological Stations	Area (Km^2)	Weight
Uyuni	3981.66	0.42
Atocha	3105.91	0.32
San Pablo de Lípez	2461.65	0.26

Table 2.4: *Results of Thiessen Polygon method.*
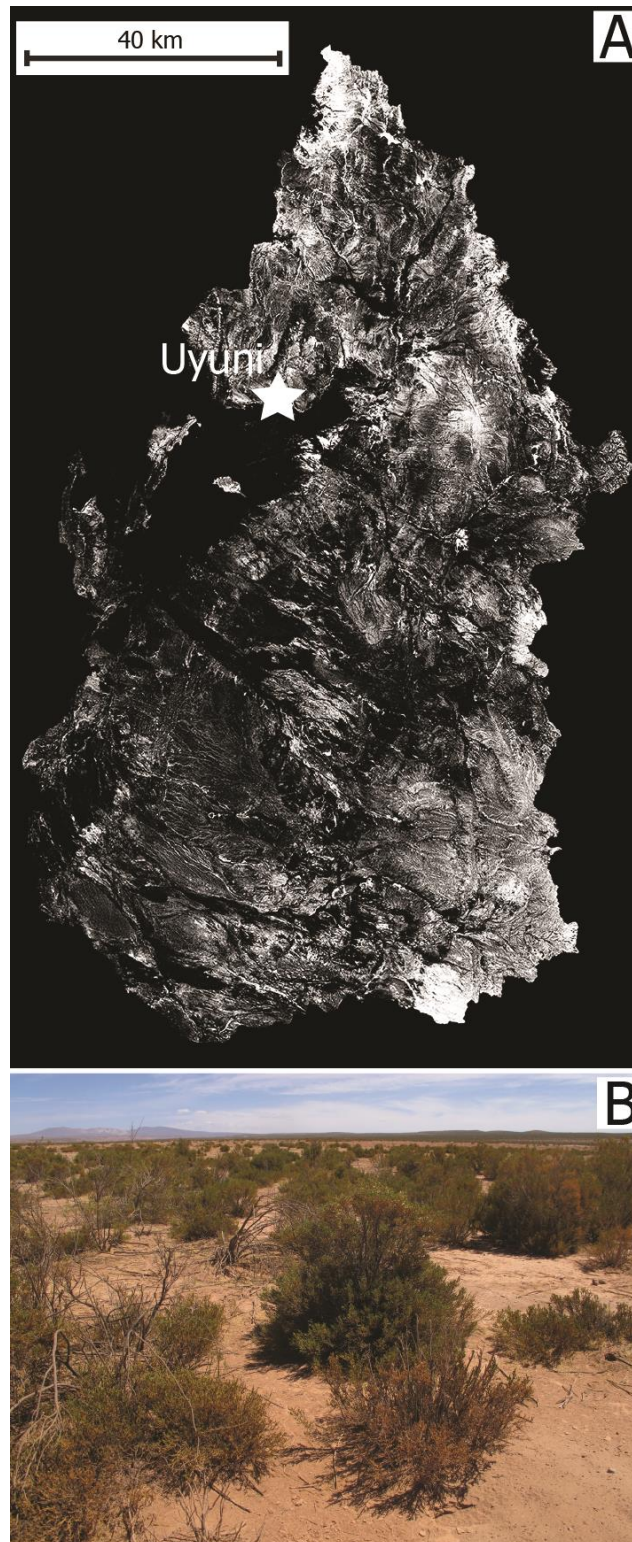
Figure 2.4: *A grey-scale image of NDVI with threshold value of 0.097 (A). The white areas are covered by vegetation and the black regions are bare land. The asterisk shows the location where the picture was taken. B: vegetation cover in the catchment area (Latitude: 20°37'6.46"S; Longitude: 66°41'51.79"W). Its NDVI value is 0.097.*
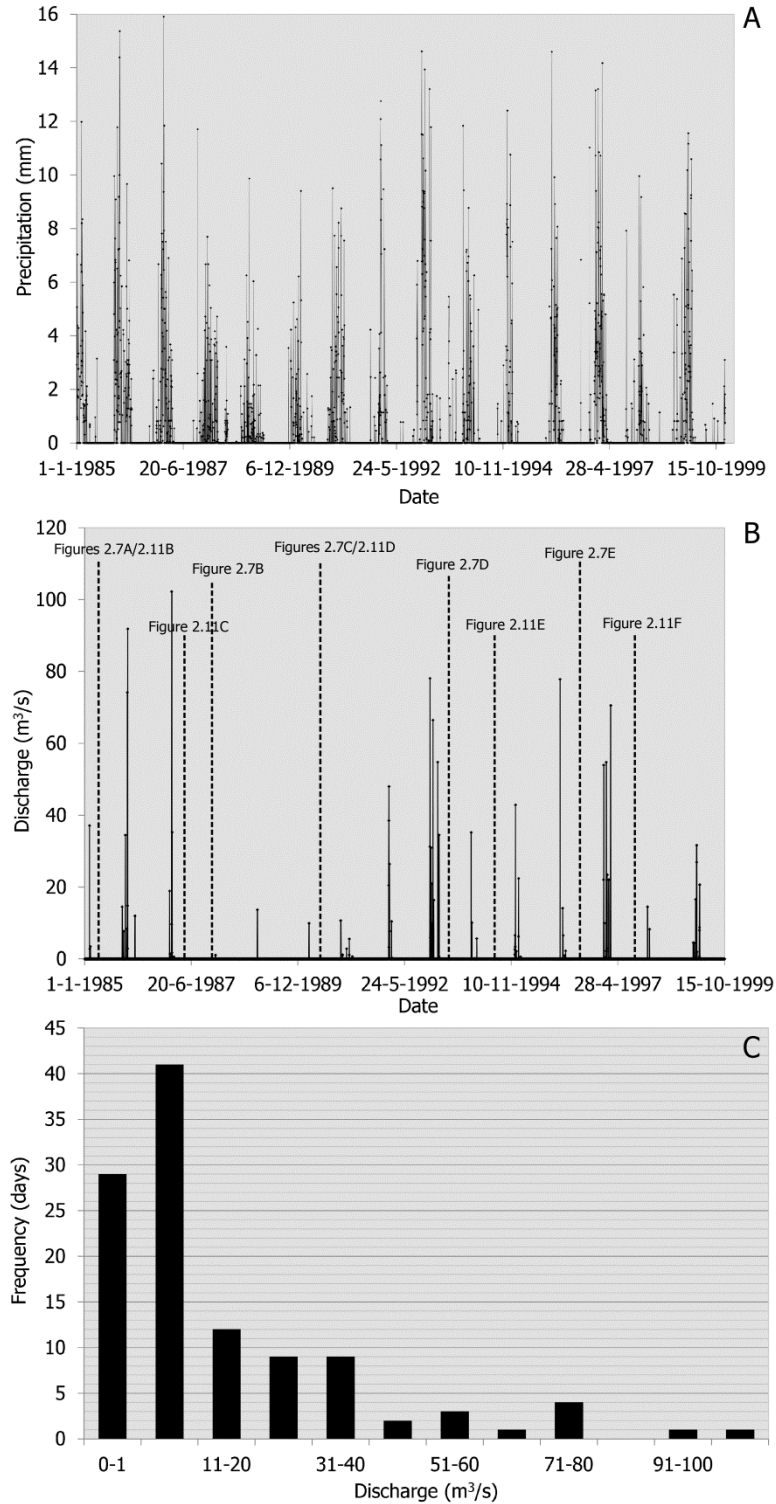
Figure 2.5: *Daily areal precipitation in the catchment area (A), and discharge modelling of the catchment in the study area from 1985-1999 (B) and frequency of peak discharge between 1985 and 1999 in the catchment area (C). Note that Figure 2.5B also shows the dates when the Landsat scenes were collected.*

Coupled with areal precipitation in the catchment (Figure 2.5A) and catchment parameters (Table 2.3), discharge was calculated based on Eq. (1). Discharge is proportional to precipitation, and in between 1985 and 1999, there are 10 peak discharge events with more than 50 m³/s (Figure 2.5B and C). The largest peak flood occurred on January 6th, 1987 and its discharge reached 103 m³/s. In the very low gradient at the river terminus (0.000148 m/m, GoogleEarth Pro) and with a cross sectional river channel area of less than 80 m² (Figure 2.6) this results in massive flood-out of water and sediment onto the floodplain. The massive over-spilling flow has an impact on the trunk channel and floodplain in the river terminus. In the following sections the emphasis will be placed on the morphology in the river terminus.
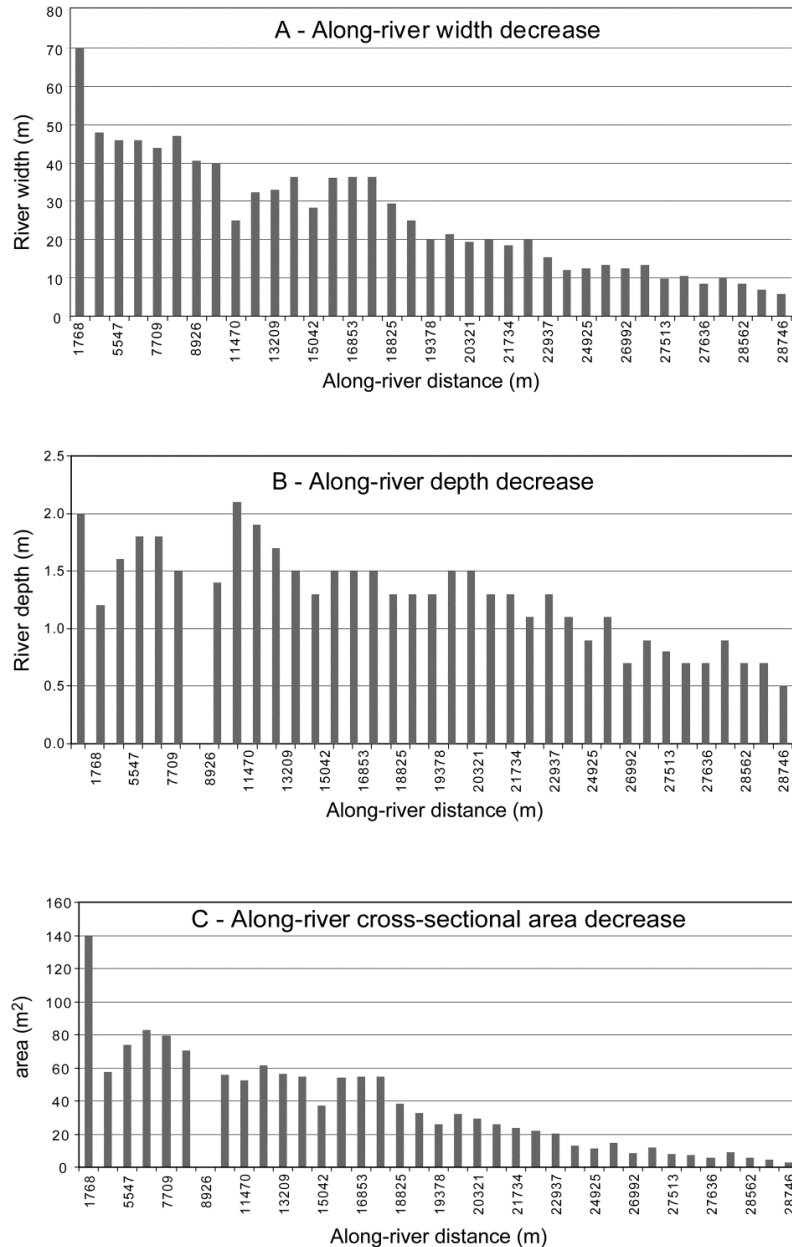
Figure 2.6: *Decreasing width (A), depth (B) and cross-sectional area (C) along the trunk channel in the study area (Donselaar et al., 2013).*

2.3.2   Landsat images comparison

2.3.2.1   Formation and expansion of crevasse splays
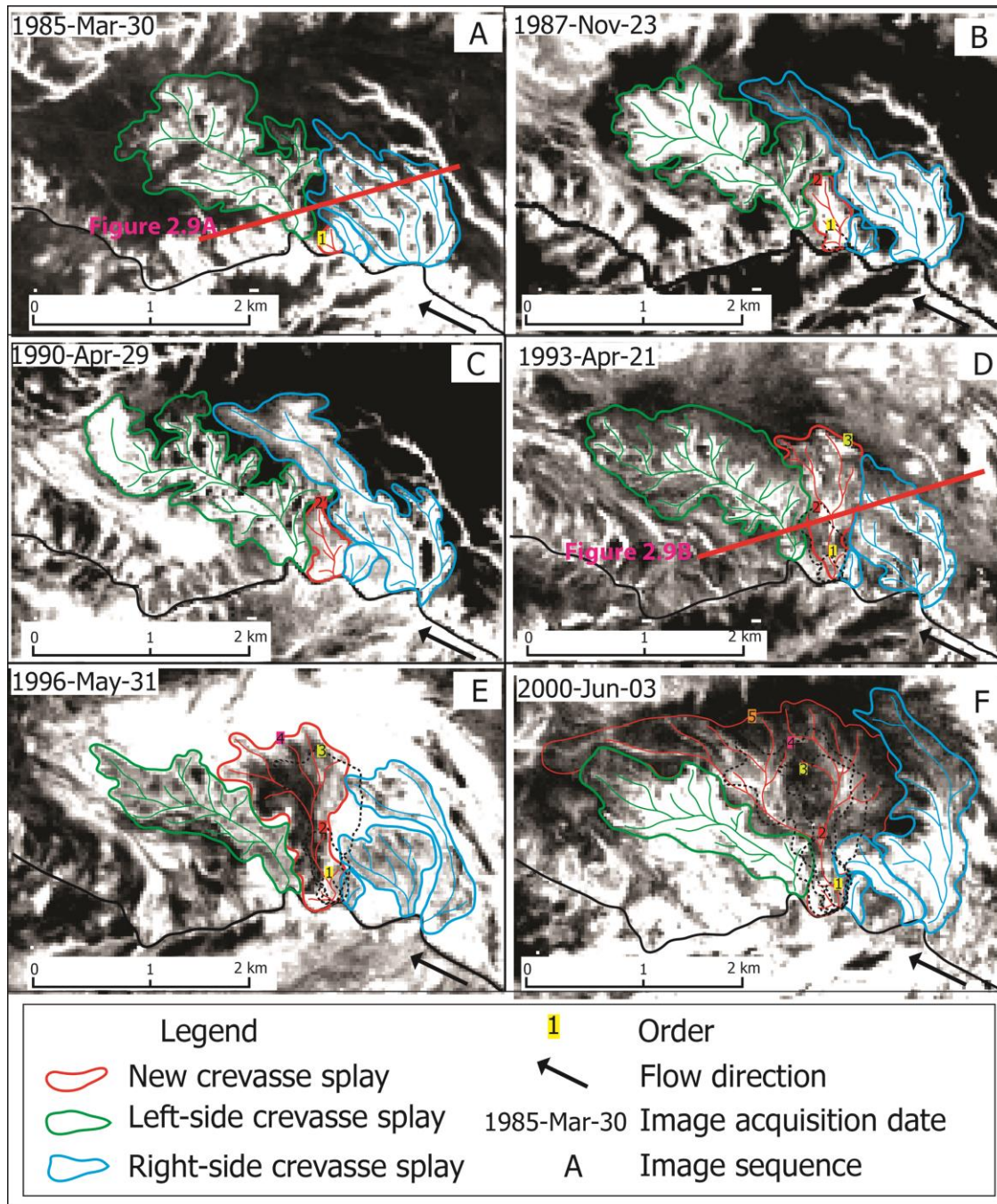
Figure 2.7: *The development of a new crevasse splay. These TM images are grey-scale and highlighted with histogram stretching. The red line indicates the crevasse splay which formed and expanded over time. Green and blue lines indicate adjacent existing crevasse splays.*

We identified a crevasse splay that showed growth over the period 1985-1999. The crevasse splay initially emerged as a small lobe in a flood event and was confined by adjacent crevasse splays (Figure 2.7A). After large flood events (Figure 2.5B), the new crevasse splay further expanded (Figure 2.7B). The new crevasse splay did not change in terms of areal extent between 1987 and 1990 (see 2 in Figure 2.7B and 2' in Figure 2.7C). However, the crevasse splay expanded again in the following years (Figure 2.7D – E). There were not peak floods in the period 1988-1991 according to discharge modelling (Figure 2.7B). Therefore, the crevasse splay expansion was attributed to peak floods. The crevasse splay expanded from a small lobe (42,300 m^2) to a large splay (2,457,900 m^2) in 15 years (Figure 2.8). The increased surface area of the crevasse splay led to amalgamation with adjacent crevasse splays (Figure 2.9) by compensational stacking, whereby the new crevasse splay expanded in the topographic low in between two adjacent existing crevasse splays (Figure 2.9).
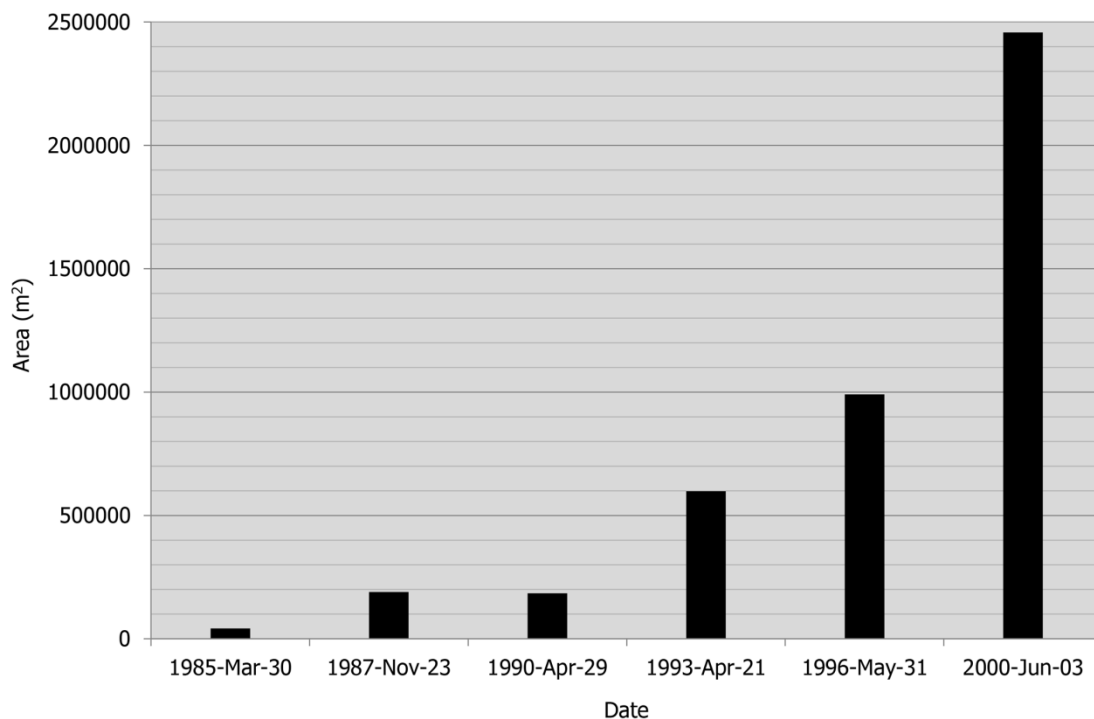
Figure 2.8: *Areal increase of the new crevasse splay from 1985 to 2000. Note order 1 to 5 represent different periods of outlines of the crevasse splay.*

Based on the analysis of the new crevasse splay, we established the relationship between peak discharge and increased area in different periods for the new crevasse splay (Figure 2.10). The crevasse splay emerged and expanded in the peak flood periods between 1985 and 1999, in which the expanded surface area was 2,415,600 m^2. The crevasse splay expanded with subsequent large floods but over time the rate of increase decelerated. This is attributed to decrease of flood intensity and decreasing flow energy due to increasing splay area and the length of crevasse channels.
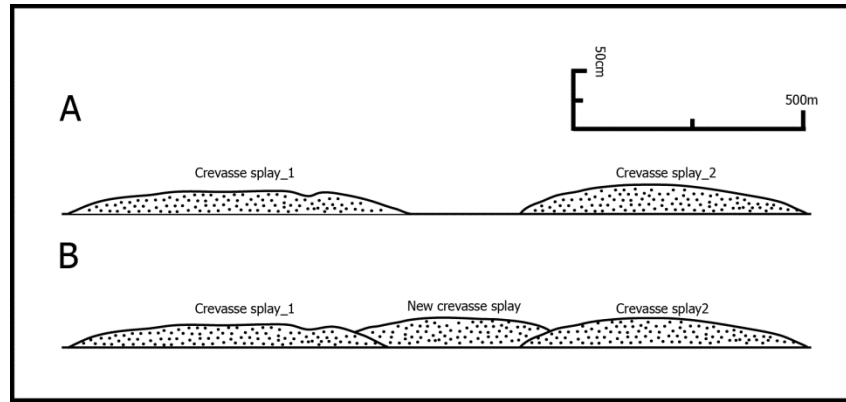
Figure 2.9: *Schematic image of compensation stacking for crevasse splays.*
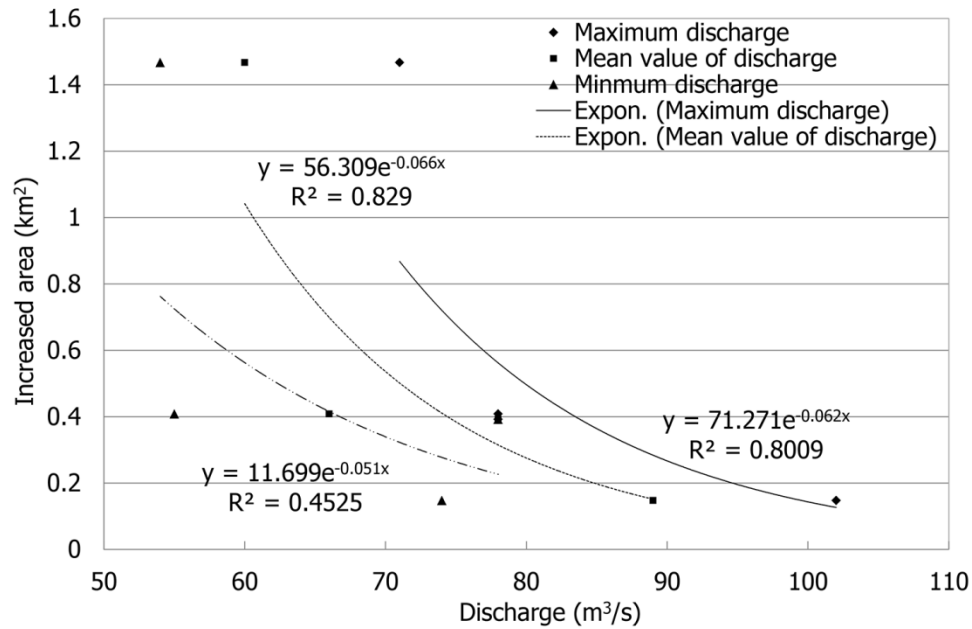
Figure 2.10: *The relationship between peak discharge and the increased area of the new crevasse splay.*

2.3.2.2   Local avulsions

The river terminus experienced multiple local avulsions from 1975 to 2001 (Figure 2.11). The avulsions occurred in the reach with average sinuosity of 1.22 (measured from Google Earth Pro) and initiated with crevasse splays. The frequency of avulsion is high in the end of the channel when the trunk channel shifts to a new path (Figure 2.11A-B and D-G). It is important to note that there was no change in channel path in periods between peak floods (Figure 2.11B and C). Downstream of the junction between the active main channel and a crevasse channel small

28

mouth bars developed by the progressive truncation of the crevasse during return flow of floodwaters in the waning stage of the flood (Donselaar et al., 2013). The bars eventually block the main channel and favor the deviation of flow through the truncated crevasse channels (Figure 2.11G). A conceptual avulsion history at the distal area of the active channel was reconstructed on the basis of these observations (Figure 2.12). In the process of development of multiple crevasse splays, some expanded their aerial extent during successive floods at the expense of others that became inactive (Figure 2.11).
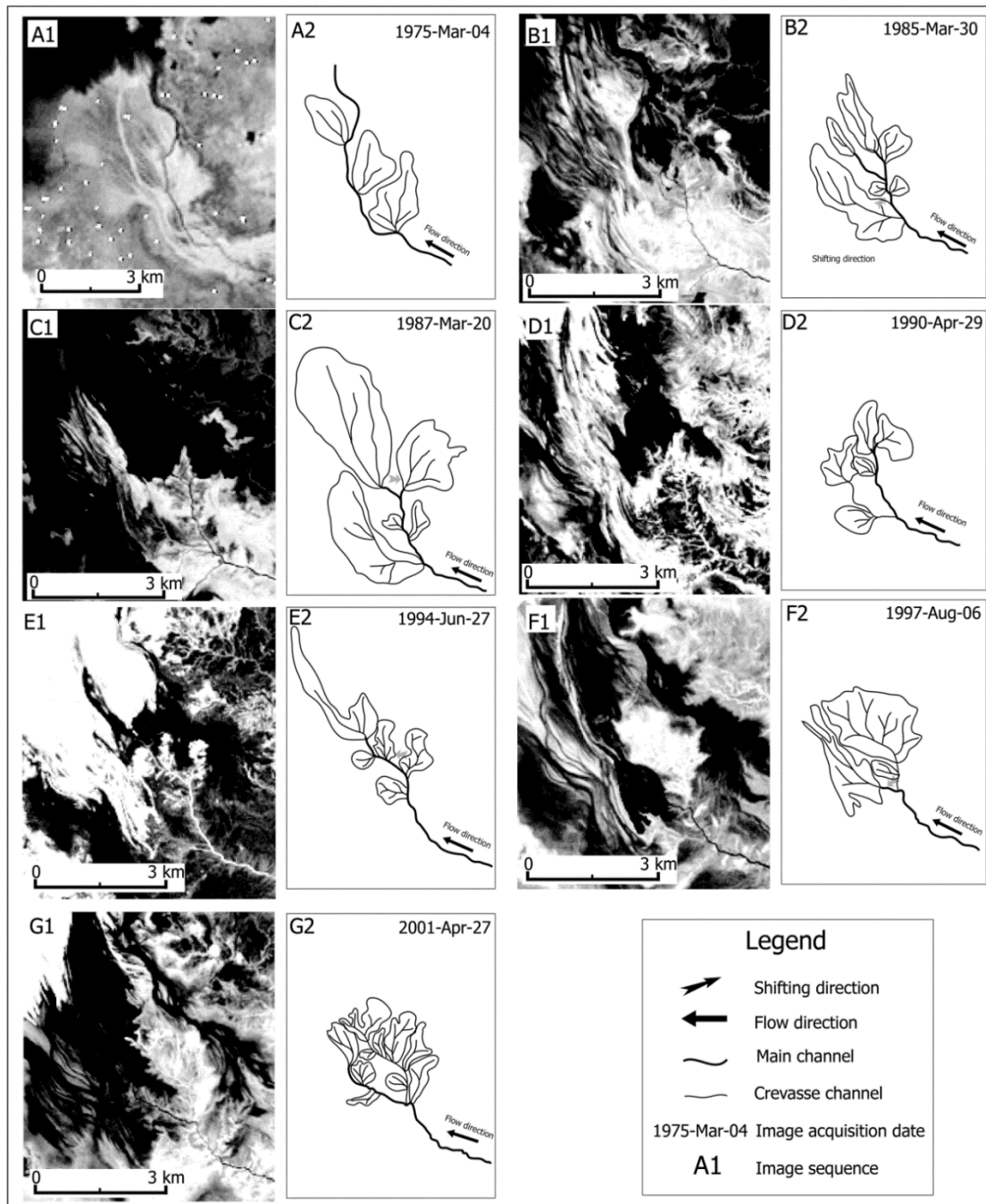
Figure 2.11: The development of avulsion in the distal part of the river terminus.
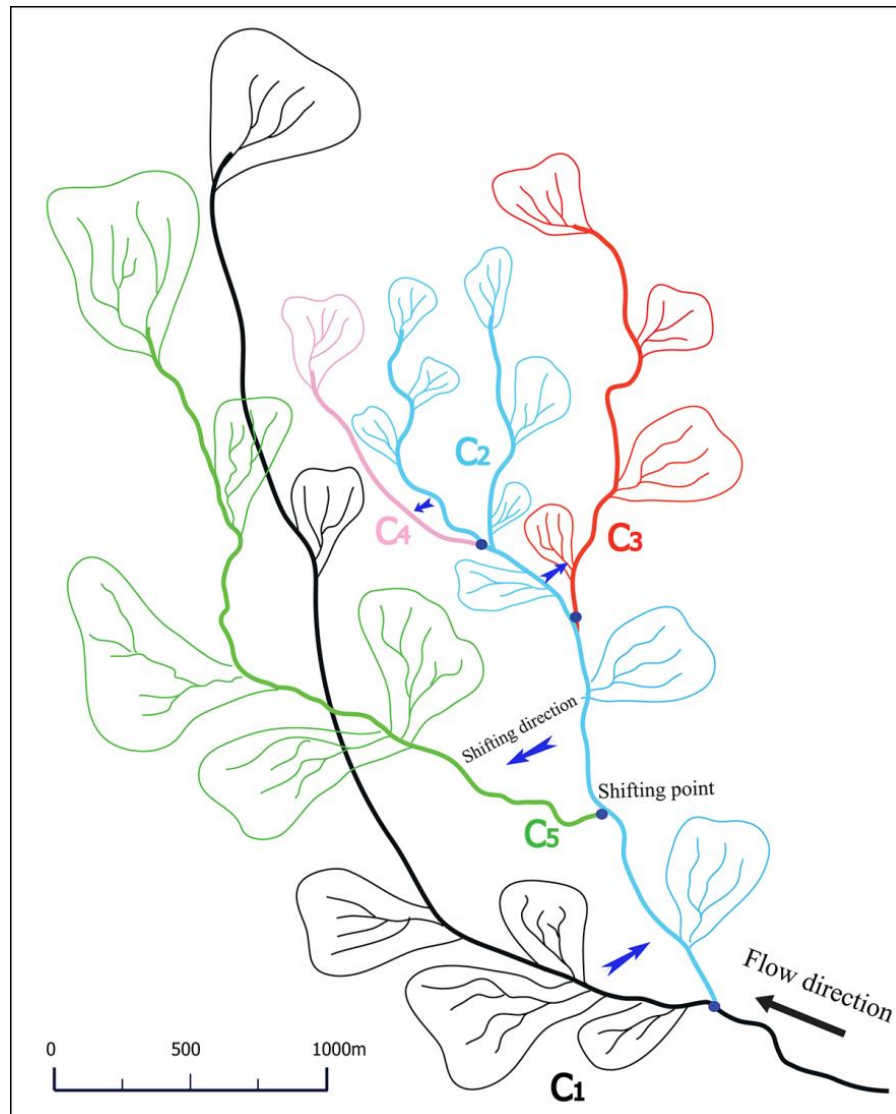
Figure 2.12: *Reconstruction of avulsion sequences in the distal zone of the active channel. C1 represents the main channel in 1975, C2 in 1985, C3 in 1987, C4 in 1994, C5 in 1997. Arrows indicate direction of shift and blue dots show shifting points.*

2.4   Discussion

The development of crevasse splays and avulsions in low-gradient, ephemeral dryland river systems differs from that in a perennial river system. The cross-sectional area of perennial rivers increases downstream, which increases their capacity to buffer peak discharge within the river banks. The year-round transport of water and sediment causes the development of levees and aggradation of sediment on the channel floor, and in the long term elevates the river bankfull level above the adjacent, compacting floodplain. Levee breach during peak discharge leads to the development of a crevasse delta and attached crevasse splay sheet sand. If the breach is not healed after the peak event it may become the locus of future avulsion, whereby the height

difference between the river bankfull and the floodplain level favors a one-directional flow of floodwater towards the lower-lying floodplain. Documented river avulsions occur over time scales of hundreds to thousands of years (Makaske et al., 2007).

By contrast, the cross-sectional area in low gradient, ephemeral dryland river systems decreases downstream due to the combined effects of energy loss, the high evapo-transpiration potential and water losses through percolation (Donselaar et al., 2013). Sporadic peak discharges cause massive flood-out in the low-gradient river terminus whereby new crevasse splays are formed and amalgamate with adjacent existing crevasse splays. The amalgamation forms sheet sands which level any height difference between the river bankfull level and the adjacent floodplain. The process is prominent along the entire length of the river channel in the study area and the investigated crevasse splay is therefore representative of the process of their formation and expansion in the river terminus. As a consequence, the floodplain has little accommodation space for the floodwaters. No ponding occurs on the floodplain and the floodwaters return to the river channel in the waning stage of the peak discharge via the same crevasse channels. Repeated peak discharge events cause progressive erosion and deepening of the crevasse channels until they reach the same depth as the main river, and thereby create an avulsion pathway (Donselaar et al., 2013). Our Landsat imagery study documents that multiple avulsions, and the formation and growth of crevasse splay have occurred in the study area in the very short time frame of 30 years (Figures 2.7 and 2.11).

The river terminus in Salar de Uyuni experiences a high frequency of avulsions, which is similar to other aggrading river systems either in the semi-arid Okavango fan in Botswana (McCarthy et al., 1992), humid subtropical river systems of the southeast Texas coastal plain (Phillips, 2011) or an experimental model (Ashworth et al., 2007). However, avulsion are triggered by sporadic peak floods in the non-vegetated river terminal, which is different from other river systems, where high vegetation cover and the floating plant debris are regarded as avulsion triggers (e.g. McCarthy et al., 1992). In addition, non-vegetated river banks reinforce levee breach, whereby the formation and expansion of crevasse splays are promoted in the study area. By contrast, in the Okavango fan crevasse splays are absent due to the channel constraints of vegetation and peat on levees (McCarthy et al., 1992).

2.5   Conclusions

The development of river avulsions and crevasse splays at the terminus of an ephemeral dryland river system over the period of 30 years was analysed. Morphological changes occur after peak discharge events and were visualized with remote sensing imagery. The highlights of this approach are:

- ASTER GDEM and Landsat data yielded catchment information such as area, slope and vegetation cover. The catchment area is characteristic of a mean slope of 0.0008 m/m with the highest slope near the margin and gradually decreasing slope downstream, as well as higher vegetation cover in the mountainous regions than that in the tributary delta and terminal fluvial fan.

- Analysis of double mass curves indicated high consistency of the precipitation pattern in the catchment area. Thiessen polygon analysis yielded areal precipitation information. In combination with catchment information an empirical discharge model was established. Ten peak discharge events with more than 50 m^3/s have been pinpointed between 1985 and 1999. The peak discharges resulted in massive flood-out of water and sediment onto the floodplain in the very low gradient river terminus and with a cross sectional channel area of less than 80 m^2.

- The development in space and time of crevasse splays and local avulsions was visualized by comparing Landsat MSS and TM images before and after peak discharge events. Crevasse splays expanded in peak discharge periods and this led to amalgamation with adjacent crevasse splays by compensational stacking. The areal extent of the crevasse splays did not change in between peak discharge events.

- Multiple local avulsions were distinguished between 1975 and 2001. Crevasse splays and their crevasse channels can evolve over time to a new channel path. A conceptual avulsion history was established by the analysis of Landsat time series images.

Chapter 3　　　Sediment source – Upstream river bank accretion and erosion[2]

Abstract.　*The Río Capilla is an important water and sediment source which feeds the World's largest salt pan, Salar de Uyuni in the southern Altiplano plateau (Bolivia). The ephemerality due to flash flow regime in combination with low-gradient and sparse vegetation cover exert a significant impact on dryland river form, process and behaviour. However, dryland river bank erosion and accretion have rarely been studied. Here we use satellite imagery and field investigations to analyse the key controls on dryland river bank behaviour and we outline the implications for the mechanisms of changes in channel planforms in the study area. On-site surveys combined with high-precision GPS and high-resolution satellite imagery show that channels are characterized by shallowness and poor development of levees. The study area of the Río Capilla is divided into two zones of different slopes: Zone 1 with a high slope and Zone 2 with a low slope. Excavations show that fine sand-dominated point-bar deposits in two reaches are characterized by a fining-upward sequence and river banks primarily consist of silt and clay. Zone 1 is relatively straight with grass-covered banks that are stable despite the high gradient, whereas Zone 2 is typified by an anabranching pattern with non-vegetated banks and experiences prominent bank accretion and erosion. Non-vegetation cover and abundance of desiccation cracks and burrows are the major causes of bank erosion in this low-gradient dryland river system. Comparison of high-resolution satellite images reveals erosion exceeds deposition, accompanied by changes in channel planform, such as meander and channel morphology. Shallow channels and poor development of levees in combination with in-channel accretionary benches result in frequent overbank flooding, which leads to a high density of crevasse splays over unconsolidated river banks and accretionary benches. Avulsion and chute channels together with reactivation of partially abandoned meanders and connection of headcuts and crevasse channels produce an anabranching pattern in the study area. Investigation on river bank erosion and accretion and their impact on changes in the channel planform provide insights into fluvial processes and mechanisms of changes in channel planform in this non-vegetated and low-gradient ephemeral river system.*

---

[2] Chapter 3 is based on the manuscript entitled "Dryland river bank accretion and erosion and their impacts on channel planform: Río Capilla, Salar de Uyuni, Bolivia". J. Li, S.M. Luthi, C.S. Bristow, M.E. Donselaar. (submitted). Earth Surface Processes and Landforms.

3.1   Introduction

River bank accretion and erosion play an important role not only in understanding sediment dispersion in river systems, but also in interpreting river morphology and behaviour (Hooke, 1980). To date, there have been many studies analysing river bank activities (Hooke, 1980; Thorne, 1982; Nanson and Hickin, 1986; Lawler, 1993; Abernethy and Rutherfurd, 1998; Millar, 2000; Couper and Maddock, 2001; Hooke, 2007; Bartley et al., 2008). It is generally proposed that bank erosion is related to a wide range of factors such as riparian vegetation, the grain size of the sediments and the stratigraphy of the banks, the stages of meander development, etc. Most of these studies, however, focused on humid regions, and few studies have investigated river bank accretion and erosion and their impacts on channel planforms in dryland river systems, possibly because of difficult accessibility (Poesen et al, 2002). The term "planform" is used here to describe the planar geometry of river features without reference to any particular processes (Nanson and Knighton, 1996). Therefore, the mechanisms of bank accretion and erosion as well as their impact on changes in channel planform in semi-arid river systems are not fully understood.

Methods such as field measurements, maps and aerial photographs of different dates, and dateable sedimentary and biological evidence have been widely used in quantifying the magnitude of bank erosion (Hooke, 1980; Lawler, 1993; Millar, 2000; Couper et al., 2002; Hooke, 2007; Bartley et al., 2008; Yao et al., 2011). Some of these studies included GIS and remote sensing techniques. Recently, Yao et al. (2011) employed a time series of Landsat Multispectral Scanner (MSS) and Thematic Mapper (TM) data and successfully detected bank erosion and accretion in the Yellow River system. However, due to some critical issues such as low resolution of the images and registration problems between aerial photographs, the data was insufficient to accurately determine the rates of change in many smaller rivers. Field measurements with erosion pins can achieve an accuracy that is at a centimetre level (Couper et al., 2002; Bartley et al., 2008), but this method is time-consuming and costly, especially in remote regions. This paper presents a viable alternative using bi-temporal high-resolution satellite images (0.5 m) to accurately analyse bank accretion and erosion of the Río Capilla in the semi-arid endorheic basin of the Salar de Uyuni, Bolivia. In this paper we have three objectives: (1) To use satellite imagery and field investigations to document river bank activities and channel morphology; (2) To investigate key factors contributing to bank accretion and erosion in such a semi-arid river system; and (3) To outline the implications of findings for the mechanisms of changes in channel planforms in the study area.

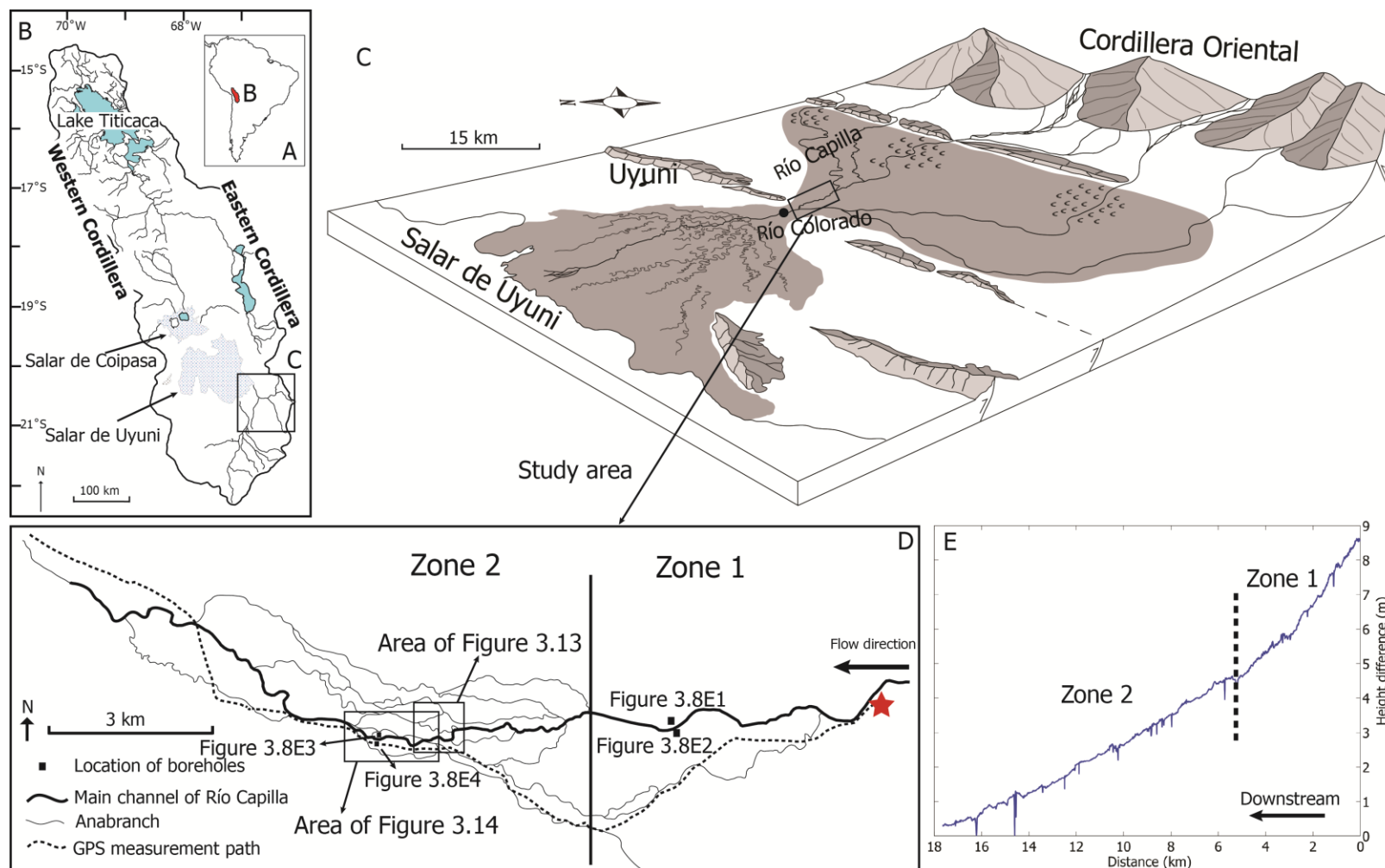## 3.2   The Río Capilla

Figure 3.1: Map of the study area. A, B and C: The location of Altiplano plateau in South America and the Río Capilla (A and B: modified after Placzek et al. 2013, and C: Donselaar et al., 2013). The black dot indicates the location of the Colorado Bridge. D: The river pattern in the study area. E: A high-precision GPS profile of the profile along the dashed line in D.

The Río Capilla flows from east to west and joins the Río Colorado at the edge of the Salar de Uyuni, Bolivia (Figure 3.1C). The study area has been tectonically quiescent in the Late Pleistocene and Holocene despite young fault escarpments (Bills et al., 1994, Baucom and Rigsby, 1999 and Rigsby et al., 2005; Donselaar et al., 2013). The rainy season in the study area is from December to March, and according to the precipitation data of 1975-2012, the average annual rainfall is about 185 mm (Chapter 2), which is greatly exceeded by the evapo-transpiration potential of 1300 mm/yr. The study reach starts at the upstream from the Colorado Bridge.

3.3 Data acquisition and methods

3.3.1 Data acquisition

We utilized the Advanced Space-borne Thermal Emission Reflection Radiometer (ASTER, Abrams et al., 2002) global digital elevation model (GDEM) data to analyse the catchment area of the river and ASTER level-2 atmospheric and cross-talk corrected surface reflectance data products (AST07XT) to quantify the vegetation cover in the study area. In addition, three high-resolution satellite images (QuickBird and Worldview) were employed to analyse river bank activities in the study (images on 2004-Oct-20 and 2013-Jul-13 were available on GoogleEarth while images on 2010-Dec-9 were WorldView-02 data available on European Space Imaging). Due to data availability, we analysed two sets of satellite images (2004-Oct-20 (QuickBird-02) and 2010-Dec-9 (Worldview-02)) for bank accretion and erosion in the study reach (Table 3.1). The QuickBird-02 and Worldview-02 images have been projected to Universal Transverse Mercator (UTM).

Type	Catalog ID	Acq. Date	Center Lat/Long	Avg. Off Nadir Angle	Avg. Target Azimuth	Sensor	Band Info
Quick Bird-02	10100100 035DE200	Nov 2, 2004	-20,419°/-66,914°	8°	293°	QB02	Pan_MS1
(Google Earth)	10100100 04912500	Oct 5, 2005	-20,281°/-67,073°	8°	261°	QB02	Pan_MS1
Quick Bird-02	10300100 084D5600	Dec 9, 2010	-20,506°/-66,932°	13°	173°	WV02	Pan_MS1_MS2
(Google Earth)	10300100 083DC100	Jan 3, 2011	-20,521°/-67,073°	26°	221°	WV02	Pan_MS1_MS2

Table 3.1: High-resolution satellite imagery information.
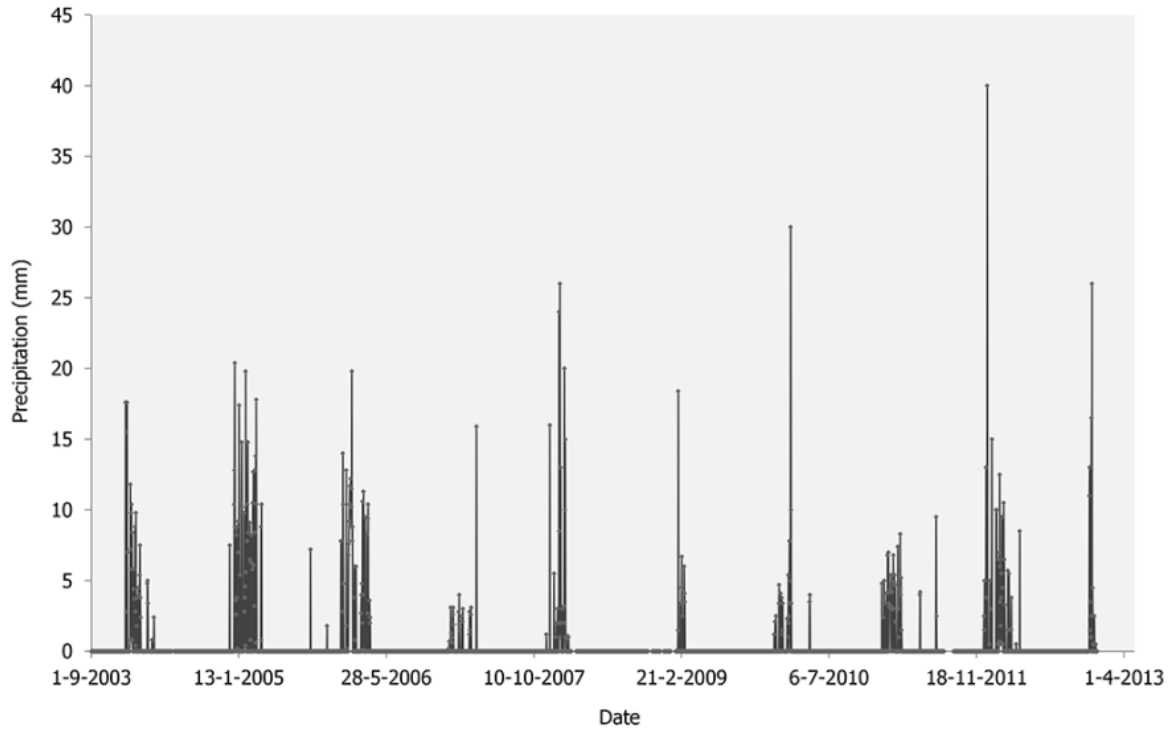
Figure 3.2: *Daily precipitation in the study area from 2003 until 2013.*

The Bolivian Servicio Nacional de Meteorología e Hidrología provided daily precipitation and 24hrs maximum precipitation data for the period 2003 – 2013 in the study area (Figure 3.2). The precipitation data were collected from a meteorological station in the study area (Latitude: 20°28′20″; longitude: 66°49′53″).

The field survey was conducted on Nov. 30, 2012. A Trimble R7 dual frequency geodetic GPS receiver was mounted on the car in the field and used to measure the gradient along the river. To measure the thickness of accretion, the first excavation site was selected at a location which was in the channel path in 2004 but by 2010 it was in the point bar. A second excavation was located on the river bank in order to sample the floodplain sediments adjacent to an eroding channel bank. The sampling interval in each borehole was 10 or 20 cm. Another two excavation sites were in the upstream reach, where the river banks were stable. The coordinate information of sampling sites was collected with a Garmin GPSmap 60CSx device. The samples were analysed in terms of grain size with a Sympatec HELOS KR laser-diffraction particle sizer with a size range from 0.1-2000 μm.

3.3.2   Methods

Analysis of ASTER GDEM data with ArcMap 10 software yielded the drainage area values as well as slope and relief therein. To understand vegetation cover in the study reach, the Normalized Difference Vegetation Index (NDVI) is a ratio that uses the NIR and red bands to distinguish the differences between vegetated and non-vegetated areas (Tucker, 1979). For AST07XT, Visible/Near-Infrared (VNIR) bands 2 (Red band, 0.63–0.69 µm) and 3 (Near-Infrared band, 0.76–0.86 µm) were used to measure the vegetation cover in the study reach (Jiménez-Muñoz et al., 2006). Two high-resolution satellite images (QuickBird-02 on 2004-Oct-20 and Worldview-02 on 2010-Dec-9) were used to quantify channel morphology in the study area. UTM WGS-84 was selected for projection and Worldview-02 images were resampled by nearest neighbour method with a resampling resolution of 0.5 m. Due to the large size of the Worldview-02 images, they were divided into several images of 2 km × 1.5 km along the river. These Worldview-02 images were registered to QuickBird-02 (GoogleEarth) images within the remote sensing image analysis software ENVI. The RMS error was less than 1.7 pixels (0.85 m).

The analysis of bank accretion and erosion focused on the main channel and recent partially abandoned channels because these channels have experienced pronounced bank activities during the period of satellite observation years, while secondary channels (continuous but narrow) and tertiary channels (recognizable but not obviously connected) (Knighton and Nanson, 1993) were relatively stable, probably due to very low sediment transport capacity (Makaske et al., 2009). The concave bank lines of the river were defined by the relief in the high-resolution satellite images, while the inner bank lines were defined by relief of the upper accretionary bench (Figure 3.3). The delineation of channel boundaries was performed with GoogleEarth Pro.
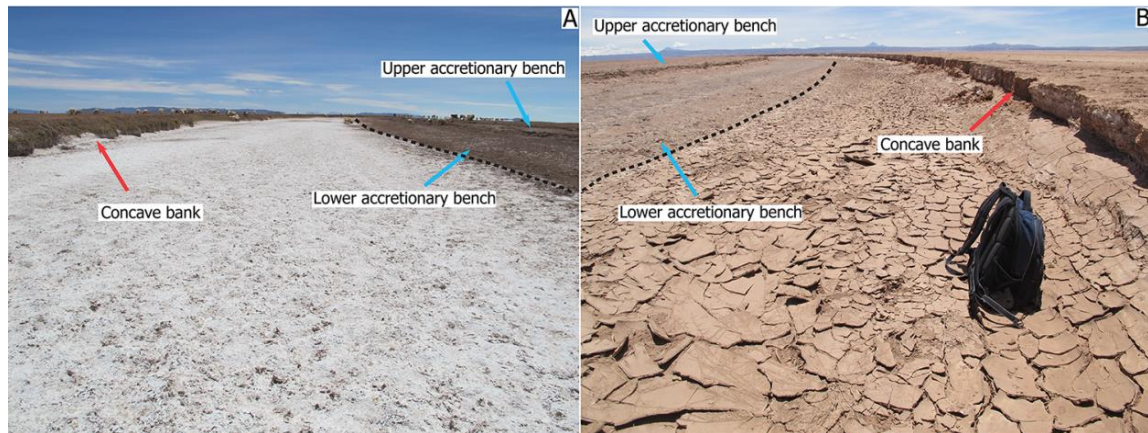
Figure 3.3: *Accretionary bench and concave bank of the river. Bag for scale is about 50 cm high. The area between the relief of the upper accretionary bench and dash line indicates the lower accretionary bench. A: River view in Zone 1 with the flow direction away from the camera. B: River view in Zone 2 with the flow direction towards the camera.*

We analysed the left bank and the right bank independently. When the 2010 left bank is on the right-hand side of the 2004 left bank, accretion must have occurred (Figure 3.4A). When the 2010 left bank is on the left-hand side of the of the 2004 bank erosion must have occurred (Figure 3.4B). We used the same method to analyse the right bank. Both accretion and erosion areas were calculated through polygons with GoogleEarth Pro. Due to RMS error of image registration, accuracy of area calculation was up to 100 m^2. The study river has been divided along its length into intervals of one kilometre and the area of accretion and erosion were calculated for each kilometre. Maximum bankline movement was measured at points where the shifting magnitude was the highest for each area. Sinuosity, referred as to the ratio of the curvilinear length to the distance between the starting point and the ending point of intervals of one kilometre along the main channel, was used to characterize the relationship between sinuosity and bank activities.

Figure 3.4: *Accretion (A: yellow areas) and erosion (B: red areas) of the river between 2004 and 2010.*

Excavation sampling makes it possible to determine the thickness of sediment accretion while the measurement of the height of the outer bank was taken to indicate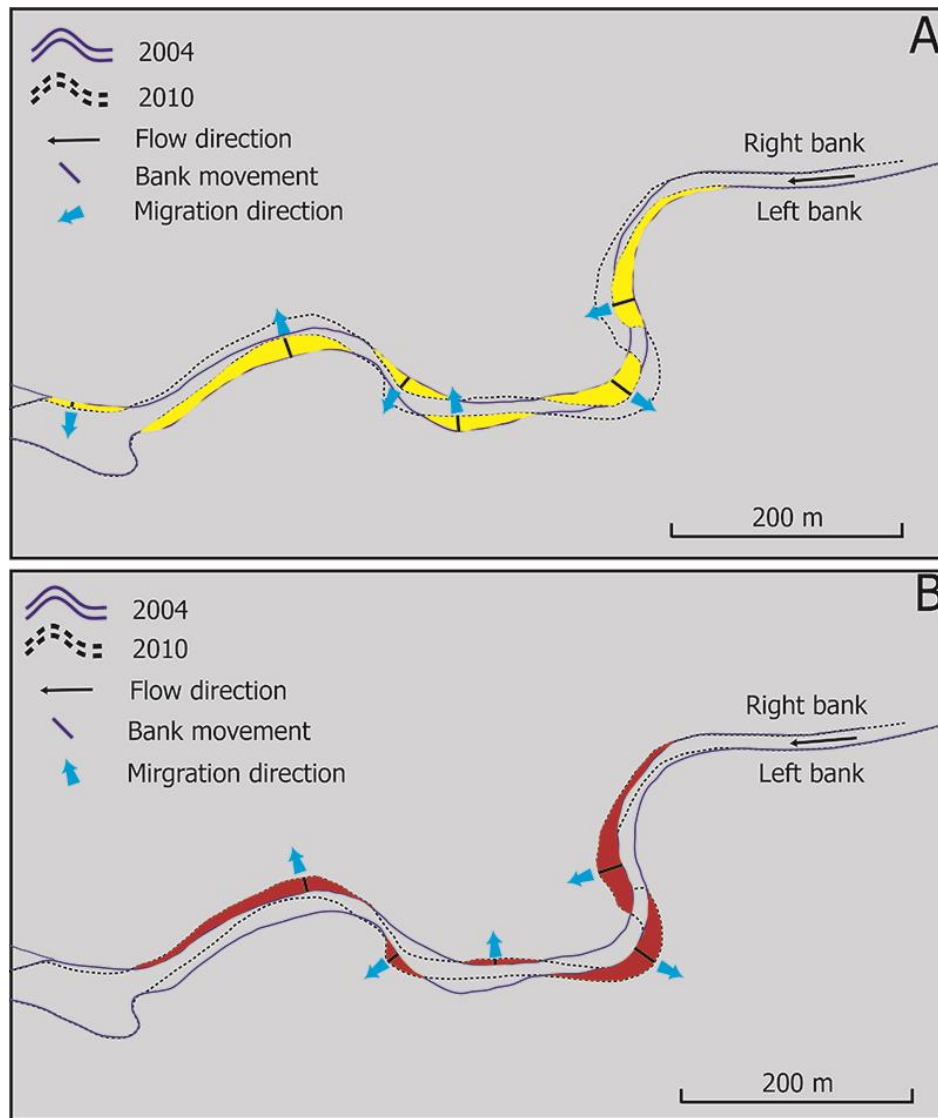 the thickness of erosion. The thickness and areas of accretion and erosion have been transformed into volume by simple multiplication (eq. 3-1 and eq. 3-2).

$$V_{ac} = Area \times Thickness \ , \qquad (3\text{-}1)$$

where V_{ac} represents the volume of accretion, area the accretion area and thickness the accretion height.

$$V_{er} = Area \times Height \ , \qquad (3\text{-}2)$$

where V_{er} represents the volume of erosion, Area the accretion area and height the eroded bank height.

The high precision GPS data were resampled to the average measurement interval (12 m) with a nearest neighbour method. Owing to topographic conditions, the GPS track did not perfectly match the river channel path. We then projected the GPS track onto a straight line, connecting the first and last GPS-location (eq. 3-3).

$$\boldsymbol{\mu} \cdot \boldsymbol{v} = \|\boldsymbol{\mu}\| \times \hat{\boldsymbol{v}} \times \cos\theta, \quad (3\text{-}3)$$

where $\boldsymbol{\mu}$ and $\boldsymbol{v}$ are vectors and $\|\boldsymbol{\mu}\|$ is the norm of $\boldsymbol{\mu}$. $\hat{\boldsymbol{v}}$ is a unit vector and θ is the angle between $\boldsymbol{\mu}$ and $\boldsymbol{v}$. $\boldsymbol{\mu}$ indicates a vector beginning at the starting point and ending at each measurement point while $\boldsymbol{v}$ means a vector starting at the starting point and ending at the finishing point. A median filtering method was used to remove anomalous depressions along the driving path (Figure 3.1).

3.4   Results
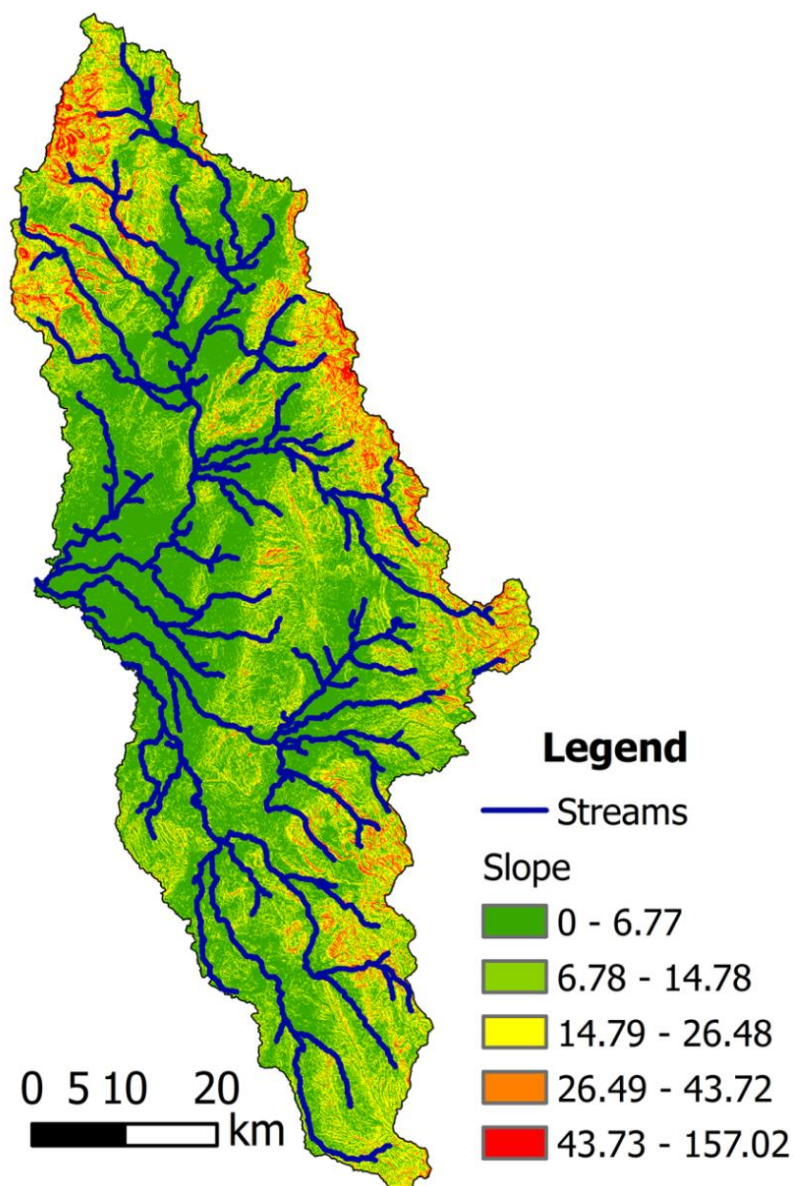
Figure 3.5: *Dendritic pattern of river system in the catchment area of Río Capilla and its map of slope. The slope is derived by rise over run times 100 (m/m*100).*

Changes in channel morphology and river bank behaviour in a dryland river system are a function of the precipitation intensity, vegetation cover and gradient in the study area. The tributary streams in the catchment of the Río Capilla have a dendritic pattern (Figure 3.5), and cover an area of 3500 km^2. The surface sediment consists of Quaternary alluvium, which comprises Upper Oligocene to Quaternary sedimentary and volcanic rocks (Marshall et al., 1992; Horton et al., 2001). The catchment profile shows the maximum slope to be up to 1.57 m/m with a mean slope

of 0.0008 m/m; the highest slope is near the margin and gradually decreases downstream (Figure 3.5). Daily precipitation data showed that between 2004 and 2013 two daily events per year exceeded 16 mm (Figure 3.6), which is regarded as the rapid onset of initiation runoff in arid regions following the principles of Hortonian overland flow (Knighton and Nanson, 1997). However, multiple events exceeding 16 mm in several rainy seasons occurred between 2004 and 2013 (e.g. 2004-2005, 2007-2008, 2012-2013) and some single event greatly exceeded the threshold value (e.g. 40 mm on Dec. 24, 2011). Overall, there is an increasing tendency of maximum magnitude for single events from 2004 to 2012 (Figure 3.6).
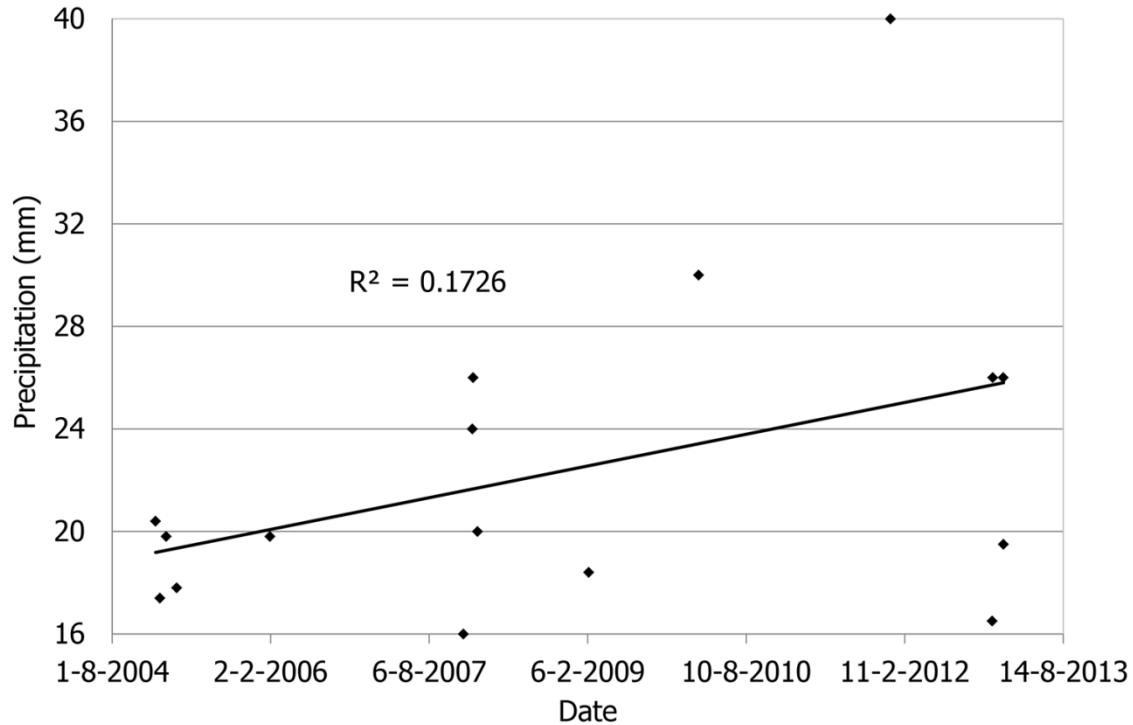
Figure 3.6: Single events exceeding 16 mm precipitation between 2004 and 2013.

Field investigation and NDVI analysis (Figure 3.7) showed that vegetation cover was grass along the study reach and there was a wide variation in distribution. Vegetation cover was higher in the relatively straight reaches whereas vegetation cover is very low in the middle and downstream reach. In addition, GPS data processing showed two zones with different gradients along the study reach (Figure 3.1E, Zone 1: 0.0009613 m/m; Zone 2: 0.0003767 m/m). Excavation analysis along the main channel revealed that accretionary deposits in the two zones were characterized by an unconsolidated fining-upward sequence with sparse gravel at the erosional base, cross-bedded fine sand in the middle, and laminated silt and clay at the top with roots (Figure 3.8E1 and E3). Field investigation also showed that the main channel in Zone 1 was wider (up to 10 m) and deeper (up to 1.3 m) at E1 than that at E3 (6 m wide and 0.7 m deep) in Zone 2. In addition, the accretionary bench in two zones is composite, consisting of a flat upper bench with a steeper bank on the channelward side, and a narrow lower bench (Figure 3.3). In

Zone 2, channel bed surfaces are coated with polygon-shape cracked laminated clay (Figure 3.3B). By contrast, concave banks in two zones show a wide variation in texture, structure and vegetation cover, although river banks are characterized by poor development of levee and more compacted than accretionary deposits in the study reach. Concave banks in Zone 1 are silt and clay dominated, interbedded with 5-10 cm fine sand (Figure 3.8E2). In addition, they contain roots at the top 20 cm. However, in Zone 2, concave banks consist primarily of silt and clay with well-developed desiccation cracks (up to 50 cm deep) and macropores (Figure 3.8E4). These variations in river banks in two zones exert a great impact on the river morphology and the processes. In the following sections the emphasis will be placed on the morphology, bank accretion and erosion, and changes in channel planform in the study reach.
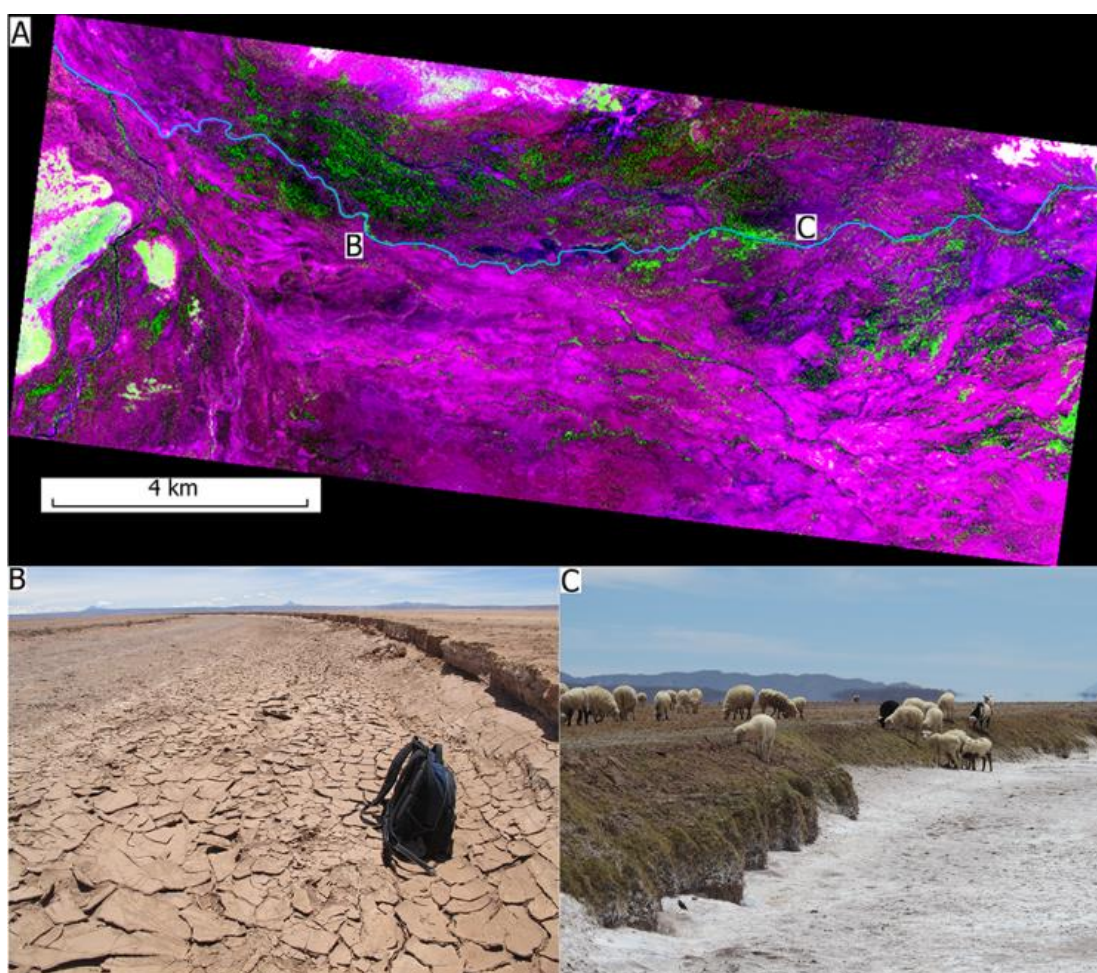
Figure 3.7: *A: A false-color image of NDVI with Red and Blue channels: Band1 and Band3 of ASTER AXT07 and G channel: NDVI result. The threshold value of 0.093 is determined by grass-cover bank (C). The greenish areas are covered by vegetation and the purple regions are bare land. B and C show bare land and grass-covered channel bank.*
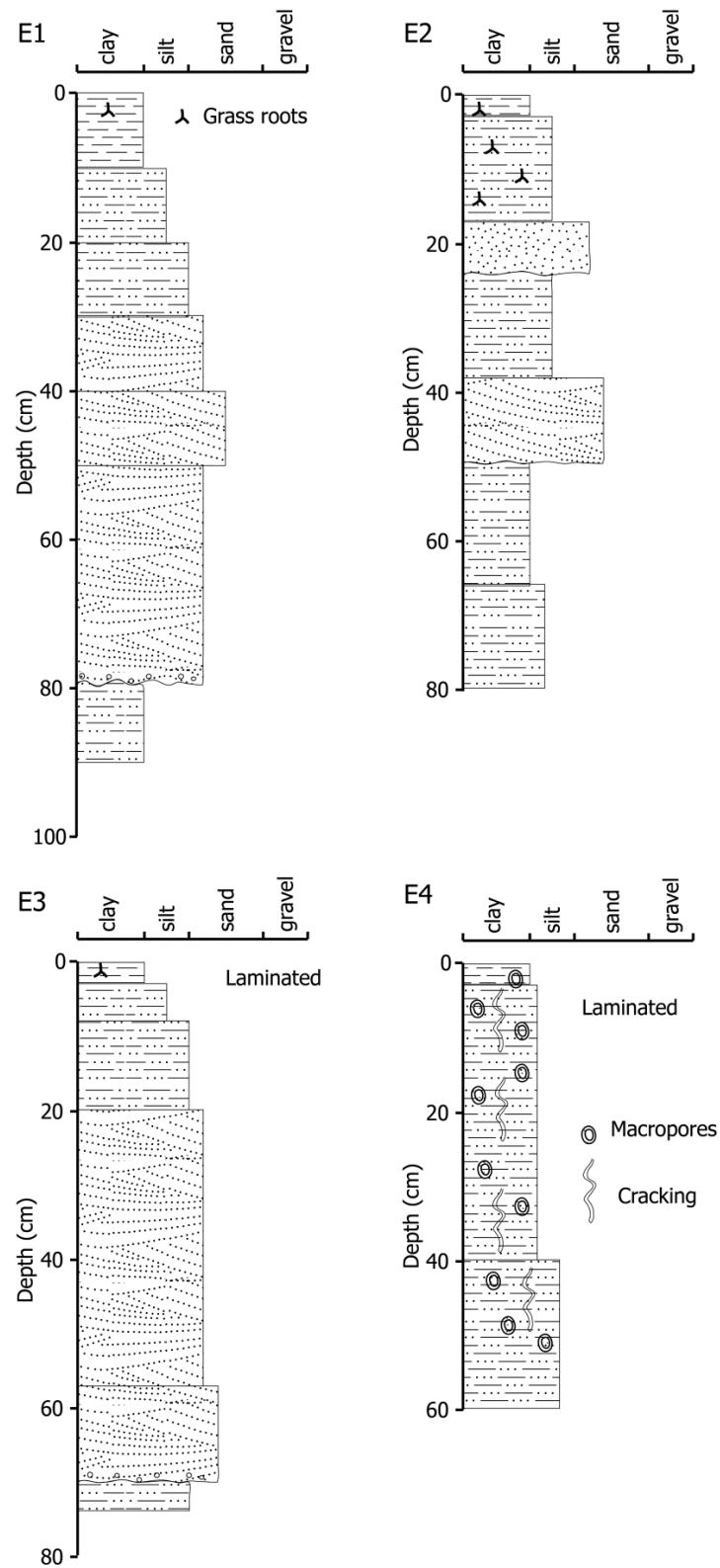
Figure 3.8: *Sedimentary logs of accretionary deposits and river bank sediment in two zones. See Figure 3.1D for the locations of the sedimentary logs.*

3.4.1   Bank accretion and erosion

3.4.1.1   Accretion

Analysis of the 2004-2010 satellite image analysis, accretion primarily occurred at point bars or curved reaches and the total area of accretion along the river was found to be 38,700 m^2, with 18,000 m^2 on the left bank and 20,700 m^2 on the right bank (Figure 3.9, lines above 0). Although kilometre-based accretion statistics shows that the highest value on the right bank (9,600 m^2) was higher than that on the left bank (4,600 m^2), the overall trends of accretion areas on the two river banks are comparable. Most bankline movement at accretion banks were 6 – 20 m, with the highest bank shift 30 m and therefore the maximum bankline movement rate was about 5 m/yr between 2004 and 2010.
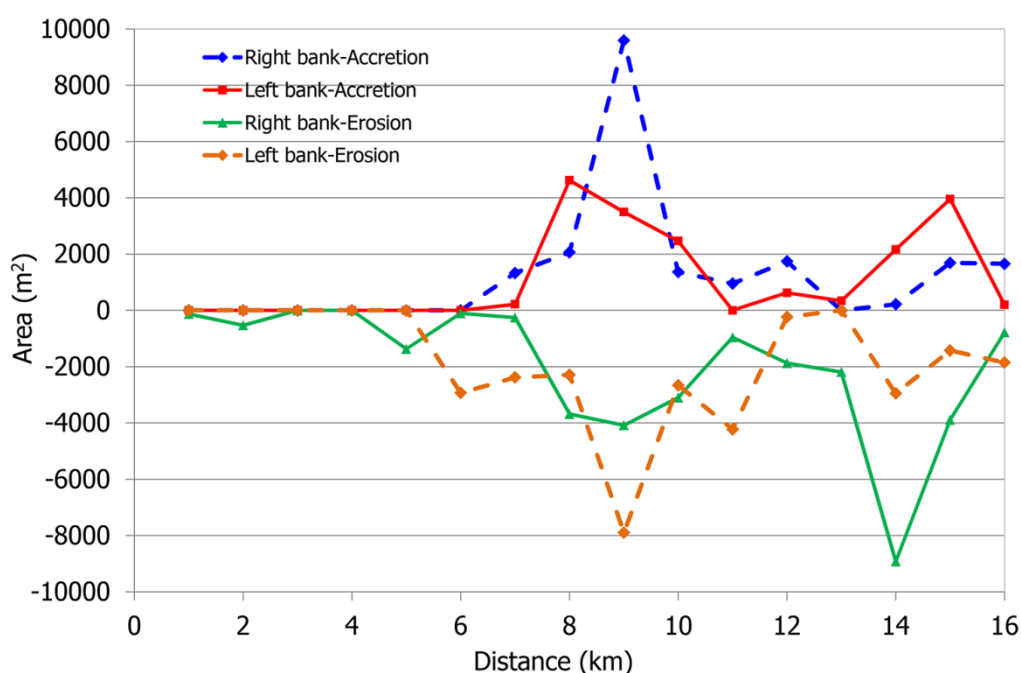
Figure 3.9: *River bank accretion and erosion area along the river.*

The sedimentary log of one accretionary point bar (Figure 3.8E3) shows a clear boundary between the sandy sediment and silt. The boundary between silt and fine sand at the base of the section is interpreted to be the base of the channel. From our analysis of the change in bank lines between 2004 and 2010 we are confident that the fining-upward section was deposited between 2004 and 2010. The approximate thickness is 60 cm, and the surface in the accretion point bar is flat. Assuming that the base of the channel was also horizontal we infer that the thickness of the point bar is 60 cm. From our analysis of the change in bank lines between 2004 and 2010 we have determined that the accretion area is 4,900 m^2 and assuming a uniform thickness for the point bar we estimate that the volume of deposited sediments is approximately 2,900 m^3 according to equation 3-1.

3.4.1.2   Erosion

Analysis of bank-line changes from the satellite images shows the total area of erosion was 60,700 m^2, with 28,800 m^2 on the left bank and 31,900 m^2 on the right bank (Figure 3.9, lines below 0). According to the analysis of erosion areas per kilometre, the erosion peak on both the left bank and the right bank was in excess of 8,000 m^2 (left bank: 8,000 m^2; right bank: 8,900 m^2) between 2004 and 2010. These two peaks in erosion are offset from each other and occurred at different reaches (left bank: 14 km; right bank: 9 km) (Figure 3.9). For the reach at 9 km, on the left bank the highest erosion occurred (7,900 m^2), while on its opposite bank, the right bank of the same reach, there is a small peak erosion area (4,100 m^2). The bankline movement for erosion banks was commonly in the range of 6 – 15 m, with the largest recorded bankline movement being 30 m. Assuming a constant rate of erosion between 2004 and 2010 the maximum bankline movement rate of erosion was an average of 5 m/yr. This rate of erosion bank has been confirmed by field observation. A field survey was conducted on Nov. 30, 2012, which was two years after the Worldview-02 satellite image was acquired (Dec. 9, 2010). The offset between the bank line during fieldwork and the bank line in 2010 was about 11 m, which is in agreement with the maximum bankline movement rate at the eroded bank of 5 m/yr between 2004 and 2010. The maximum bankline movement rate at the eroded bank is ongoing during this study and approximately equal to that of the accretion bank.

Samples for river bank sediment analysis were collected from the outer cut-bank opposite a point bar (Figure 3.8E4). The floodplain was flat, and the bank height was constant. Therefore, we assume that the samples are representative for that outer bank. The mean grain size the bank is less than 25 μm, which indicates that the bank sediments are silt-dominated. According to field measurements, the height of the bank is about 70 cm. The area of erosion at the outer bank was 2,400 m^2, and using eq. (3-2), the volume (V_{er}) of eroded sediments is estimated to be about 1680 m^3.

3.4.2   Changes in channel planform

Compared to the right bank (Figure 3.9, solid lines), the major accretion reaches tend to be more consistent with main erosion on the left bank (Figure 3.9, dashed lines), although the peak accretion and peak erosion did not occur at the same reach, and erosion is distributed along a longer interval. Accretion mainly occurred in the reaches of 7 to 10 km and 12 to 13 km, while erosion predominantly happened in the reaches of 6 to 11 km and 14 to 15 km. Overall, erosion greatly exceeds accretion on both banks of the river (Figure 3.10A). Thus, river erosion is dominant over accretion and this is associated with an evolving channel planform.
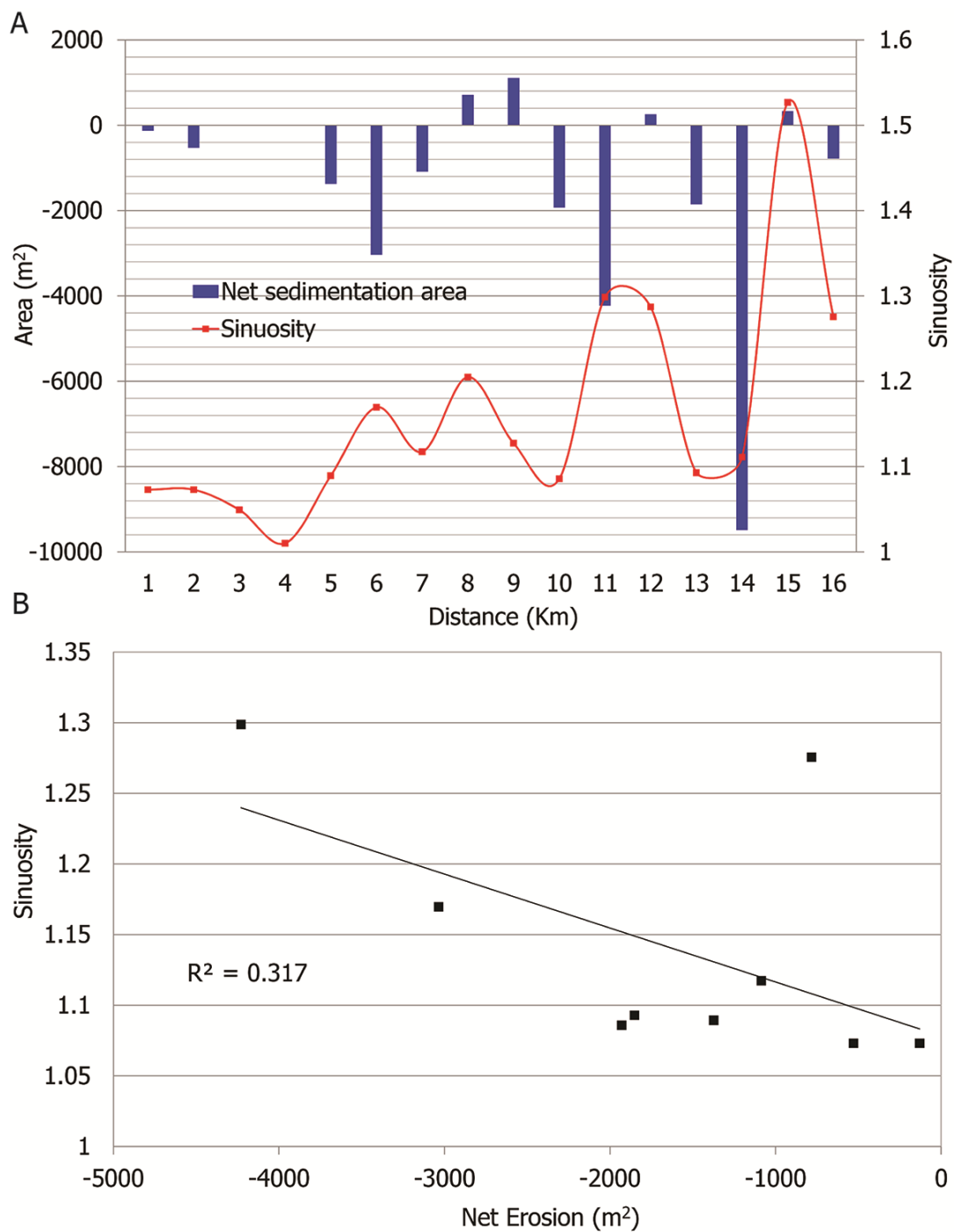
Figure 3.10: *Net sedimentation area along the river.*

3.4.2.1   Meander morphology

Prominent bank erosion results in changes in meander morphology. Meander morphology changes include a new bend, regular symmetric meanders and compound asymmetric bends,

which have been described by Hooke and Yorke (2010). A new bend (Figure 3.11, Bend-1) starts at a relative straight reach and shows continuous growth over the period of observation years. Regular symmetric meanders (Figure 3.11, Bend-2, Bend-3 and Bend-5) migrate downstream and increase in amplitude. Meander morphology shows that the maximum erosion occurs mostly at the apex or at downstream limbs (Figure 3.11). Some symmetric meanders (Figure 3.11, Bend-4) developed from simple symmetric to compound forms, which are characterized by double-heading (Hooke, 1995; Hooke and Yorke, 2010). Furthermore, we note that the net erosion is linearly associated with the channel sinuosity in the studied river (Figure 3.10). Although the bar-like islands ultimately amalgamated to a large island as the channel between them was abandoned and filled, mid-channel bars have been barely observed from high-resolution satellite images.

Figure 3.11: *Representative meander morphology in the study reach. Red arrows indicate lateral migration directions.*

3.4.2.2   Channel morphology

Comparison of high-resolution satellite images showed that chute channels, avulsions and headcuts contribute to erosion. A chute channel, which cuts across the top of a bar or across the inside of a meander bend, was observed (Figure 3.12). The chute channel was initiated as crevasse channel at the outer bank of a point bar and went through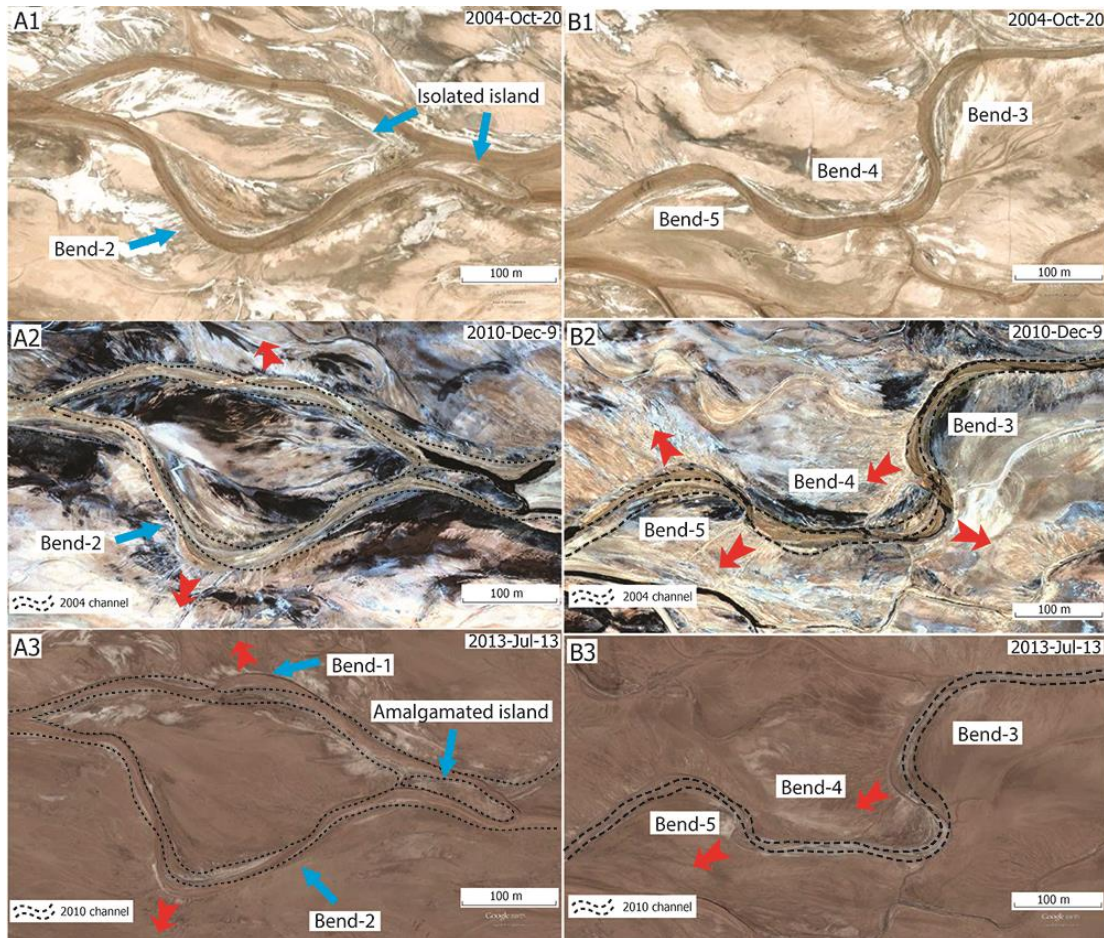 an area in the middle of two point bars and then joined the river downstream. In addition, local avulsions are also observed by comparing satellite images (Figure 3.12). In this example the flow path shifted to a new path and the depression in the previous channel still remained. The avulsion appears to have been triggered by lateral migration within a divided reach where erosion on the left bank of the right channel and the right bank of the left channel caused the channels to converge until the bank breached and the channels were reunited. Following the avulsion and the formation of the chute channel, the new courses offer a more favourable gradient and appear to have developed at the expense of both sinuous channels, ultimately leading to abandonment of the pre-existing channels. Headcuts are another important feature in the study reach (Figure 3.12), although measuring headcut areas is not possible from satellite images due to a lack of resolution. These tree-like headcuts started at anabranches downstream where they re-joined the main channel and the height difference between the floodplain level to the main channel bed level enhanced the erosive power of overbank flow and initiated a nickpoint (Schumann, 1989). The headcuts migrated upstream up to 270 m between 2004 and 2013.
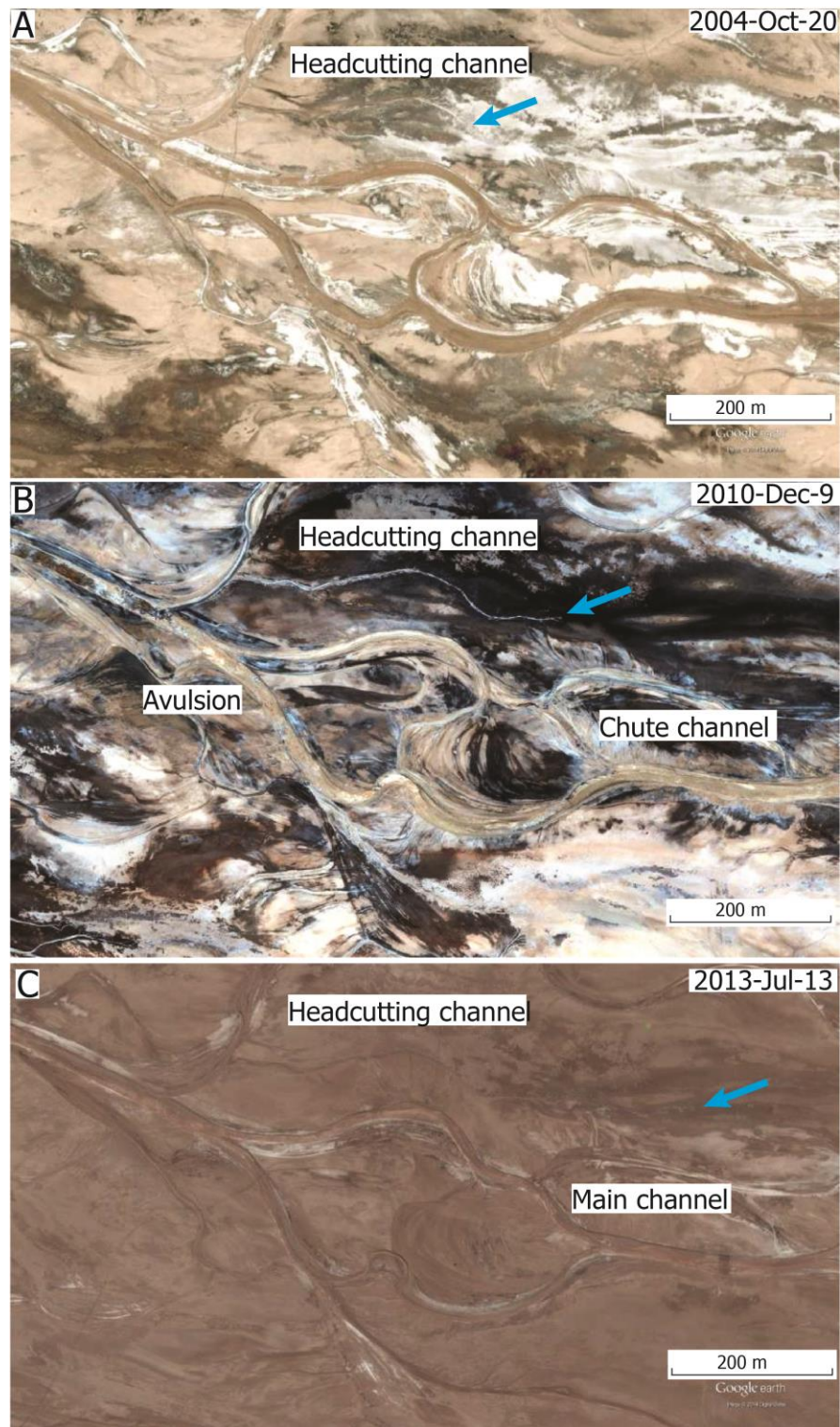
Figure 3.12: *Channel morphology and headcuts in the study reach. Cyan arrows indicate the head of headcutting channel. Three satellite images in different dates show the development of a chute channel to the main channel.*
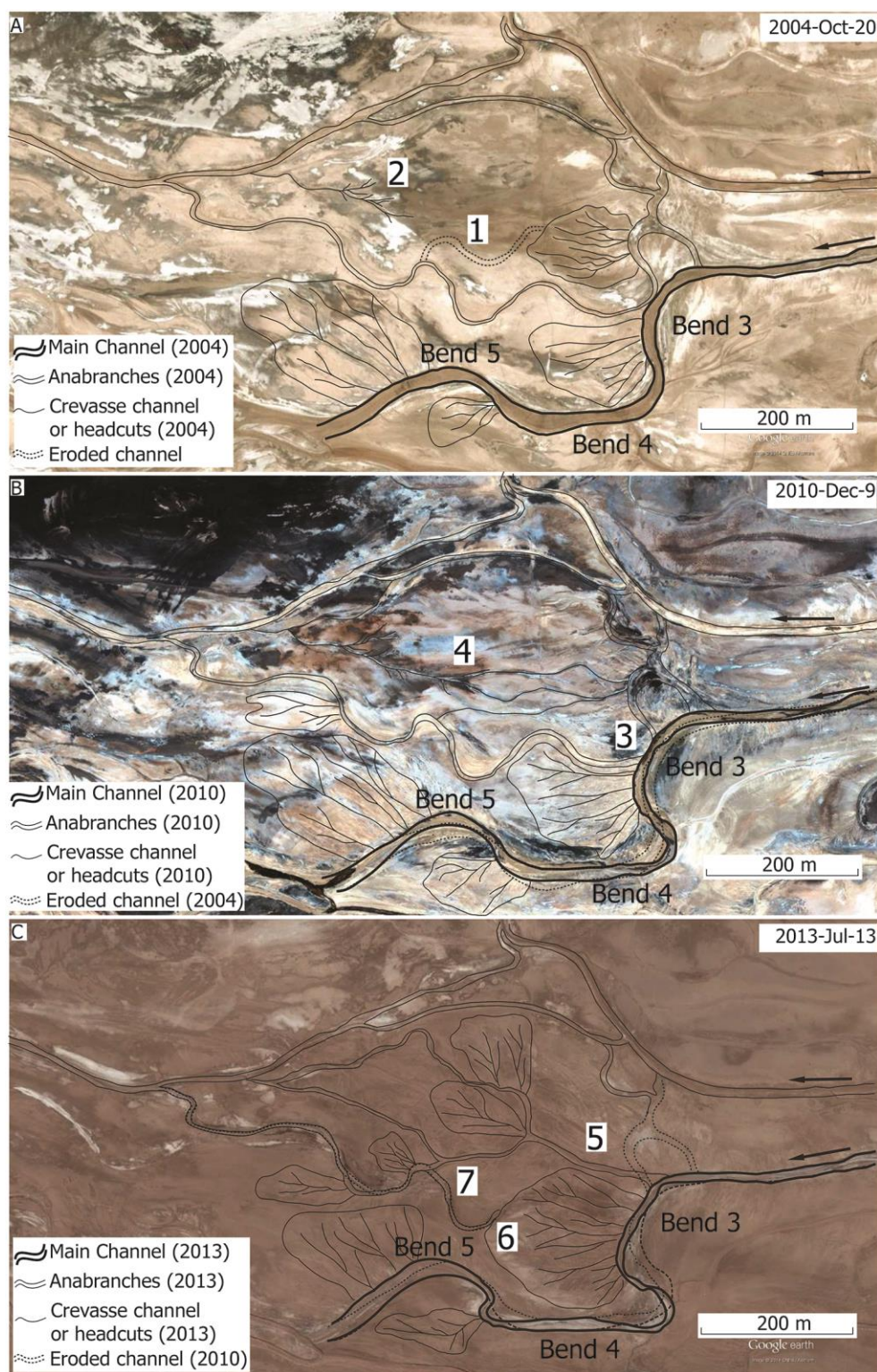
3.4.2.3   River pattern development

Figure 3.13: *The development of anabranching pattern caused by lateral migration and growth of crevasse channels. A series of numbers represents typical processes. 1: a completely filled*

meander overlapped by crevasse splays. 2: upstream-migrating headcuts. 3: Lateral migrating bend cuts an abandoned bend and reactivates the abandoned meander. 4: Connection between upstream-migrating headcuts and crevasse channels. 5: Growth of a crevasse channel leads to more crevasse splays on the floodplain. 6: Expansion of the crevasse splay blocks the meander again. 7: A crevasse channel reconnects the abandoned meander. See the location in Figure 3.1D.

River pattern changes as channel morphology develops. With the growth of meander bends, a partially abandoned meander was reactivated as the abandoned channel reconnected to the main channel (Figure 3.13). However, the connection was blocked when a crevasse splay formed and expanded. In the meantime, headcuts in the downstream anabranches migrated upstream. As the crevasse channel developed in size and elongated downstream, it connected upstream-extending headcuts as well as tended to reconnect with the partially abandoned meander channel downstream. In addition, lateral migration-induced avulsion left the partially abandoned channel (Figure 3.14). The upstream chute channel developed as the main channel over the observation years and partially abandoned previous reach. However, some abandoned channels were filled or superimposed by crevasse splays. All these processes result in the anabranching pattern found in Zone 2.

3.5   Interpretation of chute channel formation

We suggest two possible explanations for the development of the chute channel: one due to local hydraulic gradients, and a second due to the topography of the bar top. The first explanation invokes a hydraulic gradient advantage for the potential chute channel (Howard, 1996) where the flow across the bar top follows a preferable hydraulic gradient as crevasse splays occur during overbank flooding and erodes into the top of the bar as it takes short-cut across the bar instead of following the longer course around the meander bends. Studies of sand-bed meandering rivers show that chute cut-off like this is favoured by bend expansion as the sinuosity and the approach angle increase (e.g. Micheli and Larsen, 2010; Grenfell et al., 2012). Although these models are developed for sand-bed meandering rivers, we see no reason why they should not apply equally well to a bar developed between two meander bends. This is because the same processes of bed expansion, accompanied by channel elongation, and increasing approach angle on the upstream side of the bar, as well as the hydraulic gradient advantage, apply equally well across a braid bar. The braid bar is constructed as a pair of point bars as a single, bank-attached point bar in a meandering channel. Indeed, these concepts have been applied to braid bar formation in gravel-bed braided rivers (Ferguson and Werritty, 1983; Leddy et al., 1993), as wells as flume simulations (Ashmore, 1982). In the second model, we suggest that the formation of the new chute channel is attributed to the relief in the central area of two point bars, where these point bars started their accretion. This central area of the two point bars, therefore, is older than the two sides. Due to compaction, it sinks and is lower than surrounding areas (Figure 3.15). We envisage a scenario where, during peak flood events, water flows directly across the bar top following the topographic low in the middle of the bar, although this model requires more field measurements to be validated.
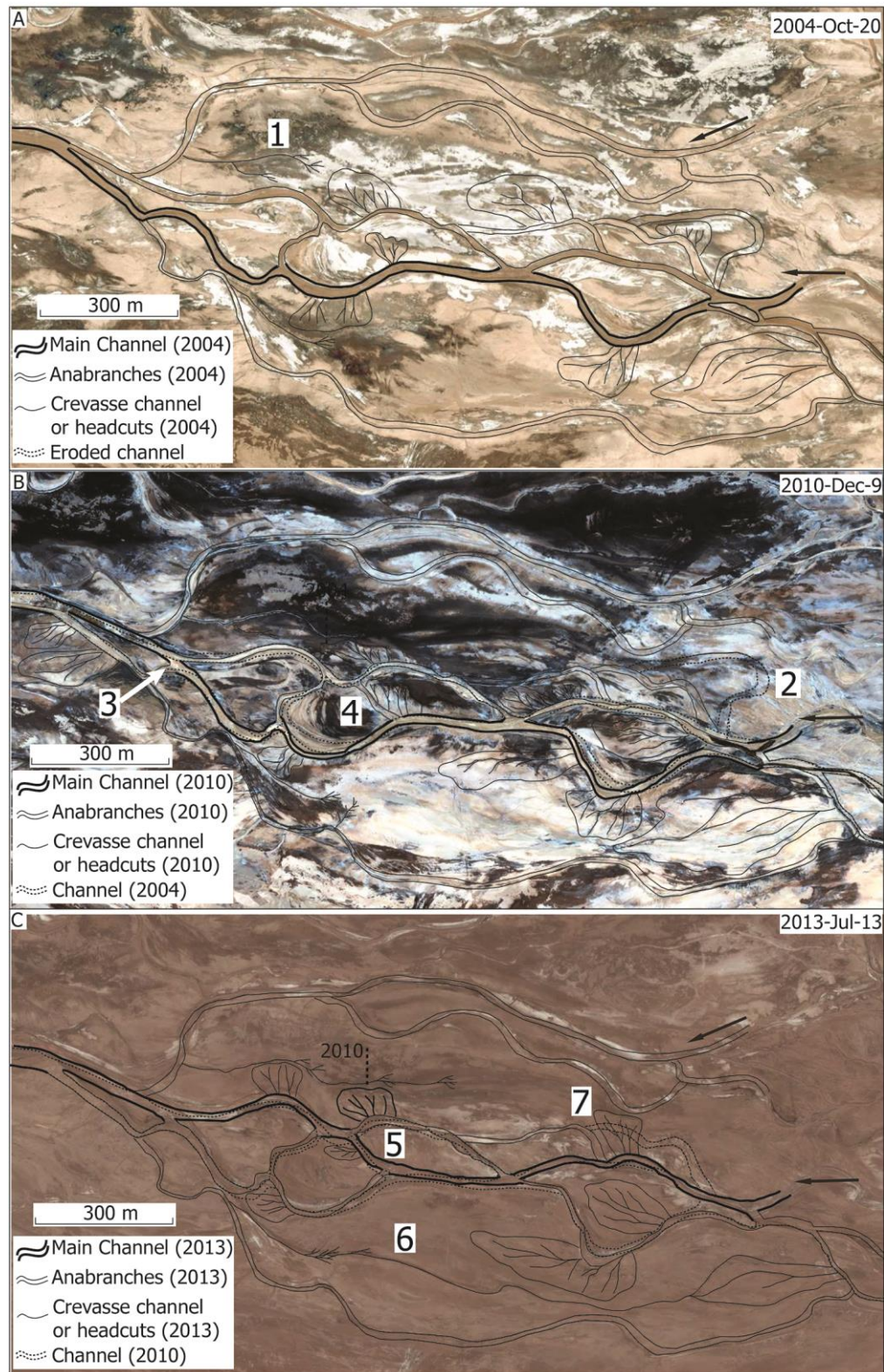
Figure 3.14: *The development of anabranching pattern caused by avulsion and chute channel. A series of numbers represent typical processes. 1: Upstream-migrating headcuts. 2: Abandoned bend to be eroded. 3: Lateral migration-induced avulsion. 4: Crevasse channel-induced chute*

channel. 5: Chute channel becomes the main channel due to preferable hydraulic gradient. 6: Connection between upstream-migrating headcuts and downstream-migrating crevasse channels. 7: Abandoned bend overlapped by crevasse splays. See the location in Figure 3.1D.
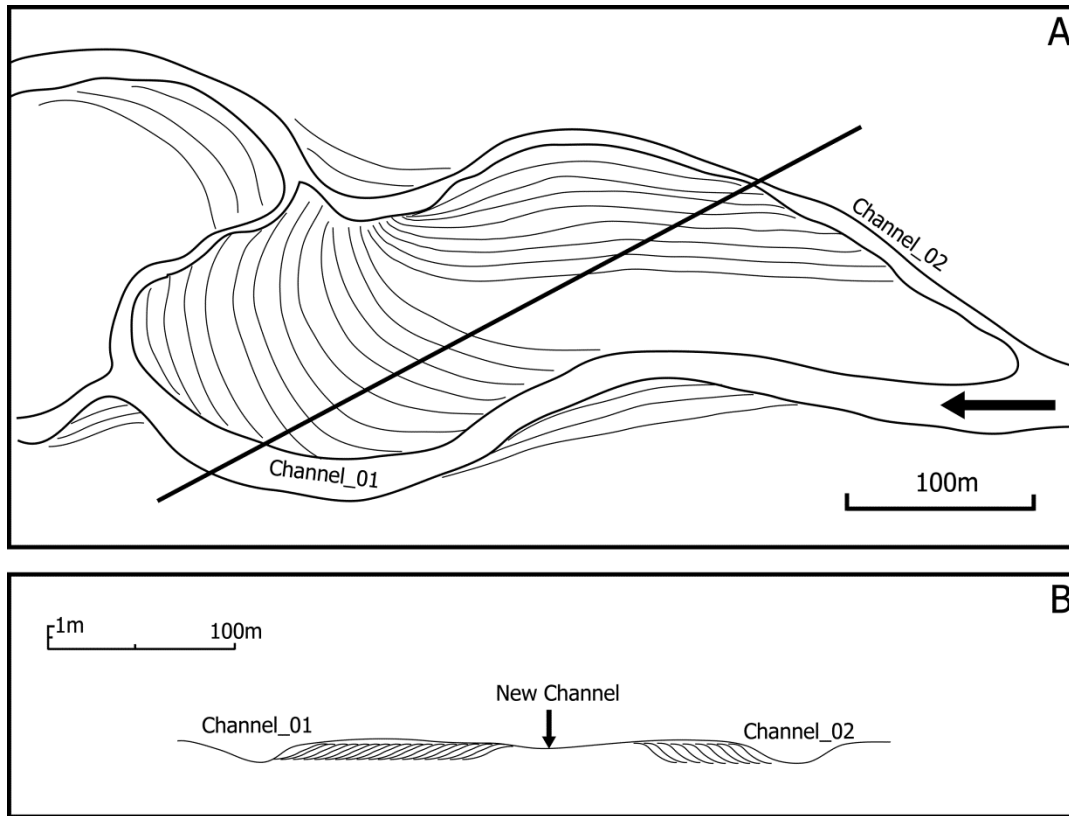
Figure 3.15: *Hypothetical profile across the bar top where the new chute channel occurs. A: a sketch illustrating two adjacent point bars; B: hypothetical profile of a topographic low in the middle of two point bars. The arrow indicates the site of the chute channel.*

3.6   Discussion

3.6.1   Bank erosion

The study reach in Río Capilla shows that two distinct zones with different gradients and vegetation covers have different river patterns, although channels on both zones have frequent overbank flooding and therefore a high density of crevasse splays develops along these channels. By contrast, the Murray River in semi-arid south-east Australia reported by Rutherfurd (1994) showed anastomosing reaches characterized by more frequent over-bank spilling than in the reaches with a single-channel morphology. Characteristics of anabranching river channels are their low gradient, moderate to high sinuosity, and the occurrence of multiple interconnected

channels separated by stable vegetated floodplain (Riley, 1975; Schumann, 1968, 1985; Knighton and Nanson, 1993; Nanson and Knighton, 1996; Makaske, 2001). In dryland environments, bank stability is normally attributed to high bank strength due to fine-grained sediment cohesion as well as low vegetation densities, which are sometimes not sufficient to effectively strengthen banks (North et al., 2007). However, in the study reach of the Río Capilla, river bank erosion and deposition are very active in Zone 2, which contrasts with the channels in Zone 1 and other dryland vegetated anabranching river systems. For instance, trees hundreds of years old lining the channels in the anastomosing river systems of the Channel Country in arid central Australia indicate channel stability over very long periods (Makaske, 2001).

A critical question raised is why bank erosion and deposition in Zone 2 is prominent in the low-gradient river system with river banks consisting primarily of cohesive silt/clay (Figure 3.8E4). For river channels, lateral stability is regarded as a function of slope, discharge and bank resistance (Makaske, 2001). Leopold and Wolman (1957) combined slope and discharge into a single parameter of stream power, which is widely used to analyse the lateral stability of river channels (e.g. Brown, 1987, Nanson and Croke, 1992; Makaske, 1998). However, Knighton and Nanson (1993) concluded that most anabranching rivers have a low stream power by comparing bankfull discharge against channel slope for anastomosing, braided and meandering rivers. Likewise, the study area is characterized by a low gradient (Figure 3.1E) and a flashy flow regime (Figure 3.6), which suggests stream power here is also low. Therefore, bank resistance is probably the major factor influencing bank erosion. Bank resistance includes the reinforcing of banks by vegetation and silt/clay sediment cohesion (Nanson and Knighton, 1996; North et al., 2007). NDVI analysis and field investigation shows those river banks characterized by prominent erosion are non-vegetated (Figure 3.7), which contrasts with other dryland anabranching river systems (e.g. dense growths of sagebrush along channels of Red Creek in the Red Desert area of the Great Divide Basin, Wyoming, Schumann, 1989; shrub and teatree in a reach of the ephemeral Marshall River, Northern Plains, arid central Australia, Tooth and Nanson, 2000). Although channel chronologies are barely reported for arid anabranching systems (Makaske, 2001), riparian vegetation in the Magela Creek in the northern Australian tropics facilitated island growth between the anabranches and an associated flow division shift over the past 2000-3000 years (Tooth et al., 2008). Other studies also demonstrated that vegetated banks significantly strengthen more resistance (up to 20,000 times) than non-vegetated banks (Smith, 1976; Beeson and Doyle, 1995). Similarly, in the study reach grass-covered banks in Zone 1 are stable while bank movement along non-vegetated banks is up to 5 m/yr on average.

Another essential issue about bank resistance is fine-sediment cohesion of the banks. River banks consisting mainly of silt and clay are widely regarded as having a strong cohesion and therefore a high resistance to bank erosion. However, in the study area, the short period of the rainy season on the Altiplano (December to March) and the long-term exposure to insolation give rise to salinization and cracking of the sediment, which combines with freeze thaw cycles due to the extreme diurnal temperature fluctuations. While these river banks are fairly well consolidated compared to those typically found in more humid climates, we still consider them unconsolidated here as they are prone to being eroded by the violent impacts that flash floods impart on them. Furthermore, as one of the objectives of this study is to compare this sedimentary setting to analogue ancient rocks, these river bank sediments are obviously much less consolidated than

their ancient counterparts in the subsurface. Field investigation and the excavated section in the dry non-vegetated bank shows that cracks develop in two types of non-vegetated river banks: one oblique but parallel to the flow direction, and the other perpendicular to the flow direction (Figure 3.16). The former cracks are attributed to gravity effect because the bank base is eroded. These cracks tend to collapse or contribute to bank erosion during the next floods. The excavation also shows that the non-vegetated bank is full of macropores, which reduce bank cohesion. These macropores are probably caused by plant roots and soil fauna (Doležal and Kutílek, 1972) or by the swell-shrink dynamics of the fine-grained sediment due to repeated drying and wetting in a setting characterized by strong seasonal activation (Vogel et al., 2005), whereby the second kind of cracks is thought to be created. Other factors (e.g. sheep in Figure 3.7C) also facilitate the development of desiccation cracks. These cracks significantly contribute to make the banks more erodible even under low stream power. Although Gibling et al. (1998) mentioned that desiccation cracks occur on accretionary bench and upper bank surfaces in the anabranching river of the Channel Country in central Australia, their cracks are not identical to those in the Río Capilla, where bank cracks perpendicular to flow direction extend deeper (up to 50 cm) (Figure 3.16).

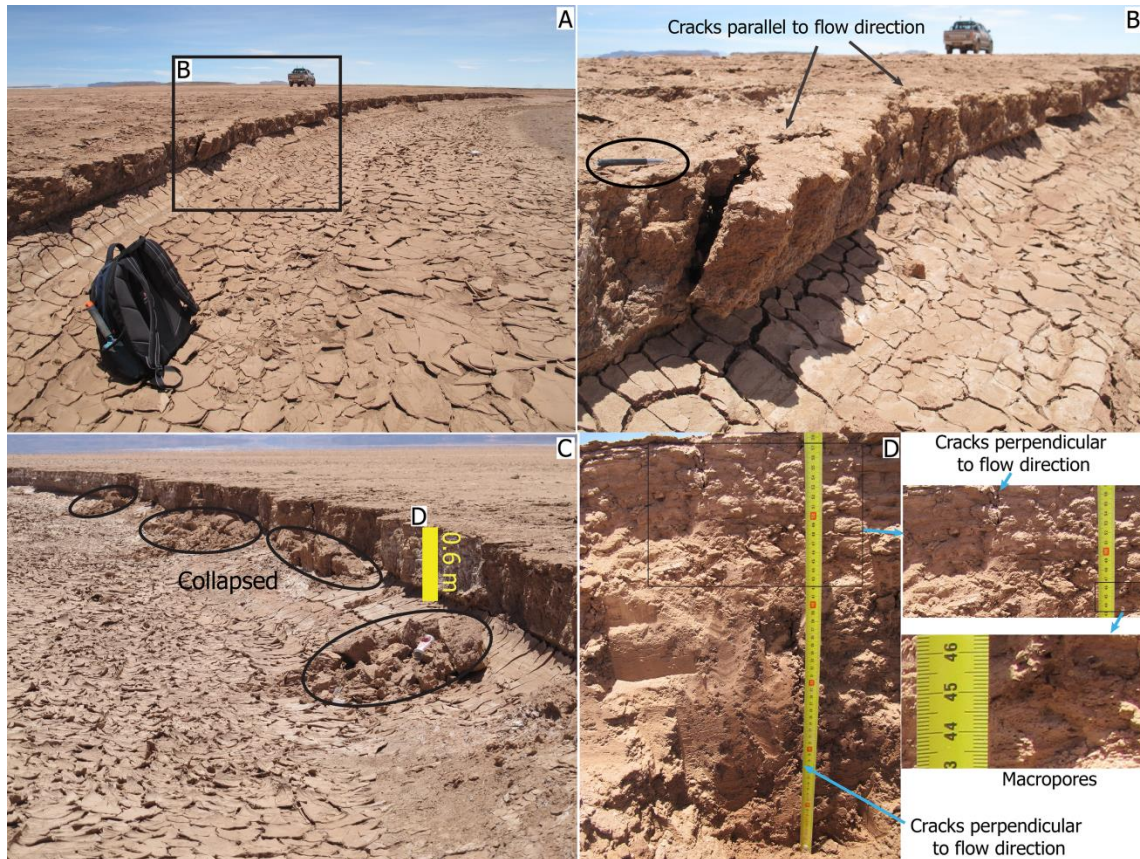**Figure 3.16:** An eroded bank along the river in the Zone 2. B shows cracks parallel to flow direction. The bag is 50cm high (A) and the pen is 13cm long (B). Flow direction is from lower left to upper right (A and B). C: Collapsed bank sediment along the river. Flow direction is towards the camera. D: Detailed analysis of a non-vegetated bank, where cracks perpendicular to flow direction are abundant.

3.6.2   Anabranch development

Lateral migration and overbank flooding in combination with headcuts on the floodplain create an anabranching pattern in the study area. Lateral migration promotes avulsion, which leaves the previous channel partially filled (Figure 3.14). In addition, lateral migration tends to reactivate the partially abandoned meanders (Figure 3.13). Besides lateral migration, crevasse splays are widely distributed along channels over both outer banks and accretionary bench due to frequent overbank flooding. Shallow channels in combination with poor development of levees favour overbank flooding in the study area. Furthermore, the narrow lower bench opposite the outer banks reduces the channel capacity and therefore promotes overbank flooding. As mentioned above, non-vegetated banks are easily scoured due to well-developed cracks and an abundance of burrows. Although the uppermost part of accretionary bars consists of silt/clay, sometimes covered by grass (Figure 3.8E1 and E3), excavations show them to be unconsolidated and therefore also easily scoured and eroded by overbank flow. Crevasse channels tend to form flow divisions (chute channels) as a low preferable hydraulic gradient is created (see Section 3.5). By contrast, Riley (1975) revealed that levees and crevasse avulsions are absent in the low-gradient and semi-arid Namoi-Gwydir distributary system, and he also mentioned that large flood events have the capability to scour new anabranches into the floodplain without crevassing. In addition, the connection between upstream-migrating headcuts and crevasse channels is another way to forming anabranches (Figure 3.13 and Figure 3.14), which contrasts with the anabranching river system in the Red Creek in Wyoming (Schumann, 1989), where crevasse splays are poorly developed and anabranches are initiated from downstream headcuts migrating upstream and connecting the main channel. Furthermore, crevasse channels in the Río Capilla tend to connect the partially abandoned meanders.

3.7   Conclusions

Bank erosion and accretion and their impact on changes in channel planform were analysed in the Río Capilla river system of the southern Altiplano plateau. Prominent bank erosion and changes in planform were measured through field investigation and high-resolution satellite imagery analysis. The major results include the following:

- ASTER GDEM yielded catchment information such as area and slope of the system. The catchment profile shows the maximum slope to be up to 1.57 m/m at the margins with a mean slope of 0.0008 m/m. Precipitation data analysis shows irregular overland flow to dominate in the study area and an increasing trend through time of the magnitude of single flood events.
- NDVI and field investigation shows a wide variation in vegetation cover in the study reach. In combination with vegetation cover distribution, GPS and excavation indicated that the study reach is divided into two zones: Zone 1, characterized by relatively straight channels with grass-covered banks, is stable despite high gradient, whereas Zone 2, typified by anabranching pattern with non-vegetated banks, experiences prominent bank accretion and erosion.

- Comparison of high resolution satellite images reveals erosion exceeds deposition and is accompanied by changes in channel planform, such as meander and channel morphology. NDVI analysis and field investigation suggest that non-vegetation cover and abundance of desiccation cracks and macropores are mainly contributing to bank erosion.
- Changes in channel planform are the product of continuous lateral migration and frequent overbank flooding. Shallow channels and poor development of levees in combination with in-channel accretionary benches result in frequent overbank flooding, which lead to a high density of crevasse splays over unconsolidated river banks and accretionary benches. Avulsion and chute channels together with reactivation of partially abandoned meanders and connection of headcuts and crevasse channels produce an anabranching pattern in the study area.

Chapter 4   Splay Morphodynamics in A River Terminus[3]

Abstract. High-resolution satellite imagery in combination with field investigation enables the analysis of splay morphological developments in time and space at the low-gradient terminus of the modern Río Colorado dryland river system in the Salar de Uyuni (Bolivia). Two sets (2004/2005, 2010/2011) of satellite images are used to visualize splay morphological developments and three types of crevasse splays are identified based on temporal changes: (1) new crevasse splays (NCS), referred to those splays that are not observed in the first set of images but can be observed on the second sets of images; (2) changing crevasse splays (CCS), representing those splays that are found on the first set of images but their geometry changed between two satellite observation periods; and (3) inactive crevasse splays (ICS), referred to those splays that are found on the first set of images but on the second set of images they remain the same, or are partially overlapped by adjacent expanding crevasse splays. These three types of crevasse splays have no correlation with the distance to the starting point of the river or the local slope. Field investigation shows that desiccation cracks and salt efflorescence of crevasse channel levees reduce their cohesion and shallow crevasse channels increase levee breach. Therefore these factors result in frequent expansions of crevasse splays. The cross-sectional area of the studied river steadily decreases downstream, and frequency analysis shows a downstream increase in the number of crevasse splays and suggests an exponential relationship with the river cross-sectional area. Development of crevasse splays is often attributed to topographic lows between adjacent crevasse splays, and they fill in the depression by compensational stacking. These amalgamated splays are capable of forming a large area of sheet sands and potentially provide an analogue for thin-bedded hydrocarbon reservoirs.

4.1   Introduction

Fluvial crevasse splays are a significant part of many dryland fluvial systems and deltas (Brackenridge, 1988; Miall, 1996; Makaske, 1998; Bridge, 2003). To date, many studies have been published on the geomorphology and sedimentology of crevasse splays (e.g. Elliott, 1974; Fielding, 1984; Mjøs et al., 1993; Smith and Pérez-Arlucea, 1994; Jorgenson and Fielding, 1996; Bristow et al. 1999; Anderson, 2005; Cahoon et al., 2011). Most of these studies of modern splays have been conducted in humid regions. Recently, more research on modern splays in

---

[3] Chapter 4 is based on the manuscript entitled "Splay morphodynamics in a dryland meandering river terminus: Río Colorado in Salar de Uyuni Bolivia". J. Li, C.S. Bristow. (submitted). Quaternary International.

drylands has been conducted (e.g., Tooth, 2005; Donselaar et al., 2013). Dryland rivers experience a downstream decrease in cross-sectional area due to low gradient, leading to loss of flow energy, as well as downstream transmission loss by high evapo-transpiration and water percolation through the channel floor (Tooth, 2000; Donselaar et al., 2013). Low gradient reduces the transport efficiency of dryland rivers and, during short-lived and high magnitude peak discharge events, flood waters spill out of the channel onto the adjacent floodplain. This process involves the breaching of levees. In addition, during the waning stage of flood events, water flows back to the trunk channel through crevasse channels, which are therefore deepened and widened (Donselaar et al., 2013). However, the impact of the downstream reduction in cross-sectional area on crevasse splays in dryland meandering systems has rarely been studied due to difficult accessibility. The aims of this study are to investigate the size and morphodynamics of modern crevasse splays from the Río Colorado in the Salar de Uyuni (Bolivia). High-resolution satellite imagery of different periods (2004/2005, 2010/2011) enables the visualization of splay morphological changes in time and space in combination with ground-truth validation. In this chapter we present an informal classification scheme for crevasse splays based upon difference recorded over a six year period. We describe their distribution along the lower distal reaches of a dryland river system that terminates in a playa lake and discuss potential controls on crevasses splay development. Crevasse splay deposits have been identified as potential hydrocarbon reservoirs (Mjøs et al., 1993) and this study aims to shed light on the size, shape, spatial distribution and connectivity of crevasse splay deposits. Therefore it also provides the volumetrics of these hydrocarbon reservoirs in this dryland meandering depositional environment.

4.2 Data acquisition and methods

We focus on the distal reaches of the Río Colorado system (Figure 4.1), where no human interference is involved. High-resolution satellite imagery (QuickBird02 and WorldView02) is used to visualize the development of the crevasse splays in space and time. Detailed information about satellite imagery and precipitation data can be found in Section 3.3.1. To quantify the impact of the river gradient on the development of crevasse splays, a high-precision global positioning system (GPS) was used in the field. A Trimble R7 dual frequency geodetic GPS receiver was mounted on a car to measure the gradient along the river. Because of the open nature of the area and absence of obstacles hindering the tracking of GPS satellites, the area was well suited for GPS-Precise Point Positioning (PPP). See detailed GPS data processing in Section 3.3.2.
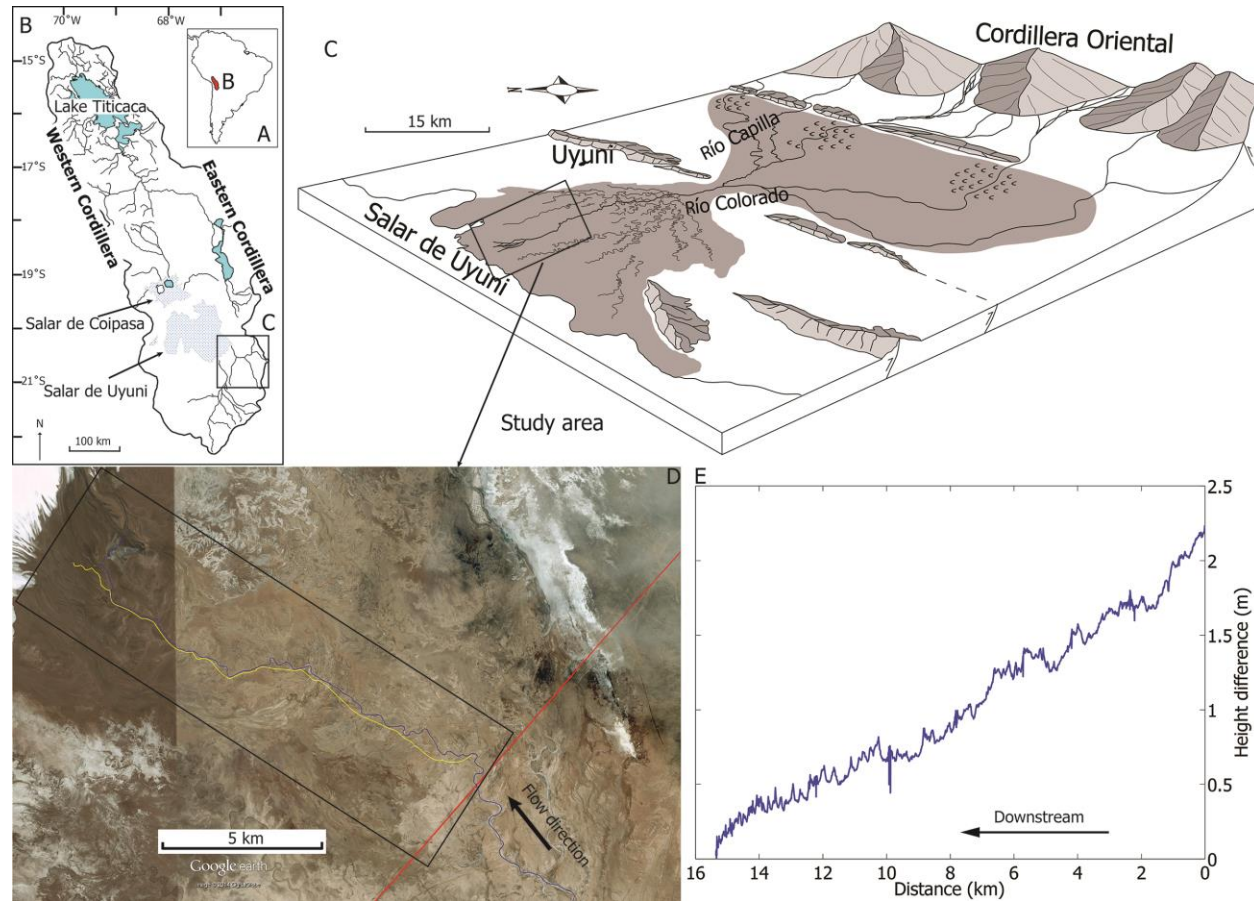
Figure 4.1: *Map of the study area. A, B and C: The location of Altiplano plateau in South America and the Río Colorado. D: The black frame indicates the study area. The blue line is the main channel, the yellow line is the GPS measurement line, and the red line is a railway. E: A high-precision GPS profile of the profile along the yellow line in D. A and B: modified after Placzek et al. (2011). C: modified after Donselaar et al. (2013).*

The QuickBird-02 and WorldView-02 images have been projected to Universal Transverse Mercator (UTM) coordinates. WorldView-02 images were rectified to QuickBird-02 (GoogleEarth) images with image-to-map registration within the remote sensing image analysis software ENVI. The RMS error was less than 1.7 pixels, or 0.85 m.
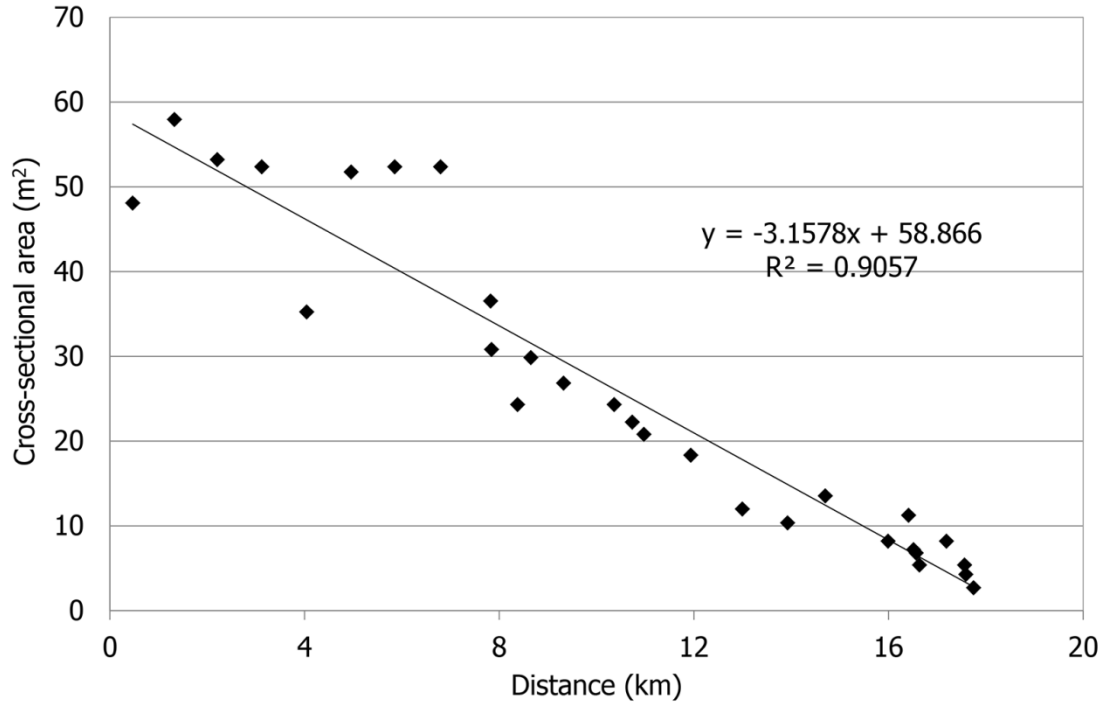

Figure 4.2: *The downstream reduction in cross-sectional area of the main channel.*

With the ASTER AST07XT data, the Normalized Difference Vegetation Index (NDVI) was employed to investigate the vegetation cover. Field data about the cross-sectional area of the main channel from Donselaar et al. (2013) were reanalysed in combination with the frequency of crevasse splays. An equation characterizing the downstream reduction of cross-sectional area along the studied river was obtained through linear regression and subsequently used to calculate the mean values of cross-sectional area in intervals of one kilometre (Figure 4.2, eq.4-1).

$$A = -3.1578 * x + 58.866 \qquad (4\text{-}1)$$

where A is the cross-sectional area (in m^2), and x is the distance from the starting point of the studied river (in km). Areas of splays were defined by colour variations between splay surface and floodplain surface based on high-resolution satellite imagery (Figure 4.4B). Field investigation was conducted in November 2012, and included measurement of the depth and width of crevasse channels. The number of crevasse splays per kilometre was calculated along the river.

4.3 Crevasse splay types

Three types of crevasse splays could be identified based on the observed temporal changes: (1) new crevasse splays (NCS); (2) changing crevasse splays (CCS); and (3) inactive crevasse splays (ICS). NCS are those splays that were not observed in the images of 2004/2005 but could be observed on the images of 2010/2011. CCS can be found on the 2004/2005 images but their geometry changed between 2004/2005 and 2010/2011 after the comparison of two sets. The most obvious indicator for changing crevasse splays is whether the crevasse channels shifted or expanded. The third type, ICS, are those crevasse splays that can be found on the 2004/2005 images but that remained the same on 2010/2011 images, or that are partially overlapped by adjacent expanding crevasse splays (Table 4.1).

Types	Number
New crevasse splays (NCS)	83
Changing crevasse splays (CCS)	83
Inactive crevasse splays (ICS)	124

Table 4.1: *Statistics of crevasse splay types along the river.*
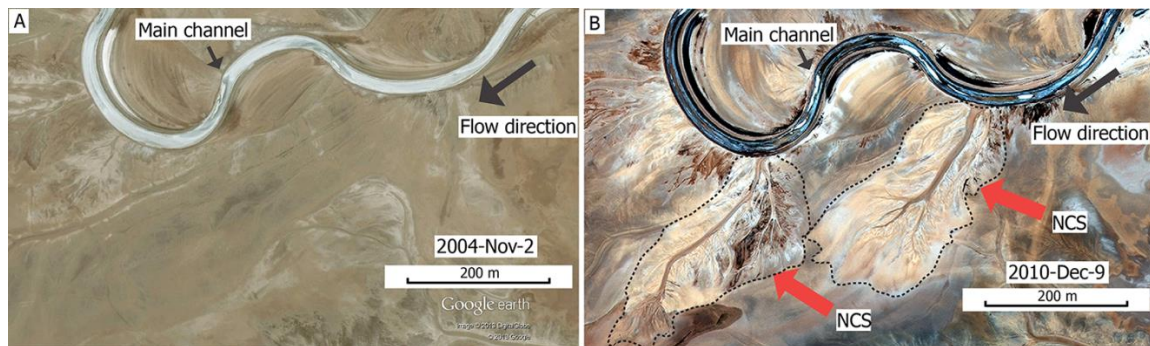
4.3.1 New crevasse splays (NCS)

Figure 4.3: *New crevasse splays along the river. These satellite images show the same area. The arrows show the areas of two NCS with the dashed lines indicating the outlines.*

Seventy-nine NCS have been found along the studied stretch of the river (Figure 4.3) and four NCS have been found at the end of the channels (terminal splays). The distribution of NCS is characterized by zonation (Figure 4.4, Appendix A). 60.2% of NCS have areas in the range of 0-20,000 m^2 (Figure 4.5, 25.3% have areas of between 20,000 m^2 and 50,000 m^2, and 14.5% with areas of more than 50,000 m^2, which indicates a significant amount of sediment transport to the terminus of the Río Colorado. There is no correlation between the area of NCS and distance downstream (Figure 4.6). The high density of NCS towards the end of the river is associated with local avulsions (Figure 4.7).
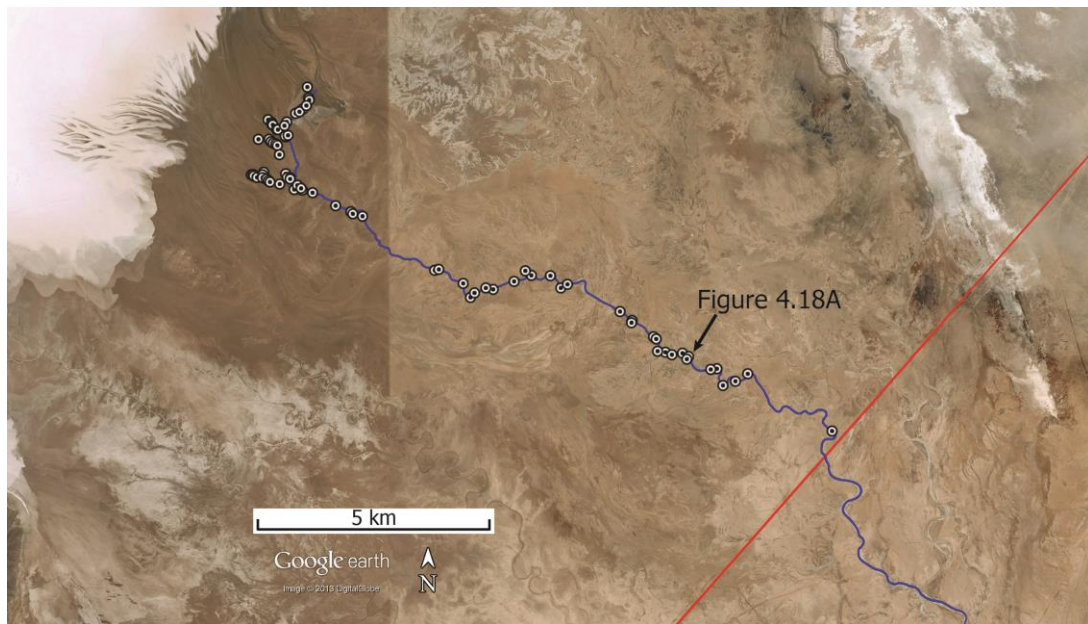
Figure 4.4: *Distribution of NCS along the main channel. Black circles show the sites of new crevasse splays and the red line indicates the railway.*
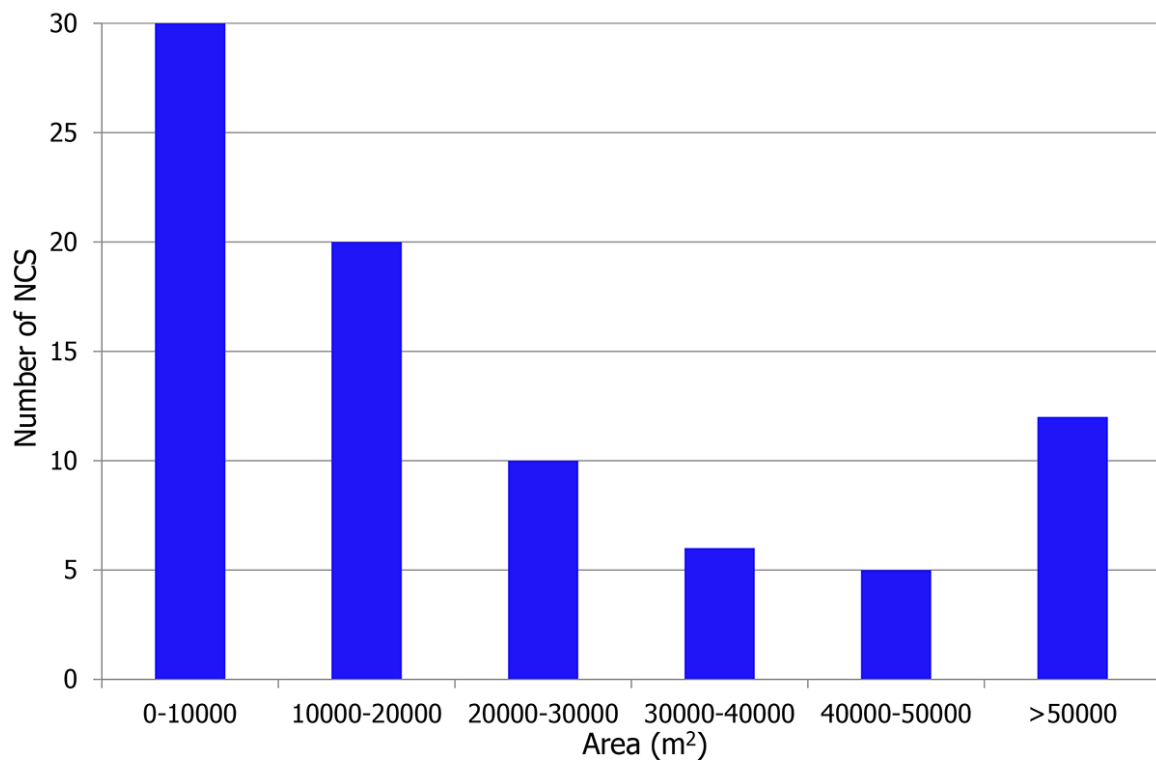
Figure 4.5: *Areal distribution of NCS along the main channel.*
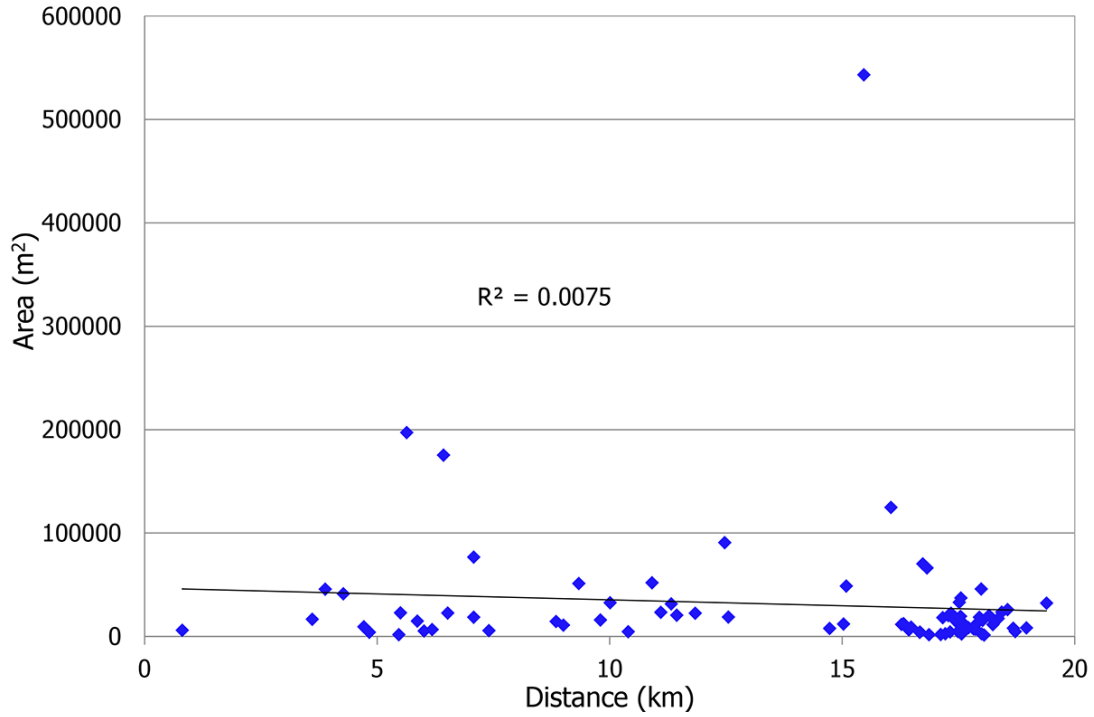
Figure 4.6: *the relationship between their areas and distance.*
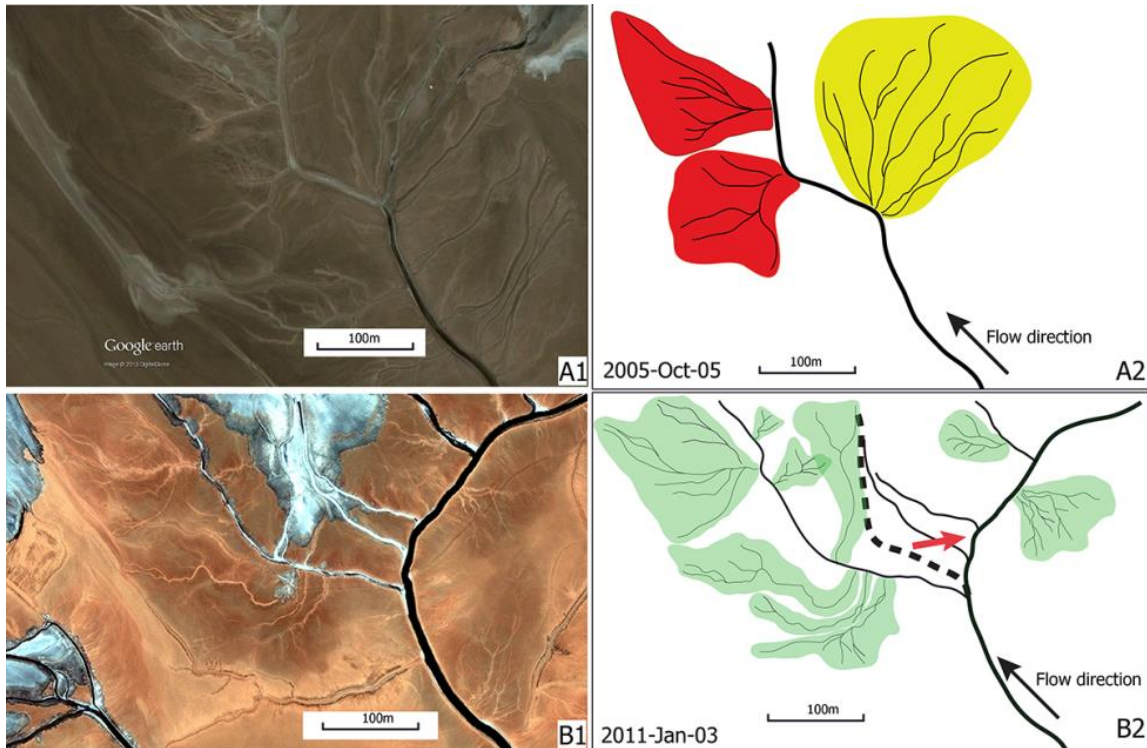
Figure 4.7: *Avulsion-led new crevasse splays. A1 and B1: The same area from satellite images in two periods; A2 and B2: Interpretative line drawing, coarse lines indicate the trunk channel. A2: red splays represent ICS; yellow splay at site where avulsion occurs. B2: green splays represent*

NCS. Dashed line indicates trunk channel path before avulsion and erosion in 2011. The arrow shows the shifting direction.

4.3.2   Changing crevasse splays (CCS)

Eighty-three crevasse splays are classed as CCS based on differences of satellite images between the periods of 2004/2005 and 2010/2011 (Figures 4.8 and 4.9, Appendix B). Analysis of the area of CCS along the river indicates that the number of individual CCS with an area greater than 500,000 m^2 was more in the 2010-2011 period (six CCS) compared to the 2004-2005 period (two CCS) (Figure 4.10). The area difference statistics for the two periods show that the most dramatic changes in area happen in the middle reaches (8 – 12 km). Comparing the area of splays over a six year period we have found that 55 have increased in area while 28 have decreased in area. There is no correlation between the area of CCS and distance downstream (Figure 4.11).
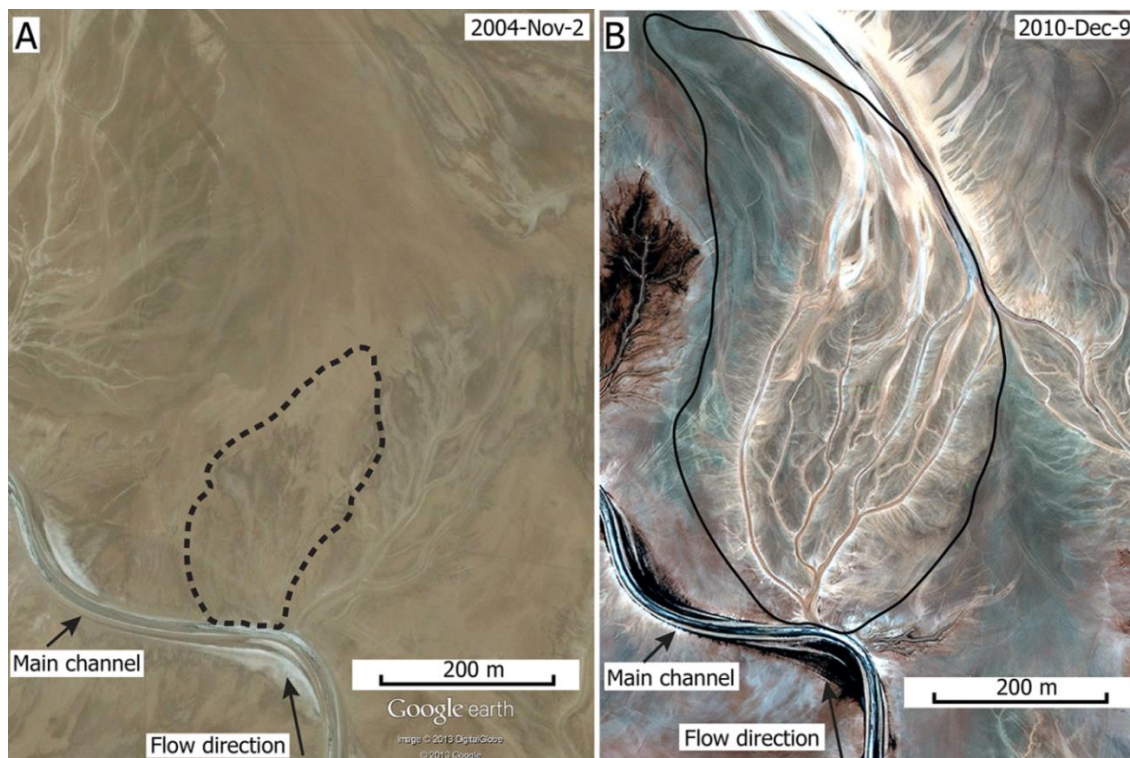
Figure 4.8: *Downstream expansion of CCS. Two satellite images show the same area.*
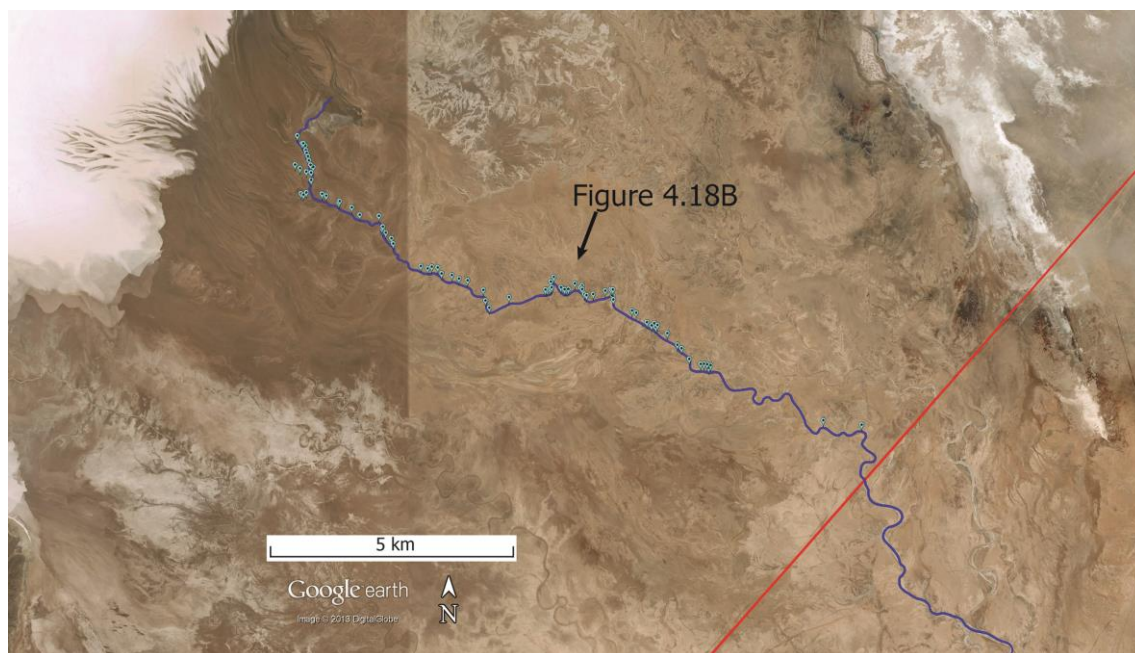
**Figure 4.9:** *Distribution of CCS along the river. Dots show the sites of CCS and the red line indicates the railway.*
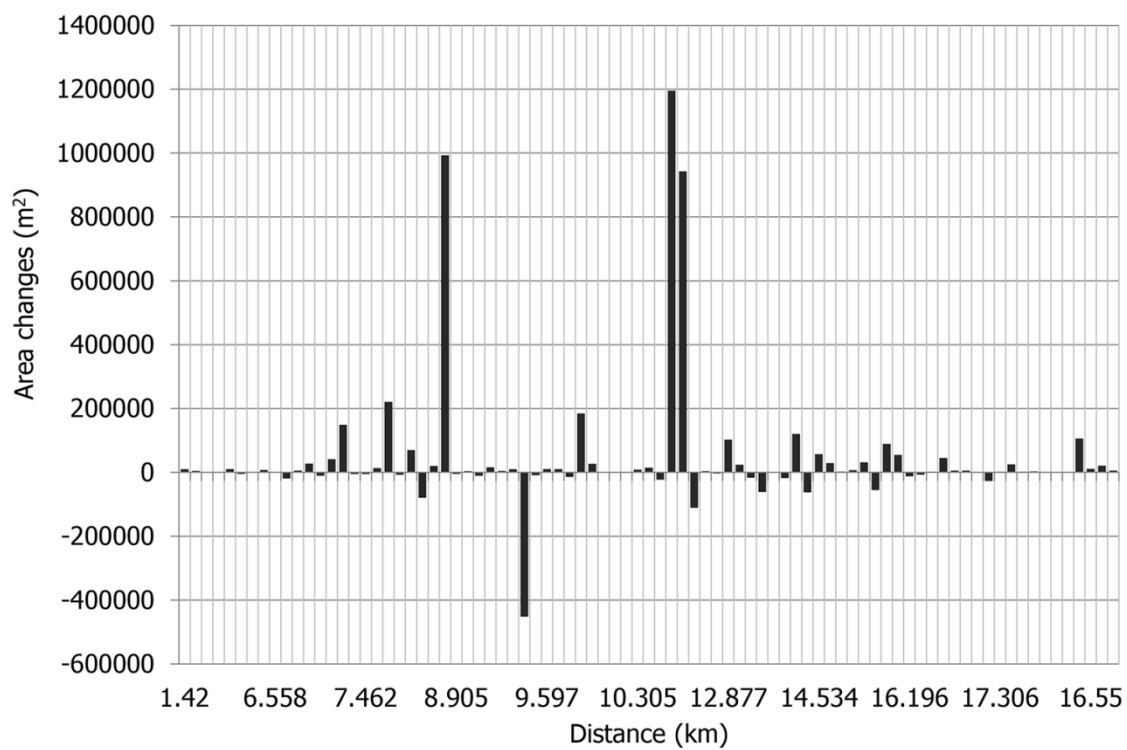
Figure 4.10: *Areal changes of CCS along the main channel in two periods (2004/2005, 2010/2011).*
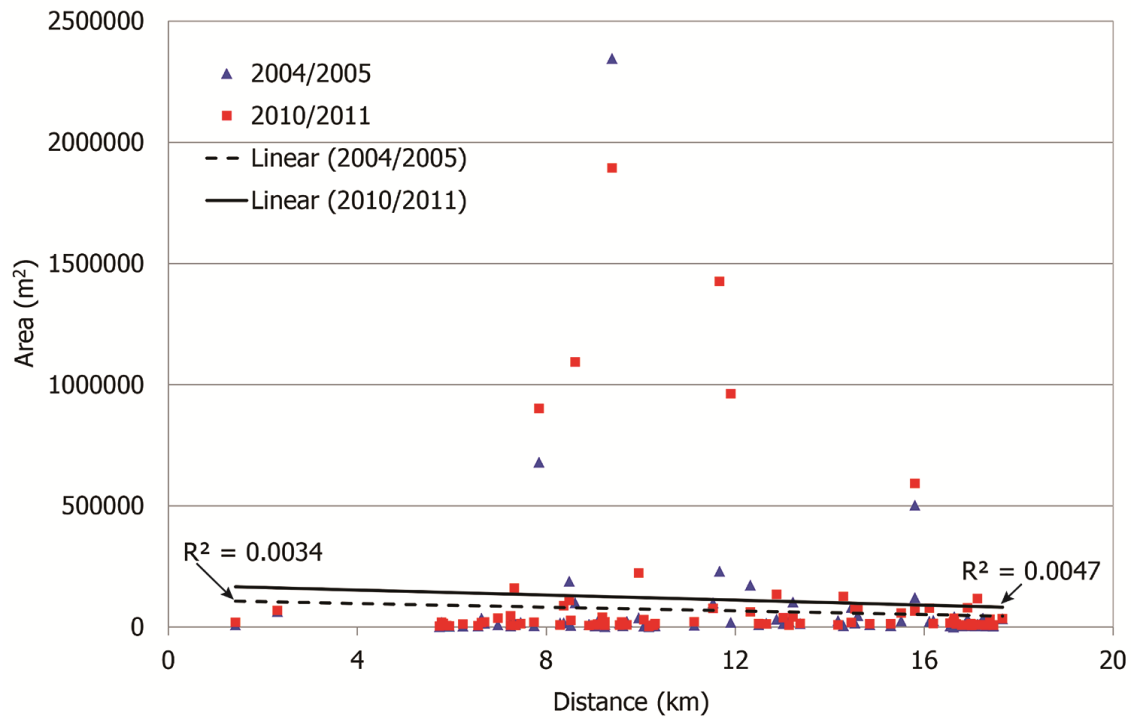
Figure 4.11: *The relationship between the areas of CCS and distance.*

4.3.3   Inactive crevasse splays (ICS)
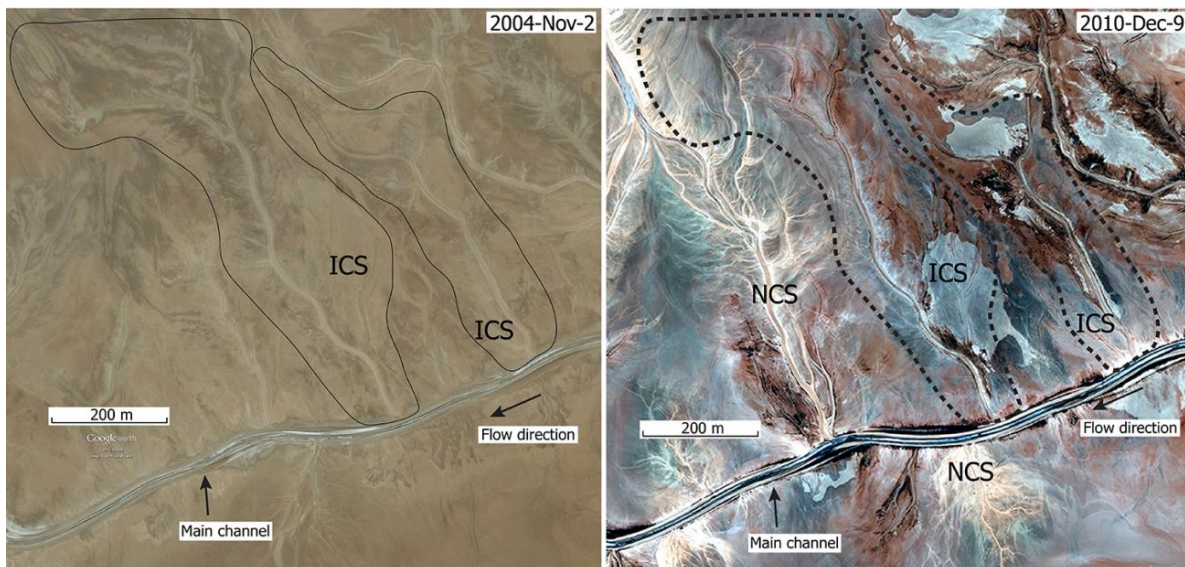
Figure 4.12: *ICS along the river. Two satellite images show the same area.*
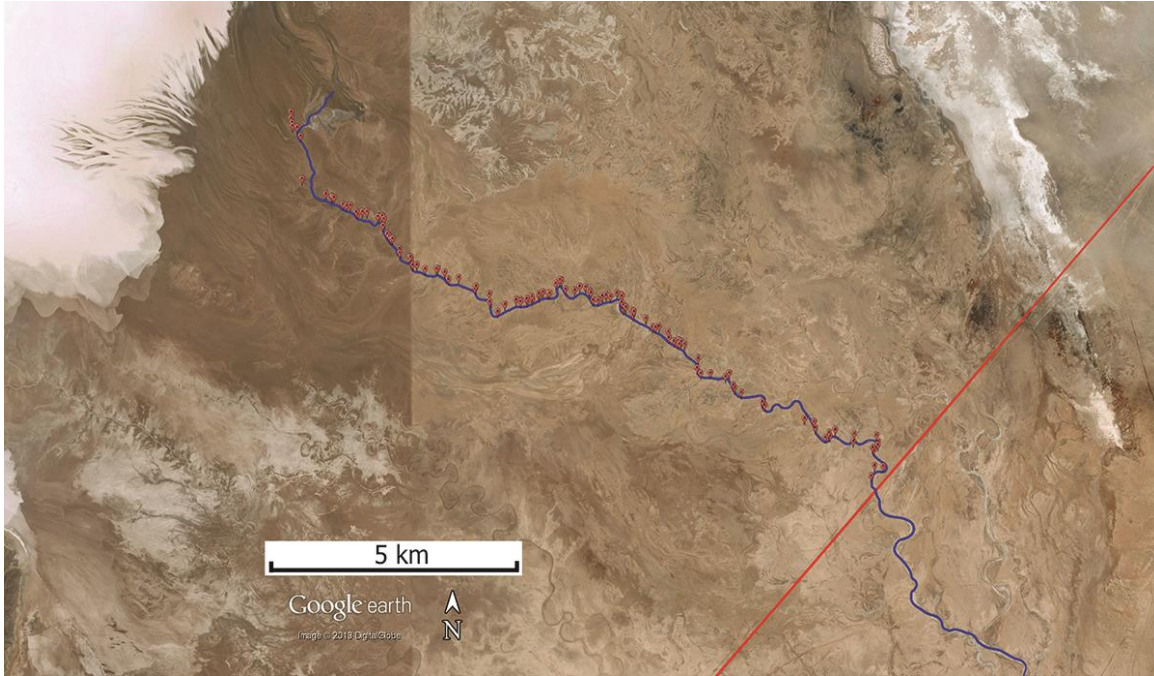
Figure 4.13: *Distribution of ICS along the river. Red dots show the sites of ICS and the red line indicates the railway.*

One hundred and twenty-four crevasse splays are classified as ICS (Figure 4.12, Appendix C). ICS are more evenly distributed along the trunk channel compared to the distribution of NCS and CCS (Figure 4.13). Except for five ICS caused by avulsion, six of the ICS have been found to be associated with the lateral migration of the main channel, two are associated with channel cut-offs, while the remaining ICS are attributed to the apex of crevasse splays being plugged by sedimentation or levee growth. 45.2% of ICS are less than 20,000 m^2 in area while 21% are between 20,000 and 50,000 m^2 and 33.8% are more than 50,000 m^2 (Figure 4.14). Compared to NCS and CCS, the high percentage of ICS with areas of more than 50,000 m^2 is related some ICS being caused by avulsion. There is no correlation between the area of ICS and distance downstream, but the maximum area of individual ICS along the river seems to increase downstream (Figure 4.15).
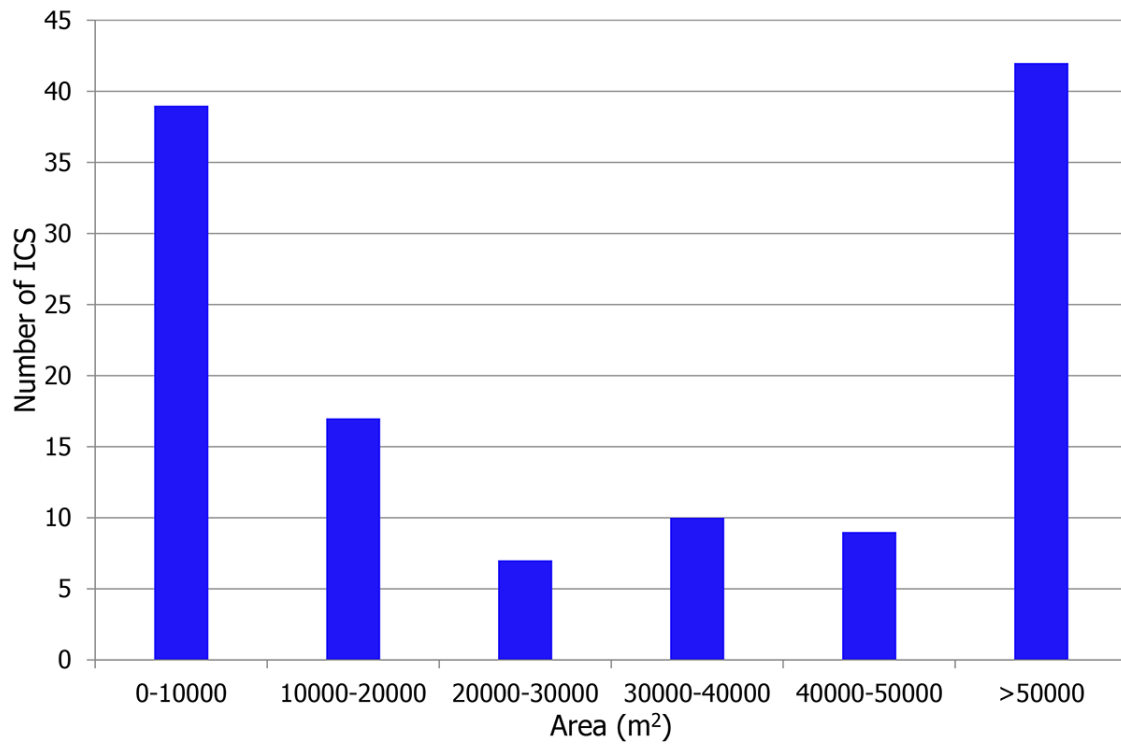
Figure 4.14: *Areal distribution of ICS along the river.*
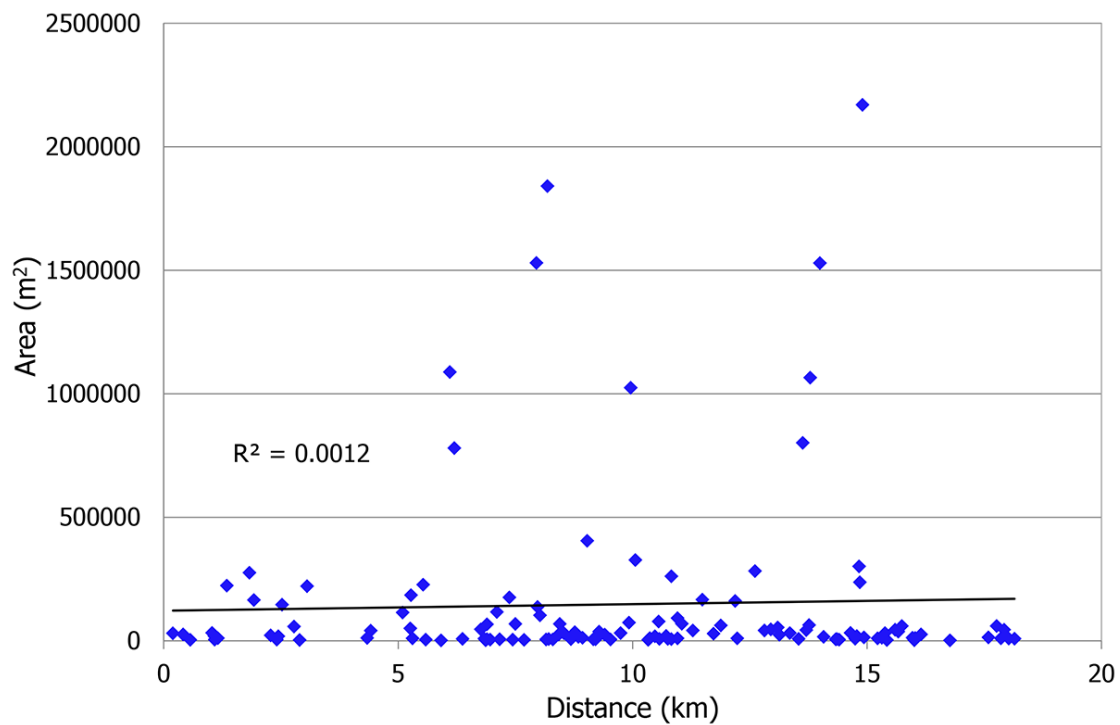
Figure 4.15: *The relationship between the areas of ICS and distance.*

4.3.4   Frequency with distance

Frequency analysis on a kilometre base shows that CCS and ICS are relatively consistent along the river (Figure 4.16A). NCS are most often found in the reaches of 4-8 km and 10-13 km distance, and in the distal part of the river, where the frequency of NCS increases due to avulsions (Figure 4.7). For CCS, there is a peak frequency at 10 km and 17 km and they are more likely to occur in the reaches of 6-11 km, where ICS also has high frequency. The frequency of ICS has the same pattern with NCS and CCS, although the first peak of ICS is at 2 km. Thus, although there is no correlation between the area of crevasse splays and distance, the density of crevasse splays increases downstream (Figure 4.16B). There are several factors contributing to the distribution of the three types of crevasse splays, which will be discussed below.
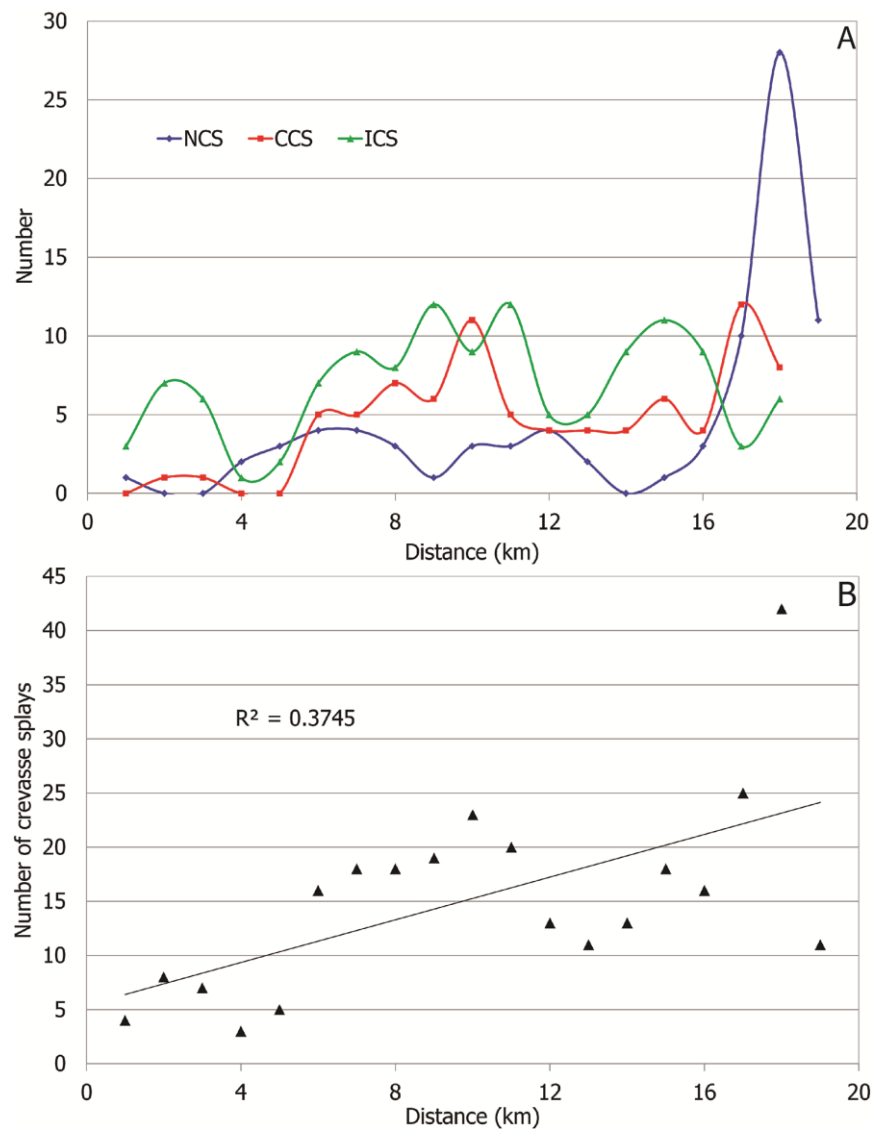
Figure 4.16: *The frequency of each type of crevasse splays along the river (A), and the frequency of all crevasse splays with distance along the river (B)*

4.4 Major factors influencing crevasse splay morphology
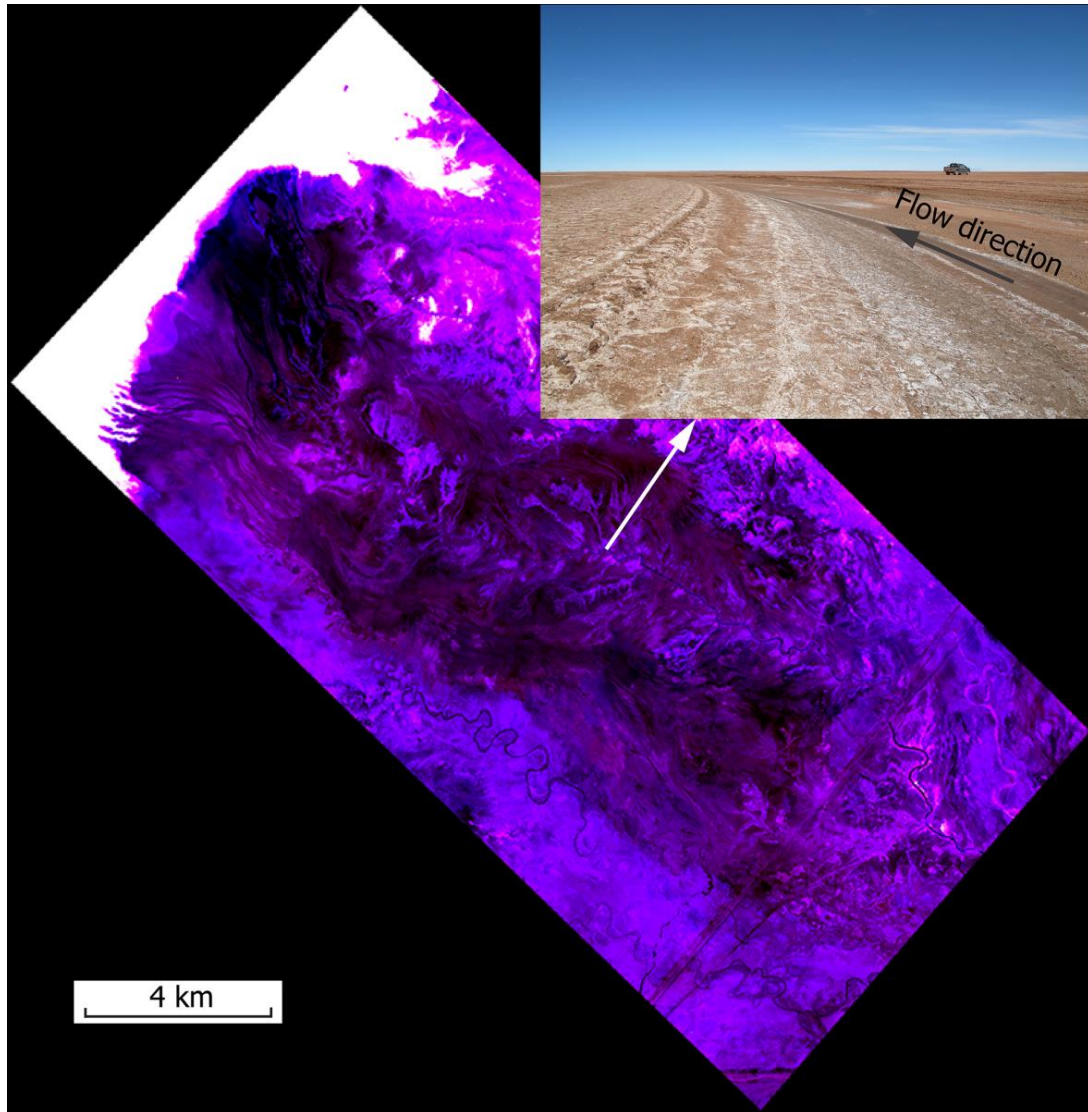
Figure 4.17: *NDVI results and photograph of the unconfined and non-vegetated study area. Purple and black areas indicate non-vegetated zones while white area is salt.*

In the non-vegetated distal part (Figure 4.17) of the Río Colorado, deposits mainly consist of very fine sand and mud, and overbank splays create about 10-cm-high smooth levees characterized by wood fragments and other organic debris (Donselaar et al., 2013). Although fine-grained sediments are dominant in the distal part of the river terminus, desiccation cracks and salt efflorescence on crevasse channel levees significantly reduce their cohesion (Figure 4.18). In addition, shallow crevasse channels (depth mostly less than 20 cm) cause frequent bank breach in the low-gradient system during peak discharge events. Therefore, crevasse splays expand frequently there.
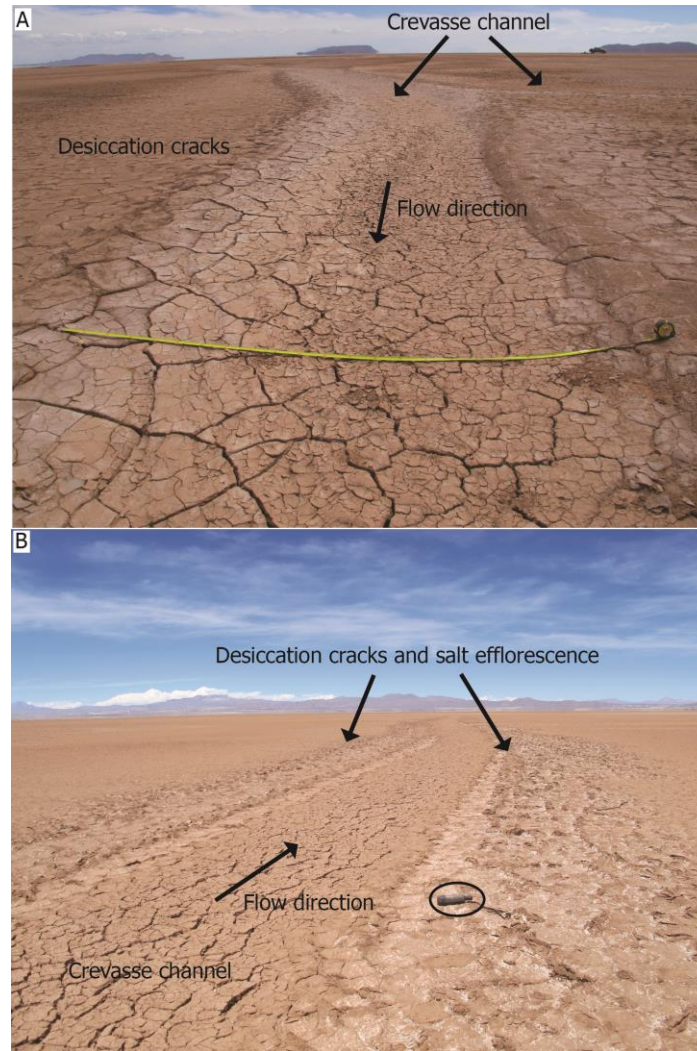
Figure 4.18: *Crevasse channels of NCS (A, see the location in Figure 4.4: Lat: 20°31'35.62; Lon: 66°55'38.38") and CCS (B, see the location in Figure 4.9: Lat: 20°30'27.86; Lon: 66°57'25.33"). A: The measure tape shows 220 cm while the GPS device (circle) is about 10 cm long in B.*

Chapter 2 of this thesis demonstrated that avulsions and the expansion of crevasse splays in the distal part of the Río Colorado were associated with peak discharges. The high magnitude but low frequency precipitation leads to over-spilling flow in the low-gradient river terminus. Data from the rainy season of 2004-2005 show that the annual precipitation was 418.3 mm, including intense rainfall events leading to several floods of high magnitude but low frequency (Figures 4.19A and C). Rainfall concentrated in a short period (January, February and March) (Figure 4.19B) and is far higher than the mean annual precipitation (184.5 mm, Chapter 2) in the study area. The intense rainfall events caused flood events resulting in overbank flow across the adjacent floodplain and bank line breaching, which promoted splay developments. Although the GPS data make it possible to accurately quantify the effect of the local gradient on the development of crevasse splays, there is no correlation between the frequencies of three types of crevasse splays and the local gradient (Figure 4.20). It is therefore suggested that local slope is not the major factor influencing the development of crevasse splays in the study area.
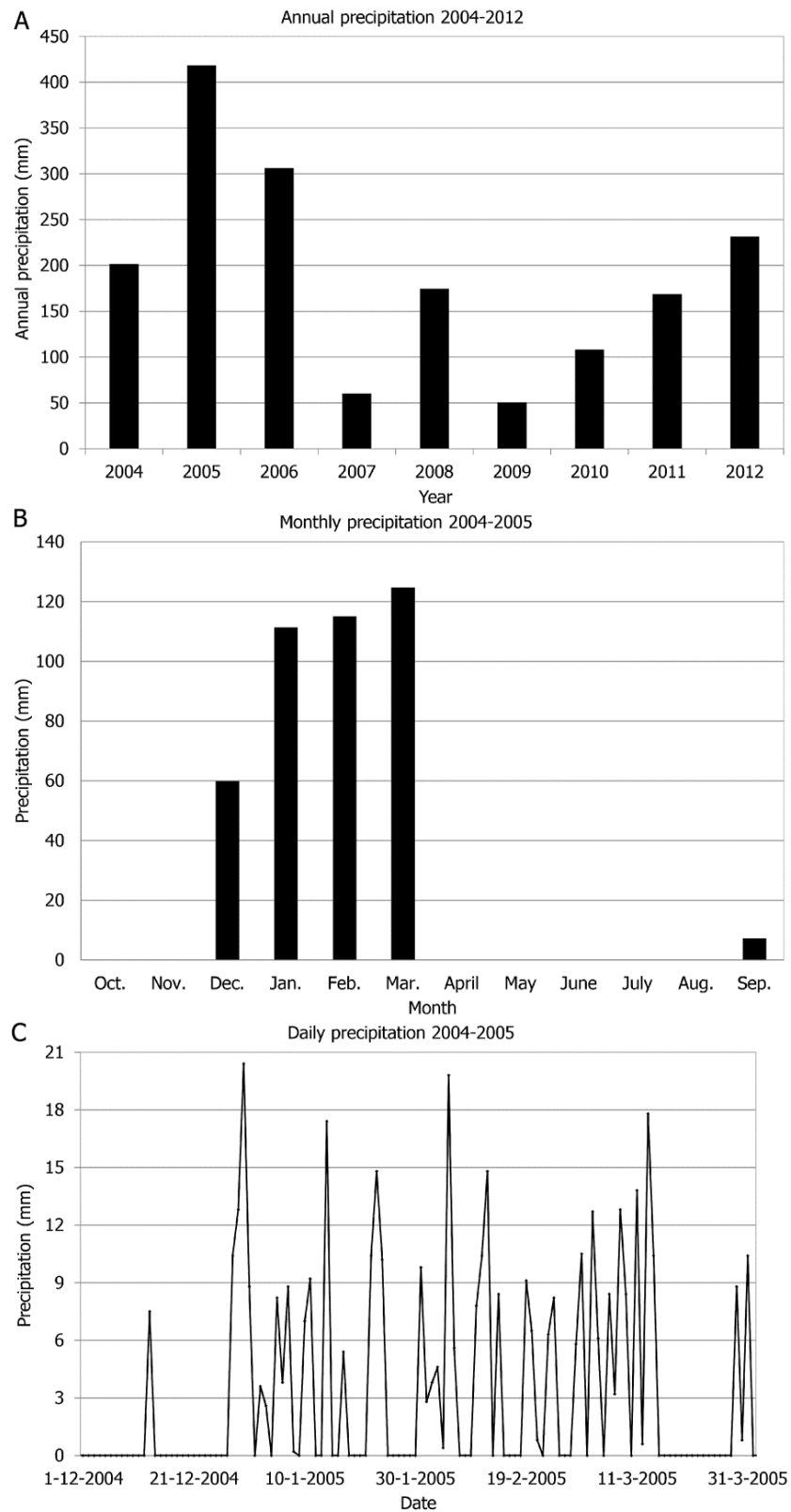
Figure 4.19: *Annual precipitation between 2004 and 2012(A), monthly precipitation between 2004 and 2005 (B) and daily precipitation in the austral summer of 2004-2005 (C).*
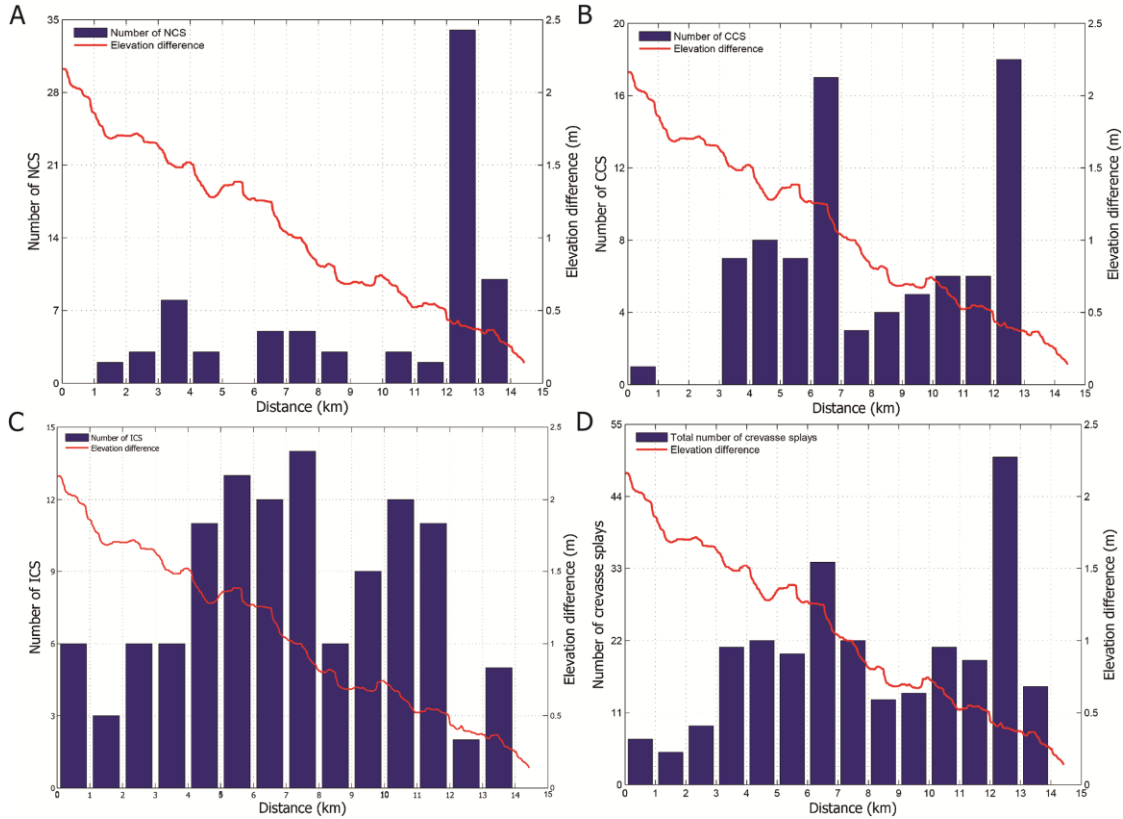
Figure 4.20: *The distribution of three types of crevasse splays and the total number of crevasse splays along the river. Columns represent of the number of crevasse splay while red line indicates projected profile along the river.*

4.4.1   Downstream decrease in cross-sectional area

One of the typical characteristics of dryland rivers is a decrease in bankfull cross-sectional area downstream (Tooth, 2000; Donselaar, et al., 2013). The number of crevasse splays and the cross-sectional area in intervals of one kilometre along the studied river show an exponential relationship (Figure 4.21). As the cross-sectional area of the main channel decreases, the number of crevasse splays exponentially increases. It is suggested that the distal part of the river terminus experiences more overbank flow than rivers in humid regions because humid-region rivers become wider and deeper towards their end point and therefore can more easily accommodate peak run-off.

$y = 96.089e^{-0.106x}$
$R^2 = 0.6733$
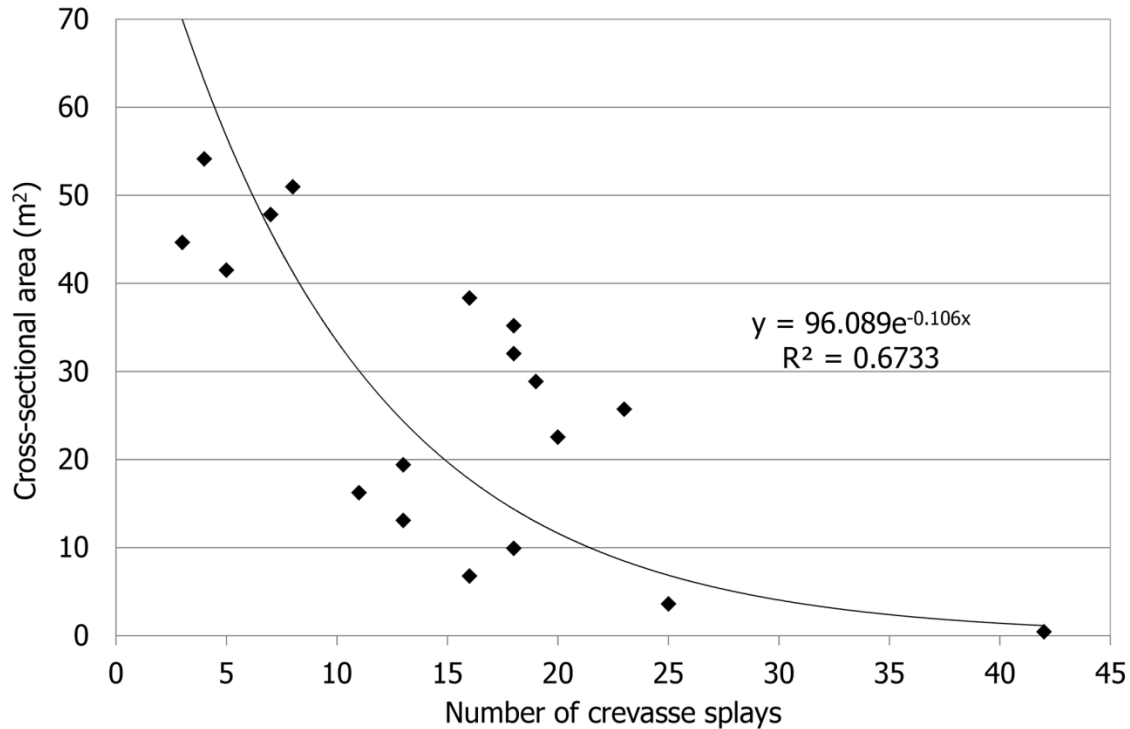
Figure 4.21: *The relationship between the number of crevasse splays and cross-sectional areas of the main channel.*

4.4.2   Compensational stacking pattern

Neighbouring crevasse splays along the river transport sediment onto the splays during floods with accretion raising the elevation of existing splays. The deposited sediments give rise to a local depression between two existing splays (Figures 4.22A and B). During floods, the over-spilled flow favours the low areas in between pre-existing splays and potentially initiates a new crevasse splay. Because the floodplain is higher than the channel floor, during the waning stage of flooding, the water is confined by the local topographic relief and converges to further erode the river bank. The process will be reinforced during the subsequent floods and induce new crevasse splays. New crevasse splays the will fill up the relief in successive floods by compensational stacking (Figure 4.22C).
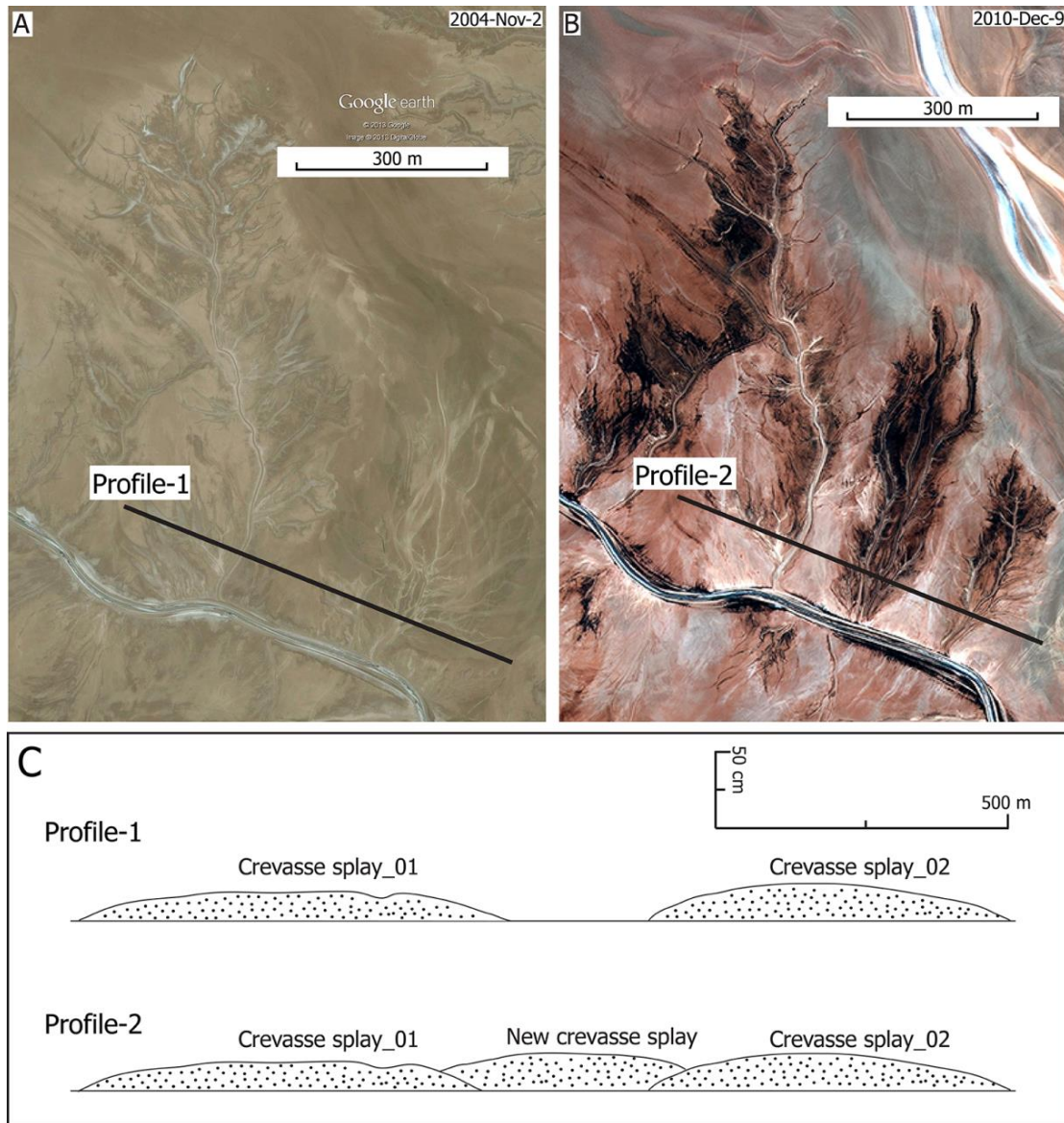
Figure 4.22: *New crevasse splay developed at a straight reach (A and B) and the diagram of compensational stacking pattern (C).*

4.5 Discussion

A1

2004/2005

NCS

Main channel floor
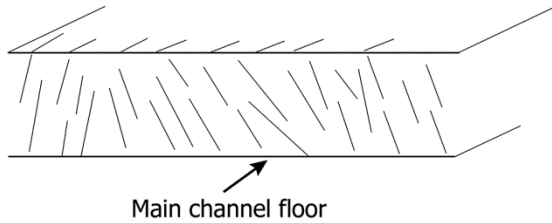
A2
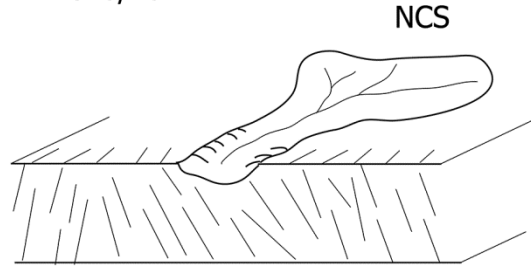
2010/2011

B1

2004/2005

B2

2010/2011

CCS

Crevasse channel
deepened and widened
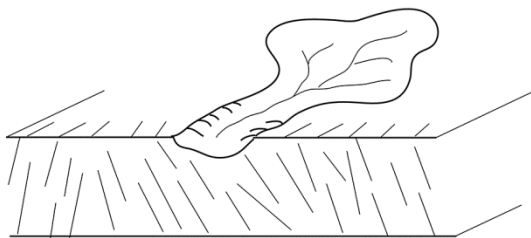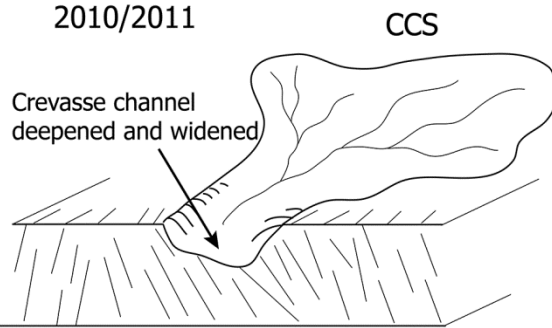
C1

2004/2005

C2

2010/2011

ICS

Apex filled-in
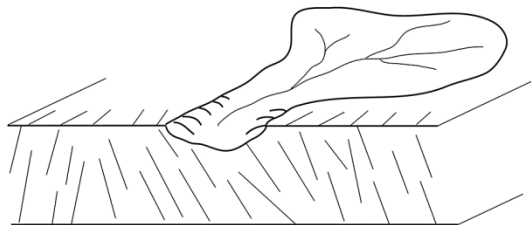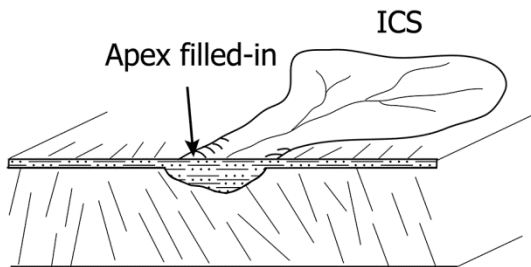
Figure 4.23: *Diagrams illustrating the development of three types of crevasse splays in different periods.*

The comparison of high-resolution satellite imagery in combination with field investigation has demonstrated the existence of three types of crevasse splays along the studied river (Figure 4.23). The distributions of NCS and CCS are characterized by zonation along the studied river (Figures 4.4 and 4.9). The gaps between two zones of NCS are often full of CCS, whose crevasse

channels in the apex are deepened and widened (Figure 4.23B2). The deepened and widen crevasse channels increase their transport efficiency and the bankline breaching decreases locally. Therefore the formation of NCS decreases along the reaches where CCS is abundant. In addition, four local avulsions have been found in the distal part of the river (Figure 4.7). This high frequency of avulsions is attributed to a dramatic decrease in cross-sectional area towards the end of the river which is too small to accommodate discharge during peak floods and to cause overbank flow and crevasse formation. Furthermore, there is no correlation between the surface areas of three types of crevasse splays and the distance from the beginning point of the studied river. The formation of some of ICS is caused by the flow diversion of the main channel. Chapter 2 has reconstructed the avulsion history of the study area with Landsat time-series imagery. The avulsed channel no longer receives peak flow discharge and the previous course is functioning as a crevasse channel and its draining area is larger than levee-breaching induced splays. Most crevasse splays have a surface area of less than 100,000 m^2 (Figures 4.6, 4.11 and 4.15), which is attributed to the low-gradient Río Colorado system having a low flow energy and transport efficiency. As crevasse splays expand, the flow energy decreases on the floodplain. However, in the apex and the intermediate areas of crevasse splays, shallow crevasse channels together with low cohesive channel levees caused by desiccation cracks and salt efflorescence (Figure 4.18) contribute to frequent expansions of crevasse splays.

Crevasses in vegetated river systems may be initiated by scour around fallen trees, animal trails such as beavers in the Cumberland Marshes (Smith and Pérez-Arlucea, 1994) or hippopotami in the Okavango (McCarthy et al., 1998). These are not the dominant factors influencing the development of crevasse splays in the distal area of the non-vegetated Río Colorado system. In the Niobrara River, crevasse splays were associated with river avulsion as a consequence of aggradation and base level rise (Bristow et al. 1999). However, the present-day Altiplano Basin is in a dry climate period, with a lake level lowstand (Donselaar et al., 2013), and base level rise does not appear to apply in the Río Colorado although we cannot rule out the effects of channel aggradation. Here we consider other local factors that appear to influence the initiation of crevasse splays.

Our results show that the number of splays exponentially increases as the channel narrows and become shallower in the distal part of the river terminus, which will experience more overbank flood events (Figure 4.21). We suggest that during peak discharges, overbank flooding will enhance bank-line breaches and further increase splay formation, which could lead to reworking of sediment on the floodplain (erosion and deposition). By contrast, Tooth (2005) stated that the proximal area of the floodout zone experiences more flooding and therefore crevasse splays are modified more frequently and rapidly in the proximal part than those in the distal part of the river system in the Sandover, Sandover-Bundey, and Woodforde Rivers in central Australia.

Some NCS have been recorded along straight reaches of the river because overbank flows can be concentrated into the low areas between two existing splays creating compensation stacking of crevasse splays. Another mechanism for the formation of new crevasse splays is flow from the overbank areas returning to the channel during the waning stage of a flood, locally eroding the river bank and creating a breach in the levee that can be exploited by succeeding floods (Tooth, 2005; Donselaar et al., 2013).

The lake level lowstand leads to a limited amount of vertical accommodation (Donselaar et al., 2013). In the low-gradient ephemeral Río Colorado system, short-lived and infrequent peak discharges contribute to massive overbank flow onto the floodplains, whereby crevasse splays are formed and amalgamate with adjacent crevasse splays (Chapter 2). As a consequence of the amalgamation of crevasse splays, the formation of sheet sands reduces the height difference between the river bankfull level and the adjacent floodplain and, therefore, reduces accommodation. Although three types of crevasse splays have been identified, these splays are not isolated but laterally amalgamate (Figures 4.12 and 4.22). Figure 4.12 shows that when crevasse splays are inactive, the adjacent NCS expands and overlaps onto the ICS. Torres Carranza (2013) investigated individual crevasse splay deposits by excavation and found deposits vertically stacked by several crevasse splays. Chapter 2 also demonstrated the amalgamation process of crevasse splays using Landsat time-series images for the period 1975-2001.

These amalgamated splays are capable of forming a large area of sheet sands (e.g. Figure 4.24), which potentially provide an analogue for thin-bedded hydrocarbon reservoirs. Because of the low quality of thin-bedded reservoirs (low porosity and permeability) under subsurface conditions, these are economically considered at best as gas-bearing reservoirs. For instance, in Figure 4.24, we consider all interconnected and neighbouring splays with a total area of 7,922,600 m^2. In order to predict the amount of gas initially in place (GIIP, eq. 4-2, Glorioso et al., 2012) in the reservoirs of such sheet sands, we assume the relevant parameters including the thickness of the sheet sands, BRV (the bulk rock volume (m^3), which is derived from the product of the reservoir area (m^2) and the gross thickness of the formation (m)), NTG (the ratio of reservoir with certain shale volume cutoff over the total gross thickness of the reservoir), $\emptyset$ (porosity), S_w (water saturation), and B_{gi} (the initial gas formation volumetric factor) (Table 4.2). The thickness of the sheet sands for single layer of crevasse splay deposits is 0.2 m according to excavations. Subsurface porosity is derived from the relationship between the initial porosity and a certain lithology with depth or experimental data (Torres Carranza, 2013). In this study, we assume that the porosity at subsurface condition is 7%, based on the Travis Peak Formation in East Texas (US) (Davles et al., 1993). The Travis Peak Formation is up to 2600 m deep. We also assume that the depth of the reservoir is 2600 m and therefore the reservoir temperature is about 78 ℃ and the corresponding reservoir pressure is about 260 bars. For a single layer of crevasse splay deposits, the net-to-gross ratio is assumed to be one because of the absence of clay layers (Torres Carranza, 2013). The average connate water saturation is assumed to be 0.2 when the reservoir is completely filled with gas (Torres Carranza, 2013). The gas formation volumetric factor (B_{gi}) is the ratio of a volume of gas at reservoir conditions to the volume of surface gas at standard conditions and is determined by the pressure and temperature of the reservoir (Hagoort, 1988). Using the formula

$$GIIP = \text{RBV} \cdot \emptyset \cdot {^N/_G} \cdot (1 - S_w) \cdot B_{gi} \qquad (4\text{-}2)$$

we find that the potential GIIP is 22 Mm^3 for the sheet sands in Figure 4.18. However, studies show that the thickness of splay deposits may reach 6 m (e.g. the middle Frio Formation by Kerr (1990) and the nonmarine Iles Formation north of Rangely, Colorado by Anderson (2005)) and the potential GIIP is then thirty times higher than the single layer of crevasse splay considered here (0.2 m).

Parameters	Abbr.	Value	Unit	Parameters	Abbr.	Value	Unit
Thickness	H	0.2	m	Water Saturation	S_w	0.2	fraction
Area	A	7922600	m^2	Reservoir Temp.	T_{res}	78	Celsius
Depth	D	2600	m	Reservoir Pressure	P_{res}	260	Bar
Porosity	Ø	0.07	fraction	Rock Bulk Volume	RBV	1584520	m^3
Net to Gross	N/G	1	fraction	Gas formation volumetric factor	B_{gi}	0.0403	

Table 4.2: *Parameters for the volumetric calculation.*
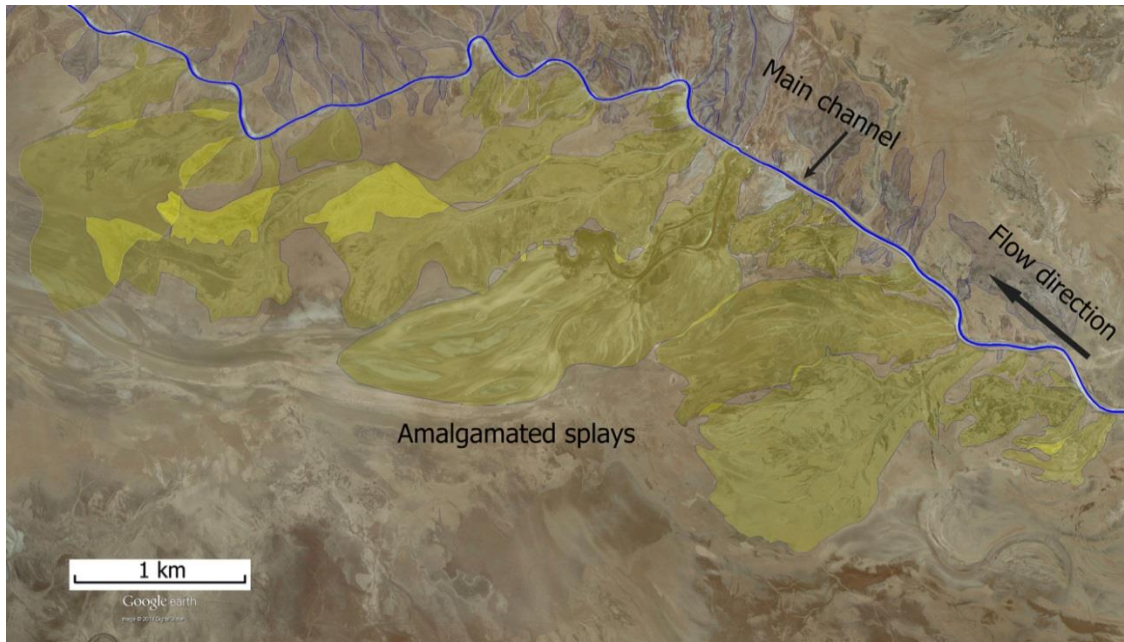
Figure 4.24: *Amalgamated splays along the studied river.*

4.6   Conclusions

The morphological development of crevasse splays at the terminus of an ephemeral dryland river system has been analysed using high-resolution satellite imagery in combination with field investigation and as a result:

- Crevasse splays have been categorized into three classes based on their development in space/time: new crevasse splays (NCS), changing crevasse splays (CCS) and inactive crevasse splays (ICS). ICS are associated with the lateral migration of the main channel,

cut-off, or attributed to the apex of crevasse splays healed by sedimentation or levee growth. ICS are more evenly distributed along the main channel than NCS and CCS.

- The occurrence of the three types of crevasse splays shows no relationship between the along-stream distance and the surface area. The majority of NCS is in the range of 0-25,000 m^2, but 14.5% of NCS have surface areas larger than 50,000 m^2, which indicates a significant amount of sediment transport to the terminus of the Río Colorado. High frequency of avulsions results in high frequency of NCS at the end of the river.

- Frequency analysis shows that the number of crevasse splays increases downstream, but the frequencies of NCS, CCS and ICS are relatively consistent along the trunk channel.

- The local gradient shows no correlation with the number of crevasse splays along the river. By contrast, the number of crevasse splay shows an exponential increase as the cross-sectional area decreases. In addition, some crevasse splays are attributed to the topographic low between adjacent crevasse splays and fill in the depression by compensational stacking.

- The amalgamated crevasse splays are capable of forming a large area of sheet sands with a considerable compound thickness, and estimates of the potential gas in place has indicated that they have the potential to become gas reservoirs.

Chapter 5   Unconsolidated Sediment Dispersion[4]

Abstract. The Río Colorado meandering river system feeds the Salar de Uyuni, the World's largest salt pan in the southern Altiplano plateau (Bolivia). It is characterized by ephemerality due to the high aridity of the region, and a downstream decrease of river bankfull width and depth in the river terminus. Dryland meandering river systems in high-altitude regions have rarely been reported. We investigated the active processes in this system from the alluvial fan to the lower coastal plain. On-site surveys combined with high-precision GPS and high-resolution satellite imagery show that Río Colorado area is typified by generally fine sediment and a low gradient in the coastal plain. In the alluvial fan, where channel meandering is weak but still recognizable, the deposits are characterized by fining-upward sequences with gravel-prone sediments at the bottom, paleosols in the middle and clay-dominated sediments at the top. In the coastal plain the channel deposits consist of coarse to fine sand with sparse basal gravel, while the river banks and thus much of the floodplain consist of clay and silt in the upper coastal plain and very fine sand, silt and clay with salt deposits in the lower coastal plain. Grain-size distribution analysis show a linear decrease in bed load sediments downstream and a concurrent increase in suspended load sediments. These longitudinal variations in the proportions of sediment load are found to be consistent with changes in the topographic slope. The river gradient shows six intervals with downstream decreasing but internally quite constant slopes and sediment composition. Characteristic geomorphologic features are found to be head-cutting channels, chute channels, avulsions and crevasse splays. They illustrate the processes of erosion and deposition in this low-gradient river system and help understand sediment dispersal.

5.1   Introduction

Ephemeral rivers characterized by rare, short-lived convective and storm-induced flows are an important geomorphological feature in many dryland regions (Knighton and Nanson, 1997; Reid, 2002; Billi, 2007; Tooth and Nanson, 2011). The high-energy flash floods lead to overbank flow due to precipitation exceeding the run-off capacity of the channels, and of the surface to absorb the water because of a lack of vegetation in these arid regions (Wainwright and Bracken, 2011;

---

[4] Chapter 5 is based on: J. Li, S.M. Luthi, M.E. Donselaar, G.J. Weltje, M.A. Prins, M.R. Bloemsma, 2014. An ephemeral meandering river system: Sediment dispersal processes in the Río Colorado, Southern Altiplano Plateau, Bolivia. Zeitschrift für Geomorphologie (accepted for publication).

Tooth and Nanson, 2011). Previous studies have demonstrated that many dryland rivers can transport large quantities of sediment, including suspended load and bed load, during these flood events (Laronne and Reid, 1993; Sharma and Murthy, 1994; Reid and Laronne, 1995; Reid, 2002). Many geomorphological, hydrological and sedimentological studies in the ephemeral river system have been conducted in dryland regions such as the southwest United States of America, the Mediterranean region and central Australia (e.g., Leopold and Miller, 1956; Renard and Keppel, 1966; Thornes, 1976; Reid et al., 1995; Tooth 2000b). However, most of these concern braided rivers and single-thread low sinuosity rivers while meandering dryland rivers in high elevation regions have rarely been reported (Donselaar et al., 2013). This paper reports on the longitudinal sediment dispersal and active processes in the Río Colorado river system on the southern Altiplano plateau (Bolivia).

The Río Colorado has a tributary catchment with a very low gradient that has not reached equilibrium due to young active faulting. It also exhibits a strongly sinuous channel morphology in its terminal reaches with channels that essentially terminate prior to reaching the salt pan (Donselaar et al., 2013). Downstream changes in the system such as width, depth, cross-section area and sediment loads are important because they provide key evidence for the processes acting during the flash floods (Tooth, 2000b). These changes in sediment load are a complex response to both sediment supply and hydraulic conditions of the flows (Hovius et al., 2000). Sediment load characteristics such as the proportions of suspended load to bed load have a major impact on depositional features, sedimentary structures and stratigraphic successions (Marren et al., 2006). For example, oblique point bar accretion has been reported as a major process of floodplain construction in dryland rivers (Nanson and Croke, 1992; Gibling et al., 1998; Page et al., 2003). While the work of Donselaar et al. (2013) focused only on the processes in the terminus of the Río Colorado river system, this paper considers the fluvial sediment dispersal from the alluvial fan to the lower coastal plain (Figure 1.2) with the following objectives: 1) To outline the sedimentology, channel morphologies and slope changes in the investigated area; and 2) To determine the major processes active in this system.

5.2   Data Acquisition

289 sediment samples were collected in the study area, from point bars along active and abandoned channels as well as from the floodplain. Typical sampling intervals in excavated holes at point bars were 10 cm or 20 cm. In the upstream part of the upper coastal plain segment point bars were not common due to vegetation-induced stable river bank and, therefore, samples were collected from channel deposits. The coordinates of the sampling sites were determined with a Garmin GPS map 60CSx device. Google Earth Pro imagery provided three high-resolution satellite images (30/07/2002, 02/11/2004 and 13/07/2013, respectively), which were used to determine channel morphology and changes through time. A Trimble R7 dual frequency geodetic GPS receiver was mounted on the car in the field and served to measure the gradient along the river.

5.3   Methods

The grain sizes of the samples were analysed with a Sympatec HELOS KR laser-diffraction particle sizer with a size range from 0.1-2000 μm. Pre-treatment of the sediment samples included three steps: (1) removing organic matter; (2) removing calcium carbonate; and (3) dispersing grains (Konert and Vandenberghe, 1997). In order to remove the organic matter, we oxidized the samples using 5 ml of 30% H_2O_2 for samples with low organic matter content and more H_2O_2 for those with a high organic content. Then 10 ml 10% HCl was added to remove the calcium carbonate and 300 mg $Na_2P_2O_7 \cdot 10H_2O$ to disperse grains.
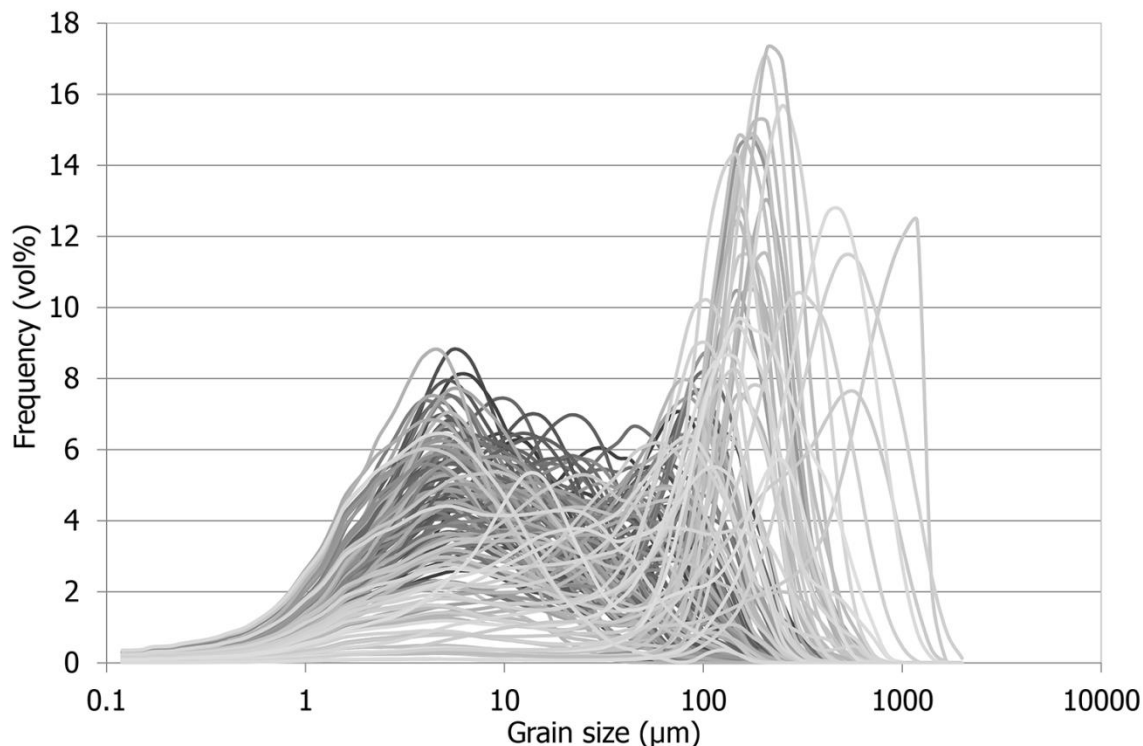
Figure 5.1: Grain-size distribution of all samples in the study area.

All grain size distribution of samples from the study area (Figure 5.1) made it possible to determine a fixed size, at which the distributions may be subdivided into mass fractions belonging to different populations. These different mass fractions tended to be indicative of transport mode due to difference between dominant modes. In combination with various mass fractions, we calculated the average proportion of all samples from each excavated hole using the centre log-ratio transformation (see Aitchison (2002) for detailed calculation) and investigated downstream change in sediment load of point bar deposits using log-ratio of proportion of suspended and bed load. We also analysed point bar deposits from the upper lacustrine coastal segment and lower lacustrine coastal segment. See detailed GPS data processing at Section 3.3.2 and GPS profile was created (Figure 5.2).
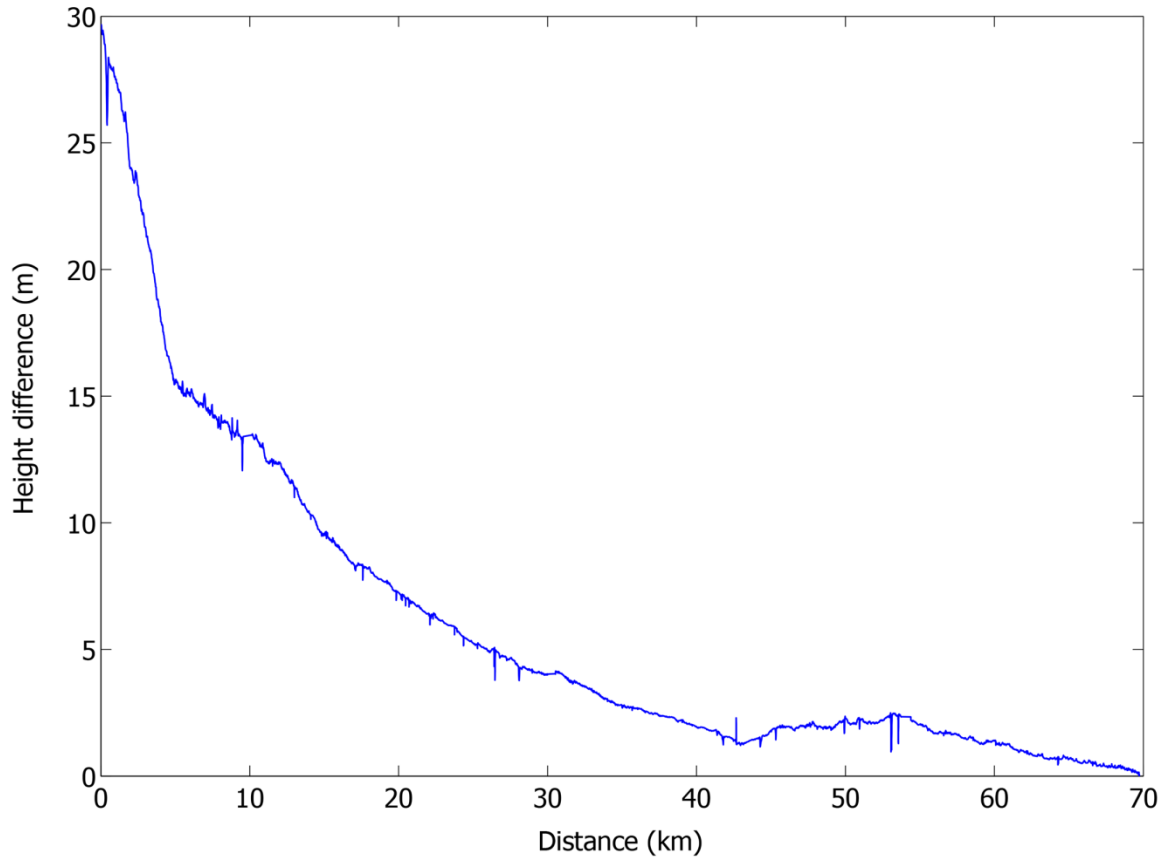
Figure 5.2: *High precision GPS topographic profile.*

5.4   Sediment Dispersal and Channel Morphology

The drainage basin of the river system considered here has an area of 15,000 km^2 (Donselaar et al., 2013) and consists of Upper Ordovician, Silurian, Cretaceous and Tertiary clastic rocks intruded by granitic plutons of late Oligocene to middle Miocene age (Horton et al., 2001; Jacobshagen et al., 2002; Risacher and Fritz, 2009). In the following the resulting sediments in the different segments are analysed.

5.4.1 Alluvial fan segment
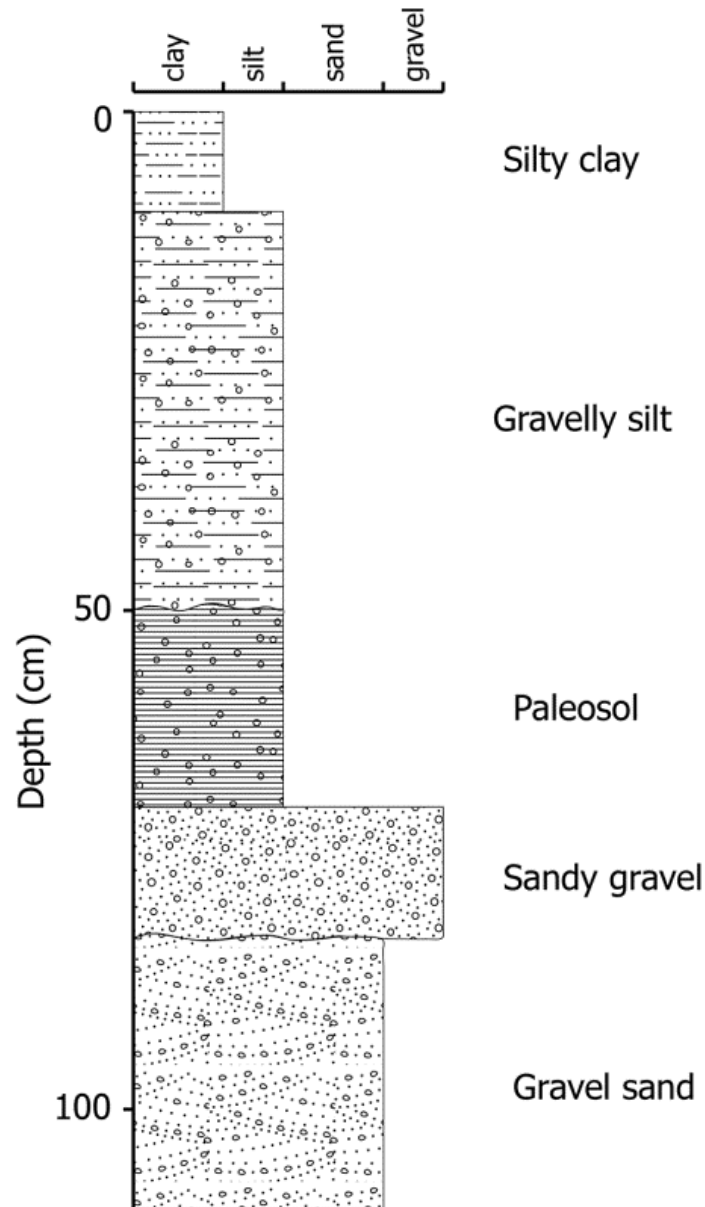
Figure 5.3: *Representative sedimentary log of the alluvial succession.*

The exposed alluvial deposits have a maximum thickness of about 0.8-1.3 m (Figure 5.3) and generally consist of fining-upward sequences. The first layer exposed at the base consists of up to 50 cm poorly consolidated, cross-bedded gravelly sand. Fine pebbles are imbricated in the sand. It is overlain with an erosional contact by an up to 20 cm thick sandy gravel layer which is well-consolidated by calcite cementation. Individual pebbles are typically sub-angular to sub-rounded and range up to 5 cm in diameter (b-axis measurements). Above this follows a yellowish brown paleosol that is up to 60 cm thick and contains pebbles. It is well consolidated and

contains small nodules of calcretes. The following layer is a massively bedded and matrix-supported gravelly silt that is up to 40 cm thick and well consolidated. The uppermost layer is 15 cm thick and consists of silty clay. Exposures of this layer exhibit mud cracks. The alluvial floodplain and the distal part of the alluvial fan are locally covered by aeolian barchan dunes; these are not further investigated here.

5.4.2 Upper coastal plain segment
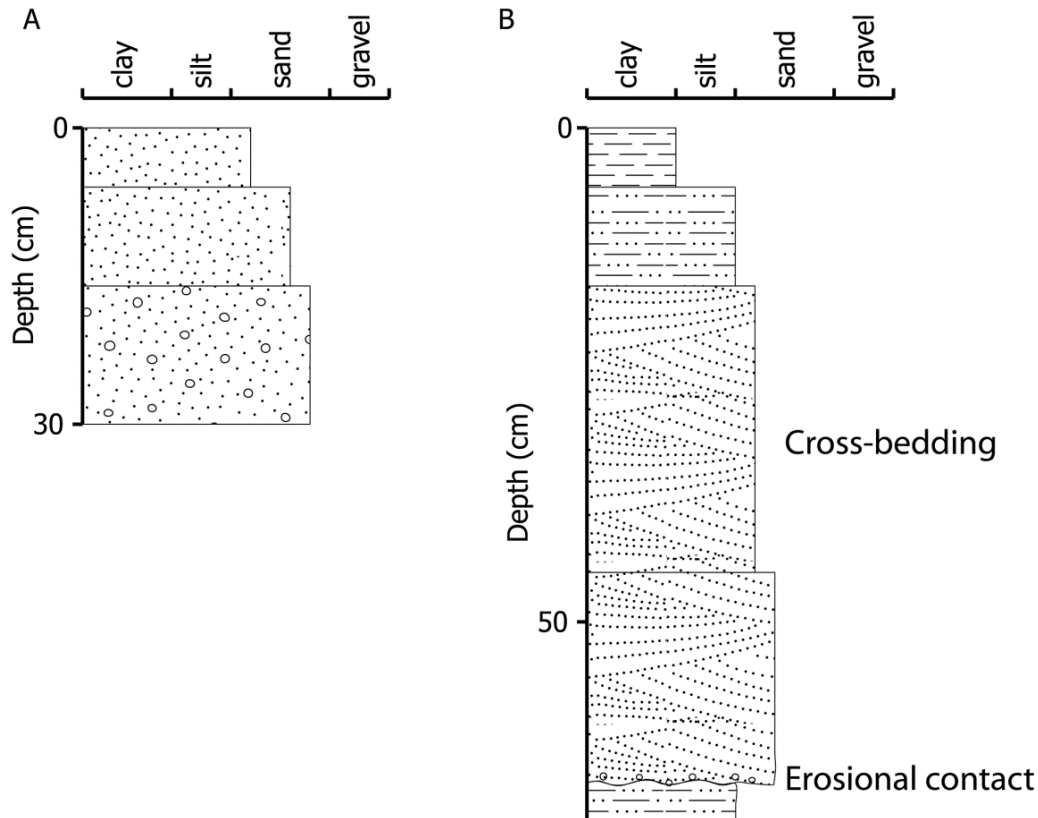
Figure 5.4: *Representative sedimentary logs of the upper coastal plain deposits. A: upstream channel deposits; B: downstream point bar deposits.*

Point bar analyses along the two channels (the Río Capilla and the Rio Colorado) show in general a fining-upward trend (Figure 5.4). The deposits consist of fine gravel and coarse sand in the upstream part (Figure 5.4A) and fine sand in the downstream part (Figure 5.4B). The grains are typically subangular to subrounded. The bases of the sequences are usually erosional with sparse pebbles, while cross-bedding fine sands in the middle and silts and clays at the top complete the sequences (Figure 5.4B). The point bars attain 1 m in thickness and are poorly consolidated. The floodplain deposits, by contrast, consist of fine sand and silt and clay and are more compacted. In the upstream area, the river banks and floodplains are covered by grass and channels are therefore relatively stable (Figure 5.5A) with point bars being quite rare. In the downstream area,

however, they are not vegetated and the outer banks are characterised by mud cracks (Figure 5.5B) that facilitate significant bank erosion. Other erosional features such as chute channels, avulsion and new crevasse splays as well as accretionary wedges (Figure 5.6 and Figure **5.12**) testify to the higher sediment mobility in this part of the upper coastal plain.

Figure 5.5: *Grass-covered bank in the upstream area of the upper coastal plain (A) and non-vegetation bank in the downstream area of the upper coastal plain (B).*
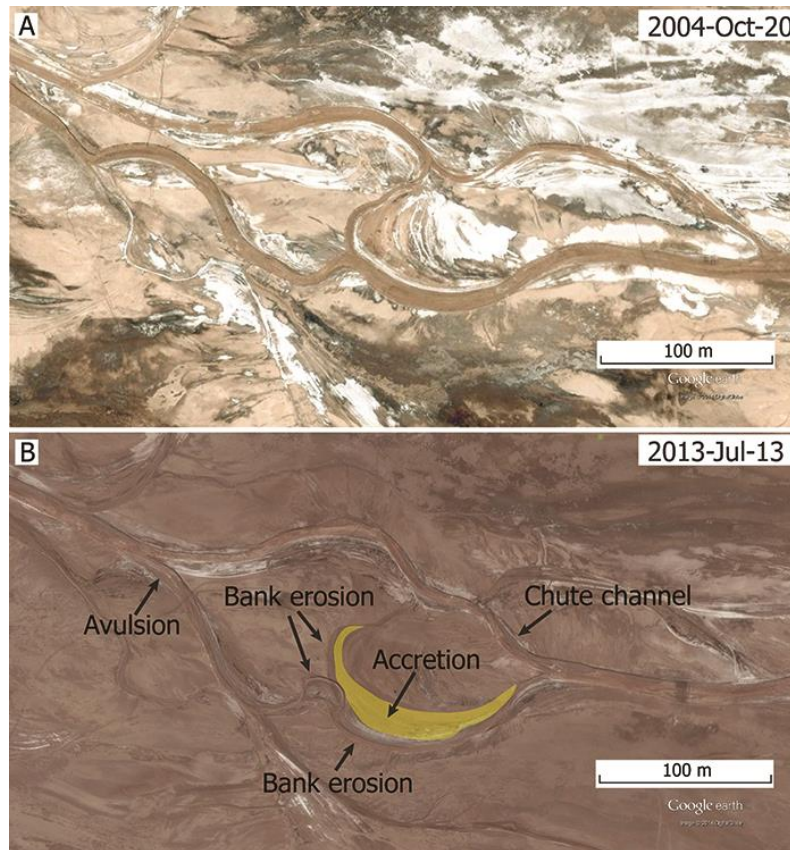
Figure 5.6: *Comparison of GoogleEarth images to illustrate erosion and accretion in the downstream of the upper coastal plain. Erosion includes bank erosion, avulsion and chute channel.*

5.4.3 Lower coastal plain segment
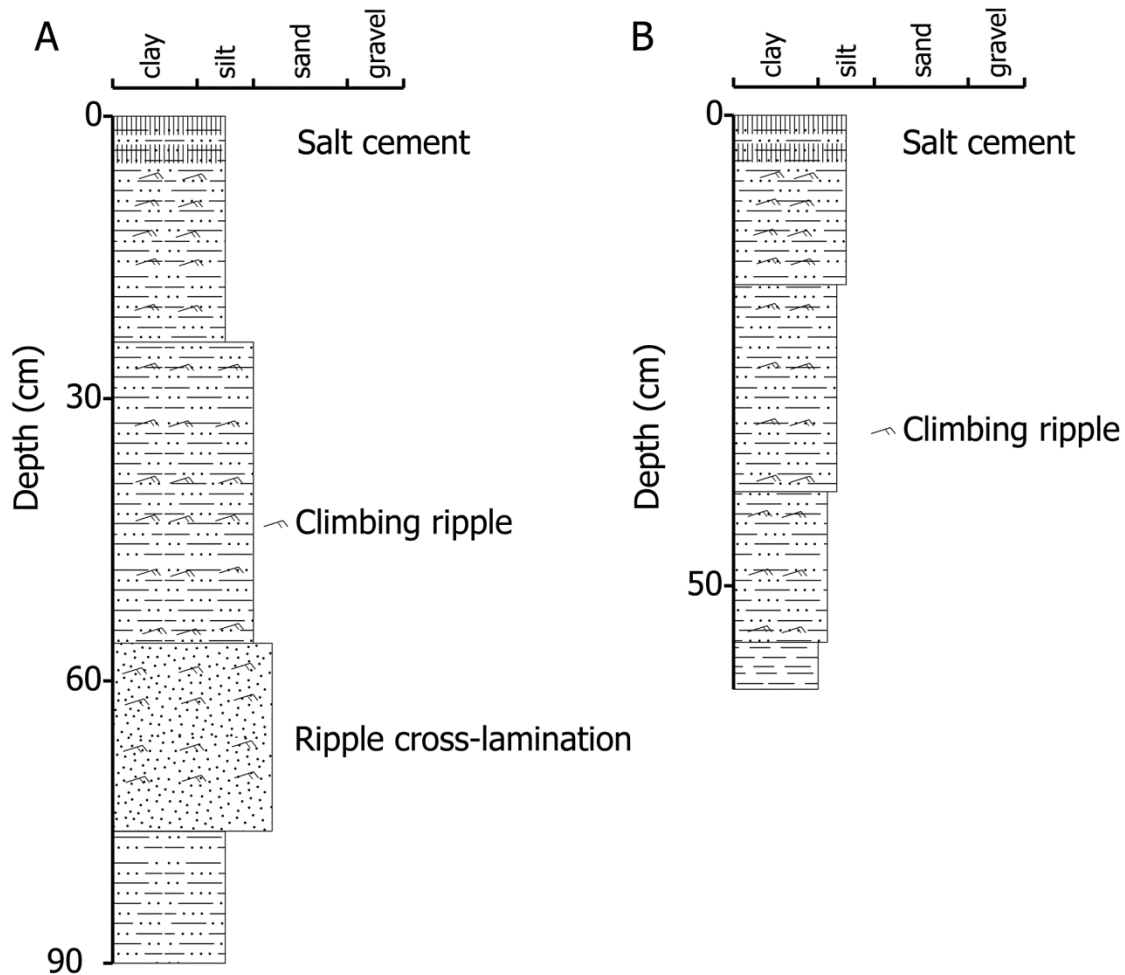
Figure 5.7: *Representative sedimentary logs of the lower coastal plain deposits. A: point bar deposits in the proximal part of the lower coastal plain; B: terminal splay deposits in the distal area.*

In the presently active channel and in two abandoned channels, point bar deposits dominate and consist of very fine sand and silt in the proximal area and silt and clay in the distal region. The point bar deposits in the proximal area are up to 2 m thick and exhibit a fining-upward sequence with cross-lamination and climbing ripples (Figure 5.7A), whereas terminal splay deposits in the distal region show a coarsening-upward sequence with climbing ripples (Figure 5.7B). The grain size data indicate a transition from polymodal distributions in the proximal area to unimodal distributions in the distal area. Overbank deposits consist of silt and clay, and salt deposits in the coastal area. The uppermost part of the sediments in the river terminus area is hardened due to salt-cementation.

5.4.4 Grain size distribution pattern

Grain-size distribution of all samples from the study area revealed bimodal dominated distribution. One of 57 reported measuring points from laser-diffraction particle sizer close to the value (30 µm) in the estuarine areas (e.g., Yellow River, Weltje G.J., Pers. Comm.) was selected (31.3 µm) as a fixed cutoff size, with which two mass fractions were identified. Two mass fractions showed a significant difference between their dominant modes (5.5 µm vs 210 µm, Figure 5.1), which was indicative of two transport modes: the one with grain size of lower than 31.3 µm is suspended load while the other with grain size of greater than 31.3 µm is bed load. The logarithmic ratio of the suspended over the bed load for point bar deposits showed a linear decrease downstream of the bed load and a simultaneous increase in the suspended load (Figure 5.8). The bed load dominates in the upper coastal plain and gradually decreases downstream, while the suspended load increases correspondingly. Although there are locally some sudden increases in bedload in the lower coastal plain presumably caused by excessive flash floods, downstream sediment dispersal is overall characterized by a logarithmic increase in fine sediment and a simultaneous decrease in coarse sediment.
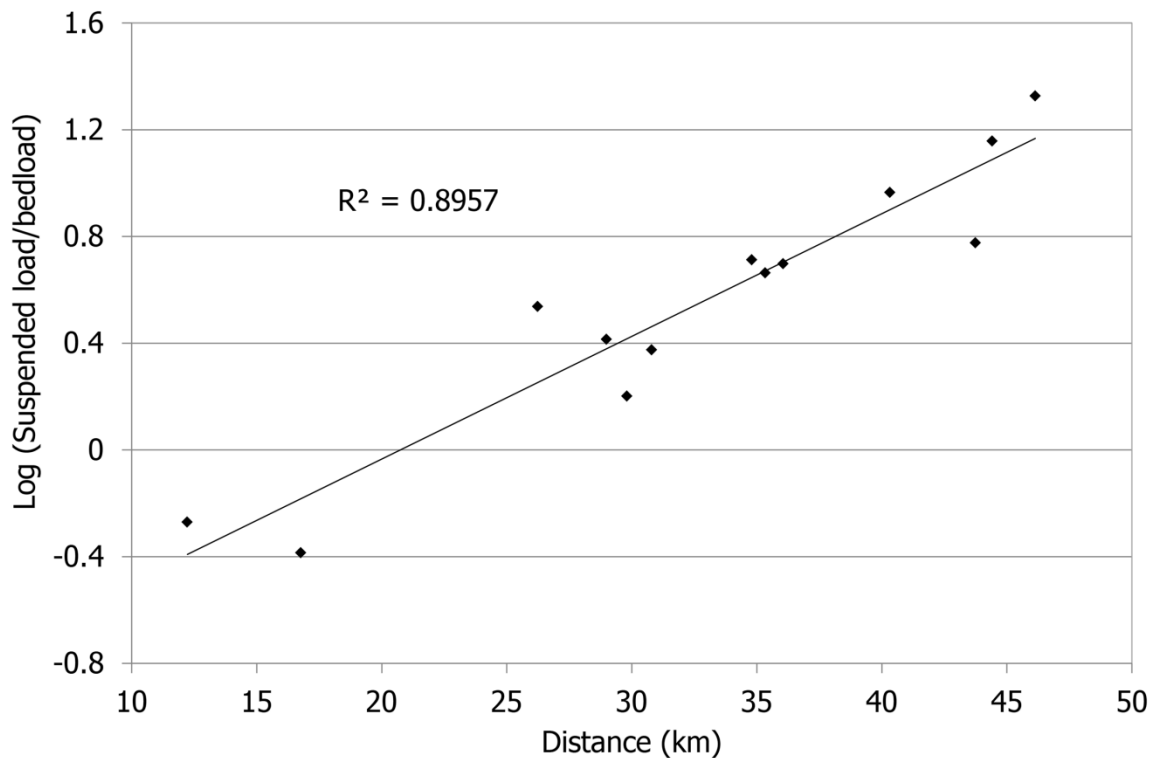
Figure 5.8: *The relationship between logratio of suspended load to bedload sediments and distance. The value of suspended load and bed load sediments is the average proportion of all samples from each excavated hole using the centre log-ratio transformation.*

5.4.5   Longitudinal GPS profile and channel morphology

The GPS data analysis indicates that six intervals can be defined along the topographic river profile with fairly constant slopes (Figure 5.9). Although the slope changes by several orders of magnitude from Interval-1 (with a mean slope of 0.002) to Interval-6 (with a mean slope of 0.00004708) (Table 5.1), most of the change occurs between the first interval and the rest. This is also illustrated in the grain size distribution along the river profile (Figure 5.10), where this transition corresponds to the change from gravel to finer-grained sediments.
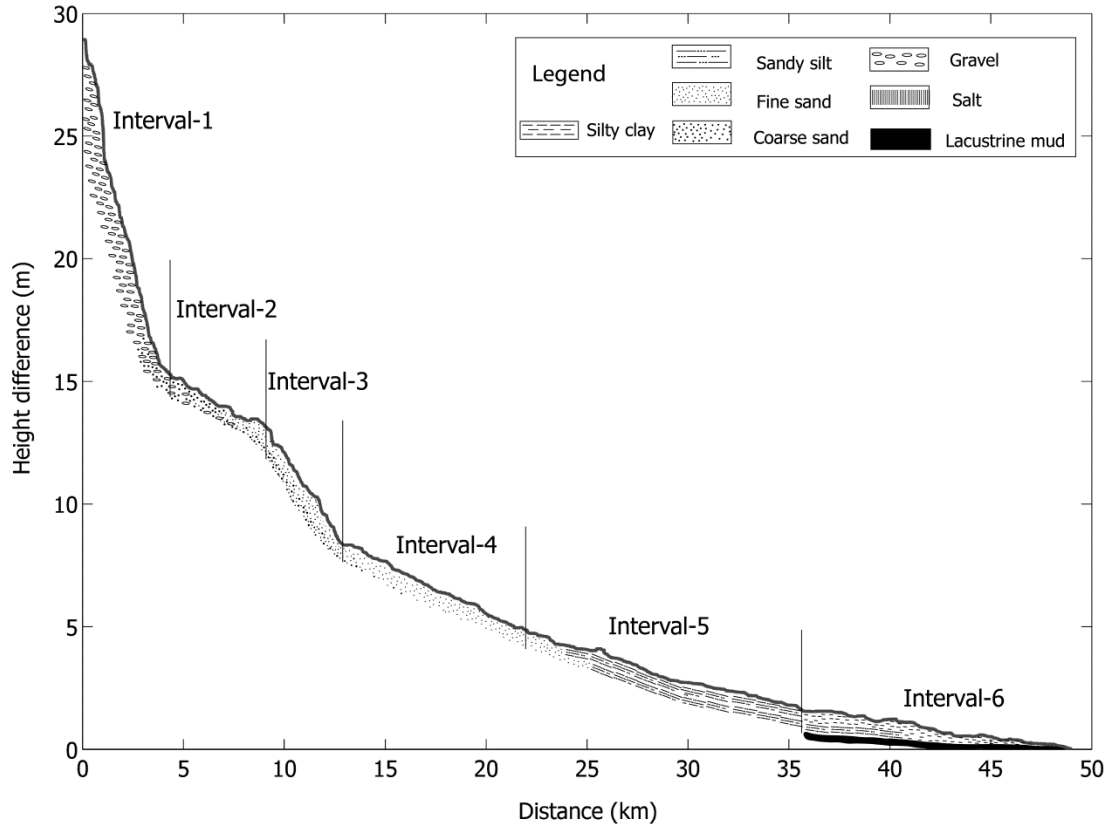
Figure 5.9: *Longitudinal high precision GPS profile by median filter smoothing method and longitudinal grain size distribution in the study area. Dash lines indicate boundaries between different intervals.*

Interval	Maximum slope	Minimum slope	Mean slope
1	3.00E-03	5.66E-04	2.00E-03
2	5.50E-04	3.48E-04	4.53E-04
3	1.10E-03	3.55E-04	7.06E-04
4	4.40E-04	2.14E-04	3.50E-04
5	2.61E-04	0.00E+00	1.48E-04
6	1.06E-04	0.00E+00	4.71E-05

Table 5.1: *Slopes at different intervals.*
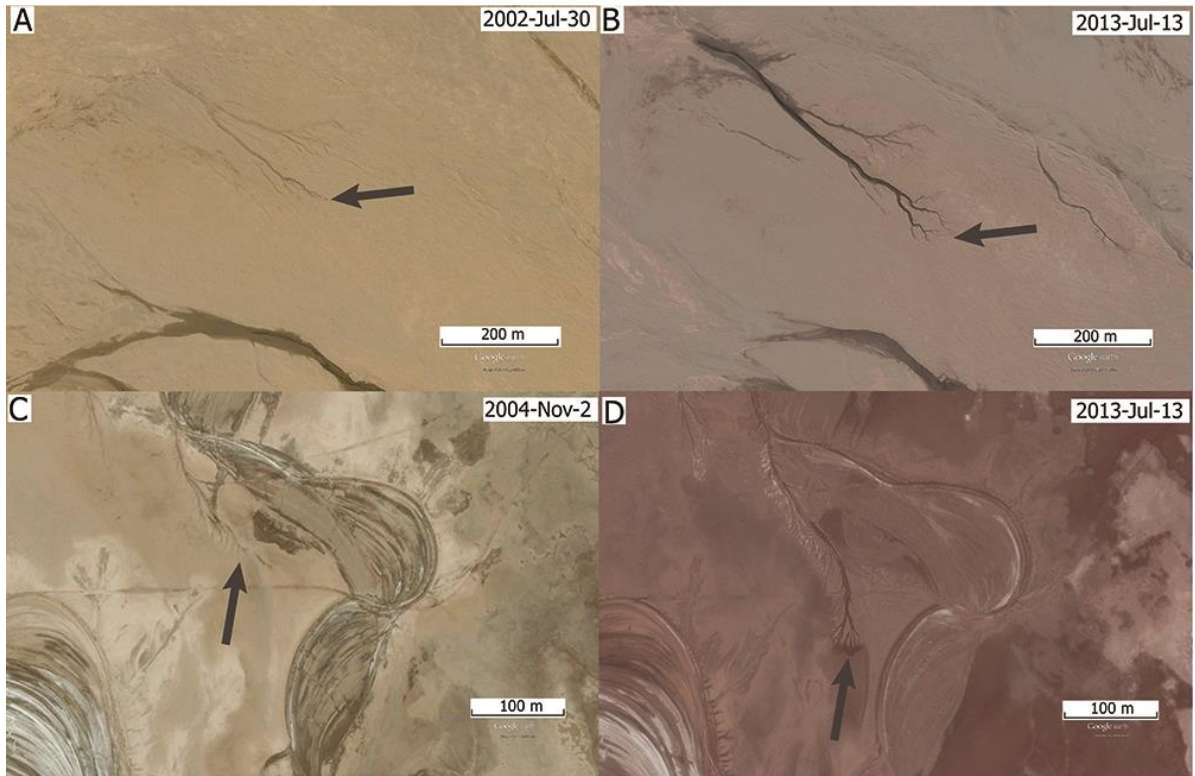
Figure 5.10: *Head-cutting channels developed over time in the Interval 2 (A and B, lat: 20°41'1.96"S; lon: 66°39'9.56"W) and Interval 5 (C and D, lat: 20°33'45.52"S; lon: 66°52'21.02"W).*

The transitions between these intervals are also accompanied by geomorphological features such head-cutting channels, chute channels and avulsions. For example, head-cutting channels develop in Interval-2 as well as between Interval-4 and Interval-5 in the lower coastal plain. In Interval-2, some tree-shaped head-cutting channels were initiated at river banks and grew headward over time with increasing width and depth of the trunk channel and branches extending in the upstream direction (Figure 5.10A and B). In addition, the head-cutting channels occur in the abandoned channel between Interval-4 and Interval-5 (Figure 5.10 C and D) and they will eventually lead to a new channel path. Some headcut channels formed in the floodplain (Figure 5.11): headcuts coalesce into a single trunk channel that conveys flow to distributary channels ending in an area of diverging sheetflow (Tooth et al., 2014). Furthermore, chute channels, avulsions and new crevasse splays occur frequently in Interval-4 (Figure 5.8 and Figure **5.12**).
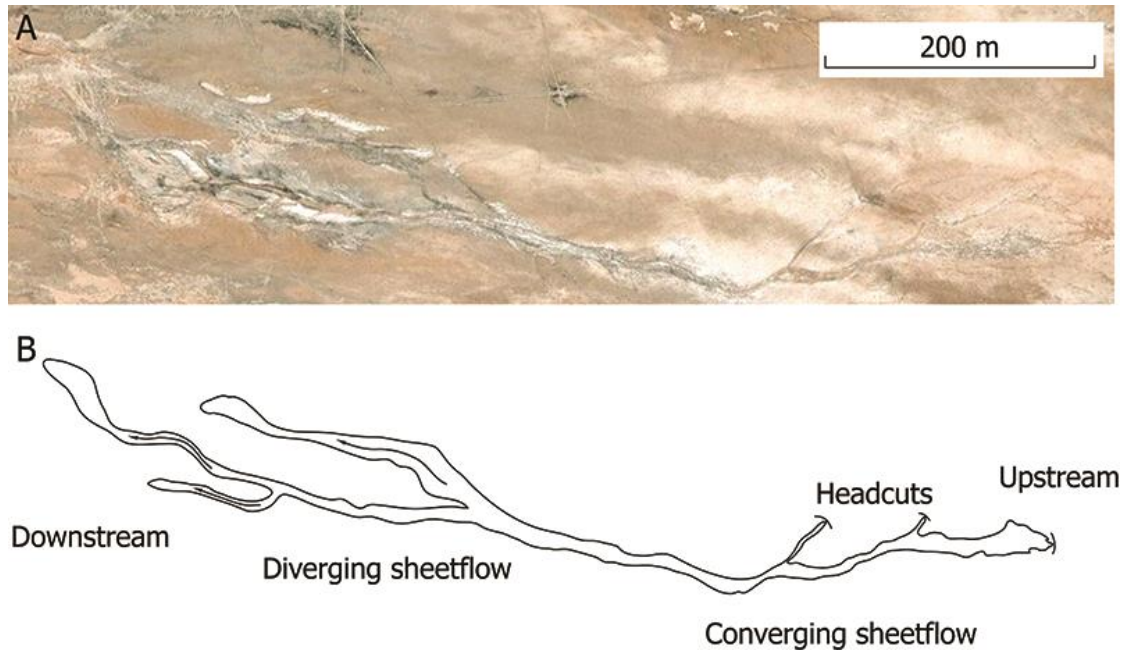
Figure 5.11: Erosion cell formed at the Interval 2 (lat: 20°43′16.18″S; lon: 66°41′28.35″W).
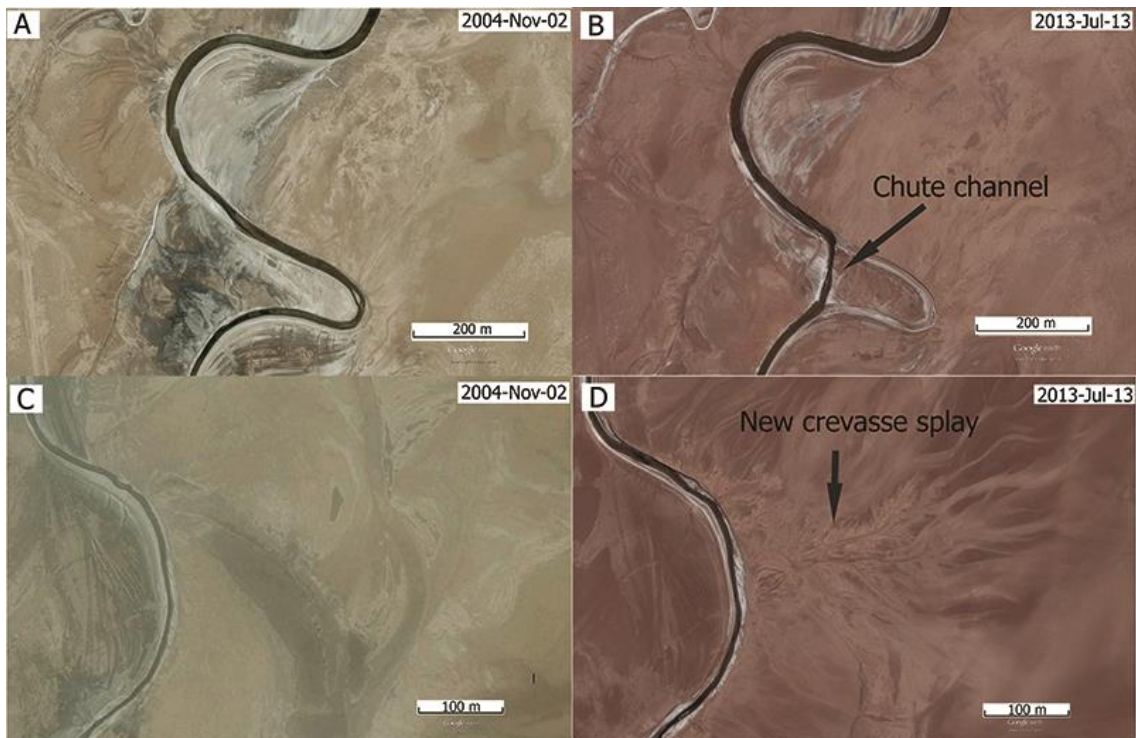
Figure 5.12: The formation of a chute channel (A and B, lat: 20°40′17.59″S; lon: 66°51′6.75″W) and crevasse splays (C and D, lat: 20°41′21.11″S; lon: 66°51′4.64″W) in Interval 4.

5.5   Discussion

Our sedimentological and geomorphologic analyses in the Río Colorado river system illustrate the processes of erosion and deposition in this dryland, high-altitude meandering river system. The present-day dry climate period in the Coipasa-Uyuni endorheic basin causes a lake level lowstand and therefore results in the progradation of the Río Colorado onto the former lake bottom (Donselaar et al. 2013). Unlike previously published dryland river systems such as the Cooper Creek and the Sandover-Bundey-Woodforde River in the central Australia (Tooth, 2000b; Nanson et al., 2002) and the Blood River and Orange River in South Africa (Tooth et al., 2013; Tooth et al., 2014), the Río Colorado river system is located above 3660 m a.s.l. and is characterized by grass in the upper coastal plain and absence of vegetation in the lower coastal plain (floodout). The linear decrease in the proportion of bedload deposits in the lower-gradient coastal plain segments of the study area contrasts with the terminal distributary system of the Ethiopian braided Dikala River, where the gravel-dominated deposits do not change from upstream to the terminal system (Billi, 2007). The different gradient intervals are characterized different proportions of sediment load, in particular between the upper coastal segment (bedload dominated) and the lower coastal segment (suspended load dominated). Ongoing research indicates that close to the boundary of the lower and the upper coastal plain segments, the river bank erosion (up to 5 m/yr) is accompanied by point-bar accretion. The accreting point-bar deposits consist of fine sand and very fine sand, whereas the non-vegetated river bank (Figure 5.7) is composed of clay and silt, suggesting lower coastal plain floodplain deposits. The occurrences of chute channels and avulsions indicate active erosional processes that provide sediment for the lower coastal plain. It is obvious that lack of vegetation cover and high ephemeral stream power promote these active erosional processes in the coastal plain.

Head-cutting channels have been reported in semi-arid river systems such as the south-western United States, the central Australia and South Africa (e.g. Pickup, 1985; Bull, 1997; Pelletier and DeLong, 2004; Benvenuti et al., 2005; Tooth et al., 2014). These discontinuous ephemeral streams highly depend on the interplay between flow, sediment supply and vegetation growth (Tooth et al., 2014). Similar processes have been described by Pickup (1985), who proposed erosional cells that include three zones: a production zone, a transfer zone and a sink zone in small-scale, low-gradient channel-floodplain systems with limited sediment supply. Shifting mosaics of erosion cells create the resulting landscape (Pickup, 1985). In our study, headcuts are common in Interval-2, where the slope decreases significantly at the end of the alluvial fan and much sediment from the headwater is deposited. This change in slope goes parallel with a decrease in stream power during flash flood events, and it may explain why the erosional headcuts may have been initiated there. Headcuts in the lower coastal plain occur in abandoned channels with low gradients and limited sediment supply (Figure 5.10C and D). They exhibit greater changes in widths and extents through time compared to relatively minor changes in headcuts of the Blood River wetlands as reported by Tooth et al. (2014). For example, the headcut shown in Figures 5.10A and B extended by more than 100 m in 11 years while the headcuts reported by Tooth et al. (2014) have extended a few tens of metres over 70-80 years in the Blood River wetland.

5.6 Conclusions

Unconsolidated sediment dispersal in the Río Colorado meandering river system of the southern Altiplano plateau showed some features that may be unique for this high-altitude arid setting. These include the following:

- The unconfined area of the system showed great variations in sediment composition downstream. The alluvial fan segment is characterized by gravel with a fining-upward sequence, whereas the upper coastal plain segment is typified by coarse sand and some fine gravel in the upstream area, grading to fine sand downstream. Silt and clay are the dominant sediments in the lower coastal plain segment, although there is also some very fine sand.

- The study area is characterized by a linear decrease downstream in bedload and correspondingly an increase in suspended load deposits. Overall gradual changes have been observed from bedload dominated deposits in the upper coastal plain to suspended load dominated deposits in the lower coastal plain.

- Five intervals with different slopes were identified based on high-precision GPS data. These intervals are characterized by relatively unique sedimentary composition.

- Head-cutting channels, chute channels, avulsions and crevasse splays are well developed in the study area. Chute channels and avulsions in combination with bank erosion provide an important sediment source for the downstream reaches. Head-cutting channels form in low-gradient areas with limited sediment supply and cut headwards at significantly higher rates than headcuts reported from other area.

Chapter 6   Playa Surface Composition[5]

Abstract. *Playas in endorheic basins are of environmental value and high scientific because of their natural habitats of a wide variety of species and indicators for climatic changes and tectonic activities within continents. Remote sensing, due to its capability of acquiring repetitive data with synoptic coverage, provides a unique tool to monitor and collect spatial information about playas. Most studies have concentrated on evaporite mineral distribution using remote sensing techniques but research about grain size distribution and geomorphologic changes in playas has been rarely reported. We analysed playa morphodynamics using Landsat time series data in a semi-arid endorheic basin, Salar de Uyuni in Bolivia. The spectral libraries about the relationship between reflectance and surficial materials are obtained from the Landsat images, the collected samples in the area, and the precipitation data, and are applied to the classification of other Landsat images from 1985 to 2011 with a supervised classifier. Four types of surficial materials on the playa are identified: salty surface, silt-rich surface, clay-rich surface and pure salt. The silt-rich surface is related to crevasse splays and river banks while the clay-rich surface is associated with floodplain and channel depressions. The classification results show that the silt-rich surface tends to have a positive relationship with the annual precipitation, whereas the salty surface negatively correlates with the annual precipitation and there is no correlation between clay-rich surface and the annual precipitation. Salty surfaces seem to consist primarily of clay due to their similar characteristics in response to precipitation changes. The classification results also show the development of a crevasse splay and avulsions. The results demonstrate the potential of Landsat imagery to determine the grain size and sedimentary facies distribution on playas in endorheic basins.*

6.1   Introduction

As a common feature of internal drainage basins, playas are vital for understanding the natural habitats of endemic microbes, plants and animals (Castañeda et al, 2005) and for interpreting the interrelation between climate and tectonic activity within continents (Bryant, 1996). Studies also

---

[5] Chapter 6 is based on the manuscript entitled "Non-vegetated playa morphodynamics using multi-temporal Landsat imagery in a semi-arid endorheic basin: Salar de Uyuni, Bolivia". J. Li, M. Menenti, A. Mousivand, S.M. Luthi. (submitted). Remote Sensing.

proved that playas sediments could be potential hydrocarbon reservoirs (McKie, 2011), as they may contain significant numbers of thin fluvial sheetflood deposits. Many researchers have suggested that a framework for surface sedimentary facies or depositional environments is needed in playas (Hardie et al., 1978; Rosen, 1991; Bryant, 1993; Bryant et al., 1994). Over the past decades, a number of studies have applied remote sensing techniques to study playas and have demonstrated the usefulness of remote sensing in such studies (e.g. Menenti et al., 1986; Menenti, 1989; Townshend et al., 1989; Drake et al., 1994; Drake, 1995; Bryant, 1996; Bryant, 1999; Bryant and Rainey, 2002; Castañeda et al., 2005). However, most of these studies have focused on mapping evaporite minerals and water bodies. There are few studies focusing on grain size and sedimentary facies distribution using remote sensing (Chapman et al., 1989; Johnston and Kamprad, 1989; Millington et al., 1989; Quarmby et al., 1989; Townshend et al., 1989), mostly due to difficult accessibility (Millington et al., 1989; Bryant, 1996) and hazardous environments during peak discharge events (Li et al., 2014). In this paper, we analyse playa morphodynamics by Landsat time series data in the semi-arid endorheic (internal drainage basin) basin of the Salar de Uyuni in Bolivia.

A basic theory about the relationship between sediment and reflectance (Bedidi et al., 1992) is used in this paper. If the sediment is very coarse, the porosity is high and thus the scatter effect is strong and the reflectance is low. The high porosity also indicates a high capacity for storing water. As grain size decreases, the water content simultaneously decreases due to a decline in porosity. When the sediment is fine sand or silt, the reflectance is high due to little scattering effect and a large specific area. However, with an increasing content of clay, the capacity of the sediment for storing water increases because of the large internal surface, which is related to adhesive, cohesive and osmotic forces (Hilhorst et al., 2001). Due to strong evapo-transpiration in the study area (1500mm/year), the water in the sediments precipitates salt in the long dry period (normally from April to November in the studied area). When the surface is covered by salt it has a strong reflectance, while for clay-rich areas, the reflectance is low due to soil moisture. In addition, crust cracking at clay-rich surface reinforces its roughness and therefore contributes to a low reflectance.

This study documents the use of Landsat imagery in combination with precipitation data and field investigation to analyse playa morphodynamics. First, we establish the relationship between the various types of sediments (e.g. salt-, sand- and clay-rich sediments) and spectral reflectance, and then build spectral libraries for each type. Such spectral libraries are then used to classify the Landsat time series data from 1985 to 2012 over the study area, with Maximum Likelihood Classification (MLC) method being used as a supervised classifier. Then we analyse the relationships between different classes and sedimentary facies, and investigate the changes of these classes in combination with precipitation data. Finally we analyse the geomorphological changes with a time series of classified maps.

6.2   Data acquisition

Daily precipitation data were used to precisely determine dry seasons and rainy seasons for each year. The field survey was carried out from 13 to 18th of November 2012 before the rainy season.

The field sampling sites were determined using Landsat ETM+ imagery and land cover samples were collected with geo-located GPS.

Landsat Surface Reflectance Climate Data Record (CDR) data was collected from the USGS website (http://earthexplorer.usgs.gov/). The surface reflectance CDR, including many Landsat TM and all ETM+ scenes, is a high-level Landsat data product and is derived from specialized software called Landsat Ecosystem Disturbance Adaptive Processing System (LEDAPS). The surface reflectance data were available in the form of 16-bit signed integer with the range of -2000 to 16000. The studied river terminus is included entirely within Landsat path 233, row 74. Thanks to the available daily precipitation data, we accurately determined the rainy and dry periods of 1985-2012. This allowed us to select Landsat images in the dry periods (Table 6.1).

Year	Month	Day	Year	Month	Day
1985	August	05	1999	November	16
1986	October	11	2000	November	02
1987	November	23	2001	November	21
1988	September	14	2002	June	25
1989	November	04	2003	October	26
1990	November	07	2004	November	13
1991	October	09	2005	October	31
1992	September	09	2006	November	19
1993	July	26	2007	October	05
1994	June	27	2008	November	08
1995	October	20	2009	October	26
1996	September	20	2010	August	26
1997	August	06	2011	September	30
1998	September	10	2012	November	11

Table 6.1: *Days for which Landsat Climate Data Record (CDR) data are used.*

6.3   Methodology

6.3.1   Landsat CDR data pre-processing

Spectral libraries of different classes (end-members) were built using Landsat images of 2012 and ground truth data collected during the field campaign (Figure 6.1). Bands with a low fraction of saturated pixels have been selected for later normalization and classification. In this paper, we used three Landsat bands 2, 4 and 7, which have low fractions of saturated pixels for the period 1985-2011 according to digital number statistics of all bands. All these selected bands were subsequently normalized to the referenced image (Nov. 11, 2012) with Iteratively Reweighted Multivariate Alteration Detection (IR-MAD) transformation (Canty and Nielsen, 2008). The IR-MAD transformation was used to find invariant pixels between each scene and the reference scene (11th of November 2012). Then these invariant pixels were used to normalize each image band-by-band to the reference image with Reduced Major Axis (RMA) regression.
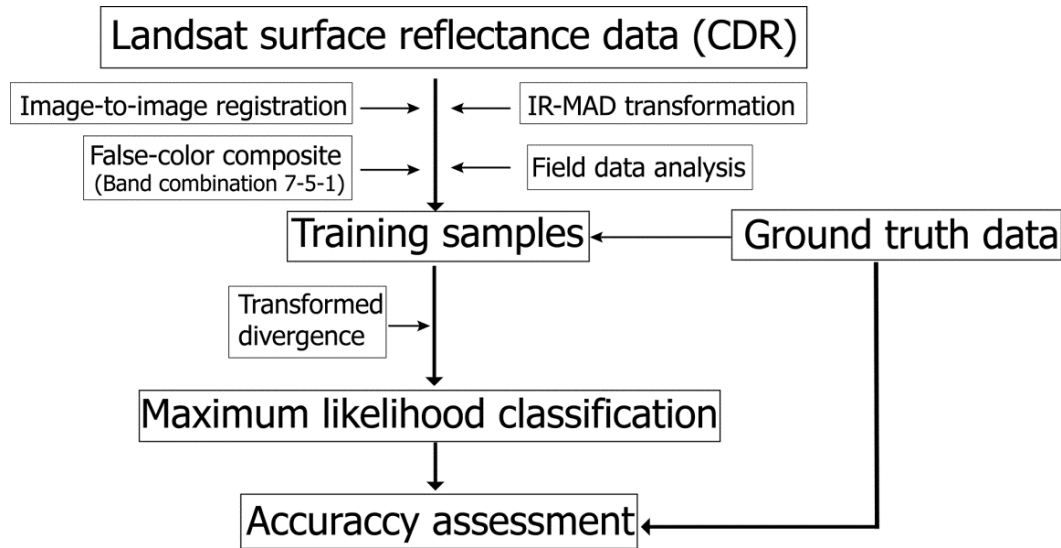
Figure 6.1: *Flow chart for the Landsat images processing.*

6.3.2 Training samples selection and analysis

The training samples were selected from a false-color composite image and field sampling data. We used false-color composites of band 7 (2.08 -2.35 µm), band 5 (1.55 - 1.75 µm) and band 1 (0.45 - 0.52 µm) (Figure 6.2) to differentiate different surface materials (in particular clay-rich and silt-rich surface). Since both bands 5 and 7 are located in the near-infrared region, they are sensitive to soil moisture and indicate water absorption regions. We identified four surface materials: A, B, C and D (Figure 6.2).

   The field campaign included surface color analysis and sampling. Surface color analysis included the four documented types of surface materials based on false-color composite map (Figure 6.3). The colours of different surface deposits were determined using Munsell colours chart in the field: A is from 2.5 YR 8/2 to 5 YR 8/2 (light pink); B is from 2.5 YR 8/4 to 5 YR 8/4 (pink); C is 7.5 YR 6/3 to 7.5 YR 5/6 (light - strong brown). The samples were then analysed in terms of grain size with a Sympatec HELOS KR laser-diffraction particle sizer with a size range from 0.1-2000 µm. The results of the grain size analysis of field samples were used to validate the analysis of the false-color composite Landsat images on the 11th of November 2012 (Figure 6.4).We assigned the following names to the classes: A, salty surface; B, silt-rich surface; C, clay-rich surface; D, salt. Here salty surface represents mixed sediments of salt and silt or clay with a light pink colour, while the silt-rich surface is coarser than the clay-rich surface. Salt indicated a thick, white salt crust on the surface.
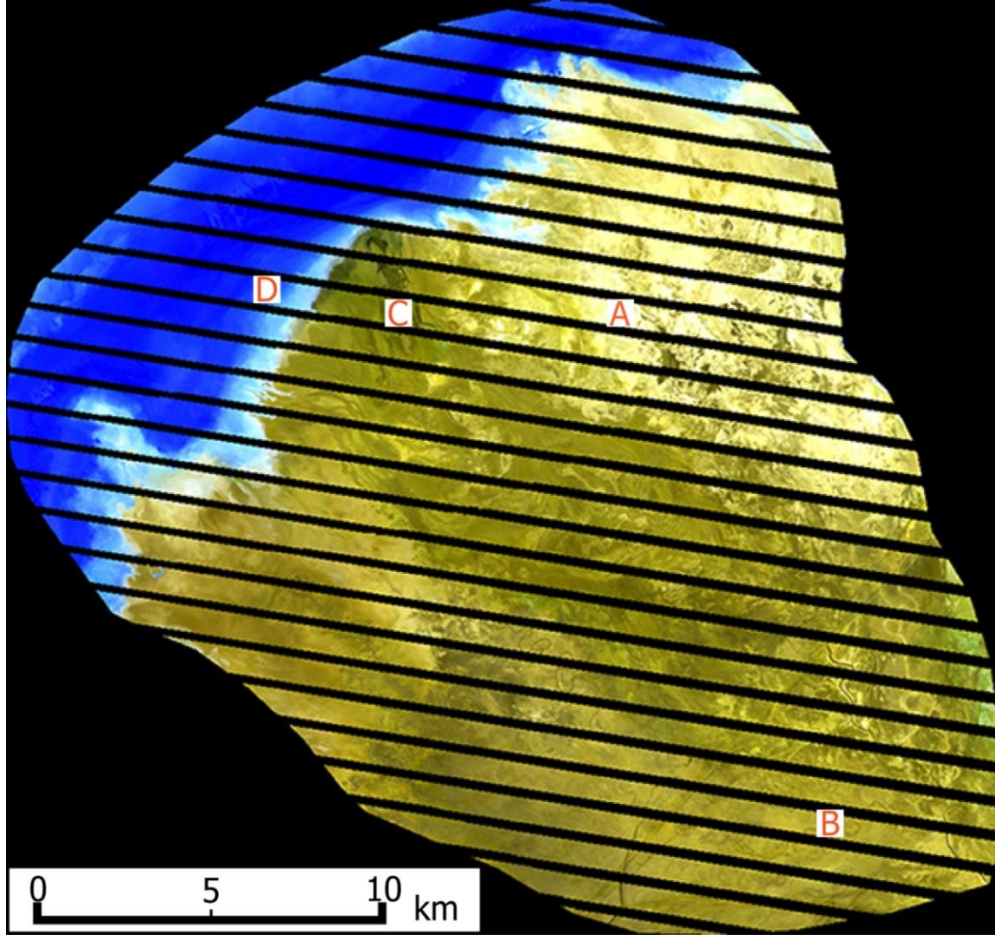
Figure 6.2: *False-color composite of bands 7 (red), 5 (green) and 1 (blue) of Landsat ETM+ on Nov. 11, 2012. A, B, C and D represent different surface materials. Stripes are caused by the failure of the scan line corrector (SLC) on Landsat-7 ETM+ imagery in 2003.*

With GPS data of the sampling sites, we collected training pixels of different surface materials on the Landsat image of Nov-11-2012. Field observation showed that the surface was flat and homogeneous around each sample point. Therefore, we added training pixels around the sampling sites. We split the spectral datasets randomly into two sets: one set for training samples (Table 6.2) and the other for ground truth accuracy assessment. The training samples were analysed in terms of separability between classes with transformed divergence method (Swain and King, 1973):

$$TD_{ij} = 2 * \left(1 - e^{\left(\frac{-D_{ij}}{8} \right)} \right), \quad (6\text{-}1)$$

where i and j represent the two signatures (classes) being compared, and T is the transposition function. The index varies from 0 and 2. When the value is greater than 1.8, the compared pairs have good separability, whereas when it is less than 1, they should combine into one single class (Petropoulos et al., 2010). The transformed divergence indices were greater than 1.97 for most of the classes (Table 6.3). These samples were then used as input for the MLC method.
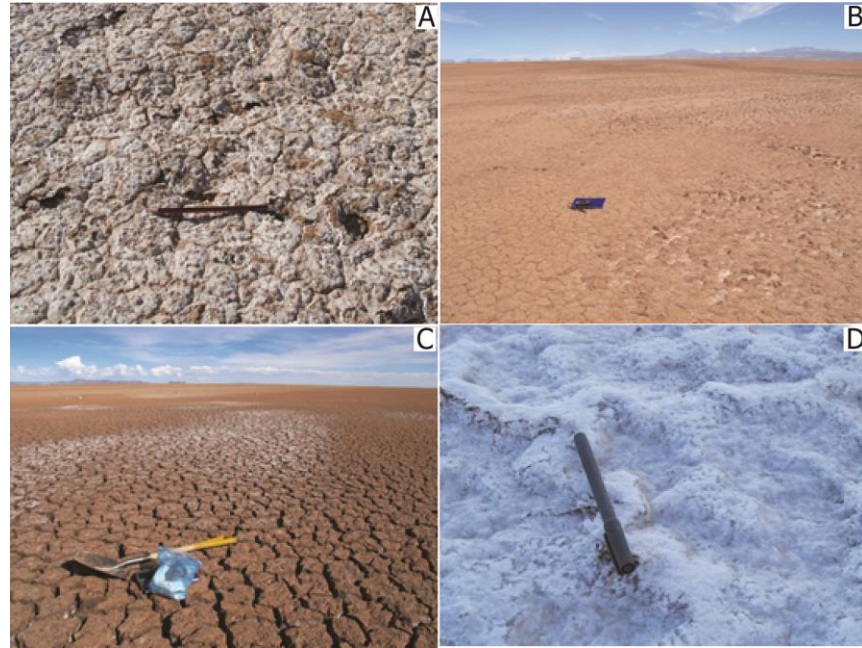
Figure 6.3: *Different types of surface materials in various locations in the river terminus on Nov. 11, 2012. A: mixture of salt and sediment; B: silt-rich surface; C: clay-rich surface; D: salt. The sites for each surface type are indicated on Figure 6.2.*
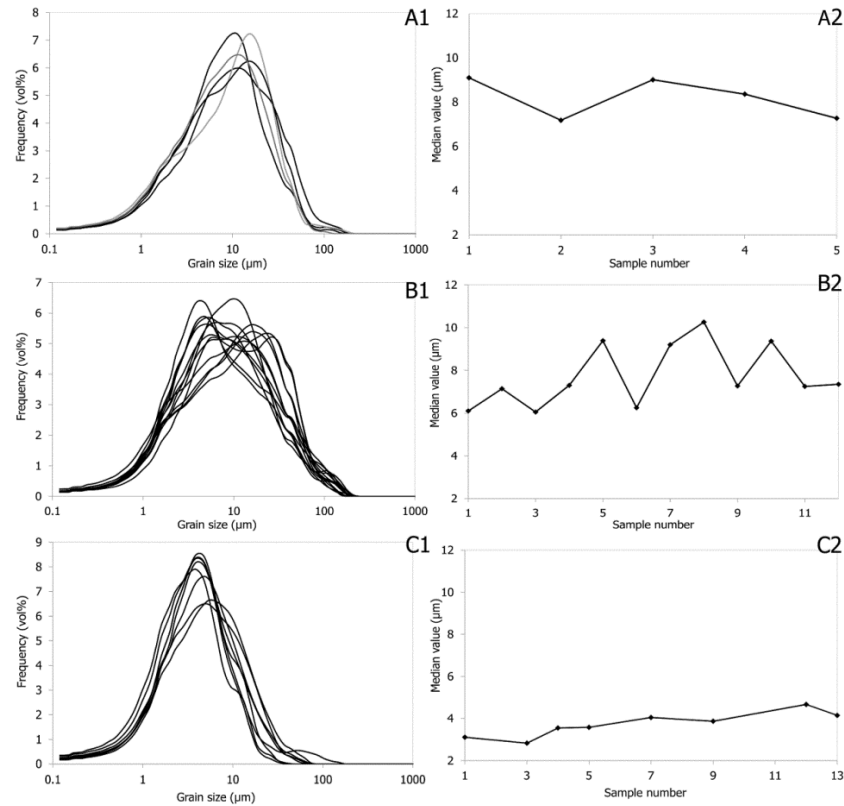
Figure 6.4: *Grain size distribution of three types of sediment. Figures on the left-hand side (A1, B1 and C1) are the grain size distributions of different surface materials (A: salty surface; B: silt-*

rich surface; C: clay-rich surface) while figures on the right-hand side (A2, B2 and C2) are their mean grain size.

Class	Pixels	Polygons
Salty surface	34	3
Silt-rich surface	41	6
Clay-rich surface	60	5
Salt	41	8

Table 6.2: *ROI statistics of each class.*

Class-1	Class-2	Separability
Salty surface	Silt-rich surface	1.998
Salty surface	Clay-rich surface	2.000
Salty surface	Salt	2.000
Silt-rich surface	Clay-rich surface	1.980
Silt-rich surface	Salt	2.000
Clay-rich surface	Salt	2.000

Table 6.3: *Report of ROI separability for training pixels.*

6.3.3 Maximum likelihood classification

Evans (1998) has proved that the prior knowledge of the relationships between input attributes and salinity in the classification of Landsat TM data is of importance for salinity mapping. We used a supervised classification, the MLC method, which employs discriminant functions to assign pixels to the class with the highest likelihood (Strahler, 1980).

$$d_k(X_i) = \ln|D_k| + \left(X_i - \mu_k\right)^{\top} D_k^{-1}(X_i - \mu_k) - 2\ln P\{w_k\}, \quad (6\text{-}2)$$

where D_k is a p by p dispersion matrix associated with a sample of observations belonging to the kth class and p is a number of measurement variables used to characterized each object or observation, X_i is a vector of measurements on p variables associated with the ith object or observation, μ_k is mean vector associated with a sample of observations belonging to the kth class, $P\{w_k\}$ is probability that an observation will be a member of class w_k. For eq. 6-2, X_i is in class k provided $d\_k(X_i) \geqslant d\_j(X_i)$ for all j = 1 ⋯ K.

6.3.4 Accuracy assessment

The classification accuracy was assessed with the overall accuracy, kappa coefficient, producer's accuracy and user's accuracy (Table 6.4). The overall accuracy was 89.32% and the Kappa coefficient was 0.85.

Class	Producer's accuracy	User's accuracy
Salty surface	66.67	100
Silt-rich surface	100	72.5
Clay-rich surface	79.31	100
Salt	100	100

Table 6.4: *Accuracy assessment of classification*

6.3.5   Application to the other Landsat images processing

The established spectral library based on the analysis of Landsat scene of Nov. 11, 2012 was applied to other Landsat scenes for the period 1985 to 2011. We expanded the spectral libraries and randomly selected more than 1000 pixels with more than 10 polygons to training samples based on the classified map on Nov. 11, 2012 (Figure 6.5). We used the toolbox 'Endmember Collection' to perform classification on Landsat images from 1985 to 2011 with the remote sensing image processing software ENVI.
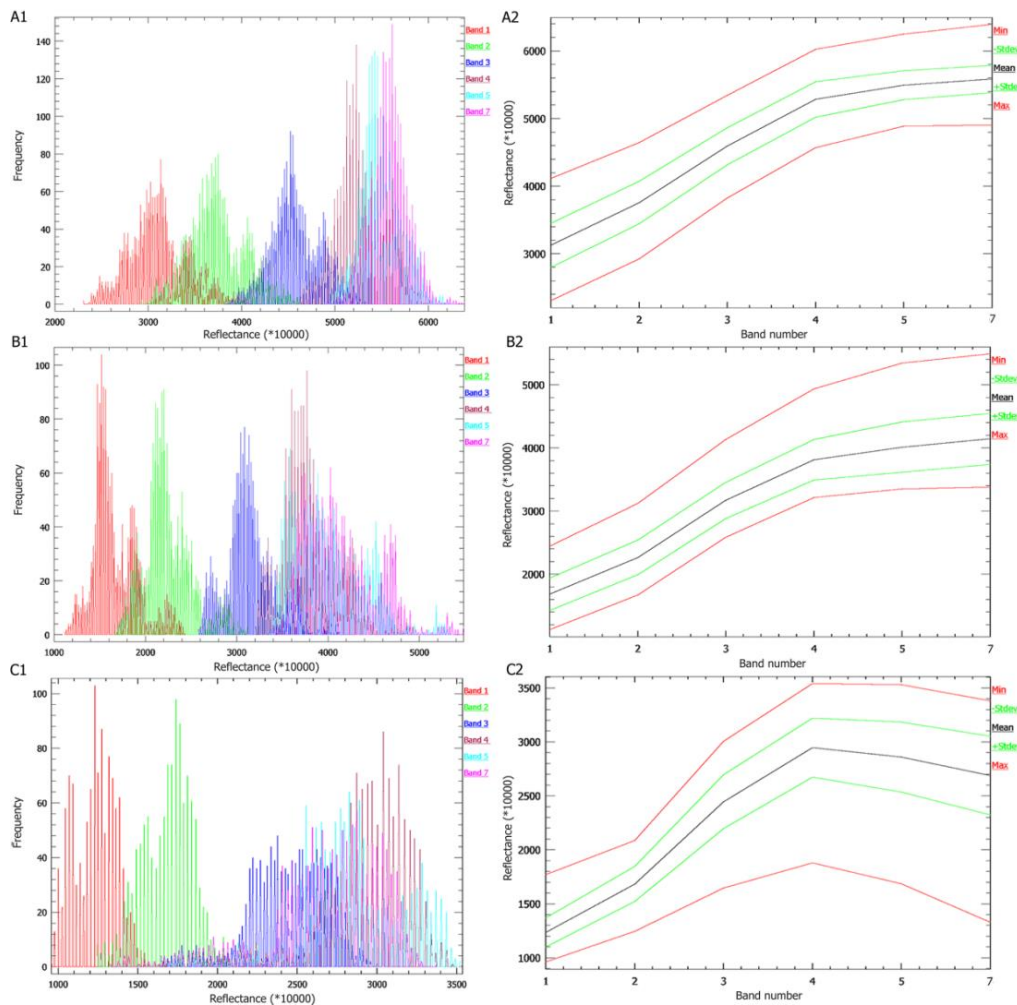
Figure 6.5: *Statistics of the spectral library on Nov. 11, 2012. A: Salty surface; B: Silt-rich surface; C: Clay-rich surface. Figures on the left-hand side (A1, B1 and C1) are about the*

histogram of training samples (greater than 1000 pixels for each class) while on the right-hand side (A2, B2 and C2) are the statistic boundary of each class.

6.4   Results

6.4.1   Areal statistical analysis of the different classes

Surface materials change over years in terms of the area that they cover (Figure 6.6). The clay-rich surface has the largest area of the four classes over the period 1985-2011 (Table 6.5). The standard deviation of areas showed that the salty surface and the silt-rich surface changed more dramatically than the area of salt. The clay-rich surface was dominant in the river terminus and also showed considerable changes.
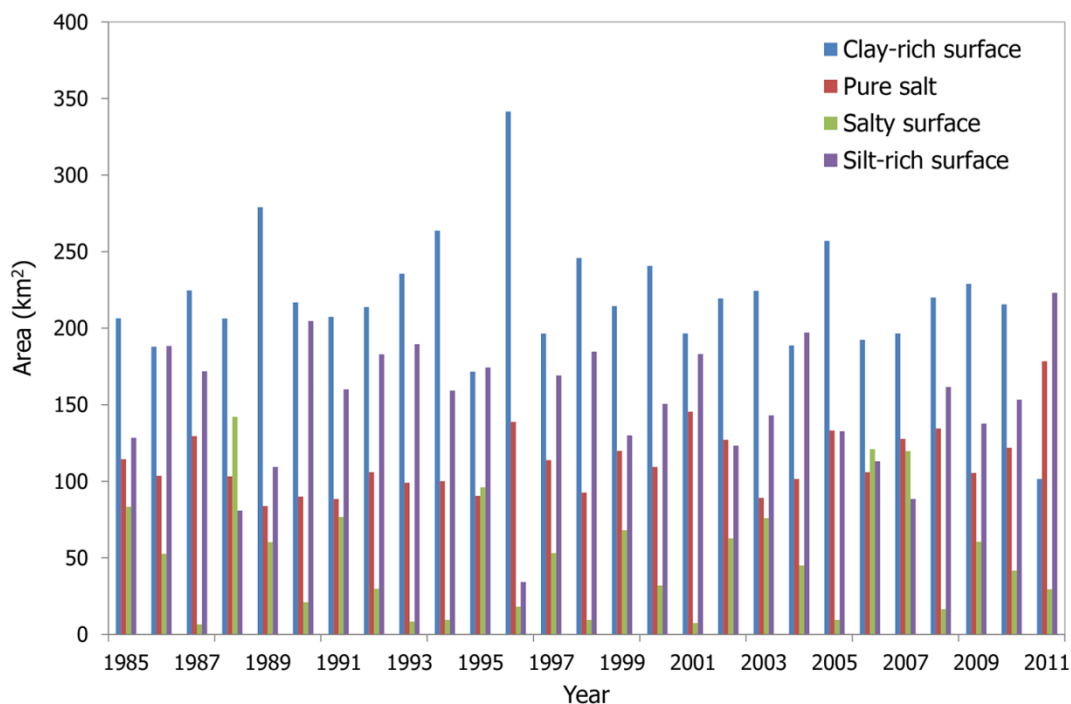
Figure 6.6: *Areal statistics of each class between 1985 and 2011.*

Class	Mean (km^2)	Max (km^2)	Min (km^2)	Standard deviation (km^2)
Salty surface	50.28	142.07	6.61	38.37
Silt-rich surface	150.92	223.09	34.22	41.96
Clay-rich surface	218.27	341.44	101.56	41.27
Salt	113.09	178.36	83.86	21.48

Table 6.5: *Statistics of areas of each class.*

6.4.2 Interpretation of the different classes

In the river terminus, the silt-rich surface and the clay-rich surface tend to be associated with different sedimentary facies. For example, the silt-rich surface is distributed on crevasse splays and levees along channels, while the clay-rich surface can be found on the floodplain between channels. In addition, the silt-rich surface was generally distributed in the proximal part of the river terminus while the clay-rich surface was commonly seen in the distal part of the terminus. The clay-rich surface sometimes could be seen in the salt lake, probably attributed to peak floods or wind. During peak floods, the water is at its highest level in the salt lake and clay is transported to the salt lake and the edge of the water body. When the water evaporates and salt is precipitated, the clay in the deep water area is covered by salt but clay at the edge of the water body is mixed with salt and exposed. Depressed channels were also covered by the clay-rich surface, although sometimes salt could be found in the present channel (Figure 6.7). The salty surface was generally distributed in the channels and the distal part of the river terminus, while the salt was generally distributed at the end of the present channel and the salt lake.
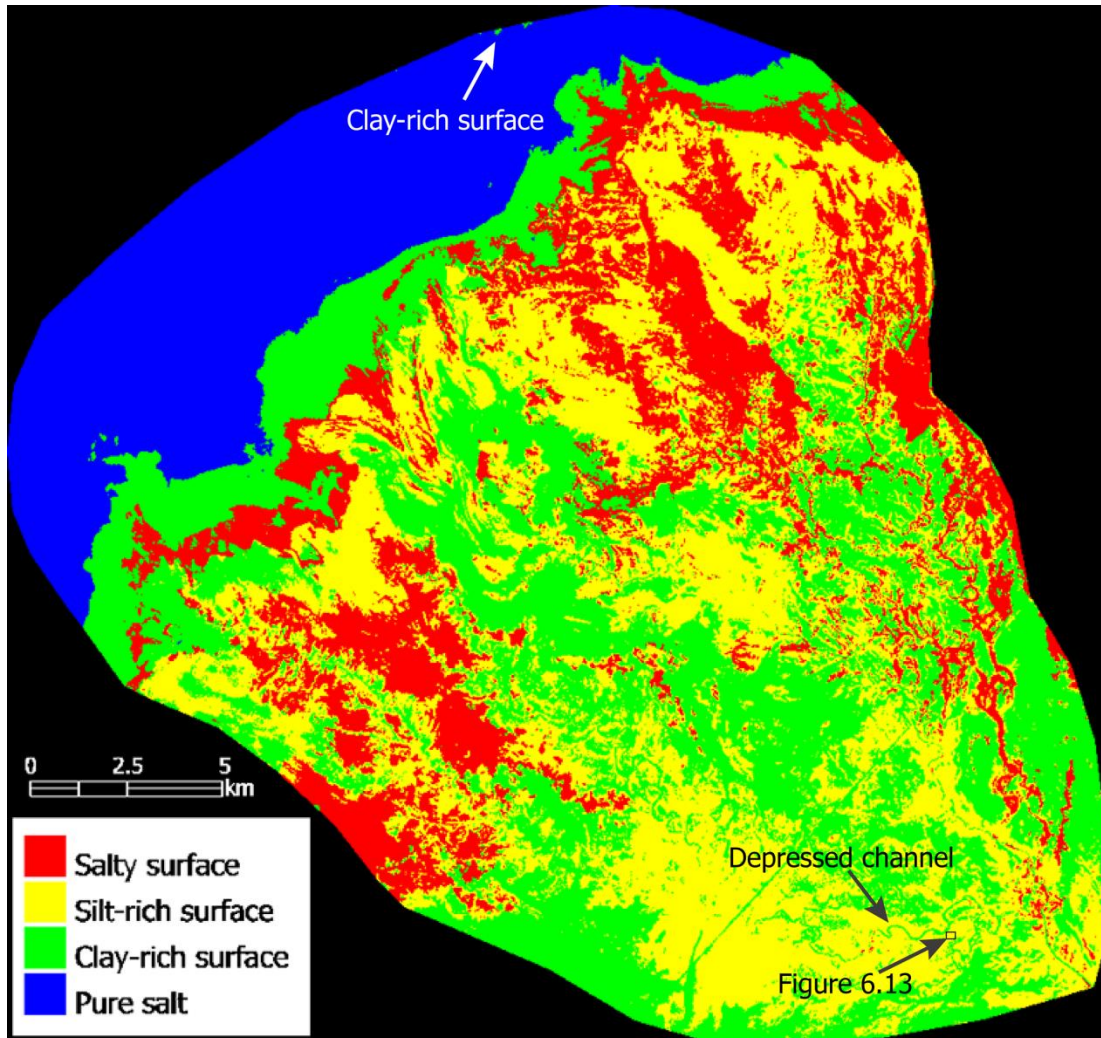
Figure 6.7: *Classification map of Landsat TM on Oct. 20, 1995.*

In combination with the annual precipitation, we analysed the areal changes of each class between 1985 and 2011. The silt-rich surface shows a weak correlation with the annual precipitation (Figure 6.8A) probably because although the annual precipitation is high, the daily precipitation all year around is low. However, some daily precipitation is high in those low annual precipitation periods and Li et al. (2014) have demonstrated that high daily precipitation would lead to peak discharges, which result in large flow and sediments transport to the river terminus. During these short-lived and high magnitude of peak floods or multiple successive floods, channels experience massive over-spilling flow due to the downstream decrease in cross-section area on the low-gradient Río Colorado river system (Donselaar et al., 2013; Chapters 2 and 4) and the spill-over flow reactivates crevasse splays and levees. For instance, the crevasse splay was partly reactivated in the rainy season of 1999-2000. However, it was completely reactivated in the rainy season of 2000-2001 because of the highest annual precipitation (406.4 mm) in the period from 1985 to 2011 (Figure 6.9).
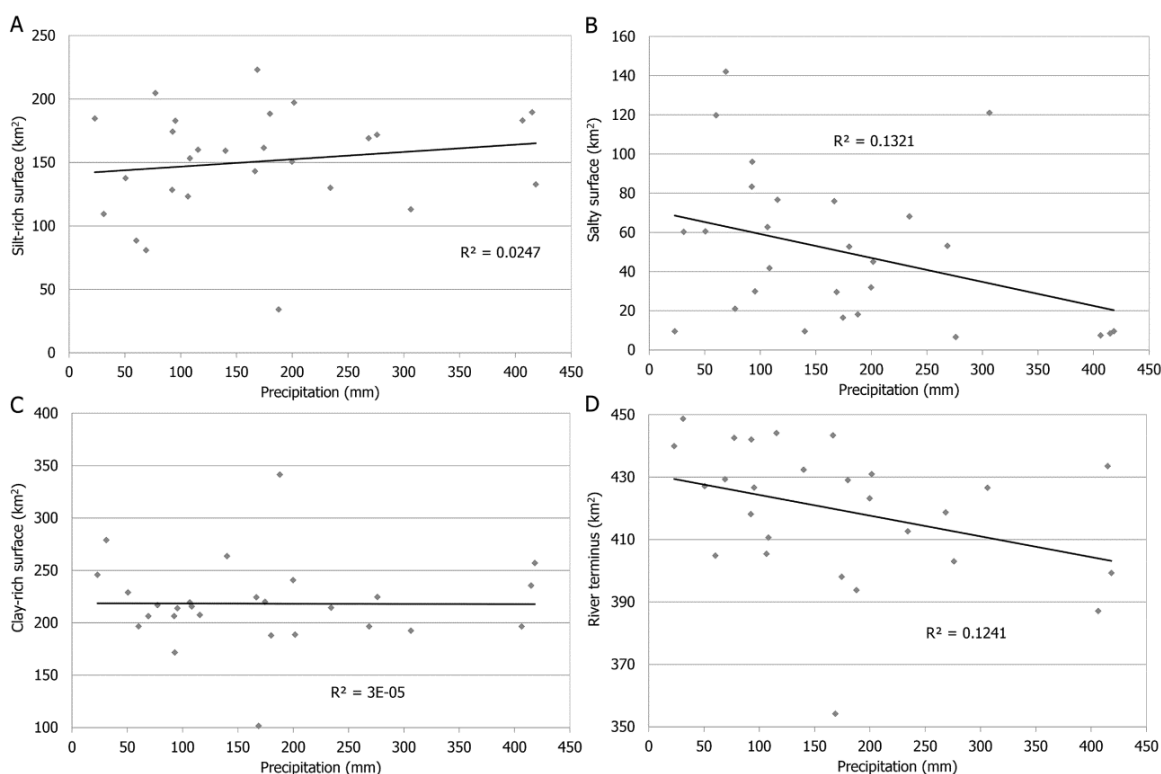
Figure 6.8: *The relationship between the annual precipitation and areas of different surface materials between 1985 and 2011.*

Figure 6.9: *Reactivation of a crevasse splay. The bold black lines indicate the trunk channel while the dashed lines show the activated splays.*

By contrast, the salty surface was negatively correlated with the annual precipitation (Figure 6.8B), i.e. when the annual precipitation increased, the salty surface decreased. For the clay-rich surface, there is no correlation with the annual precipitation (Figure 6.8C). The area of river terminus, which includes salty surface, silt- and clay-prone surface, tended to be inversely proportional to the annual 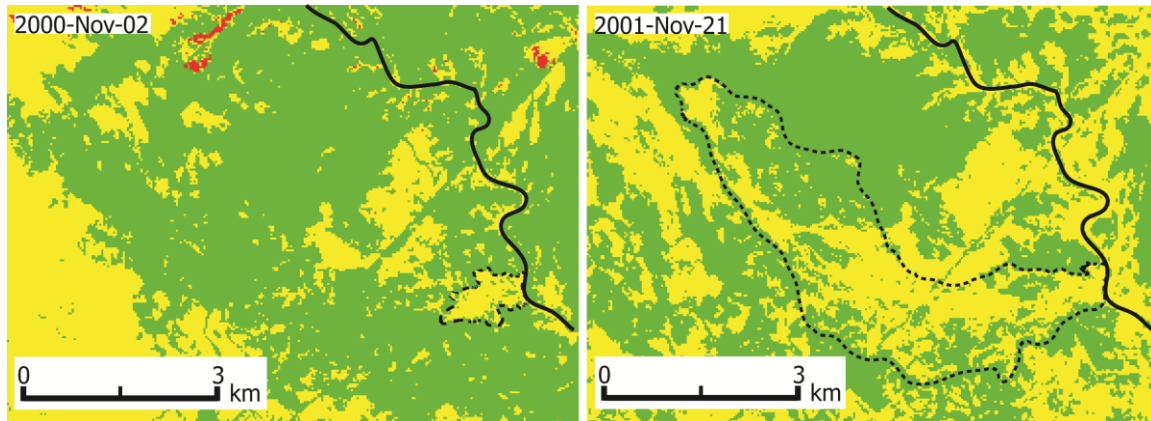rainfall (Figure 6.8D). We suggest that the higher the annual rainfall, the more water is draining to the lake, which results in high water levels in the lake. When the water evaporates, salt is precipitated on the surface. Therefore, the salt area will increase and the river terminus shrinks when the annual precipitation increases.

6.4.3   Geomorphological change detection

Geomorphological changes could be detected with comparisons of classification maps. The positive correlation between silt-rich surface and crevasse splays enables us to characterize the expansion of crevasse splays over the observation years. Specifically, the development of a crevasse splay in the distal part of the river terminus was recorded through time-series classification maps. It started with a small crevasse splay and then grew into large splays during the subsequent floods (Figure 6.10). The expansion of the crevasse splay is in agreement with that by Li et al. (2014), which also showed that this new crevasse splay was attributed to a compensational stacking pattern, whereby the new crevasse splay expanded in the topographic low between two adjacent existing splays. The expansion of crevasse splays also contributed to the increasing area of the silt-rich surface.

The avulsion history was reconstructed by comparing classification maps (Figure 6.11). The observed avulsion was initiated with a crevasse splay and then developed into an avulsion with subsequent floods. Previous studies suggested that the splay-induced avulsions attributed to downstream decrease in channel cross-section area in the dryland river system (Donselaar et al, 2013; Li et al., 2014). Therefore, rivers in the dryland region experience massive flow over-spilling onto the floodplain, which reinforces breaching levees during peak floods, and increases

the chance of bank failure. In addition, the sediment-laden water would flow back to the trunk channel during the waning flood stage. The returning flow erodes the crevasse floor and therefore deepens the crevasse channels; on the other hand, the process decreases the capacity of the trunk channel because sediments in the returning flow are deposited at the downstream side due to low energy of returning flow (Donselaar et al., 2013). These processes promote avulsions and simultaneously increase the silt-rich surface in the distal part of the river terminus.
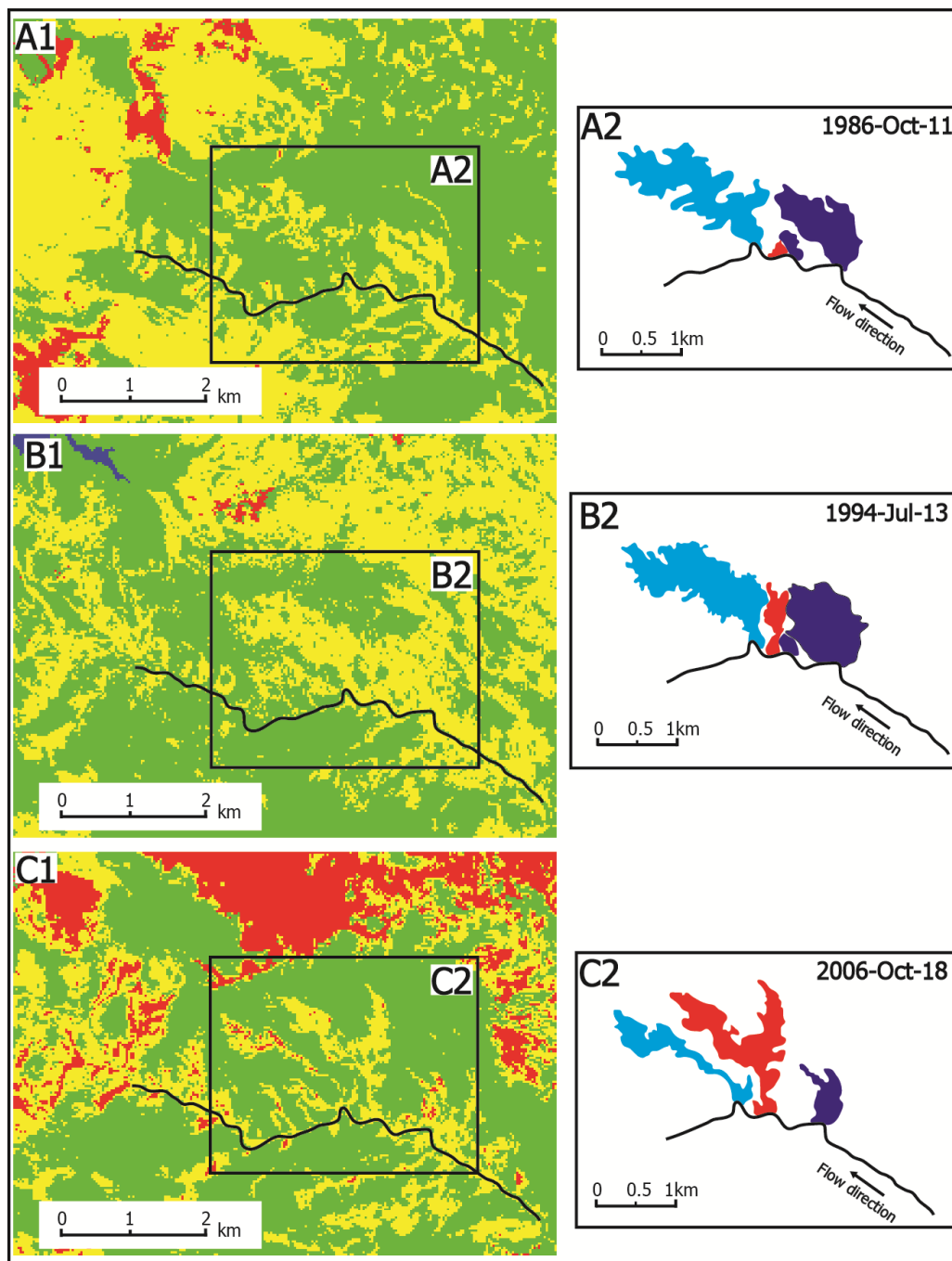
Figure 6.10: The formation and expansion of a new crevasse splay. Figures on the left-hand side are classification maps, where the yellowish area represents the crevasse splay surface, the

greenish area the floodplain, and reddish area the salty surface. Figures on the right-hand side are schematic diagrams of the development of the new crevasse splay in a time series.
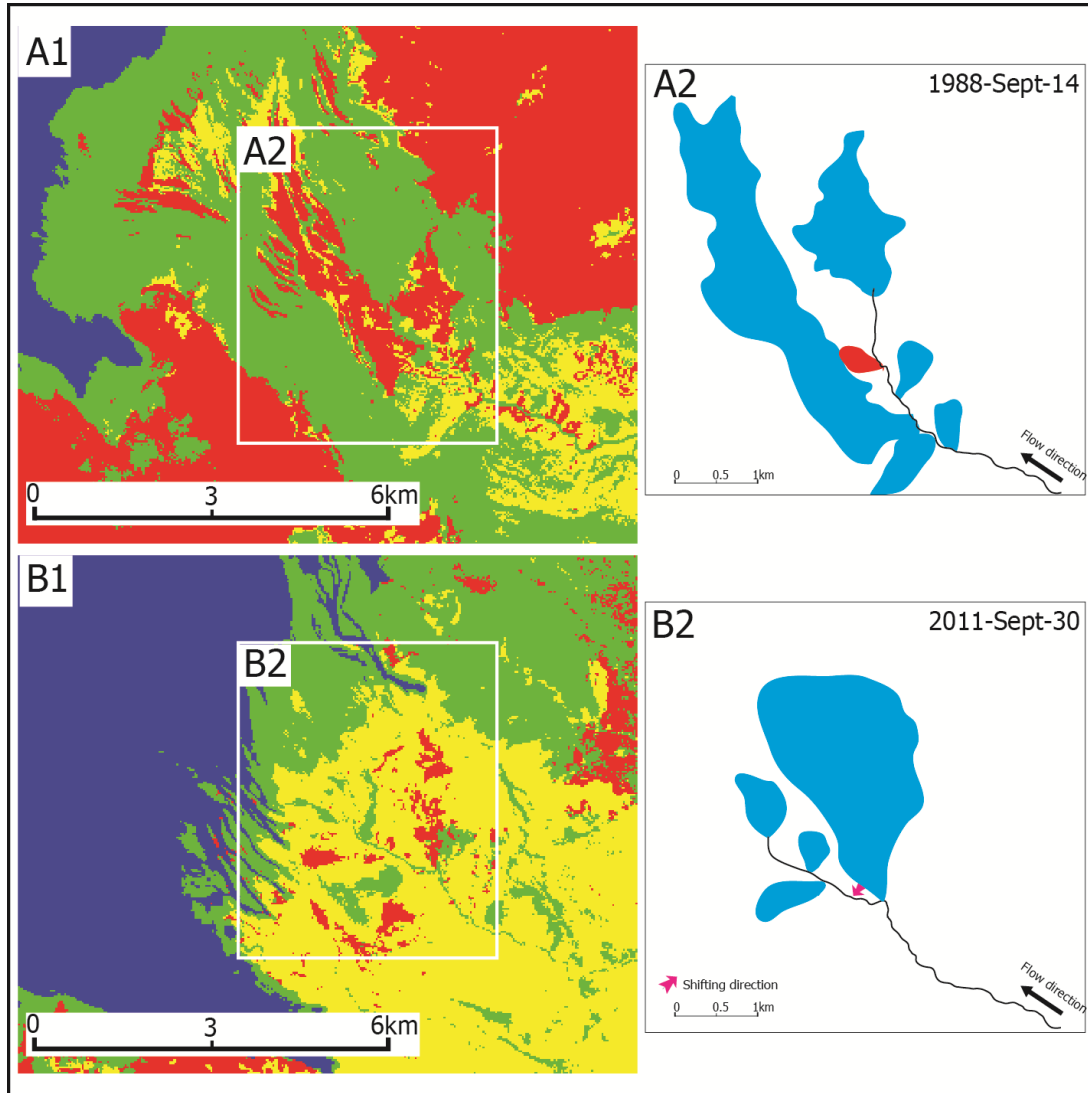
Figure 6.11: *Observed avulsion in the distal part of the river terminus. Figures on the left-hand side are classification maps, where yellowish area represents silt-rich surface and greenish area is floodplain and reddish area indicates salty surface. Figures on the right-hand side are schematic diagrams of the development of an avulsion. The red splay on the upper right indicates where the avulsion happens.*

6.5   Discussion

Due to salinity, the Time Domain Reflectometry (TDR), which is used to simultaneously obtain soil water content and electrical conductivity by a single probe with a minimal disturbance

(Noborio, 2001), did not work properly. However, field observation showed that the clay-rich surface is wetter than the silt-rich surface (Figure 6.12A). In addition, the density of desiccation cracks is also higher on the clay-rich surface than on the silt-rich surface (Figure 6.12B). Both soil moisture and desiccation cracks exert a negative impact on reflectance.
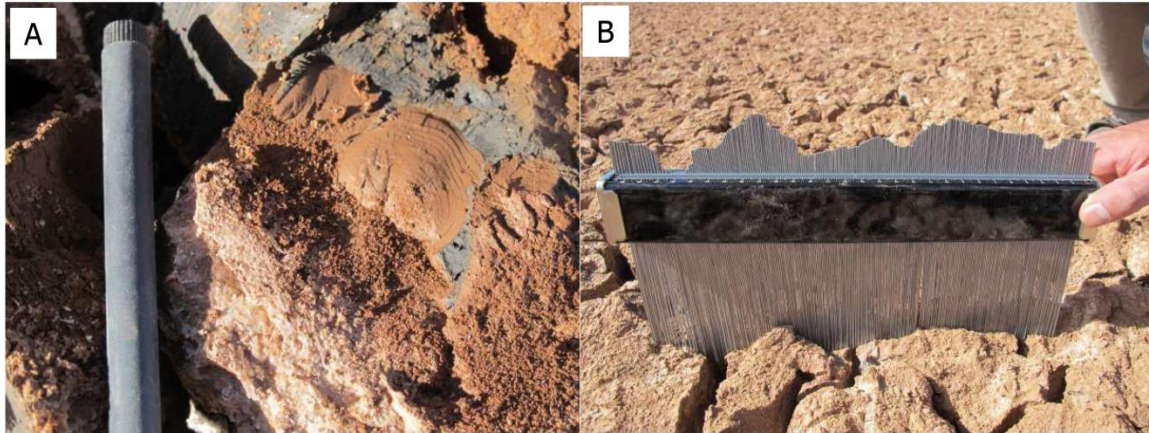
Figure 6.12: *Brownish wet clay-rich surface (A) and the roughness and cracks on the surface (B).*

To test the consistency of the surface reflectance in the study area, we selected an area with 45 pixels, which was in the centre of silt-rich surface on Nov. 11, 2012 and Sept. 30, 2011 (Figure 6.13). The tested area is along the abandoned channel belt (Figure 6.7) and has the limited influence by peak discharge. Though the reflectance on Nov. 11, 2012 is lower, its overall trend is the same as that on Sept. 30, 2011. This might seem at first a challenge in applying this spectral reflectance for the classification of the other images, but by comparing the reflectance of different classes (e.g. Figure 6.5) it can be seen that the mean values are also very different for each class, which would mitigate this problem partly. Besides, different mean values with similar trends might lead to the conclusion that classification methods based on angular mapping would work better in such a case. In order to demonstrate this, we have implemented other classification methods based on angular mapping like Spectral Angle Mapper (SAM) and as well as Support Vector Machine (SVM). However, these two methods showed lower accuracies (not shown) compared to the maximum likelihood method and failed in producing reasonable classification maps. Moreover, the classification results show the tested area is classified the same (i.e. silt-rich surface) in the two images using maximum likelihood method demonstrating that the good performance of the method.

We also suggest that post-processing such as majority/minority analysis, sieve classes should not be performed on classification maps. First of all, the inter-channel deposits are generally clay-rich and, therefore, their reflectance is low. In addition, the inter-channel area is sometimes small (e.g., crevasse channels) with the ground resolution of the Landsat TM images being 30 m by 30 m. Using these post-processing methods tends to blur these sedimentary phenomena and create errors. Therefore, the statistical analysis on playa morphodynamics was found the result of maximum likelihood classification to be better than that with post-processing.

Surface reflectance from false-color composite images was used to differentiate surface materials, and these surface materials correspond to a particular color (Figure 6.3), but still with some errors. For example, some sampling locations apparently look pink and samples from these places are supposed to be silt-rich, but the grain size analysis shows that these samples belong to clay-rich materials.
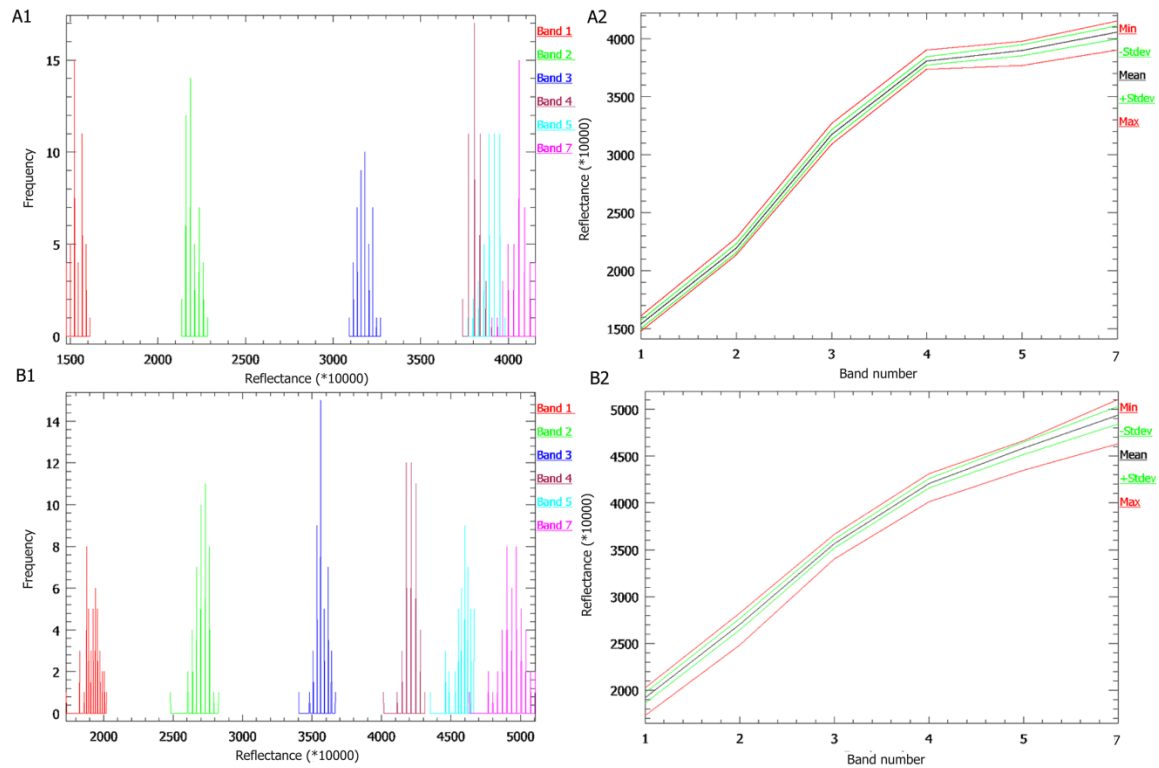
Figure 6.13: *Statistics of the tested area for the silt-rich surface. See the location of the tested area in the Figure 6.7.*

6.6   Conclusions

This chapter presents playa surface dynamics using multi-temporal Landsat images over 27 years from 1985 to 2011. The study demonstrates that mapping coarse and fine sediments in the playa with multi-temporal Landsat surface reflectance is possible, and this allows us to work on further genetic analysis in terms of sedimentary facies changes for a single pixel in a time series in the future. The highlighted points in the paper are as follow:

- A spectral library has been established for four types of surface materials using Landsat surface reflectance in combination with Landsat CDR data and field data analysis. There are four types of surface materials in the river terminus: A: salty surface; B: silt-rich surface; C: clay-rich surface; D: salt. The study area experienced changes over 27 years from 1985 to 2011. Although the difference in grain size between silt-rich materials and clay-rich materials is small, the reflectance of the latter is lower than that of the former,

probably due to increasing water content and desiccation cracks in response to decreasing grain sizes.

- The clay-rich surface dominates in the river terminus, whereas the salty surface and the silt-rich surface fluctuate significantly. The salt was relatively stable in terms of area in the study area. The silt-rich surface and the clay-rich surface are associated with different sedimentary facies in the river terminus. The silt-rich surface was widely distributed along channels and crevasse splays while the clay-rich surface was found in the floodplain and the channels. In addition, the proximal part of the river terminus was dominated by the silt-rich surface while the distal part of the terminus was mainly occupied by the clay-rich surface. The clay-rich surface occurs in the salt lake during floods or through wind-blown influence.

- The silt-rich surface has a weak correlation with the annual precipitation while the salty surface tends to be inversely proportional to the annual precipitation and there is no relationship between the clay-rich surface and the annual precipitation. Geomorphological changes have been identified such as the formation of crevasse splays and avulsions. High annual precipitation-induced avulsions also led to increased silt-rich surfaces.

Chapter 7   Summary, Conclusions and Recommendations

A synthetic summary of the previous results is presented in this chapter. Channel and splay morphodynamics, longitudinal sediment dispersion pattern in the system, and surface composition in the river terminus are the focus of this study. The preservation potential and sequence stratigraphy of the Río Colorado system is then analysed. Finally recommendations for future work on dryland river systems are proposed.

7.1   Synthetic summary

The major objective of this thesis is to investigate the morphodynamics and sediment distribution of a terminal fluvial system in a recent semi-arid endorheic basin with help of remote sensing techniques and the geographic information system (GIS), as well as to build up knowledge for establishing a 3D sedimentary architectural model. A river terminus system of the world largest salt lake, Salar de Uyuni in Bolivia is the focus of this study (Figure 1.2) because of similarities in tectonic and climatic settings of the Altiplano basin with the Southern Permian Basin (Chapter 1). The relationship between peak discharge events in an ephemeral dryland river system and the development of river avulsions and crevasse splays has been reconstructed in this field area. In addition, the resultant morphological changes at the terminus of the river system have been visualized with Landsat time-series imagery over a period of 30 years (Chapter 2). Infrequent and high-magnitude floods play an important role in the channel and splay morphodynamics of the Río Colorado river system. Many ephemeral rivers such as the Río Colorado are characterized by long periods without flow, and previous studies in such rivers typically focused on the flood events (Graf, 1988a) because they are of paramount importance for the channel morphology and sediment transport (e.g., Leopold and Miller, 1956; Schumm and Lichty, 1963; Bourke and Pickup, 1999). Four types of channelled floods in dryland rivers are identified: Flash floods, single-peak events, multiple-peak events and seasonal floods (Graf, 1988a). Of these, convective thunderstorm-induced-flash floods have been most frequently reported in dryland river regions, and due to high runoff coefficients (McDermott and Pilgrim, 1983; Rodier, 1985), rapid runoff even from low rainfall amounts leads to Hortonian overland flow (Yair and Lavee, 1985; Thornes, 1994a). Discharge modelling has shown that ten peak discharge events with more than 50 m^3/s have occurred between 1985 and 1999, with a maximum peak discharge event of 103 m^3/s. The development in space and time of crevasse splays and local avulsions by comparing Landsat MSS

and TM images before and after peak discharge events has shown that crevasse splays expanded in peak discharge periods, leading to amalgamation with adjacent crevasse splays by compensational stacking. By contrast, the areal extent of the crevasse splays did not change in between peak discharge events. Landsat time-series imagery before and after peak floods have also shown that multiple local avulsions are caused by peak floods.

The morphodynamics have been analysed using high-resolution satellite imagery of different periods (2004/2005, 2010/2011), which, in combination with ground-truth validation, enables the visualization of morphological changes of splays and river patterns in time and space (Chapters 3, 4 and 5). Similar to wet regions, vegetation reduces sediment erodibility in dryland areas, but vegetation is sparse and less runoff is available for erosion and transport than in wet regions (Tooth, 2000a). Previous studies have indicated that vegetation can exert a strong influence on dryland river processes, including channel recovery following large floods, invasive exotic species-induced channel narrowing and avulsion as well as in-channel tree growth (Schumm and Lichty, 1963; Burkham, 1972; Graf, 1979 and 1980; Lisle, 1989; Graeme and Dunkerley, 1993; Merritt and Wohl, 2003; Tooth and Nanson, 2000; Tooth et al., 2008). The Río Colorado river system is characterized by sparse vegetation of shrubs and grasses in the upland, a piedmont area transitioning to grass in the upper coastal plain, and no vegetation in most of the coastal plain. Grass in the upper coastal plain is important because grass-covered river banks are relatively stable while non-vegetated river banks are experiencing lateral migration, found to have a maximum rate of 5 m/yr (Chapter 3). High-resolution satellite imagery analysis has demonstrated that erosion exceeds deposition and is accompanied by changes in channel planform, such as meander and channel morphology. Normalized Difference Vegetation Index (NDVI) analysis and field investigation suggest that non-vegetation cover and abundance of desiccation cracks and macropores are mainly contributing to bank erosion. Changes in channel planform are the product of continuous lateral migration and frequent overbank flooding. Shallow channels and poor development of levees in combination with in-channel accretionary benches result in frequent overbank flooding, which leads to a high density of crevasse splays over unconsolidated river banks and accretionary benches. Avulsion and chute channels together with reactivation of partially abandoned meanders and connection of headcuts and crevasse channels produce an anabranching pattern in the study area.

An informal classification scheme for crevasse splays based upon differences recorded over a six year period has been proposed and their distribution and splay development along the lower distal reaches that terminates in a playa lake are discussed (Chapter 4). Crevasse splays have been categorized into three classes based on their development in space and time: New crevasse splays (NCS), changing crevasse splays (CCS) and inactive crevasse splays (ICS). Bi-temporal high-resolution satellite images in combination with field investigations have demonstrated that the dominant factor influencing splay morphodynamics is a downstream reduction in cross-sectional area of the channels. Some crevasse splays are attributed to topographic lows between adjacent crevasse splays and fill in the depression by compensational stacking. These amalgamated crevasse splays are capable of forming a large area of sheet sands, and an estimate of the potential gas-in-place for these sheet sands has demonstrated that they could contain a significant amount of gas.

The sediment dispersal in the Río Colorado river system of the southern Altiplano plateau has been analysed (Chapter 5). The system includes three segments: (1) an alluvial fan; (2) an upper coastal plain segment; and (3) a lower coastal plain segment (Figure 1.2). The two coastal plain segments are divided by a young fault escarpment (Donselaar et al., 2013). It was shown that a great variation exists in longitudinal sediment dispersal, from gravel-mixed sediments in the alluvial fan to gravel and coarse sand in the upper coastal plain and silt/clay dominated sediment in the lower coastal plain. There is a linear decrease downstream in bedload and correspondingly an increase in suspended load deposits. Aeolian dunes form in the distal part of the alluvial fan segment while no dunes develop in the lower coastal plain, probably due to salt cementation of the sediments (Donselaar et al., 2013). However, in the Alice Springs region of central Australia, strong fluvial-aeolian interaction in the lower reaches (floodouts) shows a high proportion of sand being deposited (Tooth, 1999). Another important finding in the Río Colorado river system is that field investigations show a fining-upward succession with gravel-dominated sediments at the bottom, paleosol and gravelly silt in the middle, and clay-dominated sediments at the top of the alluvial fan segment (Chapter 5). The clay deposits at the top of the alluvial succession are probably attributed to dust storms, which transport fine deposits with the prevailing north-western winds. Some headcuts form in the non-vegetated areas, for example, in the lower coastal plain as well as at the boundary between alluvial fan and upper coastal plain. Very active lateral migration in combination with overbank flooding-induced crevassing and headcuts results in an anabranching pattern in the upper coastal plain.

Chapter 6 has documented the use of Landsat imagery in combination with precipitation data and field investigation to analyse playa morphodynamics. Using Landsat surface reflectance in combination with field data analysis, four types of surface materials have been identified in the river terminus: A: a salty surface; B: a silt-rich surface; C: a clay-rich surface; and D: salt. A spectral library has been established for these four types of surface materials. Although the difference in grain size between silt-rich materials and clay-rich materials is small, the reflectance of the latter is lower than that of the former, probably due to an increasing water content and desiccation cracks in response to decreasing grain sizes. The areal extent of the silt-rich surface has a weak correlation with annual precipitation while the salty surface tends to be inversely proportional to the annual precipitation. There is no relationship between the clay-rich surface and annual precipitation. High precipitation-induced avulsions also lead to increased silt-rich surfaces. The silt-rich surface and the clay-rich surface are associated with different sedimentary facies in the river terminus. The silt-rich surface was widely distributed along channels and crevasse splays while the clay-rich surface was found in the floodplain and the channels. Buehler et al. (2011) employed Landsat time series imagery to detect avulsions on the Taquari River in Brazil, and they also tried to use these Landsat data to analyse the depositional environments over time. In analogy, our study established a spectral library between surface materials and surface reflectance, although the differences in grain size between the various surface materials are small. However, both studies suggest that the observed vertical changes with Landsat time series imagery require validation by shallow coring at multiple locations (Buehler et al., 2011; Chapter 6).
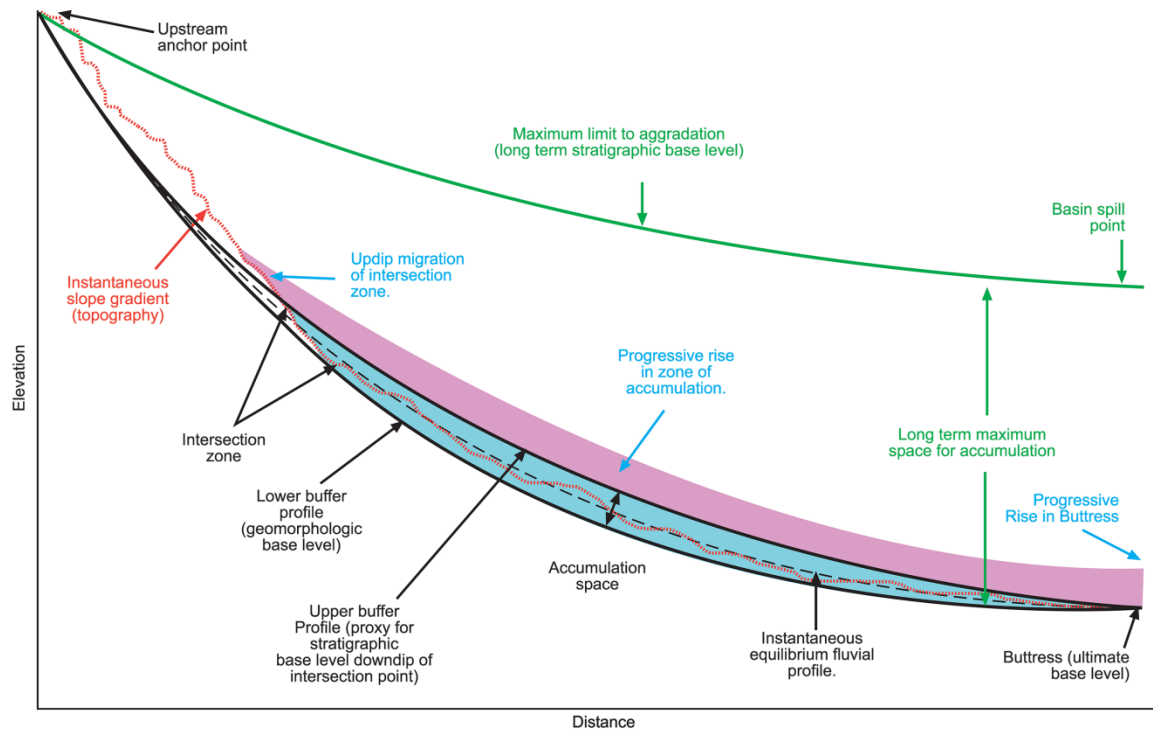
7.2   Sequence stratigraphy

Figure 7.1: *Conceptual framework to illustrate the range of temporal scales at which fluvial systems operate in internally drained basins (From Fisher and Nichols, 2013). At a given point in time, degradation or aggradation along the active river tract reflects the interplay between the instantaneous equilibrium fluvial profile (dashed line) and the elevation of the river bed (dotted line).*

Accommodation and its relationship to base level are essential for analysing sedimentary successions (Payton, 1977; Jervery, 1988). Recently, Holbrook et al. (2006) proposed the 'buffers and buttresses' model, which indicates a zone of sediment preservation defined by upper and lower buffers that show the highest and lowest ratio of transport capacity (Figure 7.1). Although Holbrook et al. (2006) stressed that the divergence of the upper and lower buffers in the upstream sector of the model is not applicable to the hinterland and proximal sectors of fluvial systems, in internally drained basins, they suggested, that the lake level or the lip or edge of a basin through which the trunk river flows out of the basin is the buttress. Previous studies using seismic and GPS surveys in the flat-lying lake terrace sediments indicated that the basin has been tectonically quiescent in the Late Pleistocene and Holocene (Bills et al., 1994, Baucom and Rigsby, 1999; Rigsby et al., 2005). Therefore, for the internally drained Uyuni basin, the buttress is the lowest position on the floodplain surface, where the rivers terminate on the alluvial plain, or lake level, and where they drain into the central lake.

However, a young fault escarpment-induced division of the coastal plain leads to an intermontane basin in the upper coastal plain, which is bordered to the mountains in the upland and small mountains at the fault escarpment. Unlike the overfilled model proposed by Carroll and

118

Bohacs (1999), part of the border caused by the fault escarpment has eroded to form an outlet of the intermontane basin (e.g., Colorado Bridge; Figure 1.2). This outlet connects the catchment area and the river terminus, transporting a low proportion of fine sand and clay- and silt-dominated sediment to the river terminus. Therefore, for the intermontane basin, the outlet is the buttress.

Fisher and Nichols (2013) suggested that time scales should be considered because the vertical limit to accommodation is different at different times in fluvial systems of internally drained basins (Figure 7.1). The dry climate period in the present-day Coipasa-Uyuni internally – drained basin signals a lake level lowstand and therefore results in the progradation of the Río Colorado onto the former lake bottom (Donselaar et al., 2013). The high frequency of avulsion and formation and the development of crevasse splays (Chapters 2 and 4) in the distal reaches of the Río Colorado indicates low accommodation space as well as high rate of aggradation, which further implies a good preservation potential (Bristow et al., 1999).

7.3   Main Conclusions

- Infrequent and high-magnitude floods play an important role in the channel and splay morphodynamics of the Río Colorado river system. The development in space and time of crevasse splays and local avulsions by comparing Landsat MSS and TM images before and after peak discharge events has shown that crevasse splays expanded in peak discharge periods, leading to amalgamation with adjacent crevasse splays by compensational stacking, as well as causing multiple local avulsions. In between peak events, by contrast, the areal extent of the crevasse splays did not change and no avulsions occurred.

- High-resolution satellite imagery analysis has demonstrated that erosion exceeds deposition and is accompanied by changes in channel planforms, such as meander and channel morphology. Normalized Difference Vegetation Index (NDVI) analysis and field investigation suggest that non-vegetation cover and abundance of desiccation cracks and macropores are mainly contributing to bank erosion. Changes in channel planform are the product of continuous lateral migration and frequent overbank flooding. Avulsion and chute channels together with reactivation of partially abandoned meanders and connection of headcuts and crevasse channels produce an anabranching pattern in the study area.

- Crevasse splays have been categorized into three classes based on their development in space and time: New crevasse splays (NCS), changing crevasse splays (CCS) and inactive crevasse splays (ICS). Bi-temporal high-resolution satellite images in combination with field investigations have demonstrated that the dominant factor influencing splay morphodynamics is a downstream reduction in cross-sectional area of the channels. Some crevasse splays are attributed to topographic lows between adjacent crevasse splays and fill in the depression by compensational stacking.

- These amalgamated crevasse splays are capable of forming a large area of sheet sands, and an estimate of the potential gas-in-place for these sheet sands has demonstrated that, in the subsurface and under the right circumstances, they could contain a significant amount of gas. This finding is relevant for petroleum geology as it shows that the studied system is a useful analogue to some low N/G reservoirs in a similar setting, such as the Ten Boer Sandstone in the Southern North Sea.

- The analysis of the sediment dispersal in the Río Colorado river system has shown that a great variation exists in longitudinal sediment dispersal, from gravel-mixed sediments in the alluvial fan to gravel and coarse sand in the upper coastal plain and silt/clay dominated sediment in the lower coastal plain. There is a linear decrease downstream in bedload and correspondingly an increase in suspended load deposits.

- Using Landsat surface reflectance in combination with field data analysis, four types of surface materials have been identified in the river terminus: A salty, a silt-rich and a clay-rich surface as well as salt. A spectral library has been established for these four types of surface materials. The areal extent and the changes through time of these facies were related to the precipitation patterns and the location in the river system.

7.4   Recommendations for future work

- Dryland floodplains may have proxy records of Quaternary hydrological and climatic change and provide modern analogues for improved interpretation of the geological record (Nanson and Tooth, 1999). Therefore, more research is needed for the mechanisms of fluvial discontinuity at the boundary between alluvial fan and upper coastal plain, which is not yet fully understood but which controls the sediment distribution and therefore the potential reservoir quality.

- In the low-gradient dryland region of the Alice Springs area of central Australia, fluvial-aeolian interaction in the floodout zones is common (Tooth, 1999). However, no dunes develop in the lower coastal plain in the Río Colorado system and the dunes only occur in the distal alluvial fan segment and along rivers in the upland. The interaction between aeolian dunes and fluvial systems has not been analysed yet in the Río Colorado river system. In addition, the silt/clay-dominated uppermost of the fining-upward alluvial succession may be the product of wind-blown process; however, also here further research is needed. Furthermore, groundwater regimes in the coastal plain exert an important influence on dust emission (Reynolds et al., 2007), which may be an important future topic for hydrologists.

Appendix A: NCS

Name	Distance (km)	NCS area (m^2)	Name	Distance (km)	NCS area (m^2)
NCS_01	0.808	5930	NCS_43	17.951	18540
NCS_02	3.604	16610	NCS_44	18.241	11480
NCS_03	3.882	45680	NCS_45	18.356	17360
NCS_04	4.272	41270	NCS_46	18.429	23470
NCS_05	4.714	9350	NCS_47	18.558	26060
NCS_06	4.834	4030	NCS_48	18.679	7880
NCS_07	5.465	1690	NCS_49	18.721	4690
NCS_08	5.500	22800	NCS_50	18.96	8250
NCS_09	5.635	197160	NCS_51	17.825	7490
NCS_10	5.864	14810	NCS_52	17.862	10990
NCS_11	6.009	5200	NCS_53	17.996	2540
NCS_12	6.181	6660	NCS_54	18.019	15500
NCS_13	6.428	175280	NCS_55	18.053	1320
NCS_14	6.518	22580	NCS_56	18.158	20360
NCS_15	7.076	18650	NCS_57	16.665	4100
NCS_16	7.076	76790	NCS_58	16.674	4220
NCS_17	7.404	5620	NCS_59	16.735	70140
NCS_18	8.850	14480	NCS_60	16.825	66270
NCS_19	9.005	10960	NCS_61	17.282	20230
NCS_20	9.335	51280	NCS_62	17.491	4820
NCS_21	9.802	15900	NCS_63	17.535	3880
NCS_22	10.009	32550	NCS_64	17.588	6380
NCS_23	10.398	4580	NCS_65	17.641	10120
NCS_24	10.910	52000	NCS_66	17.717	8410
NCS_25	11.100	23350	NCS_67	17.989	45810
NCS_26	11.323	31520	NCS_68	16.483	9070
NCS_27	11.443	20520	NCS_69	16.868	1800
NCS_28	11.842	22510	NCS_70	17.119	1900
NCS_29	12.472	90710	NCS_71	17.163	18150
NCS_30	12.554	18800	NCS_72	17.217	2620
NCS_31	14.729	7830	NCS_73	17.321	4420
NCS_32	15.029	11980	NCS_74	17.447	14600

Name	Distance (km)	NCS area (m^2)	Name	Distance (km)	NCS area (m^2)
NCS_33	15.087	48740	NCS_75	17.517	33020
NCS_34	15.464	543260	NCS_76	17.551	37190
NCS_35	16.048	124840	NCS_77	17.544	19530
NCS_36	16.277	11730	NCS_78	17.339	22470
NCS_37	16.319	12290	NCS_79	19.394	32210
NCS_38	16.435	6430	NCS_80	18.160	45610
NCS_39	17.569	2460	NCS_81	18.200	284900
NCS_40	17.600	5090	NCS_82	18.720	166230
NCS_41	17.629	11600	NCS_83	19.000	33200
NCS_42	17.863	6970			

Appendix B: CCS

Name	Distance (km)	2010/2011_area (m^2)	2004/2005_area (m^2)
CCS_01	1.420	19020	8920
CCS_02	2.310	68500	64050
CCS_03	5.742	3730	2300
CCS_04	5.786	19930	19110
CCS_05	5.822	14220	3750
CCS_06	5.888	6180	10700
CCS_07	5.950	4140	2440
CCS_08	6.235	11070	3290
CCS_09	6.558	5120	4420
CCS_10	6.632	17690	36600
CCS_10-2	6.695	21060	15480
CCS_11	6.976	36340	8970
CCS_12	7.245	6720	17200
CCS_13	7.245	45580	4290
CCS_14	7.322	160620	11540
CCS_15	7.346	5900	11220
CCS_16	7.462	13720	18880
CCS_17	7.743	19950	6310
CCS_18	7.848	901150	680100
CCS_19	8.293	8450	15870
CCS_20	8.371	87470	17950
CCS_21	8.487	109060	188760
CCS_22	8.519	27280	7030
CCS_23	8.610	1093330	100510
CCS_24	8.905	5800	10420
CCS_25	9.035	8260	4140
CCS_26	9.087	11320	22200
CCS_27	9.188	40260	24390
CCS_28	9.241	6910	2170
CCS_29	9.241	21570	11680
CCS_30	9.393	1893940	2345830
CCS_31	9.555	7830	16600

Name	Distance (km)	2010/2011_area (m²)	2004/2005_area (m²)
CCS_32	9.597	20910	10480
CCS_33	9.624	16740	6270
CCS_34	9.707	8770	22980
CCS_35	9.955	222770	38140
CCS_36	10.065	30450	3300
CCS_37	10.176	1570	2410
CCS_38	10.210	5810	5640
CCS_39	10.269	6410	5350
CCS_40	10.305	13860	4820
CCS_41	11.132	21890	7150
CCS_42	11.532	76880	99410
CCS_43	11.668	1426230	230530
CCS_44	11.904	962140	19240
CCS_45	12.322	61780	172430
CCS_46	12.496	13900	10020
CCS_47	12.659	11820	14990
CCS_48	12.877	134780	32170
CCS_49	13.019	38240	14310
CCS_50	13.138	7180	23670
CCS_51	13.224	41500	103110
CCS_52	13.374	14520	14660
CCS_53	14.178	9000	27150
CCS_54	14.288	126270	5800
CCS_55	14.457	18280	81050
CCS_56	14.534	74240	16890
CCS_57	14.597	76420	47240
CCS_58	14.849	12660	9840
CCS_59	15.291	12960	5840
CCS_60	15.515	57180	25550
CCS_61	15.805	66230	121600
CCS_62	15.805	591850	502410
CCS_63	16.108	77800	22900
CCS_64	16.196	14180	26790
CCS_65	16.637	35540	42570
CCS_66	16.799	7370	5460
CCS_67	16.921	79540	34730

Name	Distance (km)	2010/2011_area (m^2)	2004/2005_area (m^2)
CCS_68	16.989	13860	8100
CCS_69	17.085	10940	5510
CCS_70	17.173	8960	9470
CCS_71	17.245	9680	36380
CCS_72	17.306	6450	4650
CCS_73	17.395	32310	6970
CCS_74	17.465	8320	6170
CCS_75	17.457	6750	3290
CCS_76	17.658	34300	33790
CCS_77	16.850	8510	8520
CCS_78	17.006	5590	5900
CCS_79	17.130	117710	11540
CCS_80	16.550	15810	4650
CCS_81	16.623	21610	650
CCS_82	16.677	12410	6590

Appendix C: ICS

Name	Distance (km)	ICS Area (m^2)	Name	Distance (km)	ICS Area (m^2)
ICS_01	0.197	30260	ICS_62	9.923	73760
ICS_02	0.416	25960	ICS_63	9.959	1024310
ICS_03	0.565	3500	ICS_64	10.057	327120
ICS_04	1.030	31580	ICS_65	10.335	4110
ICS_05	1.080	18660	ICS_66	10.370	10510
ICS_06	1.086	4850	ICS_67	10.475	17940
ICS_07	1.153	10320	ICS_68	10.558	77720
ICS_08	1.347	223530	ICS_69	10.572	7960
ICS_09	1.826	275700	ICS_70	10.714	19840
ICS_10	1.921	164640	ICS_71	10.750	7930
ICS_11	2.282	22090	ICS_72	10.827	261390
ICS_12	2.413	4830	ICS_73	10.827	6900
ICS_13	2.446	17940	ICS_74	10.959	91670
ICS_14	2.524	145960	ICS_75	10.959	9660
ICS_15	2.779	57870	ICS_76	11.050	68690
ICS_16	2.897	3290	ICS_77	11.285	41970
ICS_17	3.056	221250	ICS_78	11.487	166790
ICS_18	4.338	11690	ICS_79	11.728	28850
ICS_19	4.414	40520	ICS_80	11.882	61710
ICS_20	5.095	113940	ICS_81	12.186	161220
ICS_21	5.257	49610	ICS_82	12.230	9510
ICS_21-2	5.273	184690	ICS_83	12.610	282350
ICS_22	5.307	9890	ICS_84	12.813	41840
ICS_23	5.533	227060	ICS_85	12.947	46380
ICS_24	5.588	4950	ICS_86	13.097	53930
ICS_25	5.916	1760	ICS_87	13.130	23960
ICS_26	6.104	1087800	ICS_88	13.356	31120
ICS_27	6.199	780310	ICS_89	13.540	7450
ICS_28	6.374	7880	ICS_90	13.627	801310
ICS_29	6.762	46260	ICS_91	13.705	43000
ICS_30	6.866	2610	ICS_92	13.766	63270
ICS_31	6.839	8140	ICS_93	13.787	1065100
ICS_32	6.894	7110	ICS_94	13.994	1529000

Name	Distance (km)	ICS Area (m^2)	Name	Distance (km)	ICS Area (m^2)
ICS_33	6.894	66640	ICS_95	14.076	16090
ICS_34	6.963	4360	ICS_96	14.332	6140
ICS_35	7.105	116530	ICS_97	14.360	7040
ICS_36	7.163	5870	ICS_98	14.406	4950
ICS_37	7.371	175250	ICS_99	14.747	8730
ICS_38	7.442	4360	ICS_100	14.649	31940
ICS_39	7.500	68390	ICS_101	14.785	19270
ICS_40	7.687	3950	ICS_102	14.831	301020
ICS_41	7.949	1529850	ICS_103	14.848	237010
ICS_42	7.971	136850	ICS_104	14.904	2170050
ICS_43	8.024	102910	ICS_105	14.935	13550
ICS_44	8.154	5430	ICS_106	15.225	10170
ICS_45	8.211	6680	ICS_107	15.318	11780
ICS_46	8.184	1840920	ICS_108	15.384	31170
ICS_47	8.300	5370	ICS_109	15.425	2900
ICS_48	8.427	25620	ICS_110	15.599	44850
ICS_49	8.447	68160	ICS_111	15.668	36970
ICS_50	8.537	30090	ICS_112	15.743	60120
ICS_51	8.686	6940	ICS_113	15.969	11910
ICS_52	8.770	34790	ICS_114	16.009	2370
ICS_53	8.843	16260	ICS_115	16.028	11020
ICS_54	8.933	11780	ICS_116	16.152	25680
ICS_55	9.031	404760	ICS_117	17.591	13660
ICS_56	9.163	6310	ICS_118	17.765	60180
ICS_57	9.211	6330	ICS_119	17.856	9660
ICS_58	9.287	37260	ICS_120	17.923	44890
ICS_59	9.406	24790	ICS_121	18.022	8900
ICS_60	9.528	5410	ICS_122	18.146	8380
ICS_61	9.743	31040	ICS_123	16.769	1270

Bibliography

Abernethy, B., Rutherfurd, I.D., 1998. Where along a river's length will vegetation most effectively stabilise stream banks? Geomorphology **23**, 55–75.

Abrams, M., Hook, S., Ramachandran, B., 2002. ASTER user handbook version 2. Jet Propulsion Laboratory/California Institute of Technology (CIT), 135.

Aceituno, P., Montecinos, A., 1993. Circulation anomalies associated with dry and wet periods in the South American Altiplano. Preprints, Fourth Int. Conf. on Southern Hemisphere Meteorology and Oceanography, Hobart, Australia, Amer. Meteor. Soc., pp. 330–331.

Aitchison, J., Greenacre, M., 2002. Biplots of compositional data. Applied Statistics **51**, 375–392.

Allmendinger, R.W., Jordan, T.E., Kay, S.M., Isacks, B.L., 1997. The evolution of the Altiplano-Puna plateau of the central Andes. Annu. Rev. Earth Planet. Sci. **25**, 139–174.

Amthor, J.E., Okkerman, J., 1998. Influence of early diagenesis on reservoir quality of Rotliegende sandstones, Northern Netherlands: American Association of Petroleum Geologists Bulletin 82, 2246–2265.

Anderson, D.S., 2005. Architecture of crevasse splay and point-bar bodies of the nonmarine Iles Formation north of Rangely, Colorado: implications for reservoir description. The Mountain Geologist **42**, 109–122.

Argollo, J., Mourguiart, P., 2000. Late Quaternary climate history of the Bolivian Altiplano. Quaternary International **72**, 37–51.

Ashmore, P.E., 1982. Laboratory modelling of gravel braided stream morphology. Earth Surface Processes and Landforms **7**, 201–225.

Ashworth, P.J., Best, J.L., Jones, M.A., 2007. The relationship between channel avulsion, flow occupancy and aggradation in braided rivers: insights from an experimental model. Sedimentology **54**, 497–513.

Baker, V.R., 1977. Stream-channel response to floods, with examples from central Texas. Bulletin of the Geology Society of America **88**, 1057–1071.

Baker, P.A., Rigsby, C.A., Seltzer, G.O., Fritz, S.C., Lowenstein, T.K., Bacher, N.P., Veliz, C., 2001a. Tropical climate change at millennial and orbital time scales on the Bolivian Altiplano. Nature **409**, 698–701.

Baker, P.A., Seltzer, G.O., Fritz, S.C., Dunbar, R.B., Grove, M.J., Tapia, P.M., Cross, S.L., Rowe, H.D., Broda, J.P., 2001b. The history of South American tropical precipitation for the past 25,000 years. Science **291**, 640–643.

Bartley, R., Keen, R.J., Hawdon, A.A., Hairsine, P.B., Disher, M.G., 2008. Bank erosion and channel width change in a tropical catchment. Earth Surface Processes and Landforms **33**, 2174–2200.

Baucom, P.C., Rigsby, C.A., 1999. Climate and lake-level history of the northern Altiplano, Bolivia, as recorded in Holocene sediments of the Rio Desaguadero. Journal of Sedimentary Research **69**, 597–611.

Bedidi, A., Cervelle, B., Madeira, J., Pouget, M., 1992. Moisture effects on visible spectral characteristics of lateritic soils. Soil Science **153**, 129–141.

Beeson, C.E., Doyle, P.F., 1995. Comparison of bank erosion at vegetated and non-vegetated channel bends. American Water Resources Bulletin **31**, 983–990.

Benvenuti, M., Carnicelli, S., Ferrari, G., Sagri, M., 2005. Depositional processes in latest Pleistocene and Holocene ephemeral streams of the Main Ethiopian Rift (Ethiopia). In: Blum, M.D., Marriott, S.B. & Leclair, S.F. (Eds.), Fluvial Sedimentology VII. Special Publication of the International Association of Sedimentologists no. 35. Blackwell Publishing, pp. 277–294.

Billi, P., 2007. Morphology and sediment dynamics of ephemeral stream terminal distributary systems in the Kobo Basin (northern Welo, Ethiopia). Geomorphology **85**, 98–113.

Bills, B.G., de Silva, S.L., Currey, D.R., Emenger, R.S., Lillquist, K.D., Donnellan, A., Worden, B., 1994. Hydro-isostatic deflection and tectonic tilting in the central Andes: initial results of a GPS survey of Lake Minchin shorelines. Geophysical Research Letters **21**, 293–296.

Bourke, M.C., Pickup, G., 1999. Fluvial form variability in arid central Australia. In: Miller, A.J., Gupta, A. Eds.., Varieties of Fluvial Form. Wiley, Chichester, pp. 249–271.

Brackenridge, G.R., 1988. River flood regime and floodplain stratigraphy. In: Baker, V.R., Kochel, R.C., Patton, P.C. (Eds.), Flood Geomorphology. John Wiley & Sons, New York, pp. 139–156.

Bridge, J.S., 2003. Rivers and Floodplains; Forms, Processes and Sedimentary Record. Blackwell, Oxford, pp. 491.

Bristow, C.S., Skelly, R.L., Ethridge, F.G., 1999. Crevasse splays from the rapidly aggrading, sand-bed, braided Niobrara River, Nebraska: effect of base-level rise. Sedimentology **46**, 1029–1047.

Brown, A.G., 1987. Holocene floodplain sedimentation and channel response of the lower River Severn, United Kingdom. Zeitschrift für Geomorphologie **32**, 293–310.

Bryant, R.G., 1993. The sedimentology and geochemistry of non-marine evaporates on the Chott el Djerid using both ground and remotely sensed data. Unpublished Ph.D thesis: University of Reading, England.

Bryant, R.G., Drake, N.A., Millington, A.C., Sellwood, B.W., 1994. The chemical evolution of the brines of Chott el Dijerid, Southern Tunisia, after an exceptional rainfall event in January 1990. In: Renaut, R.W. and Last, W.M., (Eds.), The Sedimentology and Geochemistry of Modern and Ancient Saline Lakes. SEPM Special Publication 50, Tulsa, pp. 3–12.

Bryant, R.G., 1996. Validated linear mixture modelling of LANDSAT TM data for mapping evaporate minerals on a playa surface. International Journal of Remote Sensing **17**, 315–330.

Bryant, R.G., 1999. Monitoring climatically sensitive playas using AVHRR data. Earth Surface Processes and Landforms **24**, 283–302.

Bryant, R.G., Rainey, M.P., 2002. Investigation of flood inundation on playas within the Zone of Chotts, using a time-series of AVHRR. Remote Sensing of Environment **82**, 360–375.

Bull, W.B., 1997. Discontinuous ephemeral streams. Geomorphology **19**, 227–276.

Burkham, D.E., 1972. Channel changes of the Gila River in Safford Valley, Arizona 1846-1970. United States Geological Survey Professional Paper, 655-G.

Cahoon, D.R., White, D.A., Lynch, J.C., 2011. Sediment infilling and wetland formation dynamics in an active crevasse splay of the Mississippi River delta. Geomorphology **131**, 57–68.

Cain, S.A., Mountney, N.P., 2009. Spatial and temporal evolution of a terminal fluvial fan system: the Permian Organ Rock Formation, South-east Utah, USA. Sedimentology **56**, 1774–1800.

Campbell, J.B., 2007. Introduction to remote sensing. 4th Edition. The Guilford Press, New York, pp. 164–181.

Canty, M.J., Nielsen, A.A., Schmidt, M., 2004. Automatic radiometric normalization of multitemporal satellite imagery. Remote Sensing of Environment **91**, 441–451.

Canty, M.J., Nielsen, A.A., 2008. Automatic radiometric normalization of multitemporal satellite imagery with the iteratively re-weighted MAD transformation. Remote Sensing of Environment **112**, 1025–1036.

Carroll, A.R., Bohacs, K.M., 1999. Stratigraphic classification of ancient lakes: balancing tectonic and climatic controls. Geology **27**, 99–102.

Castañeda, C., Herrero, J., Casterad, M.A., 2005. Landsat monitoring of playa-lakes in the Spanish Monegros desert. Journal of Arid Environments **63**, 497–516.

Chapman, J.E., Rothery, D.A., Francis, P.W., Pontual, A., 1989. Remote sensing of evaporate mineral zonation in salt flats (salars). International Journal of Remote Sensing **10**, 245–255.

Couper, P., Maddock, I., 2001. Subaerial river bank erosion processes and their interaction with other bank erosion mechanisms on the River Arrow, Warwickshire, UK. Earth Surface Processes and Landforms **26**, 631–646.

Couper, P., Stott, T., Maddock, I.. 2002. Insights into river bank erosion processes derived from analysis of negative erosion-pin recordings: observations from three recent UK studies. Earth Surface Processes and Landforms **27**, 59–79.

Davidson, S.K., Leleu, S., North, C., 2011. From river to rock record: the preservation of fluvial sediments and their subsequent interpretation. In: North, C.P. (Eds.), From Rivers to Rock. Geological Society of London Special Publication **97**, 3-5.

Davles, D.K., Williams, B.P.J., Vessell, R.K., 1993. Reservoir Geometry and Internal Permeability Distribution in Fluvial, Tight, Gas Sandstones, Travis Peak Formation, Texas. SPE Reservoir Engineering, 7–12.

Dewey, J.F., Bird, J.M., 1970. Mountain belts and the new global tectonics. Journal of Geophysical Research **75**, 2625–2647.

Doležal, F., Kutílek, M., 1972. Flow of water in swelling soils. Proc., 2nd Symp. Fundamentals of Transport Phenomena in Porous Media, IAHR-ISSS **1**: 292–305.

Donselaar, M.E., Overeem, I., Reichwein, J.H.C., Visser, C.A., 2009. Integrated modeling of the Ten Boer Claystone Member, SPB: a combined log correlation, outcrop analogue and numerical forward modeling study. Abstract Conference on Sediment Body Geometry and Heterogeneity: Analogue Studies for Modelling the Subsurface, 21–23 October 2009, The Geological Society of London, Burlington House, Piccadilly, London, pp. 34.

Donselaar, M.E., Overeem, I., Reichwein, J.H.C., Visser, C.A., 2011. Mapping of fluvial fairways in the Ten Boer Member, southern Permian Basin. In: Grotsch, J., Gaupp, R. (Eds.), The Permian Rotliegend in the Netherlands: SEPM Special Publication **98**, 105–118.

Donselaar, M.E., Cuevas Gozalo, M.C., Moyano, S., 2013. Avulsion processes at the terminus of low-gradient semi-arid fluvial systems: Lessons from the Río Colorado, Altiplano endorheic basin, Bolivia. Sedimentary Geology **283**, 1–14.

Drake, N.A., Bryant, R.G., Millington, A.C., Townshend, J.R.G., 1994. Playa sedimentology and geomorphology: mixture modelling applied to Landsat Thematic Mapper data of Chott el Djerid, Tunisia. In The Sedimentology and Geochemistry of Modern and Ancient Saline Lakes. Edited by Renaut, R.W. and Last, W.M., SEPM Special Publication 50, Tulsa, pp. 32–42.

Drake, N.A., 1995. Reflectance spectra of evaporite minerals (400–2500 nm): applications for remote sensing. International Journal of Remote Sensing **16**, 2555–2571.

Du, Y., Teillet, P.M., Cihlar, J., 2002. Radiometric normalization of multitemporal high-resolution satellite images with quality control for land cover change detection. Remote sensing of Environment **82**, 123–134.

Elger, K., Oncken, O., Glodny, J., 2005. Plateau-style accumulation of deformation: Southern Altiplano. Tectonics **24**, TC4020. http://dx.doi.org/10.1029/2004TC001675.

El-Hames, A.S., 2012. An empirical method for peak discharge prediction in ungauged arid and semi-arid region catchments based on morphological parameters and SCS curve number. Journal of Hydrology **456**, 94–100.

Elliott, T., 1974. Interdistributary bay sequences and their genesis. Sedimentology **21**, 611–622.

Eker, S., van Daalen, E., 2012. Investigating the effects of uncertainties associated with the unconventional gas development in the Netherlands. Third International Engineering Systems Symposium CESUN 2012, Delft University of Technology, 18-20 June 2012.

Evans, F., 1998. An investigation into the use of maximum likelihood classifiers, decision trees, neural networks and conditional probabilistic networks for mapping and predicting salinity. MSc thesis, School of Computer Science, Curtin University of Technology, Perth, Western Australia.

Faill, R.T., 1973. Tectonic development of the Triassic Newark-Gettysburg Basin in Pennsylvania. Geological Society of America Bulletin **84**, 725–740.

Ferguson, R.I., Werritty, A., 1983. Bar development and channel change in the gravelly River Feshie, Scotland. In Modern and Ancient Fluvial Systems, Collinson DJ, Lewin J (Eds). International Association of Sedimentologists Special Publication **6**, 181–193.

Fielding, C.R., 1984. Upper delta plain lacustrine and fluviolacustrine facies from the Westphalian of the Durham coalfield, NE England. Sedimentology **31**, 547–567.

Fisher, J.A., Nichols, G.J., 2013. Interpreting the stratigraphic architecture of fluvial systems in internally drained basins. Journal of the Geological Society, London **170**, 57–65.

Friend, P.F., 1978. Distinctive features of some ancient river systems. In: Miall, A.D. (Eds.), Fluvial Sedimentology. Mem. Can. Soc. Pet. Geol. **5**, 543–576.

Friend, P.F., Williams, B.P.J., Williams, E.A., 2000. Kinematics and dynamics of Old Red Sandstone basins. In: Friend, P.F., Williams, B.P.J. (Eds), New Perspectives on the Old Red Sandstone. Geological Society, London, Special Publications **180**, 29–60.

Fritz, S.C., Baker, P.A., Lowenstein, T.K., Seltzer, G.O., Rigsby, C.A., Dwyer, G.S., Tapia, P.M., Arnold, K.K., Ku, T.-L., Luo, S., 2004. Hydrologic variation during the last 170,000 years in the southern hemisphere tropics of South America. Quat. Res. **61**, 95–104.

Fornari, M., Risacher, F., Feraud, G., 2001. Dating paleolakes in the central Altiplano of Bolivia. Palaeogeogr. Palaeoclimatol. Palaeoecol. **172**, 269–282.

Gansser, A., 1973. Facts and theories on the Andes. Journal of the Geological Society **129**, 93–131.

García-Castellanos, D., Vergés, J., Gaspar-Escribano, J., Cloetingh, S., 2003. Interplay between tectonics, climate, and fluvial transport during the Cenozoic evolution of the Ebro Basin (NE Iberia). Journal of Geophysical Research **108** (B7), 2347.

Garreaud, R.D., Vuille, M., Compagnucci, R., Marengo, J., 2009. Present-day South American climate. Palaeogeogr. Palaeoclimatol. Palaeoecol. **281**, 180–195.

Gebhardt, U., Schneider, J.W., Hoffmann, N., 1991. Modelle zur Stratigraphie und Beckenentwicklung im Rotliegend der Norddeutschen Senke: Geologisches Jahrbuch A127, 405–427.

Geluk, M.C., 2005. Stratigraphy and tectonics of Permo-Triassic basins in the Netherlands and surrounding areas: Unpublished Ph.D. thesis, University of Utrecht, 171 p.

Glennie, K.W., Provan, D.M.J., 1990. Lower Permian Rotliegend reservoir of the Southern North Sea gas province. In: Brooks, J. (Eds.), Classic Petroleum Provinces: Geological Society of London, Special Publication 50, 399–416.

Glennie, K.W., 1997a. Recent advances in understanding the southern North Sea Basin: a summary. In: Ziegler, K., Turner, P., Daines, S.R. (Eds.), Petroleum Geology of the Southern North Sea: Future Potential: Geological Society of London, Special Publication 123, 17–29.

Glennie, K.W., 1997b. Quaternary Arabia: is it a palaeogeographic and climatic analogue of NW Europe's Permian Upper Rotliegend 2?: Journal of Petroleum Geology 20, 100–104.

Glennie, K.W., 1998. Lower Permian—Rotliegend. In: Glennie, K.W. (Eds.), Petroleum Geology of the North Sea, Fourth Edition: Oxford, U.K., Blackwell Science, pp. 137–174.

Glennie, K.W., 2005. The Desert of Southeast Arabia: Bahrain, Gulf PetroLink, 215 p.

Glorioso, J.C., Rattia, A., 2012. Unconventional reservoirs: basic petrophysical concepts for shale gas. SPE Paper 153004, Society of Petroleum Engineers, Richardson, Texas.

Gibling, M.R., Nanson, G.C., Maroulis, J.C., 1998. Anastomosing river sedimentation in the Channel Country of central Australia. Sedimentology **45**, 595–619.

Grenfell, M., Aalto, R., Nichols, A., 2012. Chute channel dynamics in large, sand-bed meandering rivers. Earth Surface Processes and Landforms **37**, 315–331.

Grosjean, M., 1994. Paleohydrology of the Laguna Lejia (north Chilean Altiplano) and climactic implications for late-glacial times. Palaeogeography, Palaeoclimatology, Palaeocology **109**, 89–100.

Graeme, D., Dunkerley, D.L., 1993. Hydraulic resistance by the river red gum, Eucalyptus camaldulensis, in ephemeral desert streams. Australian Geographical Studies **31**, 141–154.

Graf, W.L., 1983. Flood-related channel change in an arid-region river. Earth Surface Processes and Landforms **8**, 125–139.

Graf, W.L., 1988a. Fluvial processes in dryland rivers. Springer-Verlag, Berlin.

Graf, W.L., 1988b. Definition of flood plains along arid-region rivers. In: Baker, V.R., Kochel, R.C., Patton, P.C. (Eds.), Flood Geomorphology. Wiley, New York, pp. 231–242.

Hagoort, J., 1998. Fundamental of Gas Reservoir Engineering. New York: Elsevier Science Publishers. pp. 35-42.

Hampton, B.A., Horton, B.K., 2007. Sheetflow fluvial processes in a rapidly subsiding basin, Altiplano plateau, Bolivia. Sedimentology **54**, 1121–1147.

Hardie, L.A., Smoot, J.P., Eugster, H.P., 1978. Saline lakes and their deposits: a sedimentological approach. In Modern and Ancient Lake Sediments. Edited by Mater, A., and Tucker, M.E., Special Publication 2, Tulsa, International Association of Sedimentologists. pp. 7–41.

Hilhorst, M.A., Dirksen, C., Kampers, F.W.H., Feddes, R.A., 2001. Dielectric relaxation of bound water versus soil matric pressure. Soil Science Society of America Journal **65**, 311–314.

Hinds, D.J., Aliyeva, E., Allen, M.B., Davies, C.E., Kroonenberg, S.B., Simmons, M.D., Vincent, S.J., 2004. Sedimentation in a discharge dominated fluvial/lacustrine system: the Neogene Productive Series of the South Caspian Basin, Azerbaijan. Mar. Petrol. Geol. **21**, 613–638.

Hirst, J.P.P., Nichols, G.J., 1986. Thrust tectonic controls on alluvial sedimentation patterns, southern Pyrenees. In: Allen, P.A., Homewood, P. (Eds.), Foreland Basins, International Association of Sedimentologists Special Publication **8**, 153–164.

Holbrook, J., Scott, R.W., Oboh-Ikuenobe, F.E. 2006. Base-level buffers and buttresses: a model for upstream versus downstream control on fluvial geometry and architecture within sequences. Journal of Sedimentary Research **76**, 162–174.

Hooke, J.M., 1980. Magnitude and distribution of rates of river bank erosion. Earth Surface Processes and Landforms **5**, 143–157.

Hooke, J.M., 2007a. Complexity, self-organisation and variation in behavior in meandering rivers. Geomorphology **91**, 236–258.

Hooke, J.M., 2007b. Spatial variability, mechanisms and propagation of change in an active meandering river. Geomorphology **84**, 277–296.

Horton, B.K., 1999. Erosional control on the geometry and kinematics of thrust belt development in the central Andes. Tectonics **18**, 1292–1304.

Horton, B.K., DeCelles, P.G., 2001. Modern and ancient fluvial megafans in the foreland basin system of the central Andes, southern Bolivia: implications for drainage network evolution in fold-thrust belts. Basin Research **13**, 43–63.

Horton, B.K., Hampton, B.A., Waanders, G.L., 2001. Paleogene synorogenic sedimentation in the Altiplano plateau and implications for initial mountain building in the central Andes. Geological Society of America Bulletin **113**, 1387–1400.

Hovius, N., Stark, C.P., Chu, H. Lin, J., 2000. Supply and removal of sediment in a landslide-dominated mountain belt: central range, Taiwan. – The Journal of Geology **108**, 73–89.

Howard, A.D., 1996. Modelling channel evolution and floodplain morphology. In Floodplain processes, Anderson MG, Walling DE, Bates PH (Eds). John Wiley, Hoboken, NJ, 15–62.

Isacks, B.L., 1988. Uplift of the central Andean plateau and bending of the Bolivian orocline. Journal of Geophysical research **93**, 3211–3231.

Jiménez-Muñoz, J.C., Sobrino, J.A., Gillespie, A., Sabol, D., Gustafson, W.T., 2006. Improved land surface emissivities over agricultural areas using ASTER NDVI. Remote Sensing of Environment **103**, 474–487.

Jacobshagen, V., Müller, J., Wemmer, K., Ahrendt, H., Manutsoglu, E., 2002. Hercynian deformation and metamorphism in the Cordillera Oriental of Southern Bolivia, Central Andes. Tectonophysics **345**, 119–130.

Johnston, R., Kamprad, J., 1989. Application of Landsat Thematic Mapper to geology and salinity in the Murray Basin. BMR Journal of Australian Geology and Geophysics **11**, 363–366.

Jorgenson, P.J., Fielding, C.R., 1996. Facies architecture of alluvial floodplain deposits: three-dimensional data from the Upper Triassic Callide Coal measures of East-central Queensland, Australia. Sedimentology **43**, 479–495.

Jordan, T.E., Reynolds, J.H., Erikson, J.P., 1997. Variability in age of initial shortening and uplift in the central Andes, 16 -33.30'S, In: Ruddiman, W.F., Tectonic uplift and climate change, New York, Plenum Press, pp. 41–61.

Kääb, A., 2002. Monitoring high-mountain terrain deformation from repeated air- and spaceborne optical data: examples using digital aerial imagery and ASTER data. ISPRS Journal for Photogrammetry and Remote Sensing **57**, 39–52.

Kelly, S.B., Olsen, H., 1993. Terminal fans—a review with reference to Devonian examples: Sedimentary Geology **85**, 339–374.

Kerr, D.R., 1990. Reservoir heterogeneity in the middle Frio formation: case studies in Stratton and Agua Dulce fields, Nueces County, Texas, Trans. Gulf Coast Assoc. Geol. Soc. **40**, 363–372.

Khlaifat, A., Qutob, H., Barakat, N., 2011. Tight gas sands development is critical to future world energy resources. SPE International. SPE 142049.

Knighton, A.D., Nanson, G.C., 1993. Anastomosis and the continuum of channel pattern. Earth Surface Processes and Landforms **18**, 613–625.

Knighton, D., Nanson, G., 1997. Distinctiveness, diversity and uniqueness in arid zone river systems. In: Thomas, D.S.G. (Eds.), Arid Zone Geomorphology: Process, Form and Change in Dryland, 2nd ed. John Wiley and Sons Ltd, West Sussex, UK, pp. 185–203.

Konert, M., Vandenberghe, J., 1997. Comparison of laser grain size analysis with pipette and sieve analysis: a solution for the underestimation of the clay fraction. Sedimentology **44**, 523–535.

Kotwicki, V., Allan, R., 1998. La Niña de Australia—contemporary and palaeo-hydrology of Lake Eyre. Palaeogeography, Palaeoclimatology, Palaeoecology **144**, 265–280.

Laronne, J.B., Reid, I., 1993. Very high rates of bedload sediment transport by ephemeral desert rivers. Nature **366**, 148–150.

Lawler, D.M., 1993. The measurement of river bank erosion and lateral channel change: a review. Earth Surface Processes and Landforms **18**, 777–821.

Leddy, J.O., Ashworth, P.J., Best, J.L., 1993. Mechanisms of anabranch avulsion within gravel-bed braided rivers: observations from a scaled physical model. In Braided Rivers, Best JL, Bristow CS (Eds). Geological Society Special Publication No. 75. The Geological Society: London, pp. 119–127.

Leeder, M.R., 1978. A quantitative stratigraphic model for alluvium with special reference to channel deposit density and interconnectedness. In: Maill, A.D. (Eds.), Fluvial Sedimentology 5, pp. 587–596.

Lenters, J.D., Cook, K.H., 1997. On the origin of the Bolivian High and related circulation features of the South American climate. J. Atmos. Sci. **54**, 656–677.

Lenters, J.D., Cook, K.H., 1999. Summertime precipitation variability over South America: role of the Large-Scale circulation. Monthly Weather Review **127**, 409–431.

Leopold, L.B., Miller, J.P., 1956. Ephemeral streams – hydraulic factors and their relation to the drainage net, United States Geological Survey Professional Paper 282A.

Li, J., Donselaar, M.E., Hosseini Aria, S.E., Koenders, R., Oyen, A.M., 2014. Landsat imagery-based visualization of the geomorphological development at the terminus of a dryland river system. Quaternary International. DOI: 10.1016/j.quaint.2014.06.041.

Lisle, T.E., 1989. Channel-dynamic control on the establishment of riparian trees after large floods in Northwestern California. Proceedings of the California Riparian Systems Conference, 22-24 September 1988. USDA Forest Service General Technical Report PSW-110. Davis, California, pp. 8–13.

Lundberg, J.G., Marshall, L.G., Guerrero, J., Horton, B., Malabarba, M.C.S.L., Wesselingh, F., 1998. The stage for Neotropical fish diversification: a history of tropical South American rivers.

In: Malabarba, L., Reis, R., Vari, R., Lucena, Z., Lucena, C. (Eds), Phylogeny and classification of Neotropical fishes. Editora Universitária da PUCRS, Porto Alegre, Brazil. pp. 13–48.

Makaske, B., 1998. Anastomosing Rivers Forms, Processes and Sediments. Nederlandse Geografische Studies 249. Koninklijk Nederlands Aardrijkskundig Genootschap/Faculteit Ruimtelijke Wetenschappen, Universiteit Utrecht, Utrecht, The Netherlands.

Makaske, B., 2001. Anastomosing rivers: a review of their classification, origin and sedimentary products. Earth-Science Reviews **53**, 149–196.

Makaske, B., Berendsen, H.J.A., Van Ree, M.H.M., 2007. Middle Holocene avulsion-belt deposits in the central Rhine-Meuse delta, the Netherlands. Journal of Sedimentary Research **77**, 110–123.

Makaske, B., Smith, D.G., Berendson, H.J.A., de Boer, A.G., Nielen-Kiezebrink, M.F., Locking, T., 2009. Hydraulic and sedimentary processes causing anastomosing morphology of the upper Columbia River, British Columbia, Canada. Geomorphology **111**, 194–205.

Marek, M.A., 2011. Hydraulic Design Mannual, Texas Department of Transportation (TxDOT). Design Division (DES), Texas, USA.

Marren, P.M., McCarthy, T.S., Tooth, S., Brandt, D., Stacey, G.G., Leong, A., Spottiswoode, B., 2006. A comparison of mud- and sand-dominated meanders in a downstream coarsening reach of the mixed bedrock-alluvial Klip River, eastern Free State, South Africa. Sedimentary Geology **190**, 213–226.

Marshall, L.G., Swisher, C.C., III, Lavenu, A., Hoffstetter, R., Curtis, G.H., 1992. Geochronology of the mammal-bearing late Cenozoic on the northern Altiplano, Bolivia. Journal of South American Earth Sciences **5**, 1–19.

Menenti, M., Lorkeers, A., Vissers, M., 1986. An application of thematic mapper data in Tunesia. ITC Journal **1**, 35–42.

Menenti, M., Bastiaanssen, W. G. M., Van Eick, D., 1989. Determination of hemispheric reflectance with Thematic Mapper data, Remote Sensing of Environment **28**, 327– 337.

Merritt, D.M.,Wohl, E.E., 2003. Downstream hydraulic geometry and channel adjustment during a flood along an ephemeral, arid-region drainage. Geomorphology **52**, 165–180.

McCann, T., Kiersnowski, H., Krainer, K., Vozarova, A., Peryt, T.M., Oplustil, S., Stollhofen, H., Schnerder, J., Wetzel, A., Boulvain, F., Dusar, M., Török, A., Haas, J., Tait, J., Körner, F., 2008. Permian. In: McCann, T. (Eds.), The Geology of Central Europe. Volume 1: Precambrian and Palaeozoic: Geological Society of London, pp. 531–597.

McCarthy, T.S., Ellery, W.N., Bloem, A., 1998. Some observations on the geomorphological impact of hippopotamus (Hippopotamus amphibious L.) in the Okavango Delta, Botswana. African Journal of Ecology **36**, 44–56.

McCarthy, T.S., Ellery, W.N., Stanistreet, I.G., 1992. Avulsion mechanisms on the Okavango fan, Botswana: the control of a fluvial system by vegetation. Sedimentology **39**, 779–795.

McDermott, G.E., Pilgrim, D.H., 1983. A design flood method for arid western New South Wales based on bankfull estimates. Civil Engineering Transactions, Institution of Engineers, Australia CE25, 114–120.

McKie, T., 2011. A comparison of modern dryland depositional systems with the Rotliegend Group in the Netherlands. In: Grotsch, J., Gaupp, R. (Eds.), The Permian Rotliegend in the Netherlands. SEPM Special Publication **98**, 89–103.

METI, NASA, USGS. 2009. ASTER Global Digital Elevation Model Version 2 – Summary of Validation Results.

Miall, A.D., 1996. The Geology of Fluvial Deposits, Sedimentary Facies, Basin Analysis, and Petroleum Geology. Spring-Verlag, Berlin, pp. 582.

Micheli, E.R., Kirchner, J.W., Larsen, E.W., 2004. Quantifying the effect of riparian forest versus agricultural vegetation on river meander migration rates, central Sacramento River, California, USA. River Research and Applications **20**, 537–548.

Micheli, E.R., Larsen EW. 2010. River cutoff dynamics, Sacramento River, California, USA. River Research and Applications. DOI: 10.1002/rra.1360.

Millar, R., 2000. Influence of bank vegetation on alluvial channel patterns. Water Resources Research **36**, 1109–1118.

Millington, A.C., Drake, N.A., Townshend, J.R.G., Quarmby, N.A., Settle, J.J., Reading, A.J., 1989. Monitoring salt playa dynamics using Thematic Mapper data. IEEE Transactions on Geoscience and Remote Sensing **27**, 754–761.

Mjøs, R., Walderhaug, O., Prestholm, E., 1993. Crevasse splay sandstone geometries in the Middle Jurassic Ravenscar Group of Yorkshire, UK. In: Marzo, M., Puigdefabregas, C. (Eds.), Alluvial Sedimentation. Spec. Publ. Int. Assoc. Sedimentology **17**, 167–184.

Murray, B.P., Horton, B.K., Matos, R., Heizler, M.T., 2010. Oligocene-Miocene basin evolution in the northern Altiplano, Bolivia: implications for evolution of the central Andean backthrust belt and high plateau. Geological Society of America Bulletin **122**, 1443–1462.

Nagtegaal, P.J.C., 1979. Relationship of facies and reservoir quality in Rotliegendes desert sandstones, southern North Sea region: Journal of Petroleum Geology 2, 145–158.

Naik, G.C., 2010. Tight gas reservoirs – An unconventional natural energy source for the future. http://www.pinedaleonline.com/socioeconomic/pdfs/tight_gas.pdf.

Nanson, G.C., Croke, J.C., 1992. A genetic classification of floodplains. Geomorphology **4**, 459–486.

Nanson, G.C., Hickin, E.J., 1986. A statistical analysis of bank erosion and channel migration in western Canada. Geological Society of America Bulletin **97**, 497–504.

Nanson, G.C., Knighton, A.D., 1996. Anabranching rivers: their cause, character and classification. Earth Surface Processes and Landforms **21**, 217–239.

Nanson, G.C., Tooth, S., 1999. Arid-zone rivers as indicators of climate change. In: Singhvi, A.K., Derbyshire, E. (Eds.), Palaeoenvironmental Reconstruction in Arid Lands. Balkema, Rotterdam, pp. 175–216.

Nielsen, A.A., 2007. The regularized iteratively reweighted MAD method for change detection in multi- and hyperspectral data. IEEE Transactions on Image Processing **16**, 463–478.

Nichols, G.J., 2004. Sedimentation and base-level in an endorheic basin: The early Miocene of the Ebro Basin, Spain. Boletin Geológicoy Minero **115**, 427–438.

Nichols, G.J., 2007. Features of fluvial systems in desiccating endorheic basins. In: Nichols, G.J., Williams, E.A., Paola, C. (Eds.), Sedimentary Processes. Environments and Basins. A Tribute to Peter Friend. International Association of Sedimentologists, Special Publications **38**, 567–587.

Nichols, G.J., Fisher, J.A., 2007. Processes, facies and architecture of fluvial distributary system deposits. Sedimentary Geology **195**, 75–90.

Noborio, K., 2001. Measurement of soil water content and electrical conductivity by time domain reflectometry: a review. Computers and Electronics in Agriculture **31**, 213–237.

North, C.P., Warwick, G.L., 2007. Fluvial fans: myths, misconceptions, and the end of the terminal-fan model. Journal of Sedimentary Research **77**, 693–701.

North, C.P., Nanson, G.C., Fagan, S.D., 2007. Recognition of the sedimentary architecture of dryland anabranching (anastomosing) rivers. Journal of Sedimentary Research **77**, 925–938.

Page, K.J., Nanson, G.C., Frazier, P.S., 2003. Floodplain formation and sediment stratigraphy resulting from oblique accretion on the Murrumbidgee River, Australia. Journal of Sedimentary Research **73**, 5–14.

Payton, C.E., 1977. Seismic stratigraphy: applications to hydrocarbon exploration. American Association of Petroleum Geologists Memoirs 26.

Pelletier, J.D., DeLong, S., 2004. Oscillations in arid alluvial-channel geometry. Geology **32**, 713–716.

Petropoulos, G.P., Vadrevu, K.P., Xanthopoulos, G., Karantounias, G., Scholze, M., 2010. A comparison of spectral angle mapper and artificial neural network classifiers combined with Landsat TM imagery analysis for obtaining burnt area mapping. Sensors **10**, 1967–1985.

Phillips, J.D., 2011. Universal and local controls of avulsions in southeast Texas River. Geomorphology **130**, 17–28.

Pickup, G., 1985. The erosion cell - a geomorphic approach to landscape classification in range assessment. Australian Rangeland Journal **7**, 114–121.

Placzek, C., Quade, J., Patchett, P.J., 2006. Geochronology and stratigraphy of late Pleistocene lake cycles on the southern Bolivian Altiplano: implications for causes of tropical climate change. Geol. Soc. Am. Bull. **118**, 515–532.

Placzek, C.J., Quade, J., Patchett, P.J., 2013. A 130 ka reconstruction of rainfall on the Bolivian Altiplano. Earth and Planetary Science Letters **363**, 97-108.

Poesen, J., Vandekerckhove, L., Nachtergaele, J., Oostwoud Wijdenes, D., Verstraeten, G., van Wesemael, B., 2002. Gully erosion in dryland environments. In Bull, L.J., Kirkby, M.J. (Eds.). Dryland Rivers. Wiley, Chichester, UK, pp. 229–262.

Quarmby, N.A., Townshend, J.R.G., Millington, A.C., White, K.H. Reading, A.J., 1989. Monitoring sediment transport systems in a semi-arid area using Thematic Mapper data. Remote Sensing of Environment **28**, 305–315.

Reid, I., 2002. Sediment dynamics of ephemeral channels. In: Bull, L.J., Kirkby, M.J. (Eds.), Dryland Rivers: Hydrology, and Geomorphology of Semi-arid Channels. Wiley, Chichester, pp. 107–128;

Reid, I., Frostick, L.E., 1986. Slope process, sediment derivation and landform evolution in a rift valley basin, northern Kenya, in Sedimentation in the African Rifts. Geological Society of London Special Publication **25**, Blackwell, Oxford, pp. 99–111.

Reid, I., Laronne, J.B., 1995. Bed load sediment transport in an ephemeral stream and a comparison with seasonal and perennial counterparts. Water Resources Research **31**, 773–781.

Renard, K.G., Keppel, R.V., 1966. Hydrographs of ephemeral streams in the Southwest. Proceedings of the American Society of Civil Engineers, Journal of Hydraulics Division **92**, 33–52.

Reynolds, R.L., Yount, J.C., Reheis, M., Goldstein, H., Chavez, P., Fulton, R., Whitney, J., Fuller, C., Forester, R.M., 2007. Dust emission from wet and dry playas in the Mohave Desert, USA. Earth Surf. Proc. Landf. **32**, 1811–1827.

Rigsby, C.A., Bradbury, J.P., Baker, P.A., Rollins, S.M., Warren, M.R., 2005. Late Quaternary palaeolakes, rivers, and wetlands on the Bolivian Altiplano and their palaeoclimatic implications. Journal of Quaternary Science **20**, 671–691.

Risacher, F., Fritz, B., 2009. Origin of salts and brine evolution of Bolivian and Chilean salars. Aquatic Geochemistry **15**, 123–157.

Roscher, M., Schneider, J.W., 2006. Permo-Carboniferous climate: Early Pennsylvanian to Late Permian climate development of central Europe in a regional and global context. In: Lucas, S.G., Cassinis, G., Schneider, J.W. (Eds.), Non-Marine Permian Biostratigraphy and Biochronology: Geological Society of London, Special Publication 265, 95–136.Rodier, J.A., 1985. Aspects of arid zone hydrology. In: Rodda, J.C. (Eds.), Facets of Hydrology Volume II. Wiley, Chichester, pp. 205–247.

Roscher, M., Berner, U., Schneider, J.W., 2008. Climate modeling—a tool for the assessment of the paleodistribution of source and reservoir rocks: Deutsche Wissenschaftliche Gesellschaft für Erdöl, Erdgas und Kohle e.V. (DGMK) (DGMK German Society for Petroleum and Coal Science and Technology): Meeting Report no. 2008-1, pp. 329–339.

Rosen, M.R., 1991. Sedimentologic and geochemical constraints on the evolution of Bristol Dry Lake Basin, California, U.S.A. Palaeogeography, Palaeoclimatoogy, Palaeoecology **84**, 229–257.

Rutherfurd, I.D., 1994. Inherited controls on the form of a large, low energy river: the Murray River, Australia. In: Schumm, S.A., Winkley, B.R. (Eds.), The Variability of Large Alluvial Rivers. American Society of Civil Engineers, New York, pp. 177–197.

Sáez, A., Anadón, P., Herrero, M.J., Moscariello, A., 2007. Variable style of transition between Palaeogene fluvial fan and lacustrine systems, southern Pyrenean foreland, NE Spain. Sedimentology **54**, 367–390.

Schumann, R.R., 1989. Morphology of Red Creek, Wyoming, an arid-region anastomosing channel system. Earth Surface Processes and Landforms **14**, 277–288.

Schumm, S.A., 1968. Speculations concerning paleohydraulic controls on terrestrial sedimentation. Geological Society of America Bulletin **79**, 1573–1588.

Schumm, S.A., 1985. Patterns of alluvial rivers. Annual Review of Earth and Planetary Sciences **13**, 5–27.

Schumm, S.A., Lichty, R.W., 1963. Channel widening and floodplain construction along Cimarron River in southwestern Kansas. United States Geological Survey Professional Paper **352-D**, 71–88.

Searcy, J.K., Hardisoni, C.H., Langbein, W.B., 1960. Double mass curves. Geological Survey Water Supply Paper 1541-B, US Geological Survey, Washington, D.C., pp. 31–66.

Seluchi, M.E., Saulo, C., Nicolini, M., Satyamurty, P., 2003. The northwestern Argentinean Low: a study of two typical events. Mon. Weather Rev. **131**, 2361–2378.

Sharma, K.D., Murthy, J.S.R., 1994. Modelling sediment transport in stream channels in the arid zone of India. Hydrological Processes **8**, 567–572.

Smith, N.D., Perez-Arlucea, M., 1994. Fine-grained splay deposition in the avulsion belt of the lower Saskatchewan River, Canada. Journal of Sedimentary Research **B64**, 159–168.

Slingerland, R., Smith, N.D., 1998. Necessary conditions for a meandering-river avulsion. Geology **26**, 435–438.

Slingerland, R., Smith, N.D., 2004. River avulsions and their deposits. Annual Review of Earth and Planetary Sciences **32**, 257–285.

Smith, D.G., 1976. Effect of vegetation on lateral migration of anastomosed channels of a glacier meltwater river. Geological Society of American Bulletin **87**, 857–860.

Sobel, E.R., Hilley, G.E., Strecker, M.R., 2003. Formation of internally-drained contractional basins by arididty-limited bedrock incision. Journal of Geophysical Research **108** (B7), 2344.

Strahler, A.H., 1980. The use of prior probabilities in maximum likelihood classification of remotely sensed data. Remote Sensing of Environment **10**, 135–163.

Swain, P.H., King, R.C., 1973. Two effective feature selection criteria for multispectral remote sensing. Proceedings of the First International Joint Conference on Pattern Recognition, Washington, DC, pp. 536–540.

Sylvestre, F., Servant, M., Servant-Vildary, S., Causse, C., Fournier, M., Ybert, J.P., 1999. Lake-level chronology on the southern Bolivian Altiplano (18–23˚S) during late-Glacial time and the early Holocene. Quat. Res. **51**, 54–66.

Thiessen, A.J., Alter, J.C., 1911. Precipitation averages for large areas. Monthly Weather Review **39**, 1082–1084.

Thorne, C.R., 1982. Processes and mechanisms of riverbank erosion. In: Hey, R.D., Bathurst, J.C., Thorne, C.R. (Eds.), Gravel-Bed Rivers. Wiley, Chichester, pp. 227–271.

Thornes, J.B., 1994a. Catchment and channel hydrology. In: Abrahams, A.D., Parsons, A.J. (Eds.), Geomorphology of Desert Environments. Chapman and Hall, London, pp. 257–287.

Thornes, J.B., 1994. Channel processes, evolution and history. In: Abrahams, A.D., Parsons, A.J. (Eds.), Geomorphology of Desert Environments. Chapman and Hall, London, pp. 288–317.

Tucker, C.J., 1979. Red and Photographic Infrared Linear Combinations for Monitoring Vegetation. Remote Sensing of Environment **8**, 127–150.

Thompson, L.G., Mosley-Thompson E., Arnao, B.J., 1984. El Niño-Southern Oscillation events recorded in the stratigraphy of the tropical Quelccaya ice cap, Peru. Science **226**, 50–52.

Thornes, J.B., 1976. Semi-arid erosional systems: case studies from Spain. London School of Economics Geographical Papers No. 7.

Tooth, S., 1999. Downstream changes in floodplain character on the Northern Plains of arid central Australia. In: Smith, N.D., Rogers, J. (Eds.), Fluvial Sedimentology VI, International Association of Sedimentologists, Special Publication 28. Blackwell Scientific Publications, Oxford, pp. 93–112.

Tooth, S., 2000a. Process, form and change in dryland rivers: a review of recent research. Earth-Science Review **51**, 67–107.

Tooth, S., 2000b. Downstream changes in dryland river channels: the Northern Plains of arid central Australia. Geomorphology **34**, 33–54.

Tooth, S., Nanson, G.C., 2000. The role of vegetation in the formation of anabranching channels in an ephemeral river, Northern Plains, arid central Australia, Hydrological Processes **14**, 3099–3117.

Tooth, S., 2005. Splay formation along the lower reaches of ephemeral rivers on the Northern Plains of arid central Australia. Journal of Sedimentary Research **75**, 636–649.

Tooth, S., Jansen, J.D., Nanson, G.C., Coulthard, T.J., Pietsch, T., 2007. Riparian vegetation and the late Holocene development of an anabranching river: Magela Creek, northern Australia. Bulletin of the Geological Society of America **119**, 452–461.

Tooth, S., Nanson, G.C., 2011. Distinctiveness and diversity of arid zone river systems. In: Thomas, D.S.G. (Eds.), Arid Zone Geomorphology: Processes, Form and Change in Drylands (3rd edition). Wiley, Chichester, pp. 269-300.

Tooth, S., Hancox, P.J., Brandt, D., McCarthy, T.S., Jacobs, Z., Woodborne, S., 2013. Controls on the genesis, sedimentary architecture, and preservation potential of dryland alluvial successions in stable continental interiors: insights from the incising Modder River, South Africa. Journal of Sedimentary Research **83**, 541–561.

Tooth, S., McCarthy, T., Rodnight, H., Keen-Zebert, A., Rowberry, M., Brandt, D. 2014. Late Holocene development of a major fluvial discontinuity in floodplain wetlands of the Blood River, eastern South Africa. Geomorphology **205**, 128–141.

Torres Carranza, Y.A., 2013. Static reservoir model of crevasse splays in the Colorado River system, Salar de Uyuni, Bolivia. MSc. thesis, Technische Universiteit Delft, Delft, The Netherlands, pp. 21-30.

Toutin, T., 2008. ASTER DEMs for geomatic and geoscientific applications: a review. International Journal of Remote Sensing **29**, 1855–1875.

Townshend, J.R.G., Quarmby, N.A., Millington, A.C., Drake, N.A., White, K.H., 1989. Monitoring playa sediment transport systems using Thematic Mapper data. Advance Space Research **9**, 177–183.

Tucker, C.J., 1979. Red and Photographic Infrared Linear Combinations for Monitoring Vegetation. Remote Sensing of Environment **8**, 127–150.

Vogel, H.-J., Hoffmann, H., Leopold, A., Roth, K., 2004. Studies of crack dynamics in clay soil. II: a physically-based model for crack formation. Geoderma **125**, 203–213.

Vuille, M., 1999. Atmospheric circulation anomalies over the Bolivian Altiplano during dry and wet periods and extreme phases of the Southern Oscillation. International Journal of Climatology **19**, 1579–1600.

Vuille, M., Bradley, R.S., Keimig, F., 2000a. Interannual climate variability in the Central Andes and its relation to tropical Pacific and Atlantic forcing. Journal of Geophysical Research **105**, 12447–12460.

Vuille, M., Bradley, R.S., Keimig, F., 2000b. Climate variability in the Andes of Ecuador and its relation to tropical Pacific and Atlantic sea surface temperature anomalies. Journal of Climate **13**, 2520–2535.

Wainwright, J., Bracken, L.J., 2011. Runoff generation, overland flow and erosion on hillslopes. In: Thomas, D.S.G. (Eds.), Arid Zone Geomorphology: Process, Form and Change in Drylands, 3rd ed. John Wiley and Sons Ltd, West Sussex, UK, pp. 241.

Willetts, B.B., Hardwick, R.I., 1993. Stage dependency for overbank flow in meandering channels. Proceedings of the ICS – Water Maritime and Energy **101**, 45–54.

Yair, A., Lavee, H., 1976. Runoff generative process and runoff yield from arid talus mantled slopes. Earth Surface Processes **1**, 235–247.

Yair, A., Lavee, H., 1985. Runoff generation in arid and semi-arid environments. In: Anderson, M.G., Burt, T. (Eds.), Hydrological Forecasting. Wiley, Chichester, pp. 183–220.

Yao Z, Ta W, Jia X, Xiao J. 2011. Bank erosion and accretion along the Ningxia-Inner Mongolia reaches of the Yellow River from 1958 to 2008. Geomorphology **127**, 99–106.

Zhao, W., Wang, H., Yuan, X., Wang, Z., Zhu, G., 2010. Petroleum systems of Chinese basins. Basin Research **22**, 4–16.

Zhou, J., Lau, K.-M., 1998. Does a monsoon climate exist over South America? J. Clim. **11**, 1020–1040.

Ziegler, P.A., 1990. Geological Atlas of Western and Central Europe, Second Edition: Shell Internationale Petroleum Mij. BV, and Geological Society of London, pp. 1–239.

Summary

Many ancient sedimentary basins are interpreted as endorheic basins, internally drained basins with no direct hydrological connection to the marine environment. Some of these endorheic basins are economically important because of the abundance of hydrocarbon resources. To date, many studies have been conducted on fluvial systems in endorheic basins; however, the fluvial architecture and facies distribution in ancient fluvial systems are not fully understood. Although they are an important key to rock record interpretation, modern terminal fluvial systems in semi-arid endorheic basins are rarely reported due to difficulties such as poor accessibility. The major objectives of this study are to: (1) investigate the development in space and time of the channel morphology and sediment distribution of a distal fluvial system in a semi-arid climatic setting, and (2) to build a quantitative data set for the construction of a 3D sedimentary architecture model. The study is carried out on a river terminus system, the Río Colorado, at the edge of the world's largest salt lake, the Salar de Uyuni in Bolivia. This unconfined and largely non-vegetated river terminus provides the opportunity to acquire a large data set including field and satellite data that enables analysing the development of channel morphologies and sediment characteristics (e.g., avulsion history, splay morphology and surface dynamics). The data acquisition consists of daily precipitation data, a Global Digital Elevation Model (GDEM), a time-series Landsat imagery and high resolution WorldView-02 and QuickBird-02 satellite images, as well as surface and shallow sediment samples and high precision GPS data (Chapter 1).

Changes in channel morphology of the terminal fluvial system are a function of the precipitation intensity in the catchment area (Chapter 2). The catchment area is characteristic of a mean slope of 0.0008 m/m with the highest slope near the margin and gradually decreasing slope downstream, as well as higher vegetation cover in the mountainous regions than that in the tributary delta and terminal fluvial fan. Ten peak discharge events with more than 50 m3/s have been pinpointed between 1985 and 1999. The peak discharges resulted in massive flood-out of water and sediment onto the floodplain in the very low gradient river terminus and with a cross sectional channel area of less than 80 m2. The development in space and time of crevasse splays and local avulsions was visualized by comparing Landsat MSS and TM images before and after peak discharge events. Crevasse splays expanded in peak discharge periods, and this led to amalgamation with adjacent crevasse splays by compensational stacking. The areal extent of the crevasse splays did not change in between peak discharge events. Multiple local avulsions were distinguished between 1975 and 2001. Crevasse splays and their crevasse channels can evolve over time to an entirely new river channel.

Erosion greatly exceeds accretion on both banks of the river in the tributary catchment. The prominent river bank erosion is associated with an evolving channel planform such as meander morphology, channel morphology and river pattern development (Chapter 3). Normalized Difference Vegetation Index (NDVI) analysis and field investigations suggest that non-vegetation cover and abundance of desiccation cracks and burrows are the main contributors to bank erosion. Changes in channel planform are the product of continuous lateral migration and

frequent overbank flooding. Shallow channels and poor development of levees in combination with in-channel accretionary benches result in frequent overbank flooding, which lead to a high density of crevasse splays over unconsolidated river banks and accretionary benches. Avulsion and chute channels together with reactivation of partially abandoned meanders and connection of headcuts and crevasse channels produce an anabranching pattern in the study area.

Crevasse splays have been categorized into three classes based on their development in space and time: new crevasse splays (NCS), changing crevasse splays (CCS) and inactive crevasse splays (ICS) (Chapter 4). The occurrence of these three types of crevasse splays shows no relationship with distance along the stream. The local gradient also shows no correlation with the number of crevasse splays. By contrast, the number of crevasse splay shows an exponential increase as the cross-sectional channel area decreases. In addition, some crevasse splays are attributed to the topographic low between adjacent crevasse splays and fill in the depression by compensational stacking.

The unconfined area of the system showed great variations in sediment composition downstream. The alluvial fan segment is characterized by gravel with a fining-upward sequence, whereas the upper coastal plain segment is typified by coarse sand and some fine gravel in the upstream area, grading to fine sand downstream. Silt and clay are the dominant sediments in the lower coastal plain segment, although there is also some very fine sand. It was found that the study area is characterized by a linear decrease downstream in bedload and correspondingly an increase in suspended load deposits (Chapter 5). Thus, in the upper coastal plain bedload deposits dominate, while in the lower coastal plain suspended load deposits are prominent.

A spectral library has been established for four types of surface materials using Landsat surface reflectance in combination with Landsat CDR data and field data analysis (Chapter 6). Four types of surface materials are distinguished in the river terminus: A: salty surface; B: silt-rich surface; C, clay-rich surface; D: salt. The silt-rich surface has a weak correlation with the annual precipitation while the salty surface tends to be inversely proportional to the annual precipitation. There is no relationship between the clay-rich surface and the annual precipitation. The main geomorphological changes have been identified as the formation of crevasse splays and avulsions. High annual precipitation-induced avulsions are found to lead to increased silt-rich surfaces.

Channel and splay morphodynamics, longitudinal sediment dispersion pattern in the system, and surface composition in the river terminus are the focus of this study. The expected preservation potential and sequence stratigraphy of the Río Colorado system is discussed. Future work on such dryland river systems could include investigations of the mechanisms of fluvial discontinuity at the boundary between alluvial fan and upper coastal plain, the interaction between aeolian dunes and fluvial systems in the Río Colorado river system, and groundwater regimes in the coastal plain (Chapter 7).

Samenvatting

Veel sedimentaire bekkens zijn geïnterpreteerd als endorheïsch. Dit zijn bekkens waarin de afwatering geen hydrologisch contact heeft met een zee of oceaan. Sommige van deze bekkens zijn economisch van belang vanwege de accumulatie van olie- en gasvoorraden. Hoewel veel voorgaande studies zijn gewijd aan fluviatiele systemen in endoreïsche bekkens, kunnen de fluviatiele architectuur en facies distributie nog niet geheel verklaard worden. Moderne fluviatiele systemen in semidroge endorheïsche bekkens vormen een belangrijke sleutel voor de interpretatie van oudere systemen. Toch zijn er weinig detailbeschrijvingen vanwege complicaties zoals slechte toegankelijkheid. De belangrijkste doelen van deze studie zijn: (1) het onderzoeken van de ontwikkeling in ruimte en tijd van geulgeometrie en sedimentverdeling in de terminus van een fluviatiel systeem in een semidroog klimaat, en (2) het vergaren van kwantitatieve gegevens die dienen voor de constructie van een 3D sediment architectuur model. Het onderzoekgebied is een terminaal fluviatiel systeem, de Río Colorado, aan de rand van het grootste zoutmeer in de wereld: de Salar de Uyuni in Bolivia. De onbegrensde en grotendeels onbegroeide riviermonding biedt de mogelijkheid om een grote kwantitatieve dataset te vergaren, inclusief veld- en satellietdata. Dit maakt analyse mogelijk van de ontwikkeling van geulgeometrie en sedimentaire kenmerken zoals: avulsie geschiedenis, morfologie van crevasse complexen, en oppervlakte dynamiek. De dataverzameling bestaat uit dagelijkse neerslagmetingen, een 'Global Digital Elevation Model' (GDEM), periodieke Landsat satellietbeelden, hoge resolutie WorldView-02 en QuickBird-02 satellietbeelden, oppervlakte sediment monsters en hoge precisie GPS data (*Hoofdstuk 1*).

Veranderingen in de geulgeometrie in de terminus van het fluviatiele systeem zijn afhankelijk van de neerslagintensiteit in het afzettingsgebied (*Hoofdstuk 2*). Het afzettingsgebied heeft een karakteristieke gemiddelde helling van 0.0008 m/m met het steilste gedeelte langs de grenzen en een geleidelijk afnemende helling stroomafwaarts. De meeste vegetatie wordt gevonden aan de bergzijde; het mondingsgebied en de delta zijn minder begroeid. De grootste piekafvoer momenten zijn gemeten in 1985 en 1999. De waterafvoer bedroeg toen 50 m^3/s. Piekafvoer resulteert in het buiten de oevers treden van de geulen en overstroming van de naastgelegen alluviale vlakte. De rivier heeft een lage gradiënt en de oppervlakte van de geuldoorsnede is minder dan 80 m^2. De ontwikkeling in tijd en ruimte van crevasse complexen en lokale avulsies is in beeld gebracht door het vergelijken van Landsat MSS en TM beelden, voor en na piekafvoer. Gedurende deze momenten breidden crevasse-complexen zich uit en dit heeft geleid tot laterale stapeling van crevasse-afzettingen door hoogteverschillen. De omvang van de crevasse-afzettingen veranderde niet tussen verschillende piekafvoer momenten. Verscheidene lokale avulsies zijn herkend tussen 1975 en 2001. Crevasse-afzettingen en hun geulen kunnen zich ontwikkelen tot nieuwe riviergeulen.

Erosie is sterker dan aangroei op de oevers van het bovenstroomse riviergebied. De prominente rivieroever erosie is gerelateerd aan factoren zoals meander morfologie, geulmorfologie en rivierpatroonontwikkeling (*Hoofdstuk 3*). Analyse van de Normalized Difference

Vegetation Index (NVDI) en veldonderzoek suggereren dat de afwezigheid van vegetatie, en de overvloed aan krimpscheuren en graafgangen de belangrijkste bijdragen vormen voor de erosie van rivieroevers. Veranderingen in geulpatronen zijn het resultaat van continue laterale geulverplaatsing en frequente overstromingen. Ondiepe geulen en slecht ontwikkelde oeverwallen in combinatie met de vorming van drempels in de geulen resulteren in frequente overstromingen. Deze overstromingen leiden tot een hoge dichtheid van crevasse-afzettingen over ongeconsolideerde rivieroevers en aangroeiende bermen. Avulsie, afsnijding van meandergeulen in combinatie met het opnieuw actief worden van deels verlaten meanderbochten, en het ontstaan van verbindingen tussen crevassegeulen en terugschrijdende erosiegeulen in de alluviale vlakte produceren vlechtende patronen van vertakkende riviergeulen in het studiegebied.

Crevasse-afzettingen zijn ondergebracht in drie verschillende klassen afhankelijk van hun ontwikkeling in ruimte en tijd: nieuwe crevasse-afzettingen (NCS), veranderde bestaande crevasse-afzettingen (CCS) en inactieve crevasse-afzettingen (ICS) (*Hoofdstuk4*). Het voorkomen van deze klassen is niet gerelateerd aan locatie in de alluviale vlakte. De lokale gradiënt is ook niet gerelateerd aan de frequentie van het voorkomen van crevasse-afzettingen. Echter, er is wel een exponentiële toename herkend van crevasse-afzettingen wanneer het stroomoppervlakte van de geul afneemt. Daarbij wordt de locatie van sommige crevasses toegeschreven aan de topografische depressie tussen twee andere crevasses in. Ze vullen dan deze depressie in door middel van locale topografische compensatie.

Het onbeperkte gebied van het stroomafwaartse deel van het riviersysteem bevat grote variaties in sediment samenstelling. Het alluviale waaier segment wordt gekarakteriseerd door grind met een naar boven fijner wordende korrelgrootte trend. In het stroomopwaartse gebied is de korrelgrootte juist gekenmerkt door grof en soms fijn grind. Steeds fijner sediment wordt stroomafwaarts gevonden. Silt en klei zijn de meest voorkomende sedimenttypen in de benedenstroomse alluviale vlakte, hoewel ook fijn zand voorkomt. In deze studie is bepaald dat het onderzoeksgebied gekenmerkt wordt door een lineaire afname stroomafwaarts van sediment transport over de rivierbodem en een samenhangende toename van suspensietransport (*Hoofdstuk 5*). Ofwel, in het stroomopwaartse deel van het riviersysteem is sediment transport over de bodem dominant, en stroomafwaarts is suspensietransport het meest voorkomende proces.

Een spectrale bibliotheek is samengesteld voor vier typen oppervlaktematerialen met behulp van Landsat oppervlaktereflectie in combinatie met Landsat CDR gegevens en analyses van veldwerkgegevens (*Hoofdstuk 6*). Vier types oppervlaktematerialen worden onderscheiden in de terminus van het riviersysteem. A: een zoutrijk oppervlak; B: een siltrijk oppervlak; C: kleirijk oppervlakte; D: zout. Het siltrijke oppervlak heeft een zwakke relatie met de jaarlijkse neerslag terwijl het zoutrijke oppervlak omgekeerd evenredig staat tot de jaarlijkse neerslag. Er is geen relatie tussen het kleirijke oppervlak en de jaarlijkse neerslag. De belangrijkste geomorfologische veranderingen worden toegeschreven aan de vorming van crevasse-afzettingen en aan avulsies. Avulsies die worden veroorzaakt door hoge jaarlijkse neerslag leiden tot toenemende siltrijke oppervlakten.

In deze studie ligt de nadruk op geul en de morfologie van crevasse-complexen, verspreiding van sediment in de stroomrichting van het systeem en oppervlaktesamenstelling aan het einde

van het riviersysteem. De verwachte accumulatie van sediment en de sequentie stratigrafie van het Río Colorado riviersysteem worden besproken. Toekomstig onderzoek aan dergelijke droge riviersystemen zou gericht kunnen worden op de mechanismen van fluviatiele discontinuïteit op de grens tussen alluviale waaier en de hogere alluviale vlakte. Ook zou er gekeken kunnen worden naar de interactie tussen eolische duinen en het Río Colorado riviersysteem en grondwater regimes in de alluviale vlakte (*Hoofdstuk 7*).

Curriculum Vitae

Jiaguang Li was born on the 3rd of November, 1984 on the southeast coast of China, Fujian province. He finished his pre-college education in a southwester county of Fujian, Wuping. He started the BSc petroleum engineering study in 2004 at China University of Geosciences (Beijing) and four years later, he was granted for the master study in the same university. Jiaguang spent the second year of the MSc study doing his thesis at the Research Institute of Exploration and Development of the China National Petroleum Corporation (CNPC). For his MSc thesis, he investigated hydrocarbon reservoirs with low porosity and low permeability in Xishanyao Formation, Niujuanhu Depression, Santanghu Basin, Xinjiang province. Jiaguang published a review article and research papers in nationwide academic journals, as well as international conference abstracts during BSc and MSc study. After two years' MSc study, Jiaguang started his PhD in October 2010 under the supervision of Prof. Dr. S.M. Luthi and Dr. M.E. Donselaar at the section of Applied Geology on terminal fluvial systems in a semi-arid endorheic basin. He conducted an independent fieldwork in Salar de Uyuni, Bolivia in November 2012. The research resulted in several journal papers and several conference abstracts. Jiaguang Li will go back to China and work in a university.

Acknowledgements

List of proceedings and publications

Peer-reviewed Journal Publications

Li, J., Donselaar, M.E., Hosseini Aria, S.E., Koenders, R., Oyen, A.M., 2014. Landsat imagery-based visualization of the geomorphological development at the terminus of a dryland river system. Quaternary International. *DOI: 10.1016/j.quaint.2014.06.041*

Li, J., Luthi, S.M., Donselaar, M.E., Weltje, G.J., Prins, M.A., Bloemsma, M.R., 2014. An ephemeral meandering river system: Sediment dispersal processes in the Río Colorado, Southern Altiplano Plateau, Bolivia. Zeitschrift für Geomorphologie (accepted for publication).

Li, J. , Luthi, S.M., Bristow, C.S., Donselaar, M.E., submitted. Dryland river bank accretion and erosion and their impacts on channel planform: Río Capilla, Salar de Uyuni, Bolivia. Earth Surface Processes and Landforms.

Li, J., Bristow, C.S., submitted. Splay morphodynamics in a dryland meandering river terminus: Río Colorado in Salar de Uyuni Bolivia. Quaternary International.

Li, J., Menenti, M., Mousivand, A., Luthi, S.M., submitted. Non-vegetated playa morphodynamics using multi-temporal Landsat imagery in a semi-arid endorheic basin: Salar de Uyuni, Bolivia. Remote Sensing.

Conference Publications

Li, J., Donselaar, M.E., Bloemsma, M.R., Prins, M.A., Weltje, G.J., Torres, Y.A., 2013. Grain size distribution of unconsolidated sediments at the terminus of a semi-arid river system and its use to reconstruct paleo-geomorphology. International conference on Fluvial Sedimentology 10, Leeds, UK. (oral presentation).

Li, J., Menenti, M., Donselaar, M.E., Prins, M.A., Hosseini Aria, S.E., Koenders, R., Oyen, A., 2013. Interaction between aeolian and rivers in a dryland fluvial system with remote sensing techniques. International conference on fluvial sedimentology 10, Leeds, UK. (poster presentation)

Hosseini Aria, S.E., Donselaar, M.E., Lindenbergh, R.C., Koenders, R., Li, J., Oyen, A.M., 2012. Monitoring a river channel network at Salar de Uyuni using Landsat ETM+ images. In: Neale, C.M.U., Maltese, A. (Eds.), Remote sensing for agriculture, ecosystems, and hydrology XIV Vol. 8531. Proceedings of SPIE- International Society for Optical Engineering (pp. 1-9). SPIE.

Oyen, A.M., Koenders, R., Hosseini Aria, S.E., Lindenbergh, R.C., Li, J., Donselaar, M.E., 2012. Application of synthetic aperture radar methods for morphological analysis of the salar de uyuni distal fluvial system. In s.n. (Eds.), Proceedings of the IEEE International Geoscience and Remote Sensing Symposium IGARSS 2012 (pp. 3875-3878). Piscataway: IEEE.

Donselaar, M.E., Li, J., Hosseini Aria, S.E., Koenders, R., Lindenbergh, R.C., Oyen, A.M., 2012. Sand sheet connectivity in a low net-to-gross setting: Remote sensing-based modeling of a river channel network in a terminal fluvial system. In s.n. (Eds.), AAPG Annual Conference and Exhibition (pp. 106-106). Tulsa: AAPG**.**